ESTEC Contract 21487/08/NL/HE

Aerosols and Clouds: Long-term Database from Spaceborne Lidar Measurements

Final Report

22 June 2011

Ulla Wandinger, Anja Hiebsch, and Ina Mattis
Leibniz Institute for Tropospheric Research
Permoserstrasse 15, 04318 Leipzig, Germany

Gelsomina Pappalardo, Lucia Mona, and Fabio Madonna
Istituto di Metodologie per l'Analisi Ambientale
Contrada S. Loja, Tito Scalo zona industriale, 85050 Potenza, Italy

ESA STUDY CONTRACT REPORT

ESA CONTRACT No 21487/08/NL/HE	SUBJECT Aerosols and Clouds: Long-term Database from Spaceborne Lidar Measurements		CONTRACTOR Leibniz Institute for Tropospheric Res.
*ESA CR( )No	*STAR CODE	No of volumes: 1 This volume is no. 1	CONTRACTOR'S REFERENCE: ESA-CALIPSO

ABSTRACT:

This report describes the establishment of a long-term aerosol and cloud database from ground-based lidar network measurements taken in the frame of EARLINET (European Aerosol Research Lidar Network) and spaceborne lidar observations with CALIOP (Cloud-Aerosol Lidar with Orthogonal Polarization) onboard the polar-orbiting satellite CALIPSO (Cloud-Aerosol Lidar Infrared Pathfinder Satellite Observations). The database shall support the harmonization of continuous global observations from space with different sensors over the next decade. For this purpose, a correlative set of data taken with EARLINET and CALIOP over a period of 18 months has been collected and exploited. Sixteen EARLINET stations participated in the study. They provided measurements at multiple wavelengths which have been used to derive wavelength conversion factors to relate spaceborne observations from CALIPSO with its lidar operating at 532 and 1064 nm to future ESA missions applying 355-nm high-spectral-resolution lidars. Furthermore, the spatial distribution of stations allowed us to study the representativeness of cross sections along an orbit against network observations.

Based on the comprehensive sample of more than 1300 observations performed by EARLINET stations during overpasses of CALIPSO from May 2008 to October 2009, a relational database has been set up which contains information on EARLINET and CALIPSO Level 2 profile data, EARLINET-CALIPSO difference profiles, geometrical and optical data of a large number of selected aerosol and cloud layers from EARLINET measurements and respective comparisons of EARLINET and CALIPSO layer products. An aerosol and cloud classification scheme has been developed and applied to the database. The aerosol classification has been evaluated in detail, based on a critical assessment of the CALIPSO typing schemes and built on the expert knowledge within EARLINET and the experience of the partners gained in field experiments around the world. Conclusions and recommendations with specific view on ongoing and future algorithm development studies related to ESA's EarthCARE and ADM missions are provided.

The work described in this report was done under ESA contract. Responsibility for the contents resides in the author or organization that prepared it.

Names of authors: Ulla Wandinger, Anja Hiebsch, Ina Mattis, Gelsomina Pappalardo, Lucia Mona, Fabio Madonna

NAME OF ESA STUDY MANAGER: Paul Ingmann DIV: Mission Science Division DIRECTORATE: Earth Observation Programmes	ESA BUDGET HEADING E/0600 - General Studies Programme

* Sections to be completed by ESA

Contents

Chapter 1

Introduction

1.1 Motivation

This report describes the establishment of a long-term aerosol and cloud database from ground-based lidar network measurements taken in the frame of EARLINET (European Aerosol Research Lidar Network) and spaceborne lidar observations with CALIOP (Cloud-Aerosol Lidar with Orthogonal Polarization) onboard the polar-orbiting satellite CALIPSO (Cloud-Aerosol Lidar Infrared Pathfinder Satellite Observations). The database shall support the continuous, harmonized observation of relevant climatological parameters with active remote-sensing techniques from space over the next decade. CALIPSO provides vertically resolved information on aerosol and cloud parameters since June 2006. This date can be regarded as the starting point of a unique long-term, global, 4-dimensional data set that will substantially improve our knowledge on the role of aerosols and clouds in the Earth's climate system. The ADM–Aeolus (Atmospheric Dynamics Mission–Aeolus of the European Space Agency ESA) and EarthCARE (Earth Clouds, Aerosols and Radiation Explorer of ESA and the Japan Aerospace Exploration Agency JAXA) missions will continue such kind of observations in subsequent years and prolong the data set to at least a decade. In this way, we can expect a unique data set on the global aerosol and cloud distribution and respective trends in cloud cover, cloud amount, and aerosol pollution state.

However, the lidar instruments onboard the three missions represent different system types with different sets of measured parameters at different wavelengths (355, 532, and 1064 nm). Table 1.1 gives an overview on the ongoing and upcoming space lidar missions and their optical data products (*Winker et al.*, 2003, 2009; *Stoffelen et al.*, 2005; *Ansmann et al.*, 2006; *European Space Agency (ESA)*, 2004). CALIOP is a two-wavelength backscatter lidar operating at 532 and 1064 nm. In contrast, the Atmospheric Laser Doppler

Lidar Instrument (ALADIN) onboard the ADM–Aeolus mission and the Atmospheric Lidar (ATLID) of the EarthCARE satellite make use of the high-spectral-resolution lidar technique in the UV. Consequently, ALADIN and ATLID will deliver independent information on extinction and backscatter coefficients at 355 nm and thus on the extinction-to-backscatter ratio (lidar ratio) at this wavelength. From CALIOP we obtain backscatter coefficients at 532 and 1064 nm and thus the 1064-nm-to-532-nm color ratio. To derive extinction profiles and optical-depth information from CALIOP measurements, assumptions on the lidar ratio are needed. CALIOP and ATLID also measure the particle linear depolarization ratio at 532 and 355 nm, respectively.[1] In contrast, the radiation emitted by ALADIN is circularly polarized and the co-polarized component of the backscattered light is detected only.[2]

Table 1.1: Long-term spaceborne lidar observations (BL–Backscatter Lidar, HSRL–High Spectral Resolution Lidar).

Period	**Lidar**	**Mission**	**Products**
2006–ongoing	CALIOP (VIS/IR BL)	CALIPSO	Backscatter coefficient (532 nm) Backscatter coefficient (1064 nm) Color ratio (532/1064 nm) Linear depolarization ratio (532 nm)
after 2013	ALADIN (UV HSRL)	ADM-Aeolus	Extinction coefficient (355 nm, co-polar) Backscatter coefficient (355 nm, co-polar) Lidar ratio (355 nm, co-polar)
after 2016	ATLID (UV HSRL)	EarthCARE	Extinction coefficient (355 nm) Backscatter coefficient (355 nm) Lidar ratio (355 nm) Linear depolarization ratio (355 nm)

1.2 Objectives

In order to establish a useful common aerosol and cloud data set from the spaceborne observations, long-term, ground-based support with advanced lidar instruments is required. The ground-based instruments must deliver necessary conversion information for different aerosol and cloud types to relate the spaceborne measurements at 355, 532, and 1064 nm

[1] The EarthCARE Mission Advisory Group recommended to measure linear instead of circular depolarization after the ATLID re-design from a monostatic to a bistatic transmitter–receiver configuration in 2009/10.

[2] A discussion of the consequences is provided in Chapter 9.

to each other. A second major aspect is the investigation of the representativeness of spaceborne observations on the regional and continental scale. Here, the comparison of measurements from the orbiting satellite and from a network of ground-based stations provides the required information based on a statistically significant data set, i.e. a sufficient large number of correlative observations.

Our study represents the first dedicated activity in this context. The main objectives driving this activity were:

- Take advantage of the unique opportunity to conduct comprehensive ground-truth lidar observations at 16 EARLINET stations during overpasses of the CALIPSO satellite. The goal is to achieve an optimum adjustment of long-term aerosol and cloud data sets in preparation for later missions in view of the development of a climatological database.

- Explore aerosol optical characteristics with the goal to investigate the potential to retrieve the aerosol type, to separate man-made from natural aerosol effects, and to relate spaceborne observations carried out with different lidar instruments to each other.

- Explore cloud characteristics with the goal to distinguish water and ice clouds by means of measured sets of extinction and backscatter coefficients, lidar and depolarization ratios.

- Compare the representativeness of cross sections along an orbit against network observations over Europe for an extended period of time and investigate to what extent satellite and network observations can be combined to provide information about the characteristics of aerosols and clouds.

- Investigate the potential applications of the long-term database established as a result of the study.

1.3 Implementation

Within EARLINET, the study has been implemented under the name ESA–CALIPSO (EARLINET's Spaceborne-related Activity during the CALIPSO mission).[3] In the course of the study, the initial set of observational data for the long-term aerosol and cloud database has been sampled and evaluated in detail. EARLINET had started correlative measurements with CALIPSO already at the beginning of the CALIPSO mission in June

[3]The name is also used in this report, in particular in the description of network activities.

2006. Based on the experience gained within the first two years, an optimized observational strategy has been set up in the beginning of the study. It is described in detail in Chapter 2. During an 18-month intensive observational period from May 2008 to October 2009 correlative EARLINET–CALIPSO measurements were taken at 16 EARLINET stations distributed over Europe. Seven of the stations are equipped with instruments to measure at least extinction and backscatter coefficients at both 355 and 532 nm (two-wavelength Raman lidar). Most of them provide also backscatter coefficients at 1064 nm and the particle depolarization ratio. This detailed information from the EARLINET core stations allows us to investigate the potential of spaceborne lidar instruments to identify certain aerosol types and to distinguish man-made from natural aerosol. The data are used for the development of sophisticated aerosol-type classification schemes considering the CALIOP as well as the ALADIN/ATLID data information content. The EARLINET core stations are located such that four European core regions are covered: Central Europe (Germany and The Netherlands), the Western Mediterranean (Spain), the Central Mediterranean (Italy), and the Eastern Mediterranean (Greece). In this way, a broad variety of aerosol types and scenarios can be investigated, which include maritime aerosol as well as urban and rural continental aerosol, Saharan dust, and forest-fire smoke, including long-range-transport aerosols in the free troposphere from America and Asia.

The remaining stations participating in this study create clusters around the core stations. Most of them operate Raman lidar instruments as well, but not at several wavelengths. Highly reliable extinction and backscatter coefficients are retrieved at either 355 or 532 nm at these sites. Typical distances of neighboring stations within a cluster are 120 to about 800 km. The distribution of the stations allows us to study the temporal, regional and continental-scale representativeness of the observations and to compare these findings with the results of spaceborne lidar measurements from the polar-orbiting satellites.

Starting from the extinction and backscatter profiles provided by the individual EARLINET stations, the measurements have been investigated in detail with respect to layer-mean values of spectral backscatter and extinction coefficients, lidar ratios, depolarization ratio, extinction- and backscatter-related Ångström exponents and color ratios (or wavelength conversion factors, i.e. ratios of backscatter coefficients at 1064/532 nm, 1064/355 nm, 532/355 nm, and of extinction coefficients at 532/355 nm). Observed aerosol and cloud layers are classified. For aerosols an extended analysis of source regions, age, and state of humidification is performed with the help of models and auxiliary data. Cloud classification focuses on the discrimination of water, ice, and mixed-phase clouds. For both profile and layer products the differences to the respective CALIPSO Level 2 products are calculated in dependence on the spatial and temporal distance of the observations. Chapter 3 provides a detailed discussion of the data evaluation concept with focus on the aerosol and cloud classification.

The complete data set is stored and controlled in a relational database. Its structure is explained in Chapter 4. The database is used for the exploitation of the results and the statistical evaluation of the complete data set. Chapters 5 to 7 present the major outcome of the study in terms of the aerosol and cloud measurements and the investigations of the representativeness of satellite cross sections against network observations. Several highlights are discussed in detail. In the very beginning of the observational period, a strong Saharan dust outbreak occurred over Europe (see Sec. 5.1.2.2). This episode at the end of May 2008 gave us the opportunity to test and improve the strategies and tools and to publish early results of the study (*Pappalardo et al.*, 2010). The eruptions of several volcanos in the North Pacific between July 2008 and September 2009 initiated an unexpected focus on the properties of volcanic aerosol layers in the upper troposphere and lower stratosphere (see Sec. 5.1.6). These results have been published by *Mattis et al.* (2010). An additional activity was triggered by discrepancies found between EARLINET and CALIPSO measurements of optical properties of Saharan dust. It could be shown that multiple scattering plays a role in spaceborne observations of large dust particles which leads to a significant bias in the derived optical depth for desert aerosol (*Wandinger et al.*, 2010).

An extension of the study became necessary because of a major change in the CALIPSO data evaluation strategy in 2009. On 16 February 2009 the CALIPSO payload shut itself down due to low laser energy, a few weeks before the planned switch to the backup laser. EARLINET stopped correlative observations at that time. On 9 March 2009 the CALIPSO backup laser was turned on and successfully tested and aligned. CALIPSO has been operating in data acquisition mode with the backup laser nearly continously since 18 March 2009. EARLINET restarted correlative measurements immediately on 18 March 2009. However, at that time the CALIPSO Science Team decided that both Level 1 and Level 2 data from the backup laser will be processed with the new Version 3 code only. The delivery of Version 2 data used in the study so far was completely stopped. Unfortunately, because the new code was still in the test stage, it took a rather long time until CALIPSO data became available again. Level 1 Version 3 data have been published in November 2009, Level 2 Version 3 data which are most essential for the study became available at the end of May 2010 only. An even longer break occurred in the delivery of the EARLINET subset of data which had been directly transferred according to an bilateral agreement between NASA and EARLINET until February 2009.

The change in the CALIPSO data evaluation procedures caused not only a delay, but had several other consequences for the study. First of all, new hardware and software had to be implemented in order to handle the comprehensive Version 3 data sets. The delivery of Version 3 data from NASA to the EARLINET archive in Hamburg started at the end of October 2010. Priority was given to data of the period April–May 2008 favoring

comparison for the Saharan dust case that occurred on 25–31 May 2008. The EARLINET data archive hosted at the Max Planck Institute in Hamburg was not designed for the much larger size of the Version 3 data files, and the data transfer from NASA was stopped in November 2010. A completely new archive, specifically designed, has been implemented at CNR–IMAA. The automatic upload of CALIPSO data from NASA is foreseen for the end of June 2011. Although limited by the few Version 3.01 data available, we had the opportunity to perform first comparisons and investigate changes and improvements of the new data release. In particular, working on the dust case observed in May 2008 for which also a representativeness study was performed on Version 2 data, the utility of 5-km profiles provided in the Version 3 release was investigated. Results are presented in Chapter 8.

In Chapter 9 of this report, we summarize the major findings of the study and provide conclusions and recommendations which should be helpful in the algorithm developments for active laser remote-sensing instruments of upcoming ESA missions, in particular the high-spectral-resolution lidars ALADIN and ATLID. We also discuss deficiencies with respect to the occurrence of aerosols on the global scale and we give an outlook regarding future extensions and public use of the database.

Chapter 2

EARLINET–CALIPSO correlative observations

This chapter describes the refined strategy for EARLINET–CALIPSO correlative measurements developed for this study. Following this strategy, 16 EARLINET stations performed CALIPSO correlative measurements during a period of 18 months from May 2008 to October 2009. The products in terms of extinction and backscatter coefficient profiles were submitted by all stations to the EARLINET database, from where they were taken for further evaluation. Exploitation of EARLINET data acquired following the refined strategy allows us to obtain a classification scheme for aerosol type and clouds, to derive conversion factors, and to investigate the representativeness of satellite cross-section against network observations. Therefore, refining the EARLINET–CALIPSO correlative measurements strategy in an appropriate way was an essential pre-requisite to achieve the goals of the study. After a review of the EARLINET–CALIPSO observational strategy applied before the start of this study in Section 2.1, Section 2.2 describes the setup of the ground-based network. In Section 2.3 we discuss the requirements for a refined strategy. Section 2.4 describes the new strategy and explains the procedure for the exchange of information among the participating stations. Finally, Section 2.5 presents the measurement statistics of scheduled and performed measurements within the 18-month intensive observation period.

2.1 Previous experience

Aldready before the launch of the satellite, a strategy for CALIPSO correlative measurement was established within EARLINET. Almost all EARLINET stations agreed to perform CALIPSO correlative measurements on a voluntary basis. Therefore, there

were no commitments for any measurements, but in the measurement plan it was considered that measurements performed according to official CALIPSO validation criteria are strongly suggested (mandatory measurements), while additional measurements interesting for variability and long-range-transport studies are welcome (suggested measurements). Since June 14, 2006, EARLINET has been acting as a single big instrument for CALIPSO validation purposes. A three-stage strategy was established for CALIPSO correlative studies. This strategy foresaw that each station had to perform measurements for at least one hour when CALIPSO overpasses its location within 100 km (so-called Case 1 measurements). In this case, measurements are considered mandatory for the corresponding EARLINET station, even if there is no commitment for that. In addition, measurements were suggested to the EARLINET station and the multiwavelength EARLINET station that are closest to the one overpassed by CALIPSO (so-called Case 2 and Case 3 measurements, respectively). Such measurements were suggested for exploiting the EARLINET network capability to investigate the modification of aerosol properties over the European continent and for combining all these information with CALIPSO profiles. The Case 1 measurement schedule was calculated starting from the 1-s resolution CALIPSO ground track weekly provided by NASA to the network. Correspondingly, Case 2 and Case 3 measurements were planned. The updated measurement plan was weekly distributed to all EARLINET participants. Following this strategy, on average each EARLINET station should perform one to two CALIPSO correlative measurements during daytime and one to two during night for each 16-day CALIPSO repetition cycle. Case 2 and Case 3 measurements (only suggested) could add another one to two measurements both for day and night conditions.

2.2 Setup of the network

Sixteen EARLINET stations were selected for the ESA–CALIPSO study. They are listed in Tab. 2.1. Two types of stations are defined: high-performance and contributing stations. The seven high-performance stations are equipped with instruments to measure at least extinction and backscatter coefficients at both 355 and 532 nm (two-wavelength Raman lidar). Most of these stations provide backscatter coefficients at 1064 nm and the depolarization ratio at 532 nm as well. Their measurements are primarily used to develop cloud and aerosol-type classification schemes and to derive conversion factors for the spaceborne lidars. Six of the nine contributing stations operate Raman lidar instruments as well, but not at multiple wavelengths. Highly reliable extinction and backscatter coefficients are retrieved at either 355 or 532 nm at these sites. Measurements from the contributing stations deliver information on the regional representativeness of the observations.

Figure 2.1 shows the geographical distribution of the EARLINET stations. The sta-

Table 2.1: List of EARLINET stations contributing to the ESA-CALIPSO study. Station ID according to EARLINET convention, cluster to which the station belongs (CE–Central Europe, WM–Western Mediterranean, CM–Central Mediterranean, EM–Eastern Mediterranean), coordinates, and measured parameters (α-extinction coefficient, β-backscatter coefficient, δ–depolarization ratio, indices indicate the wavelength, parameters in parentheses have not been used in this study).

Station	ID	Cluster	Coord.	α_{355}	α_{532}	β_{355}	β_{532}	β_{1064}	δ_{532}
High-Performance Stations									
Leipzig	le	CE	51.4 N 12.4 E	x	x	x	x	x	x
Potenza	po	CM	40.6 N 15.7 E	x	x	x	x	x	(x)
Cabauw	ca	CE	52.0 N 4.9 E	x	x	x	x	x	(x)
Maisach	ms	CE	48.2 N 11.2 E	x	x	x	x	x	x
Naples	na	CM	40.8 N 14.2 E	x	x	x	x	–	–
Granada	gr	WM	37.2 N 3.6 W	x	x	x	x	x	(x)
Athens	at	EM	38.0 N 23.8 E	x	x	x	x	x	–
Contributing Stations									
Hamburg	hh	CE	53.6 N 10.0 E	(x)	(x)	x	x	(x)	(x)
L'Aquila	la	CM	42.4 N 13.3 E	x	–	x	–	–	–
Barcelona	ba	WM	41.4 N 2.1 E	–	x	–	x	x	–
Thessaloniki	th	EM	40.6 N 23.0 E	x	x	x	x	–	–
Lecce	lc	CM	40.3 N 18.1 E	x	–	x	–	–	–
Madrid	ma	WM	40.5 N 3.7 W	–	x	–	x	–	–
Belsk	be	–	51.8 N 20.8 E	–	–	x	x	x	–
Minsk	mi	–	53.9 N 27.6 E	x	–	x	x	x	x
Sofia	sf	EM	42.7 N 23.3 E	–	–	–	x	–	–

tions are located such that four European core regions are covered. Thus the stations have been grouped in clusters as follows: Central Europe (cluster CE; Germany and The Netherlands), Western Mediterranean (cluster WM; Spain), Central Mediterranean (cluster CM; Italy), and Eastern Mediterranean (cluster EM; Greece and Bulgaria). In each cluster there is at least one high-performance station. In this way, it is possible to investigate a broad variety of aerosol types and scenarios in detail, such as maritime aerosols (Cabauw, Hamburg, Lecce, Barcelona), urban aerosols (Leipzig, Naples, Athens), rural aerosols (Maisach, Potenza), fresh Saharan dust (Mediterranean stations), aged Saharan dust (all stations), fresh forest-fire smoke (Mediterranean stations), aged forest-fire aerosols (Central European stations), photochemical smog (Athens, Thessaloniki), and long-range-transport aerosols in the free troposphere from America and Asia (all stations). Typical distances of neighboring stations (high-performance and contributing stations) within a cluster reach from 120 to about 800 km. The distribution of the stations allows us to study the temporal, regional and continental-scale representativeness of the observations and to compare these findings with the results of spaceborne lidar measurements from the polar-orbiting satellite. The stations in Belsk and Minsk do not explicitely belong to a cluster, but they extend the network to Eastern Europe and, therefore, can provide additional information on important aerosol source regions.

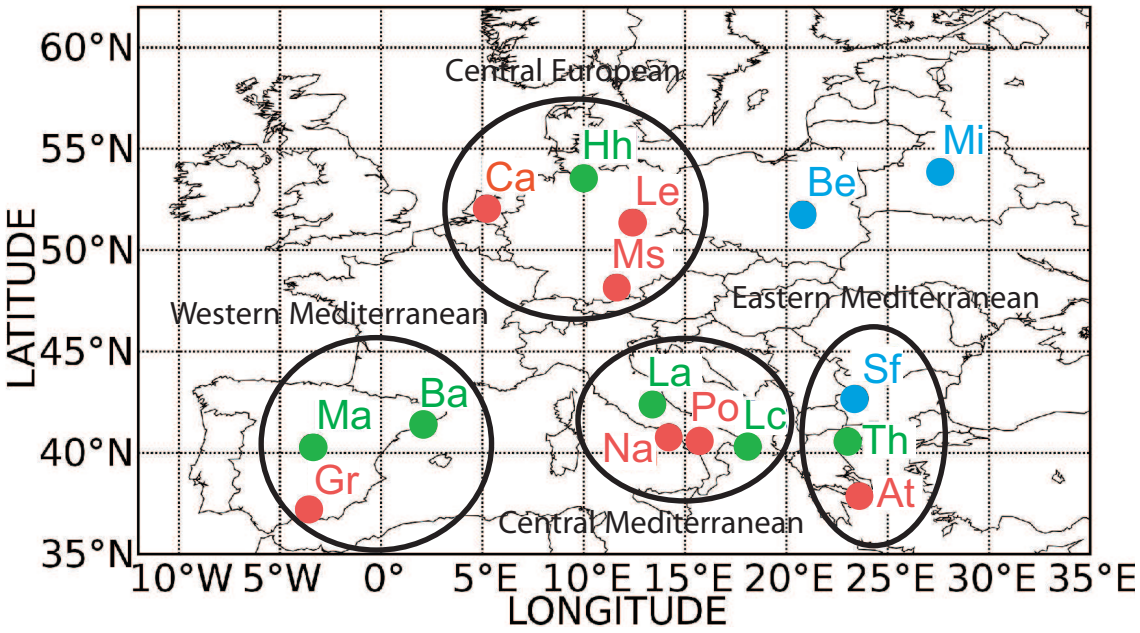

Figure 2.1: Map of EARLINET stations contributing to the long-term aerosol and cloud data set. Red dots show the high-performance core stations (At-Athens, Ca-Cabauw, Gr-Granada, Le-Leipzig, Ms-Maisach, Na-Napoli, Po-Potenza). Green and blue dots represent contributing stations (Ba-Barcelona, Be-Belsk, Hh-Hamburg, La-L'Aquila, Lc-Lecce, Ma-Madrid, Mi-Minsk, Th-Thessaloniki, Sf-Sofia).

2.3 Requirements of an updated strategy

The updated strategy for correlative measurements had to take into account the specific aims of this study. The re-definition of the strategy took advantage from the previous experience of voluntary-basis CALIPSO correlative measurements. In particular, the EARLINET experience gained in almost two years of correlative measurements (June 2006 – April 2008) showed that in about 50% of the cases mandatory Case 1 measurements were not performed because of bad weather conditions (rain, fog, low clouds) and system maintenance. This had to be taken into account for the new planning of measurements. Two main goals were identified for the study:

- providing conversion factors in dependence of aerosol and cloud type and
- investigating the representativeness of CALIPSO data by describing aerosol and cloud fields through correlation analysis with EARLINET network measurements.

To achieve both goals, a large number of EARLINET measurements has to be included in the database in order to assure statistically significant results. With respect to the old strategy we had a restricted number of participating EARLINET stations, therefore it was necessary to increase the number of measurements that each involved station had to perform for CALIPSO correlative studies. Furthermore, EARLINET measurements should allow the investigation of aerosol and cloud properties as a function of geographical region, which is an important point for representativeness studies and for the derivation of conversion factors for regions with different characteristics in terms of orography and aerosol type. Finally, a representativeness study should take into account the variability of aerosol and cloud fields. This is particularly true when a single ground-based measurement is compared to a single satellite-borne measurement with a horizontal distance between the two sampled air volumes different from zero and with a different integration time. Therefore, the refined strategy for EARLINET–CALIPSO correlative measurements should attempt to address also this point trying to quantify this variability. In summary, the strategy for the EARLINET measurement plan devoted to the CALIPSO correlative study had to be redefined in order to address each of the following points:

1. increase the number of measurements of participating stations,
2. increase the number of simultaneous measurements from more EARLINET stations in the different regions of Europe,
3. allow the investigation of spatial and temporal variability of aerosol and cloud fields.

2.4 Description of the updated strategy

The development of a new strategy for EARLINET–CALIPSO correlative measurements had as starting point the criteria established in the CALIPSO validation plan. In particular, each participating EARLINET station had to perform measurements, as close in time as possible, when CALIPSO overpasses its location within 100 km. These mandatory measurements are called Case A measurements (old Case 1). These measurements allow the point-to-point comparison between ground-based and satellite-borne lidar measurements. In this kind of comparison, as reported above, the variability both in time and space is a fundamental point. Besides source and formation mechanisms of both aerosol and cloud features, wind is of course one of the main factors driving the variability.

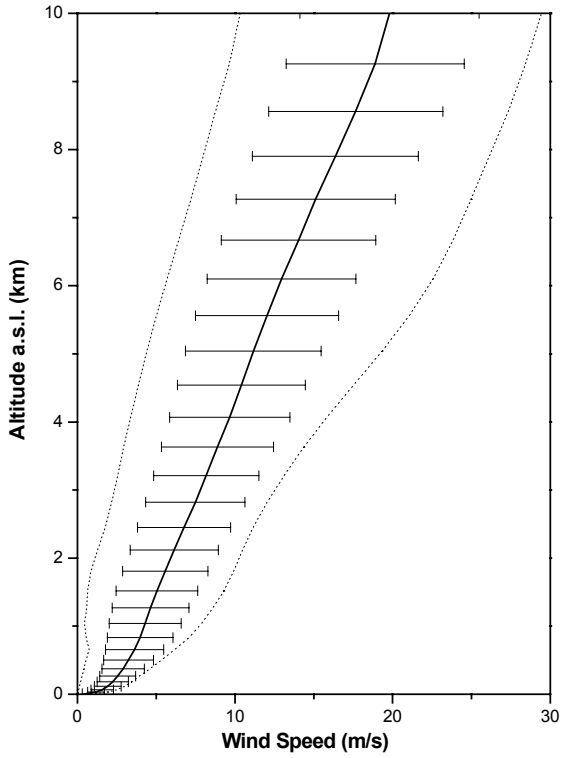

Figure 2.2: Annual mean wind speed profile over Potenza calculated from ECMWF operational forecast model profiles. Error bars represent the standard deviation of the annual mean. Dotted lines report minimum and maximum values observed.

Figure 2.2 shows the annual mean wind speed profile over Potenza as forecast by ECMWF. Although there is a large natural variability, highlighted by the large error bars, we can observe that in the free troposphere (approximately above 1 km a.s.l.), the wind speed is typically between 5 and 20 m/s and reaches also values of 30 m/s. CALIPSO Level 2 (Version 2) aerosol profiles are provided at a fixed horizontal resolution of 40 km. Therefore, in order to investigate comparable length scales, an integration time for EARLINET measurements of about 30–130 minutes was considered. It follows that to investigate the

temporal variability of aerosol/cloud fields, a temporal window of observations longer than one hour, as requested in the old strategy, is needed. Therefore, 150-min records of measurements (centered around the overpass) are requested whenever atmospheric conditions allow it.

Within this study, correlative measurements were intensified especially taking the geographical distribution of participating stations into account. The contributing stations were grouped in four different clusters (see Figure 2.1). Each cluster includes at least one high-performance station. Scheduling almost simultaneous measurements for two or more stations of the cluster, in coincidence with a CALIPSO overpass for one of these stations, allows us to study the aerosol/cloud-field spatial variability. Starting from these considerations, the refined strategy schedules additional mandatory measurements, called Case B measurements, for each participating EARLINET station, in which more stations of the same cluster perform contemporary measurements. Also for the Case B measurements, 150-min records of measurements (centered around the overpass) are requested, in order to investigate the temporal variability. The 16-day cycle of CALIPSO observations allows an almost precise schedule of the Case A and Case B measurements. The backbone of the measurement plan is summarized in Table 2.2, where all mandatory measurements are reported for the 16-day CALIPSO observational cycle for both daytime (upper panel) and night-time observations (lower panel). The start date of the ESA–CALIPSO project is chosen as starting time of the table (day 1 = 1st April 2008). In bold, overpasses within 100 km are reported. Red station short names indicate high-performance stations. In this way, on average each station performs three night-time and two daytime measurements within 16 days. The number of mandatory measurements scheduled for each contributing station for daytime and night time is reported in Table 2.3, together with the corresponding quantity related to the old strategy.

Further observations, called Case C measurements, were requested from the EARLINET stations in correspondence with special events like Saharan dust outbreaks and forest-fire events. The collection of these measurements allows us to investigate the regional and continental-scale representativeness of the observations. In summary, the updated strategy foresees as mandatory measurements:

- **Case A** (CALIPSO overpass within 100 km),
- **Case B** (more stations of the same cluster perform contemporary measurements),
- **Case C** (interesting additional cases like Saharan dust intrusions, forest fires etc.).

Case A measurements allow the point-to-point comparison with CALIPSO. Case B and C measurements contribute to increase the number of measurements. With Case B measurements, the spatial variability inside the four regional clusters can be addressed. Case C

Table 2.2: Measurement plan. Day 1 = 1 April 2008, bold = Case A, normal = Case B, red = high-performance station, blue = contributing station.

DAYTIME	**CE**	**ca**		**ms**		ca **hh** **le** ms			**ca**				ca **hh** le **ms**		**le**		
	WM				**ba** ma			**gr**									**gr** **ma** ba
	CM			**la** **na**		**po**							**la** **na** **po** lc		**lc**		
	EM		**at** **th** **sf**							**at** **th** sf							
	East		**be**						be **mi**			**be** mi					**mi**	
Day of the cycle		**1**	**2**	**3**	**4**	**5**	**6**	**7**	**8**	**9**	**10**	**11**	**12**	**13**	**14**	**15**	**16**
NIGHT TIME	**East**					**be** mi				be **mi**			**be**				**mi**
	CE		**ca**				**hh**		ca hh **le** **ms**			**ca**		ca **hh** le		hh **le** **ms**	
	WM				**ba**					**gr** ma		gr **ba** ma					**gr** **ma** ba
	CM			**la** **na** po		na **po** lc					**la**		la **na** **po** lc		**lc**		
	EM		**at** th sf							at **th** **sf**							

Table 2.3: Mandatory measurements scheduled for each station with new and old strategy.

	Refined strategy		**Old Strategy**	
Station ID	Daytime Cases	Night-time Cases	Daytime Cases	Night-time Cases
ca	4	4	2	2
hh	2	3	2	2
le	3	3	2	2
ms	3	2	2	2
gr	2	3	2	2
ma	2	3	1	1
ba	2	3	1	2
la	2	3	2	2
na	2	3	2	2
po	2	3	2	2
lc	2	3	1	1
at	2	2	2	1
th	2	2	2	1
sf	2	2	1	1
be	3	3	2	2
mi	3	3	2	2

measurements provide a description of aerosol over Europe during long-range transport events. Finally, longer observation temporal windows for all the measurements allow us to investigate the temporal variability of aerosol/cloud fields. The updated strategy has been applied since 1 May 2008. Information about the refined strategy and Table 2.2 was sent to all participating stations through an ESA–CALIPSO devoted mailing list. A weekly updated measurement time schedule has been sent to the partners by CNR–IMAA. The updated time schedule reports Case A and Case B measurements scheduled for all participating stations with exact distance between EARLINET stations and CALIPSO ground track, and time of the CALIPSO overpass. In particular, the following items have been distributed as e-mail attachments to all partners weekly:

- a table (both in txt and xls formats) reporting EARLINET station, date and time of CALIPSO overpass, day of the 16-day CALIPSO cycle, case of the measurement (Case A or Case B) and for Case B measurements the corresponding Case A measurement station,
- daily plots of the CALIPSO ground-track and EARLINET active stations.

Besides Case A and Case B measurements that can be scheduled in advance, Case C measurements have been requested for special events. For these measurements, devoted

e-mail alerts were sent by CNR–IMAA for special events involving different clusters. The communication between clusters and inside each cluster itself has been assured through appropriate mailing lists. For the coordination of measurements, a responsible person for each cluster has been nominated. However, a general coordinator (G. Pappalardo) coordinated all the clusters also alerting for special events occurring over different regions of Europe.

The updated measurement strategy remains valid also after the end of the intensive observational period supported by ESA. EARLINET stations have been operating on a voluntary basis again since November 2009.

2.5 Measurement statistics

A reporting procedure for performed measurements has been established within the network. Each participating EARLINET station has to provide a monthly report regarding the performed measurements. The reports to be filled from each station have been sent monthly by CNR–IMAA and already contain: name of the station, day of scheduled measurement, start time of CALIPSO overpass, stop time of CALIPSO overpass, distance between EARLINET station and CALIPSO at overpass time, type of measurement (Case A, Case B, or Case C). Each participating station has to fill in the following fields.

Measurements:	1 if measurement has been performed
	0 otherwise
Start Date:	start date of the performed correlative measurement (yyyymmdd format)
Start Time:	start time of the performed correlative measurement (hh:mm format)
Stop Date:	stop date of the performed correlative measurement (yyyymmdd format)
Stop Time:	stop time of the performed correlative measurement (hh:mm format)
No Measurements Motivation:	
	1 = no measurements because of low clouds
	2 = no measurements because of rain
	3 = no measurements because of snow
	4 = no measurements because of technical problems
	5 = no measurements because of current upgrading of the system
	6 = other motivations.

In this way, the status of correlative measurements was continuously updated. In Fig. 2.3 to 2.9 the number of scheduled and performed measurements for each station is reported for each month from April 2008 to October 2009, together with a statistics about the reason of not performed measurements. In Fig. 2.10 a summary for the entire 18-month observational period is given.

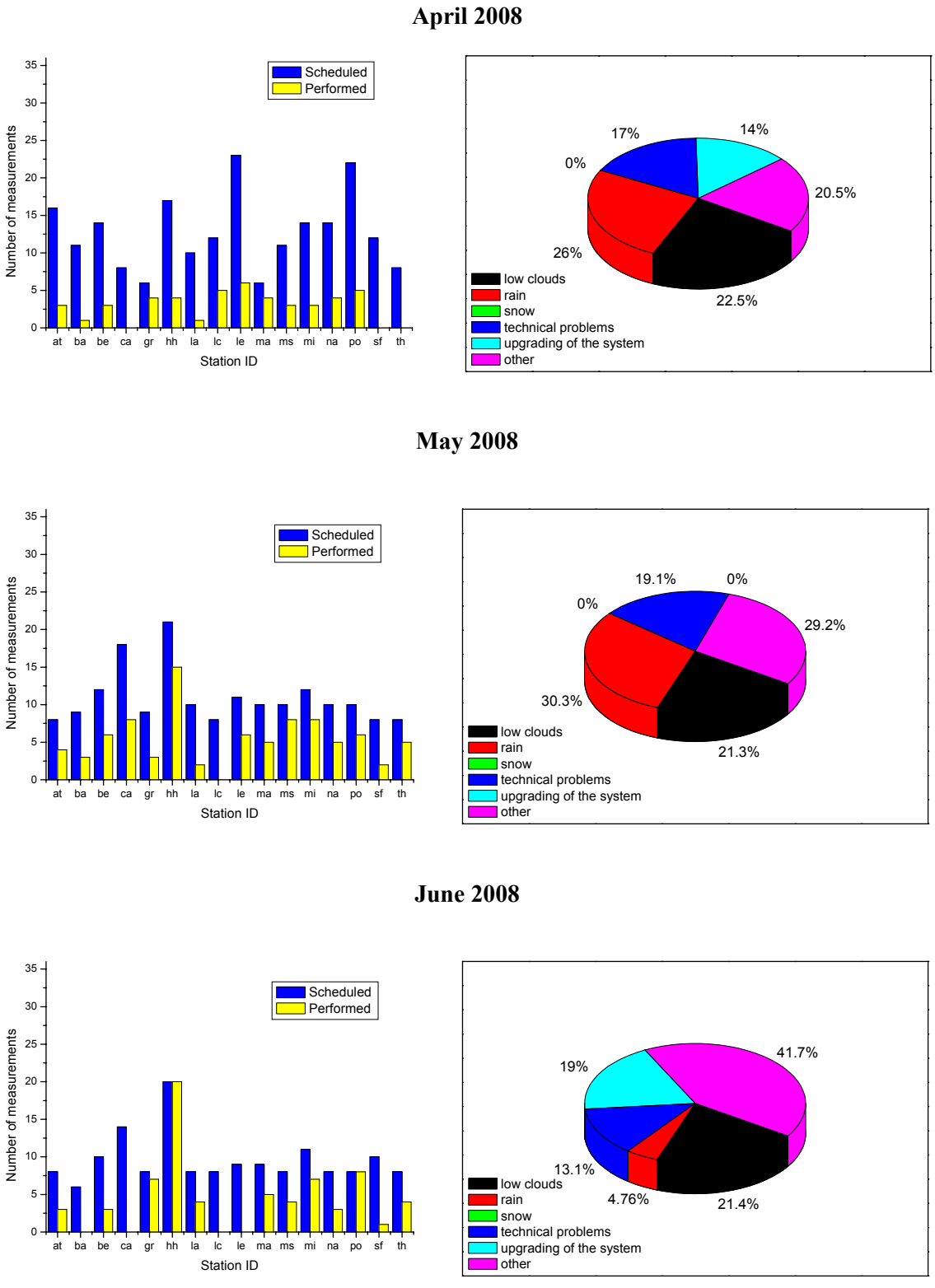

Figure 2.3: Number of monthly scheduled and performed measurements for each station from April to June 2008 (left panels) and monthly statistics about the reason of not performed measurements (right panels).

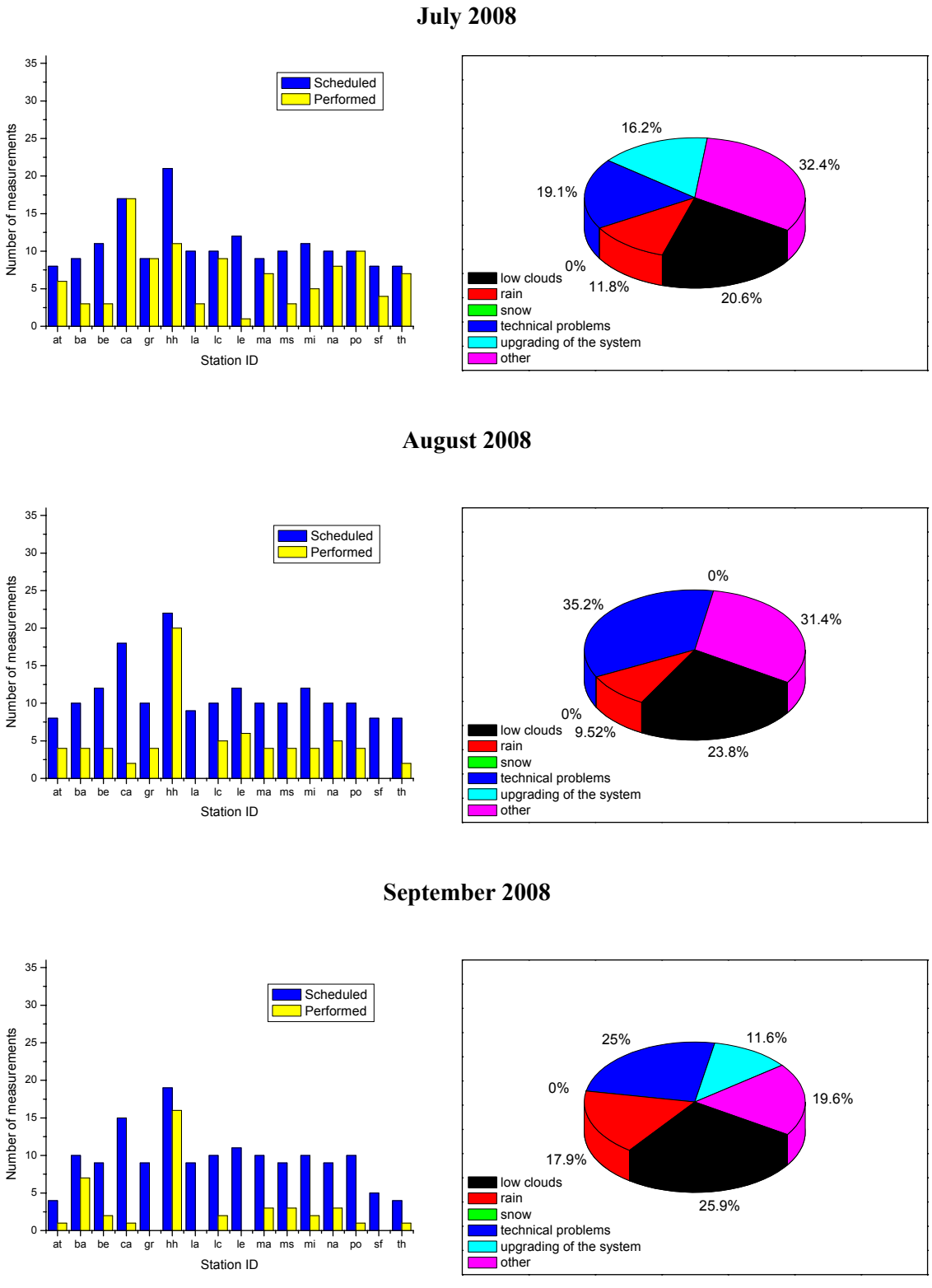

Figure 2.4: Number of monthly scheduled and performed measurements for each station from July to September 2008 (left panels) and monthly statistics about the reason of not performed measurements (right panels).

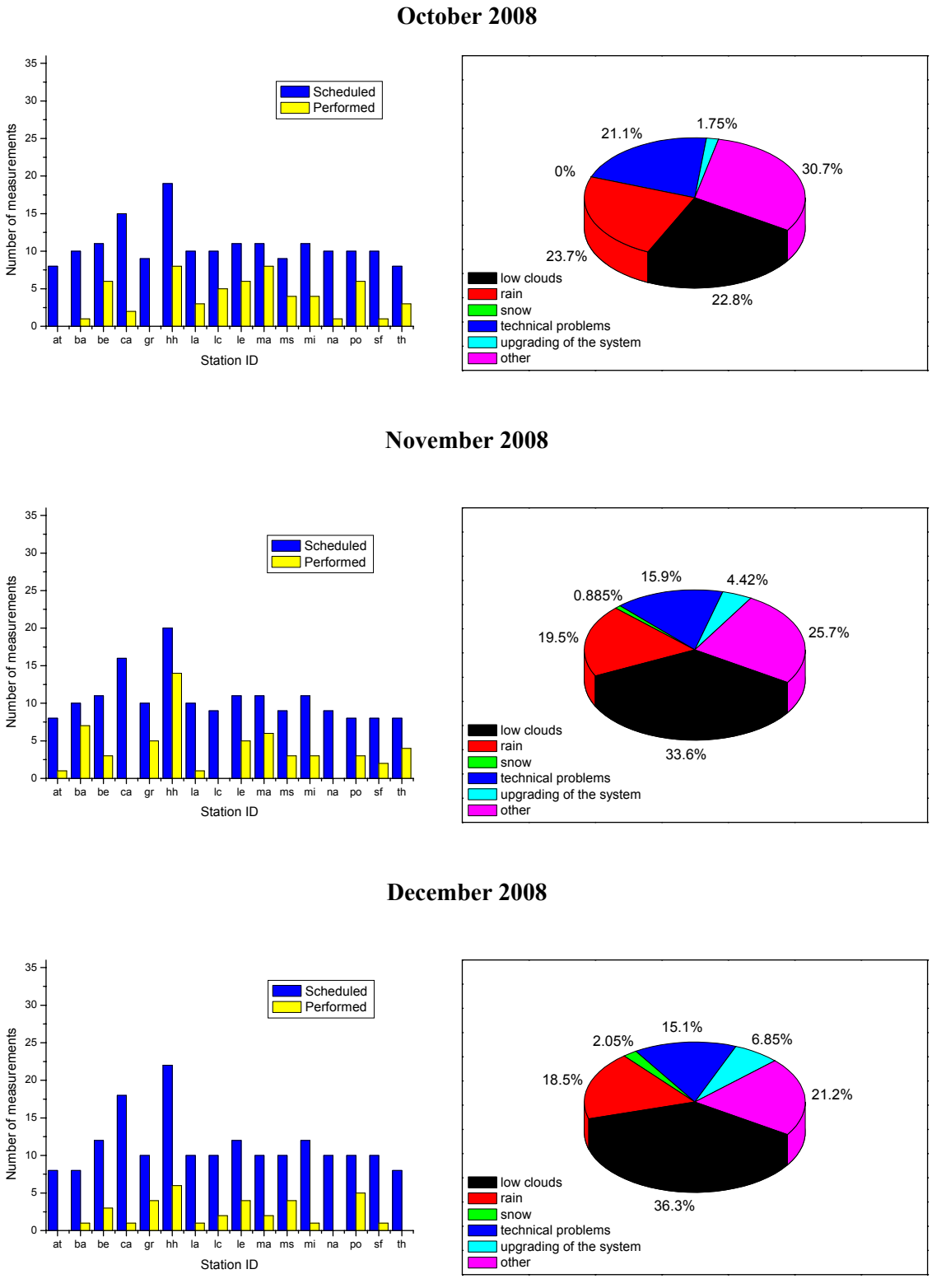

Figure 2.5: Number of monthly scheduled and performed measurements for each station from October to December 2008 (left panels) and monthly statistics about the reason of not performed measurements (right panels).

January 2009

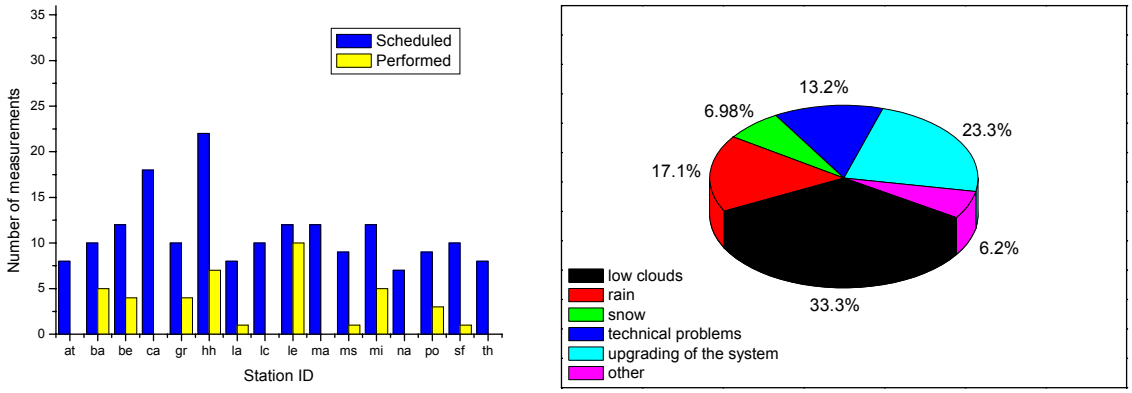

February 2009

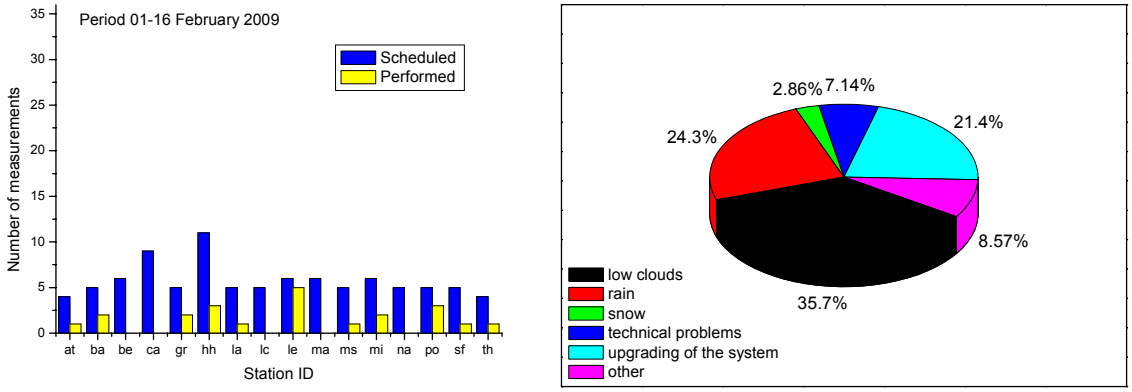

March 2009

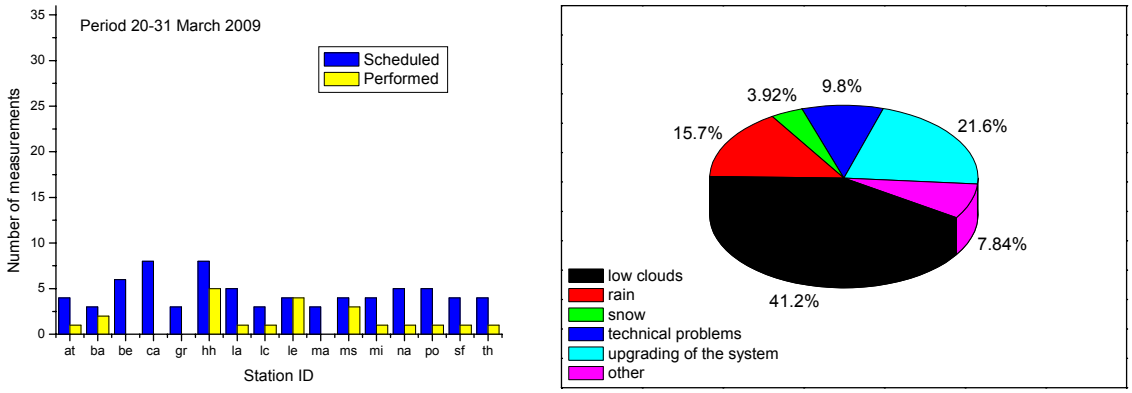

Figure 2.6: Number of monthly scheduled and performed measurements for each station from January to March 2009 (left panels) and monthly statistics about the reason of not performed measurements (right panels). CALIPSO was switched off from 16 February – 18 March 2009.

April 2009

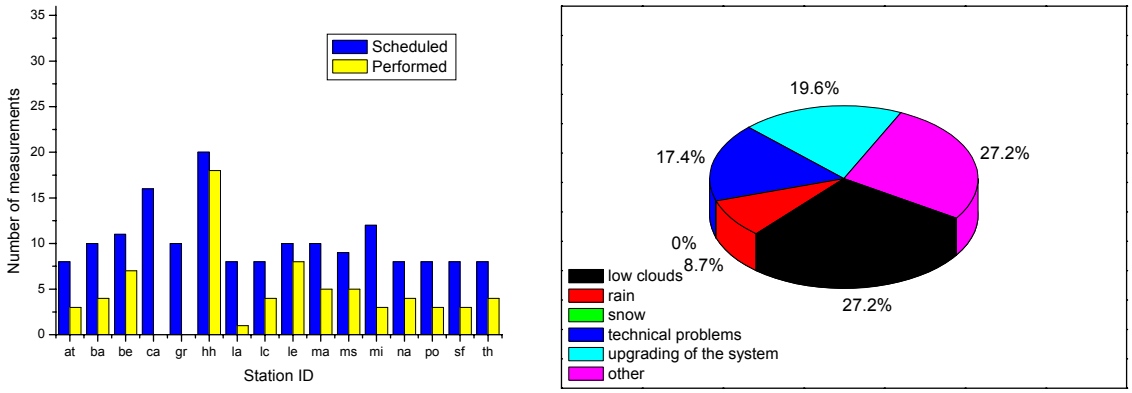

May 2009

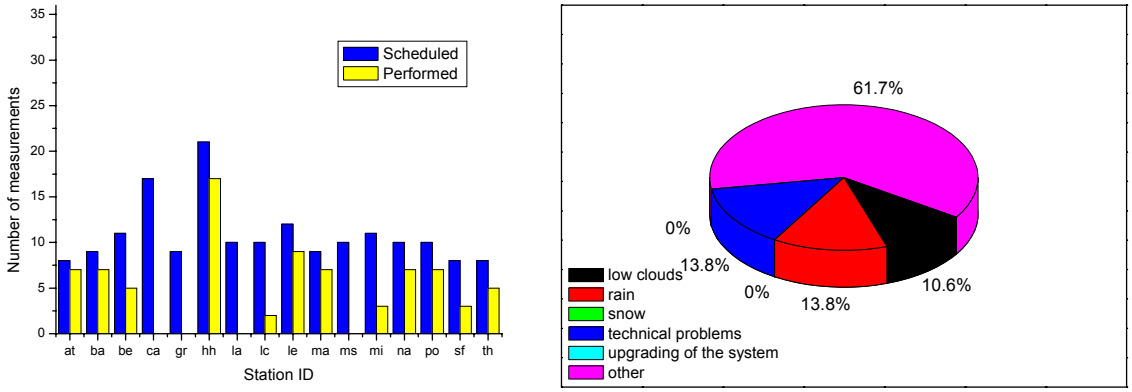

June 2009

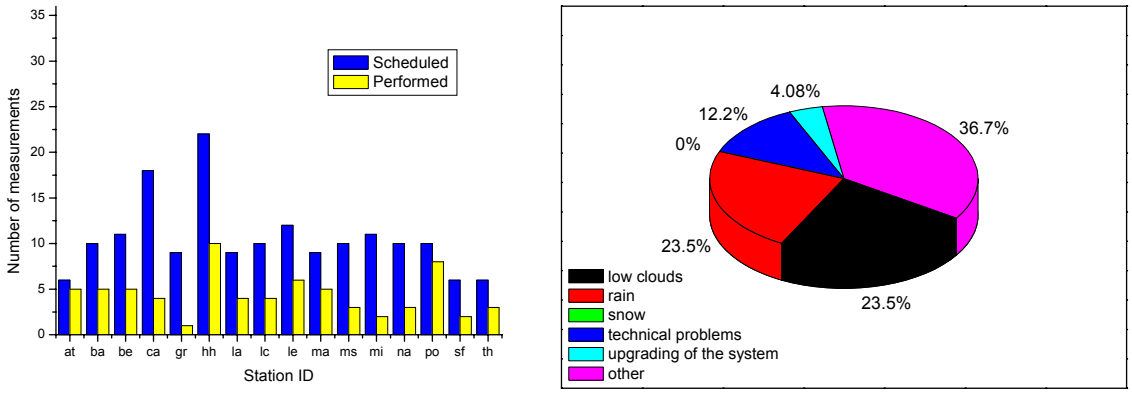

Figure 2.7: Number of monthly scheduled and performed measurements for each station from April to June 2009 (left panels) and monthly statistics about the reason of not performed measurements (right panels).

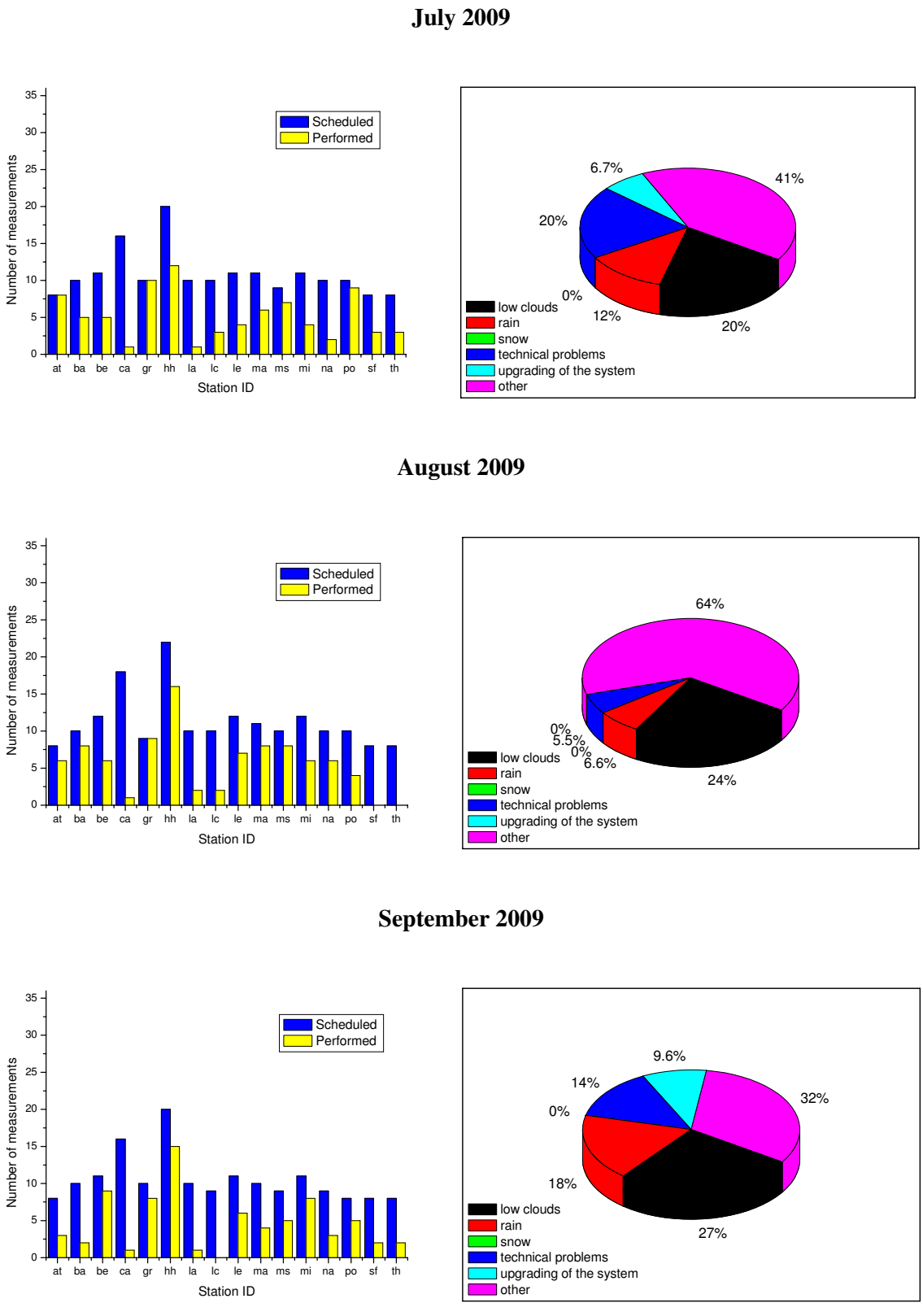

Figure 2.8: Number of monthly scheduled and performed measurements for each station from July to September 2009 (left panels) and monthly statistics about the reason of not performed measurements (right panels).

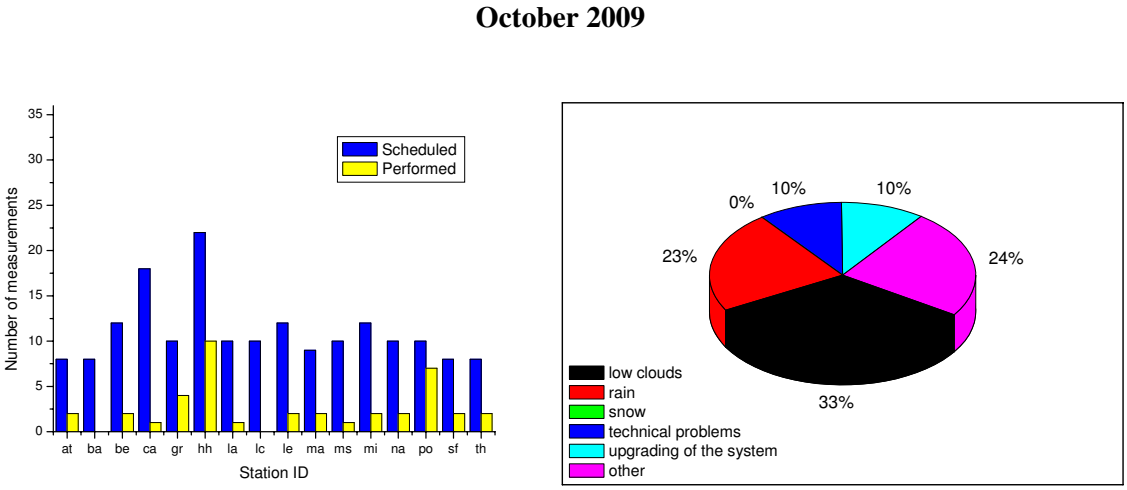

Figure 2.9: Number of monthly scheduled and performed measurements for each station in October 2009 (left panel) and monthly statistic about the reason of not performed measurements (right panel).

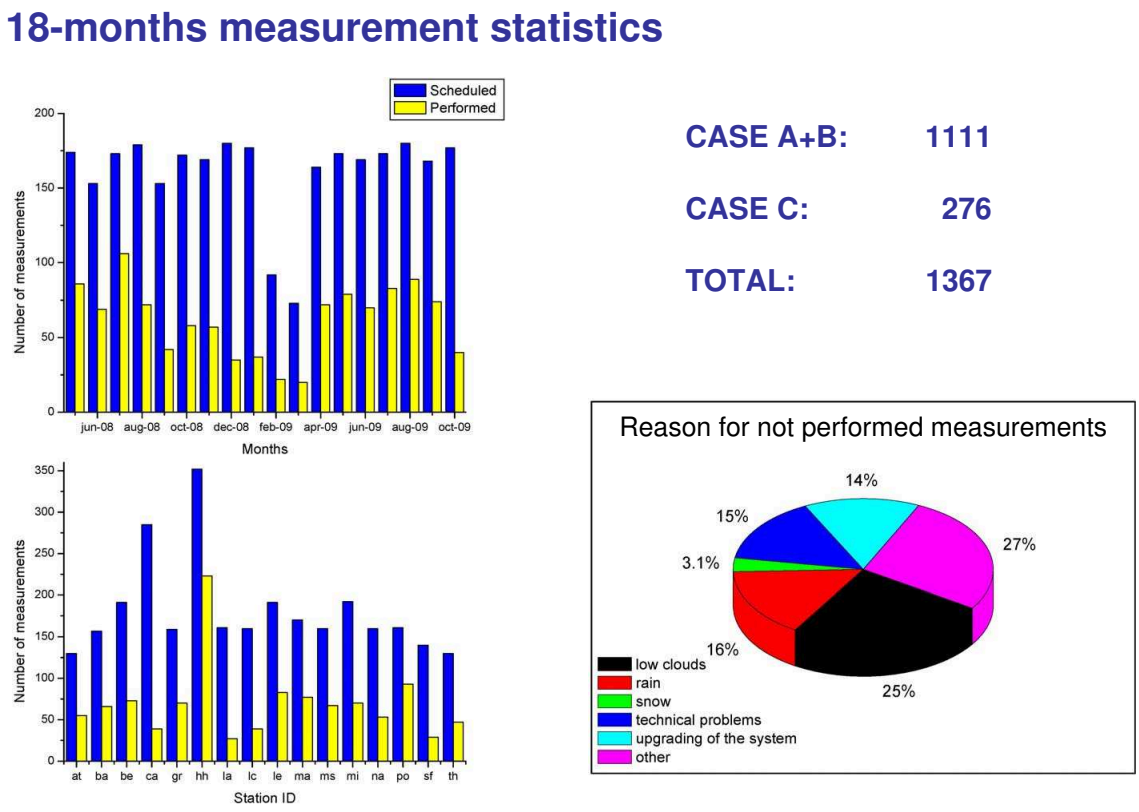

Figure 2.10: Summary of all scheduled and performed measurements for each station and each month from May 2008 to October 2009 (left panel) and statistic about the reason of not performed measurements (right panel).

In addition to these measurements, Central Europe, Central Mediterranean and Eastern Mediterranean stations were alerted for Case C measurements during two major Saharan dust events that occurred from 15–20 May 2008 and from 26–30 May 2008. During these two events, 63 additional measurements were performed.

Central and Eastern Mediterranean stations were alerted for Case C measurements for a large Saharan dust event that occurred from 28 October to 6 November 2008. During this event, 67 additional measurements were performed.

A further Case C alert was sent to the whole network on 30 March 2009 regarding the Mt. Redoubt (Alaska) eruption. The ash plume reached >15 km height. Because of the long lifetime of stratospheric aerosols and further volcanic activity, this alert was active until the end of the observational period. In the period 30 March – 30 April 2009, 161 additional measurements were performed. April 2009 was characterized by a very high aerosol load throughout the troposphere over large parts of Europe. Several aerosol sources have been identified. In the tropopause region a permanent aerosol layer obviously caused by the eruption of Mt. Redoubt in March was present. Saharan dust and smoke from urban fires north of the Black Sea was transported toward Central Europe over longer periods. Local pollution as well as pollen may have contributed to the high aerosol load as well. Several Saharan dust outbreaks also occurred in May 2009. One major event was observed during the EARLINET–ASOS intercomparison campaign at Leipzig on May 25th.

New volcanic eruptions occurred in June and July 2009. Sarychev Peak in the Kuriles erupted on 13 June 2009. Ash plumes rising to a height of 54,000 ft (16500 m) above sea level were reported on 15 June. Aerosol layers in heights between 12 and 22 km stretching over wide distances in the northern hemisphere are clearly visible in the CALIPSO browse images after that date. Several EARLINET stations observed distinct aerosol layers in this height region since the beginning of July as well. On 25 July, another eruption occurred at Shiveluch volcano, Kamchatka, with ash emissions up to 23,000 ft (7000 m). This volcano remained active for the following months, with a major eruption on 10 September 2009 leading to a plume height of 15000 m. Details of volcanic observations are reported in Sec 5.1.6.

On 16 February 2009 the CALIPSO payload shut itself down due to low laser energy, a few weeks before the planned switch to the backup laser. EARLINET stopped correlative observations at that time. However, stations were encouraged to focus their activities on regular EARLINET measurements, because these measurements can be used for the aerosol typing studies as well. On 9 March 2009 the CALIPSO backup laser was turned on. Test procedures and alignments were successful. CALIPSO has been operating in data acquisition mode with the backup laser since 18 March 2009, and EARLINET correlative measurements have been continued since then.

Chapter 3

Data evaluation concept

In this chapter, we discuss the basic requirements for the evaluation of correlative ground-based and spaceborne observations and the exploitation of the resulting data set. Section 3.1 describes feature-finding and cloud–aerosol discrimination schemes. The classification of aerosol and cloud types is discussed in Sections 3.2 and 3.3, respectively. Section 3.4 deals with representativeness issues. Auxiliary data and modeling tools needed for measurement planning and data exploitation are introduced in Section 3.5. The major conclusions are summarized in Section 3.6.

3.1 Feature finding and cloud–aerosol discrimination

3.1.1 General considerations

After applying basic signal processing procedures (e.g., background and range correction, signal calibration), the first step in lidar data evaluation with respect to optical data is the identification of aerosol and cloud layers and the determination of their base and top heights. Here we follow the CALIPSO terminology and refer to aerosol and cloud layers as "features" (*Vaughan et al.*, 2005, 2009). In general, a feature in the lidar profile is characterized by enhanced atmospheric backscattering (with respect to the molecular return) and by boundaries in the form of a more or less rapid change (in height) between enhanced and clear-air backscattering. Therefore, feature-finding algorithms are normally based on combined threshold and derivative methods. Beside a simple one-dimensional profile processing, also the two-dimensional contextual information of a lidar measurement (either a cross section along an orbit or a time series of profiles taken at a fixed location on ground) can be used. The signal-to-noise ratio is the limiting factor in automated algorithms, especially for spaceborne observations.

Cloud–aerosol discrimination (CAD) schemes depend on the information available from the lidar measurement. If only backscatter information at a single wavelength is available, the different signature of clouds and aerosols must be used. Clouds typically show stronger backscattering, higher attenuation, steeper boundaries (both in the vertical and horizontal direction) and a higher signal variation in space and time than aerosols. A trained operator easily discriminates clouds and aerosols in color contour plots of lidar signals. Automized algorithms, however, are much more difficult to implement. If the lidar delivers information at more than one wavelength, the different scattering behavior of clouds and aerosols can be used in the discrimination schemes in addition. Whereas large cloud particles exhibit a neutral scattering behavior, backscattering and extinction of aerosol particles, with some exceptions (see below), show a more or less strong wavelength dependence.

3.1.2 CALIPSO schemes

The CALIPSO feature finder applies a profile scanner which searches for feature boundaries based on a threshold algorithm first (*Vaughan et al.*, 2004, 2005, 2009). Profile processing works for strong features only. In order to identify faint features, a multi-level averaging scheme called SIBYL (Selective Iterated Boundary Location) is employed. It uses signals averaged horizontally over 5, 20, and 80 km (successively improving the signal-to-noise ratio). Besides aerosols and clouds the feature finder identifies clear-air regions, stratospheric features, and the surface return as well as subsurface regions and regions with bad or missing data. Base and top altitudes of features are determined and layer descriptors, such as layer-integrated attenuated backscatter, volume depolarization ratio, and color ratio together with descriptive statistics of these parameters, are provided.

The layer-integrated backscatter (532 nm) and color ratio (1064 nm/532 nm) together with the mid-feature altitude are used in the CALIPSO CAD scheme (*Vaughan et al.*, 2004, 2005; *Liu et al.*, 2009). The method relies on the facts that backscattering from clouds is spectrally independent (color ratio $\approx$1) and much larger than aerosol backscattering. A confidence function is applied which considers height-dependent probability distribution functions of the cloud and aerosol layer-integrated attenuated-backscatter and color-ratio values (*Liu et al.*, 2004, 2009). After feature finding and identification of clouds and aerosols, further scene classification algorithms are applied to determine specific aerosol and cloud types (see below).

3.1.3 EARLINET data evaluation

So far, EARLINET does not apply automated algorithms for feature identification. The lidar signals are evaluated individually by operators at each station. Feature finding and

cloud–aerosol discrimination is usually done "by eye" following the principles explained above. Layer boundaries are determined with the help of derivative methods or wavelet analysis (e.g. *Flamant et al.*, 1997; *Menut et al.*, 1999; *Brooks*, 2003; *Mattis et al.*, 2004; *Matthias et al.*, 2004; *Baars et al.*, 2008). Clouds are identified by the significant higher backscatter and attenuation and their pronounced structures compared to aerosols.

Separate profiles of optical data for aerosols and clouds are produced in two different ways:

1. When ice or mixed-phase clouds—which typically occur above 4 km height and can be penetrated by the laser beam—are present in a time series, the signals are averaged with the desired temporal resolution (typically 30 min) and the optical data are calculated for the entire height profile including aerosol and cloud layers. Before storing the data in the aerosol files, the height regions containing clouds are cut out. In addition, optical-data profiles with clouds (preferably with a temporal resolution of the order of 10 min) are stored in separate cloud files which include a cloud flag to identify the height region and the type of the cloud (see Chapter 4).

2. When optically thick clouds are present (e.g., low water clouds, which often are not penetrated by the laser beam) the respective observational periods are removed from the time series, before the profiles are averaged and aerosol optical data are computed. The cloud-containing periods may be evaluated separately if proper signals are available (that is often not the case because of detector overload or missing calibration possibilities).

3.2 Aerosol classification

3.2.1 General considerations

Aerosols are of specific interest in atmospheric research and climate modeling because they influence the Earth's radiation budget directly through scattering and absorption of Sun light and indirectly through their influence on clouds and precipitation. Our knowledge on these processes is highly uncertain because of the complex nature of atmospheric aerosols and their variability in space and time (*Diner et al.*, 2004). A practical way to characterize different aerosols in the climate system adequately without describing their physical and chemical properties in detail is the typing of aerosols. This approach neglects detailed information on size distributions, composition, phase, shape, and the internal and external mixing state of particles and uses macroscopic parameters such as the mean optical properties of the ensemble of particles for the description instead. Depending on the application, a number of 5–10 aerosol types appears to be sufficient to cover the major

global aerosol components. However, a general and unique aerosol classification scheme is not available so far.

The most important aerosol types from natural sources are sea salt and mineral dust. Smoke from biomass burning can be of natural origin as well, but is often related to anthropogenic activities. Periodically, when a major volcanic eruption injects large amounts of sulfuric gases into the stratosphere where they condense to sulfuric acid droplets, volcanic aerosols influence the global radiation budget significantly. Ash and gases emitted from volcanic sources into the troposphere may contribute to the regional aerosol load in certain areas.

Anthropogenic activities modify the natural aerosol load of the Earth's atmosphere drastically. Through industrial combustion processes, car, train, air and ship traffic, agricultural and individual human activities particles and precursor gases are emitted. Sulfates, soot, nitrates, ammonium, and organic carbon are typical constituents of the anthropogenic aerosol. Furthermore, soil particles, pollen, and other biogenic material may contribute to the aerosol at continental sites. Thus the separation of man-made from natural aerosol effects is a challenge.

Lidar has turned out to be an effective tool for aerosol characterization and aerosol type determination. The size of aerosol particles is of the order of the optical wavelengths. Thus aerosol parameters measured with lidar sensitively depend on the actual particle properties. Particles from different sources which show different sizes, absorption properties, and shapes, can be distinguished with lidar by their spectral scattering characteristics and their light-depolarizing behavior. When independent information on extinction and backscattering and thus on the lidar ratio is available, when extinction and backscattering are measured at several wavelengths, and/or when the depolarization of the backscattered light is determined, information on the particle type can be retrieved from lidar observations. On the other hand, lidar inversion algorithms for standard backscatter lidars, such as CALIOP, have to assume a lidar ratio and, therefore, require assumptions on the aerosol type present in the atmosphere.

Multiwavelength Raman lidars as operated in EARLINET typically measure the extinction coefficient at 355 and 532 nm and the backscatter coefficient at 355, 532, and 1064 nm. They allow us to derive lidar ratios in the ultraviolet and visible wavelength regions as well as spectral extinction and backscatter properties in terms of Ångström exponents and color ratios. Mostly, the lidars have a depolarization measurement capability as well (see Chapter 2 and 4). These systems represent optimum tools for aerosol type characterization.

So far, only very few attempts have been made to derive aerosol-type-dependent lidar parameters in a systematic way. *Cattrall et al.* (2005) have published lidar parameters of five

key aerosol types (marine, urban, biomass-burning, dust, and Southeast Asian aerosol) derived from AERONET Sun photometer measurements. These values are indirectly obtained from sky radiance and solar transmittance measurements and the application of scattering models for spherical or spheroid particles. The findings are summarized in Tab. 3.1. The distribution of the parameters was found to have a Gaussian shape, and the given standard deviation is observed from the Gaussian fit. A deficiency of this study is that it is not based on a distinct case-by-case aerosol typing. Instead, mean values are derived for specific geographic locations and times of the year, for which it is assumed that a certain aerosol type dominates the atmospheric column.

Table 3.1: Lidar parameters retrieved from selected AERONET sites, after *Cattrall et al.* (2005). S–ratio: ratio of lidar ratios, β–ratio: ratio of backscatter coefficients, α–ratio: ratio of extinction coefficients; all ratios are given for the wavelength pair 550 nm/1020 nm.

Aerosol type	Lidar ratio sr (550 nm)	S–ratio	β–ratio	α–ratio	Ångström exp. (α-related)
Marine	28±5	1.0±0.2	1.4±0.1	1.5±0.4	0.7±0.4
Urban/industrial	71±10	1.9±0.3	1.6±0.2	3.3±0.5	1.7±0.2
Biomass burning	60±8	2.1±0.3	1.8±0.3	3.8±0.4	1.8±0.2
Dust (spheroids)	42±4	1.2±0.1	0.9±0.1	1.2±0.1	0.1±0.1
Southeast Asia	58±10	1.5±0.3	1.6±0.2	2.4±0.3	1.3±0.2

Aerosol-type-dependent optical parameters solely based on multiwavelength lidar measurements and case-by-case aerosol typing have been published by the IfT group (*Müller et al.*, 2007). The data were determined from long-term aerosol and cloud observations in the frame of the German Aerosol Lidar Network (1996–1999) and EARLINET (since 2000) with a stationary multiwavelength Raman lidar at Leipzig for more than a decade. Furthermore, data with transportable Raman lidars were taken in several field campaigns in Europe, Africa, and Asia. From these measurements, aerosol-type-dependent lidar ratios, backscatter-related Ångström exponents and color ratios, and the depolarization ratio have been derived. As an example, Fig. 3.1 shows the 1064 nm/532 nm color ratio plotted versus the 355-nm lidar ratio for a variety of cloud and aerosol types. Depolarization characteristics are indicated by the color of the symbols. The study distinguishes marine aerosol, desert dust, urban haze, arctic haze, forest-fire smoke, and Southeast Asian aerosol. It also shows that significant differences are found when the same type of aerosol is investigated in different regions of the globe or after different transport times. Details are discussed below.

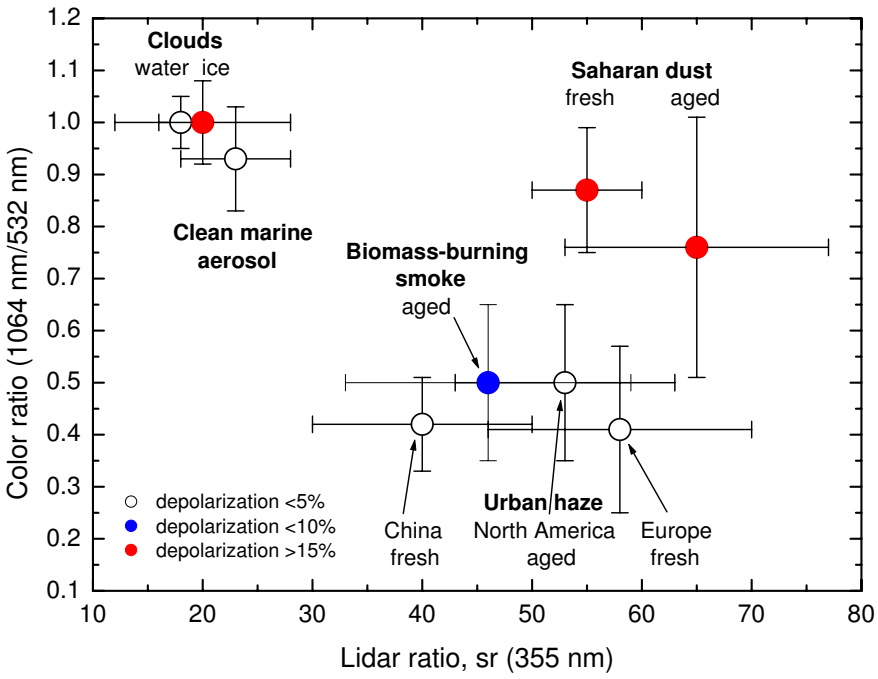

Figure 3.1: Color ratio (ratio of the backscatter coefficients at 1064 and 532 nm) versus lidar ratio at 355 nm for different aerosol and cloud types observed with IfT lidars from 1996–2007. Data are derived from Tab. 1 of *Müller et al.* (2007). Error bars indicate one standard deviation of each quantity from the mean of all observations.

3.2.2 CALIPSO aerosol typing

Tab. 3.2 presents the six aerosol types used in the CALIPSO aerosol classification scheme and the respective lidar ratios at 532 and 1064 nm chosen in the CALIPSO retrievals (*Liu et al.*, 2005). The CALIPSO aerosol typing is based on modeled aerosol properties, taking typical size distributions and refractive indices of the chosen aerosol types into consideration, and on experimental findings. The input parameters mainly rely on AERONET (Aerosol Robotic Network) Sun photometer retrievals and the respective studies by *Omar et al.* (2005) and *Cattrall et al.* (2005). Mie scattering calculations are performed to retrieve the optical data (lidar ratios) from size distribution and refractive index, except for dust for which a non-spherical scattering model is applied.

Figure 3.2 shows the CALIPSO aerosol typing scheme (*Omar et al.*, 2009). The scheme applies external information on geographical location, surface type, and season and lidar-derived information on the feature height and feature-integrated values of depolarization, attenuated backscattering, and color ratio. Validation of the CALIPSO aerosol typing is ongoing. Preliminary investigations indicate satisfactory results (*Omar et al.*, 2009). The database established in the present study can contribute to this task.

Table 3.2: CALIPSO aerosol types and lidar ratios chosen in the retrieval, after *Liu et al.* (2005); *Omar et al.* (2009). The lidar ratio for dust at 1064 nm was changed for the CALIPSO Version 3 data release from 30 to 55 sr.

No.	Aerosol Type	532 nm	1064 nm
1	clean marine	20 sr	45 sr
2	dust	40 sr	30 sr (55 sr)
3	polluted continental	70 sr	30 sr
4	clean continental	35 sr	30 sr
5	polluted dust	65 sr	30 sr
6	smoke	70 sr	40 sr

3.2.3 Major aerosol types and special considerations for the study

In the following, we briefly summarize findings on the major aerosol types with focus on results from EARLINET and the specific considerations for observations over Europe.

3.2.3.1 Marine or oceanic aerosol

Marine or oceanic aerosol predominates in the shallow marine boundary layer (typically of 500–1000 m height) over the oceans. Sea-salt particles (actually, sea-salt-containing water droplets) are produced by wind stress on the ocean surface. The release of dimethyl sulfide (DMS) from phytoplancton contributes to aerosol production over the oceans as well. The microphysical and optical properties of marine aerosol are relatively well understood. The particles are comparably large, liquid, and non-absorbing, and the real part of the refractive index is low. These properties result in low lidar ratios of the order of 20–30 sr, low depolarization ratios, and in a low Ångström exponent (*Ansmann et al.*, 2002; *Franke et al.*, 2001, 2003; *Müller et al.*, 2007; *Cattrall et al.*, 2005). Thus marine aerosols can be well distinguished from other aerosol types in terms of their optical properties. However, they show a similar light-scattering behavior as water clouds which may lead to ambiguities when using optical parameters in cloud–aerosol discrimination schemes in the marine boundary layer.

Clean marine aerosols are hard to observe at continental sites. EARLINET stations close to the coast may detect pure marine aerosol under certain meteorological conditions (*De Tomasi et al.*, 2006). Europe's shorelines are densely populated and obtain intense ship traffic. Therefore, a mixture of marine aerosols with anthropogenic pollution must also be taken into consideration when exploiting data from stations close to the North

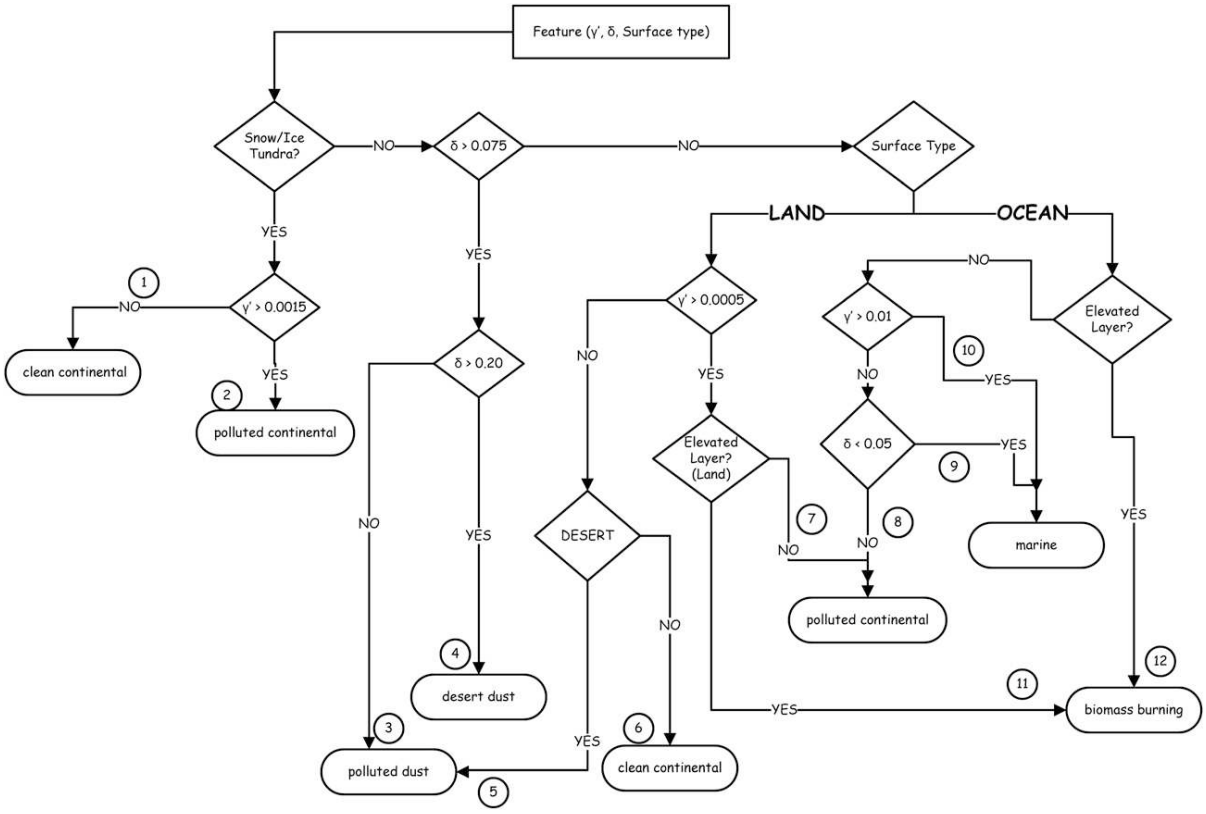

Figure 3.2: CALIPSO aerosol typing and lidar-ratio selection scheme, taken from *Omar et al.* (2009); δ– volume depolarization ratio, γ'–integrated attenuated backscatter.

Sea (Cabauw, Hamburg) or the Mediterranean Sea (Barcelona, Naples, Lecce, Athens, Thessaloniki) (*Wandinger et al.*, 2004).

3.2.3.2 Mineral dust

Mineral dust lofted by dynamical processes over arid regions is often transported over distances of several thousand kilometers. Mineral dust particles show considerably different properties compared to other aerosol types. The most important feature is their non-spherical shape and their large size. The non-spherical shape causes a significant depolarization of the backscattered light. It also leads to comparably high lidar ratios (*Mattis et al.*, 2002). The large size is reflected in an almost neutral spectral extinction and backscattering behavior, i.e. the Ångström exponent is 0–0.4, the color ratios are of the order of 1. Therefore, desert dust is most easy to distinguish from all other aerosol types.

The Saharan desert is the largest aerosol source of the globe. Europe is quite frequently influenced by Saharan dust outbreaks (*Mattis et al.*, 2002; *Müller et al.*, 2003; *Ansmann*

et al., 2003; *Papayannis et al.*, 2008). EARLINET has performed numerous coordinated observations of dust plumes over Europe. Statistical results from the period 2000–2002 are presented by *Papayannis et al.* (2008). The study indicates a high variability of the lidar ratio (20–100 sr) and the backscatter-related Ångström exponent (−0.5–3), especially at Southern European stations. In contrast, lidar ratios measured in the source region in Morocco during the Saharan Mineral Dust Experiment (SAMUM) (*Tesche et al.*, 2009b) showed very stable values of the order of 55±10 sr at 355, 532, and 1064 nm. They are clearly larger than the values reported by *Cattrall et al.* (2005) and the ones used in the CALIPSO retrieval (see above). The values for 1064 nm are in agreement with those derived by *Liu et al.* (2008) from CALIPSO observations in the Saharan dust plume, whereas discrepancies occur at 532 nm again.

The dust optical properties observed over Europe obviously depend on the actual source region and transport pattern. Absorption properties of dust particles depend on the mineral constituents and thus on the area of origin (white, yellow, red sand). Mixing with marine aerosols, when the transport occurs at low levels over the Mediterranean Sea, and with anthropogenic aerosol or smoke has to be taken into account. Cloud processing of particles plays a role as well. Coating of dust particles with sulfuric components is likely to occur during long-range transport.

The CALIPSO aerosol typing scheme distinguishes between dust and polluted dust (see Sec. 3.2.2). Polluted dust is the only explicit mixture of different aerosol types in this scheme, and it considers the mixture of dust with biomass-burning smoke or anthropogenic pollution during transport (*Omar et al.*, 2009). As we will show later in this report, the mixing of different aerosol types plays an important role over the European continent and requires special attention when aerosol typing schemes are developed.

3.2.3.3 Biomass-burning aerosol (smoke)

Biomass-burning aerosol or smoke is produced by both anthropogenic activity (e.g., wood and crop burning) and natural processes (natural forest fires). The production of smoke aerosols strongly depends on land use, vegetation cycle, seasonal weather conditions, and human behavior. During the dry season biomass-burning aerosol dominates in tropical and subtropical regions of South America, Africa, and Asia. Boreal forest fires are major aerosol sources at higher latitudes.

The kind of burning strongly influences the size of the smoke particles and the released amount of soot and thus the optical properties of biomass-burning aerosol. Smaller and highly absorbing particles are observed in flaming fires, whereas smoldering fires emit larger and less-absorbing particles. Furthermore, smoke particles tend to grow and change their optical properties during transport due to processes such as hygroscopic growth,

condensation of organic and anorganic vapors, coagulation, and photochemical and cloud-processing mechanisms.

At European stations, long-range transported biomass-burning aerosol originating from forest fires in Canada and Siberia is frequently observed between May and October (*Wandinger et al.*, 2002; *Mattis et al.*, 2003; *Müller et al.*, 2005). For this boreal forest-fire smoke, *Müller et al.* (2007) found a decrease in the Ångström exponent from 1.8 to 0.4 due to an increase in effective particle radius from 0.12 to 0.4 μm during a travel time of 25 days or a travel distance of 25 000 km.

Fresh smoke from wild fires is frequently obtained in Southern Europe in summer. *Amiridis et al.* (2008) analyzed lidar and Sun photometer data for the period 2001–2005. They obtained a decrease in the backscatter-related Ångström exponent from 2.5 to 1.0 when the age of the smoke increases from 5 to 17 days. The lidar ratio increased from values around 45 to values of 80–100 sr with decreasing backscatter-related Ångström exponent.

3.2.3.4 Anthropogenic pollution (urban aerosol)

Anthropogenic pollution is the major aerosol type obtained in the planetary boundary layer of highly industrialized regions of the globe, and thus determines the observations in the lower troposphere in Europe. This aerosol type is dominated by sulfate particles and contains soot, nitrates, ammonium, and organic carbon as well. Fossil fuel combustion and traffic are major aerosol sources. Only a part of the particles is emitted directly into the atmosphere. The emission of precursor gases followed by gas-to-particle conversion in the atmosphere plays an important role in the aerosol production. Therefore, mainly small particles are present in the urban aerosol. They cause a strong wavelength dependence of the optical properties, i.e. Ångström exponents >1 and color ratios <0.5. The small particles do not significantly depolarize the backscattered light. The carbon content determines the absorption properties and thus also the lidar ratio of urban aerosol. Typical lidar-ratio values of anthropogenic pollution are 50–70 sr (*Mattis et al.*, 2004; *Cattrall et al.*, 2005; *Müller et al.*, 2007). Smaller values have been observed in urban aerosol transported over long distances from North America to Europe (*Müller et al.*, 2007).

It should be noted that different stages of industrial development and environmental regulations obviously lead to significant differences in the urban aerosol properties. Whereas small particles dominate the urban aerosol in Europe and the US, an increased amount of large particles is found in Southeast Asian aerosol. These particles are produced by low-temperature combustion processes in domestic heating, wood and crop burning, but are also due to relaxed environmental regulations. Accordingly, lower Ångström exponents and lidar ratios are observed in Southeast Asian aerosols compared to European or North

American aerosols (*Franke et al.*, 2003; *Cattrall et al.*, 2005; *Ansmann et al.*, 2005; *Müller et al.*, 2006, 2007; *Tesche et al.*, 2007).

Two specific types of anthropogenic pollution can be observed in Europe under certain circumstances, Arctic haze and photochemical smog. Arctic haze might be present in Northern and Central Europe from time to time in spring (*Heintzenberg et al.*, 2003; *Müller et al.*, 2004). This type of aerosol is an extremely aged anthropogenic pollution aerosol which is captured by the polar front in the polar region in winter. Sedimentation and coagulation over a long time result in a very narrow size distribution of the aerosol particles. Solar-induced conversion processes lead to a maximum in Arctic haze in springtime.

Photochemical smog is mainly observed in highly polluted areas in summer. Photochemical conversion of precursor gases into particles and an enhanced ozone production lead to hazardous atmospheric pollution levels. Episodes with photochemical smog are often observed in Southeastern Europe during the summer months. A deeper investigation of particle optical properties in photochemical smog is not available so far.

3.2.3.5 Continental background aerosol (rural aerosol)

The continental background aerosol is a mixture of (aged) urban components with particles from agricultural activity and natural sources. Therefore, it may consist of a variety of substances such as sulfates, nitrates, ammonium, soot, organic carbon, mineral soil particles, pollen, and other biogenic material. Depending on the relative contributions of these constituents it may show optical properties reaching from those of urban pollution to those of mineral dust. A systematic investigation of the optical properties of this type of aerosol is not available so far. For the CALIPSO retrieval (lidar-ratio estimate) it is assumed that large particles dominate the aerosol distribution of rural aerosols, i.e. small lidar ratios of the order of 30–35 sr are derived which are consistent with observations under background conditions in Portugal (*Ansmann et al.*, 2001).

3.2.3.6 Volcanic aerosol in the troposphere

The eruption of Eyjafjallajökull on Iceland in April 2010 demonstrated that sudden volcanic events may have a severe impact on the regional to continental scale for limited time periods. Fresh ash, which is especially dangerous for air traffic, consists of large, non-spherical mineral particles. The optical signature is practically identical to the one of desert dust. Particle depolarization ratios of about 0.35 and lidar ratios of 50–65 sr have been measured in the young Eyjafjallajökull ash plume about 1.5–2 days after the eruption (*Ansmann et al.*, 2010). However, besides ash volcanic eruptions inject large

amounts of sulfur dioxide into the atmosphere from which sulfate particles develop within several days. The sulfate aerosol consists of small droplets and therefore does not show a depolarization effect. Both components, a fine mode consisting of sulfate particles and a coarse mode consisting of ash, can be observed in the aged volcanic plume and might be separated via depolarization-ratio measurements (*Tesche et al.*, 2009a, 2011). Occasionally, also eruption plumes of Mount Etna have been observed by Southern European EARLINET stations in the past (*Pappalardo et al.*, 2004a; *Zerefos et al.*, 2006; *Wang et al.*, 2008). Lidar ratios of 50–60 sr and backscatter-related Ångström exponents of 2.7, characteristic for small sulfate particles, have been reported.

The eruptions of Eyjafjallajökull and Mount Etna did not fall into the 18-month observational period of this study. Therefore, respective data sets are not considered in the database yet and the aerosol type is not further discussed in this report.

3.2.3.7 Stratospheric aerosol

Stratospheric aerosol consists of well-defined sulfuric-acid droplets. They are produced through photochemical gas-particle conversion. The major source of precursor gases are volcanic eruptions which inject large amounts of sulfur dioxide directly into the stratosphere. The removal of the small particles via sedimentation and tropopause foldings takes several years. In case that very strong eruptions inject also ash particles into the stratosphere, these large particles are usually removed within a few weeks. At the beginning of this study, the stratosphere was extremely clean since the last major volcanic eruption was the one of Mt. Pinatubo in 1991. Conditions changed drastically in the course of the 18-month observational period. Details are discussed in Chapter 5.

The optical properties of stratospheric aerosols are relatively well understood (e.g. *Wandinger et al.*, 1995; *Jäger and Deshler*, 2002). The refractive index depends on the acidity and can be calculated in dependence on atmospheric temperature and water-vapor mixing ratio. The actual size distribution of the droplets determines the measured lidar ratios and Ångström exponents. Values of the lidar ratio reach from 20 sr for large mean droplet diameters to 70 sr for small mean droplet diameters (*Wandinger et al.*, 1995; *Ansmann et al.*, 1997).

3.3 Cloud classification

3.3.1 General considerations

Clouds represent an extremely variable four-dimensional atmospheric structure. The cloud spectrum reaches from geometrically and optically thick convective and precipitating sys-

tems to faint, subvisible cirrus and polar stratospheric clouds. Accordingly, the effects of clouds on the Earth's radiation budget are manifold, and the investigation of clouds in the climate system is a challenging task and requires enormous efforts. Active remote sensing from ground and space is a powerful tool in cloud research. However, it is not possible to meet the requirements of cloud observations with a single instrument. Lidar is especially useful to detect thin cirrus clouds and to investigate the properties of high ice clouds and mid-level mixed-phase clouds of low optical depth. Lidar observation are typically limited to an optical depth of about 2. In contrast, radar is able to penetrate optically thick clouds and precipitation, but is less sensitive for optically thin clouds. Therefore, both missions A-TRAIN with the CALIPSO and CloudSat satellites and EarthCARE with ATLID and a cloud-profiling radar onboard follow the strategy of combining lidar and radar measurements to cover the complete spectrum of clouds. The synergistic effect is expected to be of great importance, but is beyond the scope of the present study.

The driving task of spaceborne cloud observations with lidar is the detection of optically thin ice clouds. Comparisons of CALIOP measurements with CloudSat, MODIS (Moderate Resolution Imaging Spectroradiometer), and AIRS (Atmospheric Infrared Sounder) observations reveal that only the lidar is able to detect the uppermost ice clouds in the atmosphere adequately (*Weisz et al.*, 2007). A second major capability of lidar measurements is the discrimination of the ice and water phases in thin and moderately thick clouds. The capability relies on the detection of the depolarization ratio which in principle allows the separation of spherical, non-depolarizing water droplets from irregularly shaped, depolarizing ice crystals. However, there are two effects which lead to ambiguities and must be carefully considered in this context.

The first one is the occurrence of settling ice crystals which are oriented with their largest surface parallel to the ground. These crystals cause strong specular reflections and a depolarization ratio of zero, if the lidar is vertically pointing. This effect practically prohibits the discrimination of layers with super-cooled water droplets from layers of settling ice crystals in mixed-phase clouds. The effect can be avoided by tilting the lidar a few degrees off zenith/off nadir. Because it was found that specular reflections remarkably influenced the CALIPSO measurements at the original tilt angle of 0.2°, the CALIPSO Science Team decided to change the pointing of the lidar in course of the mission to 3° off nadir. This configuration is valid since November 28, 2007. For ATLID a tilt angle of 3° is foreseen as well. ALADIN points to 35° anyhow (in order to get the wind information). The majority of EARLINET instruments perform observations under 0° zenith angle. Thus the effect of specular reflection must be taken into consideration when comparing the ground-based and spaceborne observations.

The second effect that influences the depolarization ratio of clouds is multiple scattering. Cloud droplets of spherical shape cause zero depolarization only for backscattering at ex-

act 180°. However, in clouds, one or more scattering events in the forward direction may occur, before or after a photon is scattered backward at an angle somewhat different from 180°. According to Mie scattering theory, this angular deviation causes a depolarization of the light scattered by droplets. Therefore, the depolarization ratio is increasing with penetration depth in water clouds. The effect depends on the cloud droplet size as well as on the instrument configuration and plays an important role for spaceborne measurements. Sophisticated algorithms are able to distinguish depolarization caused by irregular ice crystals and by multiple scattering from water droplets (*Hu et al.*, 2007). These algorithms rely on the combined investigation of depolarization and attenuated backscatter and require the elimination of specular reflections through off-nadir pointing.

Multiple scattering is a severe problem for space-based cloud lidar measurements and influences the observed cloud optical properties in general. Particles much larger than the detection wavelength, i.e. cloud droplets and ice crystals, direct about 50% of the scattered light into the forward direction. This light partially remains in the laser beam, so that the effective extinction measured with the lidar is reduced compared to the single-scattering extinction of the cloud. For spaceborne lidar, also a delay in the photons' time of flight must be taken into account. Multiple-scattering effects on the measured extinction and lidar-ratio values depend on size and number concentration of the hydrometeors as well as on lidar system parameters, specifically on the receiver field of view and on the distance to the cloud. The multiple-scattering influence on space-based lidar measurements is considerably larger than on ground-based measurements. So far, the CALIPSO retrievals apply a rough multiple-scattering estimate which is based on look-up tables only. Thus care must also be taken when comparing optical cloud data derived from spaceborne and ground-based measurements.

With respect to the spectral dependence of extinction and backscattering, it is expected that clouds exhibit a neutral scattering behavior in the UV-IR spectral range, because hydrometeors (cloud and rain droplets, ice crystals) are much larger than the lidar detection wavelengths. Typically, color ratios are ∼1 and Ångström exponents ∼0. Thus spectral conversion factors to relate CALIOP/ALADIN/ATLID measurement are expected to be of minor importance for clouds. A recent study by *Tao et al.* (2008) reports a 1064/532-nm backscatter color ratio of 0.88±0.06 for cirrus clouds in the 7–13.5-km height region at the east coast of the United States, which is considerably lower than expected. However, these values are not supported by our own long-term observations in different regions of the globe and might be due to calibration uncertainties (calibration of IR lidar measurements requires specific efforts, e.g., a high dynamic range of signal detection in order to get a molecular background signal). In any case, a deeper investigation of the wavelength behavior of cloud extinction and backscattering might be useful.

3.3.2 CALIPSO cloud classification

If the preceding algorithms have identified a feature to be a cloud, an ice–water discrimination algorithm is applied next in the CALIPSO retrieval (*Liu et al.*, 2005; *Hu et al.*, 2009). Different algorithms have been used in the CALIPSO Version 2 and 3 data releases. In principle, the temperature of the cloud, the layer-integrated depolarization ratio and its signal-to-noise ratio, and the layer-integrated attenuated backscatter are considered in the algorithms. In the Version 2 algorithm, probability functions are introduced which consider first the measured integrated depolarization ratio and its uncertainty, second, if this measure is ambiguous, the feature top temperature, and third, the relation between layer-integrated depolarization and attenuated backscatter to calculate the probability of the cloud phase being ice, water, or mixed-phase. The feature flag for the cloud classification (ice/water phase) is (*Anselmo et al.*, 2006):

0 = unknown/not determined,
1 = ice,
2 = water,
3 = mixed phase.

For the Version 2 release of the Vertical Feature Mask the following quality statement was given: "The algorithm used in the Version 2.01 release identifies obvious water and ice clouds and clear cases of oriented ice crystals. Improvements for recognizing mixed phase clouds are planned for future release" (see CALIPSO Quality Statements: Lidar Level 2 Vertical Feature Mask Version, Release: 2.01, available at http://eosweb.larc.nasa.gov/PRODOCS/calipso/Quality_Summaries/CALIOP_L2VFMProducts_2.01.html).

In Version 3 a new algorithm is applied (*Hu et al.*, 2009). The following statement is given: "Cloud phase is determined from relations between depolarization ratio, backscatter intensity, temperature, and attenuated backscatter color ratio. The cloud phase algorithm used in Version 3 is new and completely different from that used in Version 2. The Version 3 algorithm classifies cloud layers as water, randomly-oriented ice, or horizontally-oriented ice. In those cases where the classification is ambiguous, the phase is reported as "unknown/not determined". The classification of "mixed phase cloud" has been eliminated; the Version 3 algorithm does not attempt to determine if more than one phase is present within a layer. The Version 3 algorithm distinguishes between two separate classes of ice clouds: those dominated by randomly oriented particles, and those containing a substantial fraction of horizontally oriented crystals" (see http://eosweb.larc.nasa.gov/PRODOCS/calipso/Quality_Summaries/CALIOP_L2VFMProducts_3.01.html).

Accordingly, the new feature flag for the cloud classification is:

0 = unknown/not determined,
1 = randomly oriented ice,
2 = water,
3 = horizontally oriented ice.

3.3.3 Cloud types and special considerations for the study

The study concentrated on the investigation of optically thin ice, water, and mixed-phase clouds with focus to the middle and upper troposphere. In the following, we briefly summarize the most important facts for cloud lidar measurements.

3.3.3.1 Water clouds

Pure water clouds typically occur in the planetary boundary layer and the lower free troposphere at temperatures above −20 °C. Extinction coefficients of water clouds are usually $\gg$1 km^{-1} (and the optical depth $\gg$1) so that the penetration depth of the lidar is of the order of a few hundred meters. Thus the cloud properties can be investigated either near the cloud base with the ground-based lidar or near the cloud top with the spaceborne system only. Therefore, in many cases it is not possible to relate ground-based and spaceborne lidar observations directly, because that requires that both instruments penetrate the cloud. Furthermore, it has to be considered that the horizontal extension of water clouds often is much smaller than the distance of the satellite ground track to the ground station (see also Sec. 3.4). Thus great care must be taken in the investigation of water clouds.

According to Mie scattering calculations for typical cloud droplet size distributions and optical wavelengths, the lidar ratio in water clouds has a nearly constant value of 18–19 sr over a broad range of wavelengths and cloud droplet diameters (*O'Connor et al.*, 2004). This fact may help in the retrievals (because of the known input parameter for backscatter lidar retrievals) as well as in cloud–aerosol and cloud phase discrimination schemes to be developed for spaceborne HSRL. However, it has to be considered that the effective lidar ratio derived from the Raman/HSRL (direct extinction measurement) or Klett methods is smaller due the influence of multiple scattering (*Wandinger*, 1998).

The depolarization ratio measured in water clouds is caused by multiple scattering, as mentioned above. A direct relationship between depolarization ratio and multiple-scattering fraction has been discovered by *Hu et al.* (2006). Relationships between depolarization ratio and attenuated backscatter (*Hu et al.*, 2007) and between depolarization ratio and effective lidar ratio (*Hu*, 2007) have also been found.

3.3.3.2 Ice clouds

Pure ice clouds exist at temperatures below −20 °C preferably above 5 km height. Extinction coefficients in ice clouds are typically <1 km^{-1}, the optical depth is often <2. Thus normally the lidar penetrates ice clouds and comparisons of ground-based and spaceborne observations are possible. Ice crystals strongly depolarize the backscattered light, except when pristine crystals are horizontally oriented and exactly vertically hit by the laser light. Typically, ice clouds show a strongly varying backscatter both in the vertical and horizontal directions, so that they can also be identified from their two-dimensional signatures.

The lidar ratio of ice clouds has typical values of 15–30 sr, depending on ice crystal size and shape. The values are drastically reduced when specular reflection occurs. In this case, the backscatter is enhanced by a factor of 10 on average, but variations up to a factor of 1000 while "rocking over the zenith" have been observed. The cloud extinction is not influenced by specular reflection. As mentioned above, most of the EARLINET lidars point vertically, so that specular reflections influence the ice cloud observations.

Multiple scattering plays an important role also for ice clouds. Typical ice crystals are much larger than liquid cloud droplets. Thus the forward scattering peak is very narrow. About one half of the scattered light remains in the lidar receiver field of view and travels with the laser beam over considerable distances (several kilometers). Therefore, the measured effective extinction at the near cloud edge (cloud base for the ground-based lidar, cloud top for the space-based lidar) is about a factor of two smaller than the single-scattering extinction (*Wandinger*, 1998). This effect reduces with penetration depth depending on the actual measurement geometry, the crystal size, and the cloud's optical depth. Multiple scattering can also complicate the determination of ice cloud boundaries at the far end from the lidar and the calculation of the cloud optical depth from the "elevated-layer method" (i.e. molecular returns from above and below the cloud are used to determine the transmittance (e.g. *Liu et al.*, 2005)). Because multiply scattered light leaves the receiver field of view continously over long distances, a tail-like structure is obtained at the far edge of the cloud. This effect is especially important for the spaceborne geometry (large observed volume), but is also observed with ground-based instruments. It should be noted, that multiple scattering does not influence the depolarization ratio of ice clouds.

3.3.3.3 Mixed-phase clouds

In the temperature range from 0 to −35 °C water and ice can coexist in the atmosphere. Different types of mixed-phase clouds occur in the atmosphere. Whereas ice and hail

within thick cumulonimbus clouds are beyond the optical detection capabilities, lidar is very useful for the characterization of optically and geometrically thin mixed-phase clouds in the middle troposphere (altocumulus, altostratus). These clouds have typical optical depths of 0.5–5 and often a vertical extent of only 100–300 m. In such clouds, thin layers of supercooled liquid water droplets may occur next to extended regions with (falling) ice crystals. In principle, depolarization measurements would clearly indicate the liquid-water regions. However, for vertical pointing lidars the ambiguity due to non-depolarizing, oriented ice crystals practically prohibits this kind of investigation.

Hogan et al. (2004) have shown that layers with supercooled water in mixed-phase clouds exhibit a much stronger backscattering than regions containing ice crystals. Therefore, they used a threshold method to identify layers of supercooled water in LITE (Lidar In-space Technology Experiment, flown on the Space Shuttle in 1994) measurements. If Raman measurements are available, the lidar ratio can be used in addition to distinguish orientied ice crystals from supercooled droplets. As already mentioned, the lidar ratio is drastically reduced to values of the order of 2, when specular reflection occurs. In our study, we use combined criteria from backscatter, depolarization, and lidar-ratio observations to identify ice and water in mixed-phase clouds. The above-given statements regarding multiple-scattering effects hold for mixed-phase clouds as well, of course.

3.4 Representativeness of satellite observations

Tropospheric aerosols and their interaction with clouds are one reason for global-scale changes in the Earth's heat balance, but the respective forcing estimations are space/time integrals over highly variable quantities and, therefore, sources of high uncertainties (*Forster et al.*, 2007). Thus estimates of global and regional climate forcing must address the difficult issue of integrating highly variable quantities over space and time. A synergistic approach of satellite and ground-based observations together with model calculations is strongly requested by the scientific community in order to achieve an accurate quantification of aerosol and cloud radiative forcing (e.g. *Diner et al.*, 2004).

The CALIOP lidar onboard the CALIPSO mission provides a first unique opportunity to study the 4-dimensional distribution of aerosols and clouds on a global scale. The main characteristics of the lidar is to provide a small footprint on the ground, i.e. a high horizontal resolution, very high vertical resolution, a high sensitivity to the presence of aerosols, and an excellent discrimination against noise thanks to laser purity. All these factors allow also measurements between clouds and the penetration of optically thin clouds and, therefore, the profiling of the troposphere underneath. However, CALIOP has a small footprint and a revisiting time of 16 days. Therefore, the representativeness of the satellite measurements is a big issue to be investigated.

Until now, the study of spatial and temporal variability with respect to the altitude was inhibited by the lack of global vertical profiles. Only high-resolution vertical profiles allow the inspection of stratospheric and free-tropospheric layer dynamics and the investigation of complex effects of mixing processes that influence the microphysical and optical properties of aerosols and clouds.

A first experience with lidar in space was gathered by LITE. Several campaigns were organized all around the world in order to validate and exploit lidar measurements from space. From those first ground-based and spaceborne comparisons it came out that aerosols and clouds cannot be considered to be homogeneous for distances greater than 2 hours/50–100 km and 30 minutes/20 km, respectively. However, the LITE experimental mission lasted for only 11 days. More can be learnt with long-term lidar satellite measurements, and such a database is becoming available starting from the CALIPSO mission and going further on with ALADIN and ATLID.

An attempt to assess the representativeness of sun-synchronous polar-orbiting satellite columnar measurements was reported by *Kaufman et al.* (2000). They used ground-based aerosol optical depth measurements of the Aerosol Robotic Network (AERONET) to determine if measurements at a single time of the day are representative, in a climatological sense, of daily averaged measurements. In particular, the different measurements provided at one site by AERONET during one day was compared to the mean. Almost no bias and a standard deviation (therefore a variability) of about 20% was obtained.

The mesoscale variation of tropospheric aerosol has been extensively discussed by *Anderson et al.* (2003), starting from a correlation analysis of high-resolution column-integrated measurements of optical properties. It came out that there is little variability below 20 km horizontal scale, but a sharp increase in variability is observed over horizontal scales of 20–100 km. This is mainly ascribed to major aerosol sources (like dust storms, biomass burning and anthropogenic pollution) and the main sink for aerosol (precipitation) that typically are characterized by comparable horizontal extension. In this sense, aerosol plumes cover large areas but are internally not homogeneous. The main result of this paper is that on scales larger than few hours or few tens of kilometres, aerosol cannot be considered as homogeneous in space and time. The authors made use of a threshold criterion on autocorrelation of 0.8 and found out that coherent timescales and space scales for aerosol columnar load are less than 10 h and 200 km, respectively. This paper highlighted the need of a statistically significant amount of data to address representativeness issues. In these previous works, a large source of variability not considered at all is the vertical mixing, which leads to horizontal inhomogeneities due to large vertical concentration gradients.

The CALIPSO mission with its high resolution both in time and in horizontal and vertical dimensions provides the first opportunity to investigate 4-dimensional aerosol and cloud

fields in detail. Because of the long revisiting time and of the small footprint, it is highly questionable how well these measurements represent the atmospheric conditions of a surrounding area over a longer time. EARLINET correlative measurements provide a unique opportunity to investigate the representativeness of CALIPSO observations, thanks to the well-established high quality of EARLINET data and to the geographical distribution of EARLINET stations over Europe, covering a large variety of different aerosol contents in the free troposphere and the local planetary boundary layer (*Matthias et al.*, 2004; *Wandinger et al.*, 2004; *Papayannis et al.*, 2008; *Amiridis et al.*, 2008; *Pappalardo et al.*, 2004a). In the current ESA–CALIPSO study, CALIPSO and EARLINET observations are investigated in order to learn about spatial (both horizontal and vertical) and temporal representativeness of polar-orbit satellite measurements also in terms of revisit time. In particular, long-term series of measurements allow studies of temporal variability; the spatial variability within 100 km is investigated through CALIPSO–EARLINET differences at different horizontal distances; the horizontal variability on larger scales is studied with almost simultaneous measurements at different stations of the same cluster (typically within 500 km; see Chapter 2). Observations of long-range transport over Europe provide information on the variability that can be particularly high in such cases both in terms of geometrical and optical properties as demonstrated also by previous EARLINET studies (e.g. *Papayannis et al.*, 2008; *Mona et al.*, 2006; *Wang et al.*, 2008; *Villani et al.*, 2006).

For this kind of study, individual CALIPSO profiles taken in correspondence of correlative measurements at a single station would not be sufficient. Therefore, a specific subset of CALIPSO data related to Europe and surrounding areas is considered as fundamental. This subset provided to EARLINET by NASA is included in the current study database thanks to an ESA–NASA agreement (see Chapter 4).

3.5 Modelling tools and auxiliary data

Aerosol and cloud classification requires the careful analysis of atmospheric state parameters, meteorological situations, and air-mass transport. Therefore, within the study a number of auxiliary data and modeling tools have been used for the aerosol-type identification and the cloud classification in addition to the information derived from the lidar observations themselves. Part of the models also served as forecast tools in the measurements planning.

3.5.1 Atmospheric state parameters

Temperature, pressure, and humidity information is necessary, e.g., to classify cloud types (see Sec. 3.3) and to evaluate humidity growth of particles. Actual pressure and tempera-

ture profiles are needed in the lidar data evaluation as well (see Chapter 4). The radiosonde network of the national meteorological services in Europe provides information on pressure, temperature, and humidity on a fixed spatial and temporal grid. Radiosonde data can be downloaded, e.g., from http://weather.uwyo.edu/upperair/sounding.html. "Modeled" radiosonde data for specific times and grid points are available from the re-analysis of meteorological fields with forecast models. The latter data often fit better to the actual lidar observations when a nearby radiosonde station is missing.

3.5.2 Sun photometer data

Sun photometers deliver useful data on columnar aerosol optical and microphysical properties and provide complementary information to the lidar data. The aerosol optical depth derived from Sun photometer measurements can be used as a constraint for daytime lidar retrievals. Europe is covered by a dense network of AERONET (Aerosol Robotic Network) stations. Several of the EARLINET stations are directly equipped with an AERONET Sun photometer. The optical and microphysical data are retrieved on an operational mode at the AERONET data center at the NASA Goddard Space Flight Center (Greenbelt, VA, USA). The results can be downloaded from the AERONET website (http://aeronet.gsfc.nasa.gov).

3.5.3 Backward trajectories

The airmass origin can roughly be investigated through backward trajectory analysis. The German Meteorological Service (DWD) provides 4-day backward trajectories on a daily schedule for all EARLINET stations for 6 arrival heights between 925 and 200 hPa and for 2 arrival times (13 UTC and 19 UTC). For specific studies (i.e. longer transport times, other height levels), trajectories can be calculated with the HYSPLIT (Hybrid Single-Particle Lagrangian Integrated Trajectory) model. A discussion of the model is given by *Draxler and Hess* (1997), *Draxler and Hess* (1998), and *Draxler* (2003). HYSPLIT is available at http://ready.arl.noaa.gov/HYSPLIT.php.

3.5.4 Transport modeling and aerosol forecast

For detailed studies of aerosol origin, transport, and mixing the Lagrangian particle dispersion model FLEXPART, operated by the Norwegian Institute for Air Research, is used (*Stohl et al.*, 1998; *Stohl and Thomson*, 1999). The model simulates the long-range transport, dry and wet deposition, dispersion, and radioactive decay of air pollutants released from point, line or volume sources. It treats advection and turbulent diffusion of linear

tracers by calculating the trajectories of a multitude of particles. The model parameterizes turbulence in the boundary layer and in the free troposphere by solving Langevin equations (*Stohl and Thomson*, 1999). To account for convection, a parameterization scheme is used (*Emanuel and Živković-Rothman*, 1999) which is based on the buoyancy sorting principle.

The IfT lidar group has implemented FLEXPART on an own server which allows extensive model runs. The model is driven by global model-level data. We use the archived meteorological data from the NCEP FNL (National Centers for Environmental Prediction final analysis) Global Tropospheric Analyses with a temporal resolution of 6 hours (00, 06, 12, 18 UTC) and a horizontal resolution of $1^\circ \times 1^\circ$. The FNL data are provided by the CISL (Computational & Information Systems Laboratory) Research Data Archive which is managed by NCAR's (National Center for Atmospheric Research) data support section (see http://dss.ucar.edu/datasets/ds083.2/). Particles are transported both by the resolved winds and by parameterized subgrid motions.

The Dust REgional Atmospheric Model (DREAM) (*Nickovic et al.*, 2001; *Pérez et al.*, 2006a,b) is used within EARLINET for the coordination of intensive measurement periods during dust outbreaks over Europe. DREAM predicts the atmospheric life cycle of eroded desert dust and is plugged to the NCEP/ETA model, the forecast model of the National Center for Environmental Prediction for the African region. It solves the Euler-type partial differential non-linear equation for dust mass continuity. The model is implemented at the Barcelona Supercomputing Center. Daily updated analysis data and forecasts up to 72 h are provided. For EARLINET the vertical profiles of the dust concentration at 20 sites are predicted. The data are available at http://www.bsc.es/plantillaH.php?cat_id=519.

The Navy Aerosol Analysis and Prediction System (NAAPS, see http://www.nrlmry.navy.mil/aerosol) provides a 120-h global aerosol forecast for tropospheric sulfate, smoke, and dust. Furthermore, NAAPS provides near-real-time access to global aerosol observational products such as satellite images and AERONET data. A quick evaluation of the actual aerosol situation over Europe on a daily basis is possible with this tool.

3.5.5 Aerosol source information

Aerosol source information is required in order to interprete the findings from trajectory and transport modeling. Anthropogenic emissions from industry or traffic, including ship traffic, remain more or less constant in time and with respect to the source locations. Information can thus be obtained from emission inventories such as EMEP (European Monitoring and Evaluation Programme, see http://www.emep.int). Other aerosol sources, especially those of dust, smoke, and volcanic emissions are highly variable in space and time.

Dust uptake is determined by the atmospheric dynamics over the deserts. It can thus be modeled and forecasted as mentioned above. In contrast, the fire activity and thus the production of smoke is highly dependent on a variety of natural (region of the globe, season, precipitation, weather conditions) and anthropogenic factors (land use, human activity). Fire maps produced from data of the Moderate Resolution Imaging Spectroradiometer (MODIS) are of major value to characterize smoke source regions. MODIS flies onboard NASA's Aqua and Terra satellites and covers most of the globe every day. Fire maps are available from the MODIS Rapid Response System at http://rapidfire.sci.gsfc.nasa.gov. Volcanic activity is regularly reported by the Smithsonian Institution's Global Volcanism Program (GVP). Weekly and monthly reports, including active volcanoes, date and time of eruptions, as well as plume heights can be found at http://www.volcano.si.edu/index.cfm.

3.6 Conclusions

3.6.1 General observational strategy

Sixteen EARLINET stations distributed over Europe contributed with measurements to the study. Seven stations performed multiwavelength observations. They deliver the basic data set for the aerosol and cloud classification study. Data from all 16 stations are used to investigate the representativeness of satellite observations against ground-based network measurements. Details on the parameters provided by each station, the calculation schemes, and the structure of the long-term aerosol and cloud database are discussed in Chapter 4.

3.6.2 Aerosol typing

The aerosol typing scheme applied in the present study mainly relies on the CALIPSO aerosol typing. This is necessary, on the one hand, to compare the ground-based findings with the CALIPSO aerosol typing and, on the other hand, to derive conversion factors to relate future spaceborne observations directly to the available CALIPSO data. However, as our investigations show, the occurrence of mixtures of different pure aerosol types requires specific care. The only mixture considered in the CALIPSO aerosol typing is *polluted dust* the definition of which is a bit vague: "This aerosol model is designed to account for episodes of dust mixed with biomass burning smoke, which are frequent in regions close to strong sources of both [e.g., in West Africa (cf. MODIS images) and Asia (cf. ACEAsia, INDOEX)]. It also accounts for instances of dust mixed with urban pollution as is frequently encountered in parts of Asia and Europe (*Omar et al.*, 2009)."

In the long-term database the following pure aerosol types are considered in accordance with the CALIPSO typing scheme:

1. marine aerosol,
2. mineral dust,
3. polluted continental aerosol,
4. continental background aerosol,
5. biomass-burning aerosol (smoke),
6. stratospheric aerosol.

Volcanic aerosol (in the troposphere) is implemented as an additional type, so that respective datasets can be added to the database in the future. Furthermore, in our aerosol typing scheme we consider any kind of possible mixtures of the pure types listed above. In this way, conversion factors for the CALIPSO *polluted dust* type can be derived from the database by taking mixtures of dust with polluted continental aerosol and/or with smoke into account. In addition, other mixing states, e.g., dust and marine aerosol can be distinguished and investigated in more detail.

For the investigation of aerosol origin, aging, modification, and mixing processes, we introduced the following specific parameters in the database:

- source region,
- age,
- humidity.

The source region and the age of the observed aerosol are identified from transport model calculations with FLEXPART. A source-region code for each aerosol type has been developed based on the actual observations:

- marine aerosol: 1–Atlantic Ocean, 2–North Sea, 3–Baltic Sea, 4–Mediterranean, 5–Black Sea;
- mineral dust: 1–Western Sahara, 2–Central Sahara, 3–Eastern Sahara, 4–Arabian Peninsula;

- polluted continental aerosol, continental background aerosol, and biomass-burning aerosol (smoke): 1–Central Europe, 2–Northern Europe, 3–Western Europe, 4–Southwestern Europe, 5–Southern Europe, 6–Southeastern Europe, 7–Eastern Europe, 8–Europe, 9–Arctic, 10–North America, 11–Siberia.

Details are discussed in Chapter 5. The aerosol age is estimated in terms of transport days from the source region. The relative humidity of an air mass influences the actual particle size depending on the hygroscopic growth properties of the particles. Therefore, an estimate of the relative humidity in the observed air mass is taken from the re-analyzed meteorological fields (NCEP FNL, see above) at the corresponding observational site and stored in the database.

3.6.3 Cloud classification

The cloud classification in the present study follows the original CALIPSO cloud classification (Version 2 data release) and considers:

1. water clouds,
2. ice clouds,
3. mixed-phase clouds.

Ambiguities due to specular reflection and multiple scattering have to be taken into account in the data evaluation. Therefore, a multi-criteria approach is applied for the cloud classification, which takes the following parameters into account:

1. temperature profile within the cloud:
   –threshold values for pure water and pure ice clouds are 0 °C and −35 °C, respectively;
2. absolute backscatter and extinction values of the cloud:
   –with a threshold backscatter value of 0.05 $km^{-1}sr^{-1}$ or a threshold extinction value of 1 km^{-1} a rough discrimination of water (above threshold) and ice clouds (below threshold) is possible;
3. depolarization-ratio profile:
   –high and varying depolarization ratios indicate ice particles;
   –a low, but slightly increasing depolarization ratio with height indicates multiple scattering in water clouds;
   –low depolarization ratios are also a sign for horizontally oriented ice crystals when

the lidar is vertically pointing; in this case usually a significant higher depolarization is observed at the layer base where the ice crystals evaporate;

4. lidar-ratio profile:
   –effective lidar ratios of 13–16 sr at the cloud base which slightly increase to values of 17–19 sr point to water clouds (with multiple-scattering effect);
   –strongly varying lidar ratios indicate ice clouds;
   –very low lidar-ratio values together with low depolarization ratios clearly identify horizontally oriented ice crystals.

Because of different pointing angles and receiver fields of view, a common typing scheme to distinguish horizontally and randomly oriented ice crystals as in the CALIPSO Version 3 data release is not available for EARLINET. However, as discussed, respective information could be retrieved at least from vertically pointing systems. However, such an approach is beyond the tasks of the present study. The pointing angle and the receiver field of view of each instrument is given in the database.

3.6.4 Strategies for the representativeness study

The representativeness of ground-based network measurements versus spaceborne cross-section observations is investigated separately for clouds and aerosols. The typical averaging times are 10 minutes for clouds and 30 minutes for aerosols. Due to the large variability in space and time, cloud comparisons are mainly restricted to CALIPSO overpasses within 10 km and 10 min from the ground-based observation. Because of the cloud variability, the influence of multiple scattering and of the observing geometry on the optical parameters determined with lidar, an in-depth comparison of cloud optical properties derived from EARLINET and CALIPSO measurements appears to be not very reasonable. Therefore, the cloud investigations concentrate on comparisons of the determined cloud geometrical properties and on the cloud classification (ice/water phase discrimination).

In contrast, the representativeness of aerosol observations is studied in detail with respect to geometrical and optical properties. Correlation analysis is performed in dependence on the spatial and temporal distance of the satellite cross-section observation from a single ground-based measurement. In addition, the representativeness of the cross-section observation against the measurements within a cluster of stations is investigated. Details are discussed in Chapter 4. Results are presented in Chapter 7.

3.6.5 Auxiliary tools

For measurement planning and data evaluation a number of auxiliary tools have been applied. Meteorological data were taken form re-analyzed model fields (NCEP FNL). FLEXPART transport model calculations were used to identify source regions and age of aerosols. The DREAM model supported the forecast and analysis of dust transport. MODIS fire maps, the EMEP emission inventory, and the NAAPS model helped identifying aerosol sources. Backward trajectory calculations and additional observational data, e.g., from AERONET Sun photometers, were used for the investigation of specific situations.

Chapter 4

Structure of the long-term database

This chapter describes the structure of the long-term aerosol and cloud database established from the correlative EARLINET–CALIPSO observations. Calculation procedures and typical errors are discussed. Data formats and exploitation and visualisation tools are presented as well. After an overview on the general structure and contents of the database in Section 4.1, Section 4.2 summarizes the products which are available from the individual EARLINET stations. Section 4.3 discusses the geophysical products derived from the multiwavelength ground-based observations. The available CALIOP products are summarized in Section 4.4.1. In Section 4.4 the database products describing the representativity of spaceborne against ground-based observations are defined. Measurement examples are used to illustrate the procedures. Finally, the implementation and the internal structure of the database is described in Section 4.5.

4.1 Overview on the database structure and contents

The aerosol and cloud database virtually consists of four parts, i.e. Part A, B, C, and D, with the following contents:

- *Part A*: This part contains profiles of extinction and backscatter coefficients and of depolarization ratios measured at pre-defined laser wavelengths at 16 EARLINET stations during pre-defined observational periods (usually during a CALIPSO overpass) according to the measurement plan (see Chapter 2). Hereafter, an observational period is called a *measurement*. A measurement typically takes 150 min, centered around a CALIPSO overpass, but can also be shorter or longer depending on the actual atmospheric situation. For each measurement, several profiles of extinction and backscatter coefficients at different wavelengths and for a number of successive averaging periods (typically 30 min) are provided (see Section 4.2).

These profiles (Level 2 data), which represent the primary information available from the ground-based network, are evaluated by the project partners at each station individually. Extinction and backscatter coefficients are extensive aerosol or cloud parameters, i.e. they depend on the absolute concentration of aerosol and cloud particles in the atmosphere and are not necessarily characteristic values for certain aerosol and cloud types.

- *Part B*: This part of the database contains layer-mean cloud and aerosol geophysical products. Intensive particle parameters are calculated by relating the primary optical data to each other. Information on the cloud or aerosol type can mainly be extracted from such intensive parameters, which do not depend on the absolute concentration of aerosol and cloud particles, but on characteristic properties of an ensemble of scattering particles. Typical products of Part B of the database are depolarization ratios, lidar ratios, different color ratios as well as backscatter-related and extinction-related Ångström exponents (see Chapter 3 and Section 4.3). These parameters are calculated for pre-defined cloud and aerosol layers which we call *features*. The type/origin of each distinct feature in a measurement is investigated in detail with the help of atmospheric state parameters, trajectory and transport models, and by interpreting the ground-based and spaceborne data themselves (e.g., depolarization measured in clouds is used for cloud classification; see also Chapter 3).

- *Part C*: This part of the database contains conversion factors that relate measurements of different spaceborne instruments (CALIOP, ALADIN, ATLID) to each other. A typical conversion factor would be the 532-nm or 1064-nm backscatter coefficient (CALIOP product) versus the 355-nm backscatter coefficient (ALADIN, ATLID product; see Chapter 1 and Section 4.3). The conversion factors are derived from Part B of the database. Conversion factors are given in dependence on the aerosol and cloud types (feature types, see Chapter 3 and Section 4.5).

- *Part D*: This part of the database is dedicated to the comparison of EARLINET and CALIPSO measurements and the results of the correlation analysis. CALIPSO Level 2 products (see Section 4.4.1) are included and compared to the correlative EARLINET measurements. Profiles (backscatter and extinction coefficients) as well as layer products (boundaries, layer-mean backscatter and extinction values) are related. Deviations between ground-based and spaceborne data are given in terms of geometrical parameters, such as the difference of cloud and aerosol layer base and top heights, and in terms of optical data, such as difference backscatter-coefficient profiles (see Chapter 3 and Section 4.4). These quantities are given in the database in dependence on the spatial and temporal distance of the spaceborne and ground-based observations.

In the following, we discuss the retrieved products in more detail.

4.2 EARLINET products – Part A of the database

4.2.1 Definition of Part A products

According to Tab. 2.1, the following products are available for Part A of the database from the high-performance stations:

- backscatter-coefficient profile at 355 nm (mandatory),
- extinction-coefficient profile at 355 nm (mandatory),
- backscatter-coefficient profile at 532 nm (mandatory),
- extinction-coefficient profile at 532 nm (mandatory),
- backscatter-coefficient profile at 1064 nm (optional),
- depolarization-ratio profile (optional).

The contributing stations deliver the following products to Part A of the database:

- backscatter-coefficient profile at 355 or 532 nm (mandatory),
- extinction-coefficient profile at 355 or 532 nm (optional),
- depolarization-ratio profile (optional).

Well-defined algorithms are used at each station to evaluate the lidar signals and to calculate the profiles listed above. Within EARLINET, the individual algorithms underwent extensive qualitiy-assurance activities which are described in detail in the literature (*Pappalardo et al.*, 2004b; *Böckmann et al.*, 2004). Whenever possible, the Raman method is applied, because independent information on the extinction and backscatter coefficients is derived from the elastic-backscatter profile and the respective nitrogen Raman signal in this case. No critical assumptions are necessary. In principle, the low signal-to-noise ratios allow Raman measurements throughout the troposphere only at nighttime. At daytime, measurements in the lower troposphere are possible. However, the majority of daytime data is evaluated using elastic backscatter signals and applying the so-called Klett method (see below). For the sake of completeness, we briefly recall the principle calculation schemes and the error discussion here.

Extinction retrieval (Raman method)

The particle[1] exinction coefficient $\alpha_{\mathrm{par}}(Z,\lambda_0)$ at wavelength λ_0 and height Z is directly derived from the nitrogen Raman signal $P(Z,\lambda_{\mathrm{Ra}})$ at the Raman-shifted wavelength λ_{Ra} (*Ansmann et al.*, 1990):

$$\alpha_{\mathrm{par}}(Z,\lambda_0) = \frac{\frac{\mathrm{d}}{\mathrm{d}Z}\ln\frac{N_{\mathrm{Ra}}(Z)}{Z^2P(Z,\lambda_{\mathrm{Ra}})} - \alpha_{\mathrm{mol}}(Z,\lambda_0) - \alpha_{\mathrm{mol}}(Z,\lambda_{\mathrm{Ra}})}{1+\left(\frac{\lambda_0}{\lambda_{\mathrm{Ra}}}\right)^{\mathring{a}_\alpha(Z)}}\,. \tag{4.1}$$

The contribution of molecular extinction is corrected by calculating the profiles $\alpha_{\mathrm{mol}}(Z,\lambda_0)$ (for the way to the scatterer) and $\alpha_{\mathrm{mol}}(Z,\lambda_{\mathrm{Ra}})$ (for the way back) from actual atmospheric temperature and pressure profiles. Theses profiles are also needed to determine the nitrogen number density profile $N_{\mathrm{Ra}}(Z)$. To obtain the particle extinction coefficient at the transmitted wavelength, we introduce the extinction-related Ångström exponent $\mathring{a}_\alpha$ which describes the wavelength dependence of the particle extinction coefficient:

$$\frac{\alpha_{\mathrm{par}}(\lambda_0)}{\alpha_{\mathrm{par}}(\lambda_{\mathrm{Ra}})} = \left(\frac{\lambda_{\mathrm{Ra}}}{\lambda_0}\right)^{\mathring{a}_\alpha}\,. \tag{4.2}$$

Measurement errors strongly depend on the actual system parameters which can differ significantly from instrument to instrument. Therefore, error profiles are individually calculated by each group. Some general estimates are given in the following. However, the numbers should be taken as rough estimates only.

For extinction retrievals, appropriate averaging in space and time is necessary in order to reduce the noise in the weak Raman signals. A statistical error of the Raman signal of <5% reached by the averaging permits one to retrieve extinction coefficients with a statistical error of <10%–20%, if a sufficient extinction of the signal of >0.05 km^{-1} occurs. The detection limit is of the order of 0.005 km^{-1}.

Because particle extinction coefficients are determined from a single molecular signal profile, measurements close to the lidar are biased by the incomplete overlap of laser beam and receiver field of view. In the case of measurements with large telescopes, this effect may prohibit extinction-coefficient determination up to distances of several kilometers from the lidar. To overcome this problem, two methods are applied. Several lidars are equipped with an additional small telescope, that is used for measurements in the near range. For other instruments the overlap function is experimentally determined and corrected for (*Wandinger and Ansmann*, 2002). Therefore, in both cases, measurements can typically start at a distance of 300–800 m from the lidar. The remaining error of the extinction

[1]Particle stands for any kind of solid or liquid constituent in air. The index represents aerosol particles as well as cloud droplets, ice crystals and precipitating hydrometeors.

coefficient because of the overlap effect is estimated to be <0.02 km^{-1} for distances <2 km and is negligible above.

Other systematic errors, which might result from uncertainties in the input parameters needed to evaluate the molecular signals (*Ansmann et al.*, 1990, 1992b), are negligible in most cases. Data from nearby radiosonde stations are normally used to get actual pressure and temperature profiles, from which Rayleigh-extinction and nitrogen-number-density profiles can be calculated with high accuracy. The Ångström exponent is determined from measurements at two wavelengths in the case of the high-performance stations. At the other sites, estimates resulting from the long-term EARLINET experience are used. Overestimation and underestimation of the value of $\mathring{a}_\alpha$ by 0.5 leads to relative errors of the order of 5%.

In summary, the extinction-coefficient measurement is limited to relative errors of the order of 10%–20% by the statistical uncertainty. Systematic errors of the order of <0.02 km^{-1} mainly occur in the near range.

Backscatter retrieval (Raman method)

The particle backscatter coefficient $\beta_{\mathrm{par}}(Z,\lambda_0)$ is determined from the ratio of the elastic-backscatter signal $P(Z,\lambda_0)$ and the nitrogen Raman signal $P(Z,\lambda_{\mathrm{Ra}})$ (*Ansmann et al.*, 1992a):

$$\begin{aligned}\beta_{\mathrm{par}}(Z,\lambda_0) &= -\beta_{\mathrm{mol}}(Z,\lambda_0) + [\beta_{\mathrm{par}}(Z_0,\lambda_0) + \beta_{\mathrm{mol}}(Z_0,\lambda_0)] \\ &\quad \times \frac{P(Z_0,\lambda_{\mathrm{Ra}})P(Z,\lambda_0)}{P(Z_0,\lambda_0)P(Z,\lambda_{\mathrm{Ra}})}\frac{N_{\mathrm{Ra}}(Z)}{N_{\mathrm{Ra}}(Z_0)} \\ &\quad \times \frac{\exp\{-\int_{Z_0}^{Z}[\alpha_{\mathrm{par}}(z,\lambda_{\mathrm{Ra}}) + \alpha_{\mathrm{mol}}(z,\lambda_{\mathrm{Ra}})]\mathrm{d}z\}}{\exp\{-\int_{Z_0}^{Z}[\alpha_{\mathrm{par}}(z,\lambda_0) + \alpha_{\mathrm{mol}}(z,\lambda_0)]\mathrm{d}z\}}\,. \end{aligned} \tag{4.3}$$

Input parameter is the particle backscatter coefficient at a specific distance Z_0 from the lidar. In order to minimize the influence of this reference value, it is usually set into a height region, where molecular scattering is much stronger than particle scattering. Appropriate regions of clear air can be identified from the extinction profiles derived before, but also from the signal-ratio profile itself. The systematic error of the backscatter coefficient caused by an incorrect estimate of the reference value is usually <0.0001 km^{-1}sr^{-1}. The statistical error of the backscatter coefficient because of signal noise is reduced to $<5\%$–10%, if similar averaging in time and space is applied as in the extinction-coefficient retrieval, and for absolute particle backscatter coefficients of >0.0002 km^{-1}sr^{-1}. Profiles of molecular extinction and backscatter coefficients at the primary and at the Raman wavelengths needed in the evaluation are again calculated from actual radiosonde data and do not lead to significant errors. The overlap effect is cancelled out, because the ratio of two signals is taken. In principle, profiles of the backscatter coefficient determined with

the Raman method are obtained with high accuracy, i.e., statistical errors of <5%–10% and systematic errors of <0.0001 $km^{-1}sr^{-1}$, even at distances of 100 m or less from the lidar.

Backscatter retrieval (Klett method)

When the Raman method cannot be applied, backscatter coefficients are evaluated with the so-called Klett method. Achievements and limitations of this method have been discussed in the literature for decades, e.g., *Fernald et al.* (1972), *Klett* (1981), *Fernald* (1984), *Klett* (1985), *Sasano et al.* (1985), *Bissonnette* (1986), *Gonzales* (1988), *Ansmann et al.* (1992a), *Kovalev* (1995), *Kunz* (1996), *Ackermann* (1998), and *Kovalev and Eichinger* (2004), and will not be repeated here. The procedure, with all its modifications and improvements, suffers from the fact that two physical quantities, the particle backscatter coefficient and the particle extinction coefficient, must be determined from only one measured quantity, the elastic lidar return.

Two critical input parameters are required, a reference value of the backscatter coefficient as in the Raman method and the lidar ratio which, in principle, is range-dependent. The two input parameters influence the solutions for backscatter coefficients below and above ∼550 nm in different ways. For the shorter wavelengths, the most critical input parameter is the lidar ratio, because it serves to correct the backscatter signals for particle optical depth, which has a higher influence on lidar signals with shorter wavelength. Because of long-term experience with Raman measurements and available lidar-ratio values from nighttime observations, EARLINET operators are expected to make a good estimate of this input parameter in most cases. The reference value is of minor importance for the short wavelengths and is set, as in the Raman method, into a region with low particle load.

Because of weak Rayleigh scattering, the clear-air assumption for the reference value does not apply for longer wavelengths, specifically not for 1064 nm. To calibrate the IR measurements, the reference height should be located inside a layer of appropriate particle scattering. The reference value is found by taking the short-wavelength results and by extrapolating these under the assumption of a certain wavelength dependence. Lidar ratios determined at 532 nm are usually taken as input parameter for the Klett solutions at 1064 nm. Because the atmospheric transmission effect on the lidar signals is small, an error in the lidar-ratio estimate is not crucial here.

The statistical error of particle backscatter coefficients determined from elastic backscatter signals with the Klett method is <5% for the temporal and spatial resolution used here. Even though the Klett method suffers from its critical input parameters, and systematic errors of the order of 100% must be expected from conventional data analysis, a careful evaluation of the elastic backscatter profiles under consideration of all information that is

available from multiwavelength Raman observations can reduce the systematic errors to 10%–20%.

Depolarization ratio

When linearly polarized laser light is transmitted and two receiver channels with linear polarization analyzers oriented parallel and perpendicular to the plane of polarization of the transmitted light are employed, the volume linear depolarization ratio $\delta(Z, \lambda)$ is defined as the ratio of the calibrated lidar returns received in these two channels:

$$\delta(Z, \lambda) = C \frac{P_{\perp}(Z, \lambda)}{P_{\parallel}(Z, \lambda)} \,. \tag{4.4}$$

The calibration factor C can be found in different ways. Sophisticated procedures apply rotating half-wave plates in the receiver chain to obtain an absolute instrument calibration. In an easier approach, the signal ratio is calibrated to the known molecular depolarization ratio in clear regions of the atmosphere. The latter method leads to somewhat higher uncertainties, since the molecular contribution to the return signal depends on instrument parameters such as the receiver bandwidth (e.g., bandwidth of interference filters). Thus the resulting systematic error can be of the order of 10%–30%. The statistical error of the measurement is easily obtained from signal noise and is typically <5%.

4.2.2 EARLINET data format

For storing the primary optical data, we make use of existing structures already established for EARLINET. In the EARLINET database, profiles of backscatter and extinction coefficients at multiple wavelengths, together with complementary measurement and data-evaluation information, are stored in the Network Common Data Format (NetCDF), for which also visualization tools have been developed (see below). Some refinements have been made for the present study. The name convention for EARLINET NetCDF files is:

ooyyMMddhhmm.tw

with

oo:	originate code (station ID, see Tab. 2.1)
yy:	year since 2000
MM:	month of the year (1–12)
dd:	day of month (1–31)
hh:	hour of day (0–23)
mm:	minute of hour (0–59)
t:	type code (e = extinction, b = backscatter)
w:	wavelength given in nm (3 or 4 digits)

Depolarization profiles are stored in the b-files. The e-files always contain both extinction and backscatter profiles with the same time and height resolution to allow calculation of secondary optical data such as the lidar ratio. Additional b-files for the same wavelength may be produced with higher resolution. Storing of time series of successive profiles is also possible.

An example of the file structure is presented in Fig. 4.1. The file name follows the convention. The header explains the variables stored in the files and the global attributes which give information on the station, the system, and the input data for the data evaluation. The variables are 1-dimensional fields, except the dust layer height which is a single number.

The EARLINET database is a pure aerosol database established for external users. Except in a specific cirrus category, cloud measurements are not collected in this database to avoid misuse of the data. Any periods or height regions containing clouds are removed from the stored profiles. Therefore, we have defined a new name convention and file structure specifically for cloud measurements to be used in the aerosol and cloud database of the present study. The name convention is:

ooyyMMddhhmm.ctw

where c stands for cloud and all definitions remain the same as for aerosol files. An example of the cloud file structure is presented in Fig. 4.2. In principle, the structure is the same as for aerosol, but an additional integer variable *cloud flag* has been introduced in order to identify the height regions where clouds are present. The cloud flags are defined as:

0: no cloud
1: water
2: ice
4: cloud of unknown type

4.2.3 Exploitation and visualization tools for NetCDF data

NetCDF files can easily be accessed by a variety of programming languages. Access libraries for C, Fortran, C++, Java, IDL and other languages are available. With ncBrowse an easy-to-use, open-source, and platform-independent visualization tool is available. ncBrowse is a Java application that provides flexible, interactive graphical displays of data and attributes from NetCDF data files.

```
                                        po0606260056.e355
netcdf po0606260056 {
dimensions:
        Length = UNLIMITED ; // (162 currently)
variables:
        float Altitude(Length) ;
                Altitude:AltitudeUnits = "m" ;
                Altitude:LongName = "Height above sea level" ;
        float Backscatter(Length) ;
                Backscatter:BackscatterUnits = "1/(m*sr)" ;
        float ErrorBackscatter(Length) ;
                ErrorBackscatter:BackscatterUnits = "1/(m*sr)" ;
        float Extinction(Length) ;
                Extinction:ExtinctionUnits = "1/m" ;
        float ErrorExtinction(Length) ;
                ErrorExtinction:ExtinctionUnits = "1/m" ;
        float DustLayerHeight ;
                DustLayerHeight:LongName= "Top of dust layer above sea level" ;

// global attributes:
                :System = "CNR-IMAA" ;
                :Location = "Tito Scalo, Italy" ;
                :Longitude_degrees_east = 15.73 ;
                :Latitude_degrees_north = 40.6 ;
                :Altitude_meter_asl = 760 ;
                :EmissionWavelength_nm = 355 ;
                :DetectionWavelength_nm = 386 ;
                :DetectionMode = "digital" ;
                :ZenithAngle_degrees = 0 ;
                :ShotsAveraged = 93000 ;
                :ResolutionRaw_meter = 60 ;
                :ResolutionEvaluated = "360m up to 2430, 600m above" ;
                :StartDate = 20060626 ;
                :StartTime_UT = 5607 ;
                :StopTime_UT = 12624 ;
                :EvaluationMethod = "Combined Raman-elastic" ;
                :InputParameters = "" ;
                :Comments = "" ;
data:

 Altitude = 390, 450, 510, 570, 630, 690, 750, 810, 870, 930, 990, 1050,
    1110, 1170, 1230, 1290, 1350, 1410, 1470, 1530, 1590, 1650, 1710, 1770,
    1830, 1890, 1950, 2010, 2070, 2130, 2190, 2250, 2310, 2370, 2430, 2490,
 .....
    9030, 9090, 9150, 9210, 9270, 9330, 9390, 9450, 9510, 9570, 9630, 9690,
    9750, 9810, 9870, 9930, 9990, 10050 ;

 Backscatter = 3.8e-006, 3.72e-006, 3.34e-006, 3.04e-006, 3.1e-006,
    3.19e-006, 3.32e-006, 2.45e-006, 2.14e-006, 2.28e-006, 2.09e-006,
    1.73e-006, 1.89e-006, 1.56e-006, 1.16e-006, 7.04e-007, 7.51e-007,
 ......
    -3.73e-008, 6.35e-008, -1.7e-007, 2.01e-007, -2.93e-007, -3.51e-008,
    -1.01e-007 ;

 ErrorBackscatter = _, 2.81e-008, 2.72e-007, 7.77e-008, 2.87e-008, 2.39e-008,
    2.89e-008, 2.33e-008, 2.14e-008, 2.62e-008, 2.08e-008, 1.98e-008,
    2.42e-008, 2.13e-008, 2.32e-008, 1.83e-008, 3.47e-008, 2.68803e-008,
 .....
    2.07e-007, 1.51e-007, 1.95e-007, 2.39e-007, 2.01e-007, 4.61e-007,
    3.21e-007, 1.89e-007, 1.29e-007, 2.45e-007, 1.35e-007, 1.75e-007 ;

 Extinction = _, _, _, _, _, 0.000195751, 0.000189345, 0.000153182,
    0.000108749, 0.000108634, 9.01572e-005, 6.71814e-005, 4.5469e-005,
    3.32521e-005, 2.65854e-005, 2.60172e-005, 3.91025e-005, 4.88228e-005,
 .....
    _, _, _, _, _, _, _, _, _, _, _, _, _, _, _, _, _, _, _, _ ;

 ErrorExtinction = _, _, _, _, _, 8.81e-006, 8.81e-006, 8.2e-006, 4.83e-006,
    9.23e-006, 9.94e-006, 6.81e-006, 1.07e-005, 1.33e-005, 1.18e-005,
    1.42e-005, 1.92e-005, 1.24e-005, 1.35e-005, 2.29e-005, 1.42e-005,
 .....
    _, _, _, _, _, _, _, _, _, _, _, _, _, _, _, _, _, _, _, _ ;

DustLayerHeight = 1750 ;
}
```

Figure 4.1: Example of a NetCDF file from the EARLINET database dumped to ASCII format (data are reduced to show the principle layout of the file). The file name indicates station ID, measurement date and start time. The extension shows that an extinction-coefficient profile at 355 nm is stored. The file contains the respective backscatter-coefficient profile (with the same resolution) and the measurement errors.

```
                                po0610250050.ce532
netcdf po0610250050 {
dimensions:
      Length = UNLIMITED ; // (365 currently)
variables:
      float Altitude(Length) ;
            Altitude:units = "m" ;
            Altitude:long_name = "Height above sea level" ;
      float Backscatter(Length) ;
            Backscatter:units = "1/(m*sr)" ;
      float ErrorBackscatter(Length) ;
            ErrorBackscatter:units = "1/(m*sr)" ;
      float Extinction(Length) ;
            Extinction:units = "1/m" ;
      float ErrorExtinction(Length) ;
            ErrorExtinction:units = "1/m" ;
      int CloudFlag(Length) ;
            CloudFlag:long_name = "0-No clouds; 1-Low water clouds;
2-Cirrus; 4-Cloud of unknown type" ;

// global attributes:
            :System = "CNR-IMAA" ;
            :Location = "Tito Scalo, Italy" ;
            :Longitude_degrees_east = 15.72 ;
            :Latitude_degrees_north = 40.6 ;
            :Altitude_meter_asl = 760 ;
            :EmissionWavelength_nm = 532 ;
            :DetectionWavelength_nm = 607 ;
            :DetectionMode = "digital" ;
            :ZenithAngle_degrees = 0 ;
            :ShotsAveraged = 93000 ;
            :ResolutionRaw_meter = 15 ;
            :ResolutionEvaluated = "60m" ;
            :StartDate = 20061025 ;
            :StartTime_UT = 5000 ;
            :StopTime_UT = 12000 ;
            :EvaluationMethod = "Combined Raman-elastic" ;
            :InputParameters = "" ;
            :Comments = "" ;
data:

 Altitude = 1330, 1390, 1450,  .....

 Backscatter = 2.62e-006, 2.58e-006, 2.3e-006, ....

 ErrorBackscatter = 7.15e-009, 8.23e-009, 8.67e-009, ....

 Extinction = 6.71e-005, 6.71e-005, 6.71e-005, ....

 ErrorExtinction = 3.01e-006, 3.01e-006, 3.01e-006, ...

 CloudFlag = 0, 0, 0,
   }
```

Figure 4.2: Example of a NetCDF cloud file dumped to ASCII format (data are reduced to show the principle layout of the file). The file name indicates station ID, measurement date and start time. The extension shows that an extinction-coefficient profile at 532 nm containing a cloud is stored. The file contains the respective backscatter-coefficient profile (with the same resolution), the measurement errors, and the cloud flag.

4.2.4 Examples of Part A products

4.2.4.1 Aerosol profiles from contributing stations

Figure 4.3 presents an example of an aerosol measurement taken at L'Aquila on May 27, 2008, during a strong Saharan dust event (Case C measurement, see Chapter 5). At this *contributing station* an excimer laser at 351 nm is operated. The wavelength is close to the frequency-tripled emission of the Nd:YAG laser at 355 nm, and the wavelength difference is assumed to be neglible for this study.

The primary observables of the one-wavelength Raman lidar are the UV backscatter and extinction coefficients. Two NetCDF files are stored in the database. The *b-file la0805272122.b351* contains the high-resolved backscatter-coefficient profile, which is calculated with a height resolution of 30 m in this case (thin line in the left panel of Fig. 4.3). For the calculation of extinction-coefficient profiles from (weak) Raman signal, a stronger smoothing must be applied. The smoothing length depends on the instrument's power and on the actual atmospheric conditions and typically varies with height. Here, a gliding average length from 280 to 1050 m was applied. The smoothing length is an individual parameter set by the operator, who must find a compromise between a good vertical resolution and a low statistical measurement error. The retrieved extinction-coefficient profile is stored in the *e-file la0805272122.e351* and shown in the middle panel of Fig. 4.3. The latter file also contains a backscatter-coefficient profile derived with the same resolution (thick line in the left panel of Fig. 4.3). Further geophysical products, such as the lidar-ratio profile presented in the right panel of Fig. 4.3, can only be correctly calculated from primary lidar profiles given with the same resolution.

4.2.4.2 Aerosol profiles from high-performance stations

Figure 4.4 shows a complete set of aerosol profiles available from a *high-performance station*. The measurement was taken at Leipzig on May 27, 2008, as well. Backscatter-coefficient profiles at 355, 532, and 1064 nm and extinction-coefficient profiles at 355 and 532 nm, as presented in the first and second panel of Fig. 4.4, are stored in the files *le0805272024.b355*, *le0805272024.b532*, *le0805272024.b1064*, *le0805272024.e355*, and *le0805272024.e532*, respectively, which can be found in Part A of the database.

As can be seen from Fig. 4.4, the lower and upper cut-off heights may be different for different parameters. In the present case, the upper cut-off height was determined by the presence of clouds above 6 km height. In other cases, the absence of significant aerosol load or a low signal-to-noise ratio in the upper troposphere (both in conjunction with a large statistical measurement error) are used as cut-off criteria. The lower cut-off height usually depends on the specific instrument parameters and is mainly determined by the

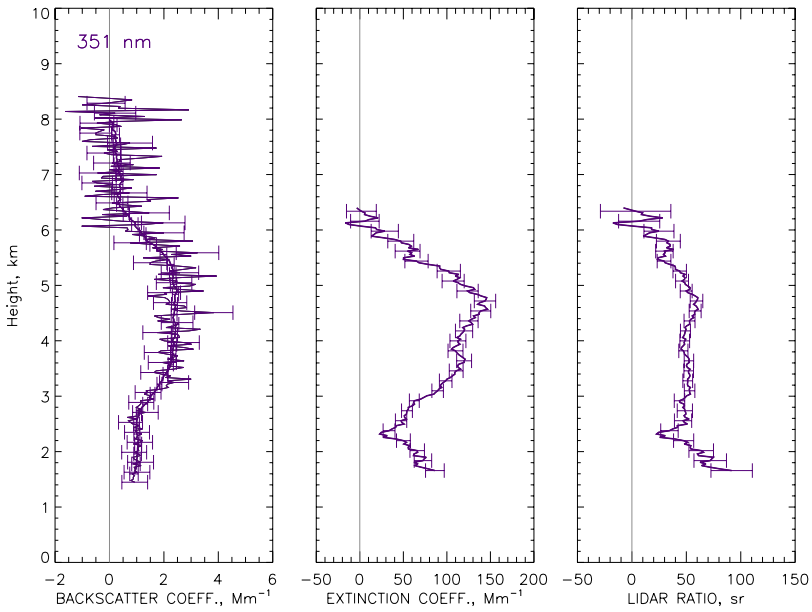

Figure 4.3: Example of a measurement from the contributing station at L'Aquila. The measurement was taken on May 27, 2008, 21.22–22.26 UT (Case C measurement).

incomplete overlap between laser beam and receiver field of view in the near range. For powerful lidars with large telescope mirrors the range of incomplete overlap can be of the order of 1–2 km. Systematic biases inhibit a trustworthy determination of parameters from single lidar signals in this region (extinction coefficients from the Raman method, backscatter coefficients from the Klett method, see Chapter 4). The effect of incomplete overlap normally cancels out when signal ratios are used in the retrieval (backscatter coefficients from the Raman method, depolarization ratio). Such profiles can be obtained close to the ground as shown in Fig. 4.4. (It should be noticed in this context that all heights in the database and in the graphs refer to mean sea level, and not to the actual ground level or station height.) Similar to the smoothing lengths, the cut-off heights are individually chosen by the operator in dependence on the specific measurement conditions and differ from case to case and from station to station.

The third and fourth panels of Fig. 4.4 show profiles of optical parameters derived from the primary extinction-coefficient and backscatter-coefficient profiles, namely the lidar ratios at 355 and 532 nm, the short-wavelength and long-wavelength backscatter-related Ångström exponents, and the extinction-related Ångström exponent. The depolarization-ratio profile is plotted in the fifth panel. The representation of Fig. 4.4 is an intermediate result of the data-exploitation procedure. It is used to quality-check each single measurement, to identify features, and to determine feature boundaries. The follow-up procedures of data exploitation are explained in Sec. 4.3.

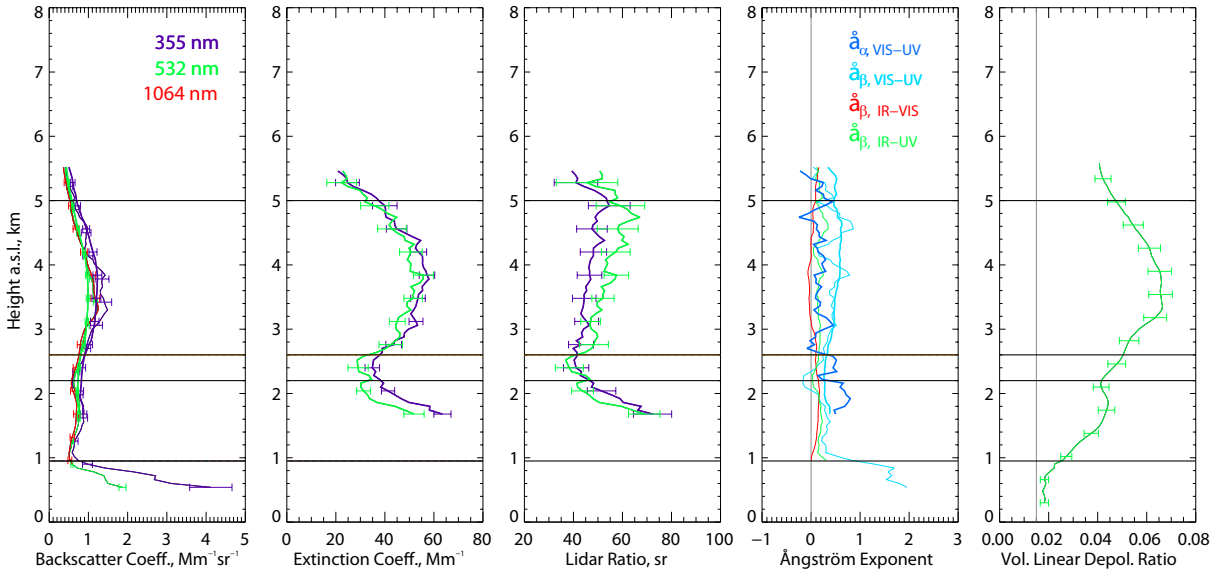

Figure 4.4: Example of a measurement from the high-performance station at Leipzig. The measurement was taken on May 27, 2008, 20.24–21.30 UT (Case C measurement). The horizontal lines indicate the feature boundaries.

4.2.4.3 Aerosol profile timeseries

In order to investigate the temporal variability of the aerosol conditions and the representativeness of spaceborne against ground-based observations, timeseries of 30-min profiles centered around CALIPSO overpasses are stored in the database as well. We concentrate on backscatter-coefficient profiles in this context, because this parameter is the primary CALIPSO product, it is available from all EARLINET stations, and it can be determined with high temporal and spatial resolution. Fig. 4.5 shows an example of a timeseries as it can be found in Part A of the database. The Case A measurement was taken at Leipzig in the night of 25/26 May 2008. As can be seen from the time-height contour plot of the range-corrected 1064-nm signal (quicklook), the measurement started at 21.26 UT on 25 May 2008 and was stopped at 04.21 UT on 26 May 2008. The CALIPSO overpass was at 01.33 UT at a distance of 42.8 km. Therefore, five 30-min backscatter-coefficient profiles starting at 00.17 UT and ending at 02.48 UT were created and stored with the filenames *le0805260017.b532*, *le0805260048.b532*, *le0805260118.b532*, *le0805260148.b532*, *le0805260219.b532*. These high-resolved *b-files* contain the depolarization-ratio profiles as well.

4.2.4.4 Cloud profiles

Cloud measurements are treated in a similar way as aerosol measurements. However, because of the higher variability of clouds in space and time, a higher spatial and temporal

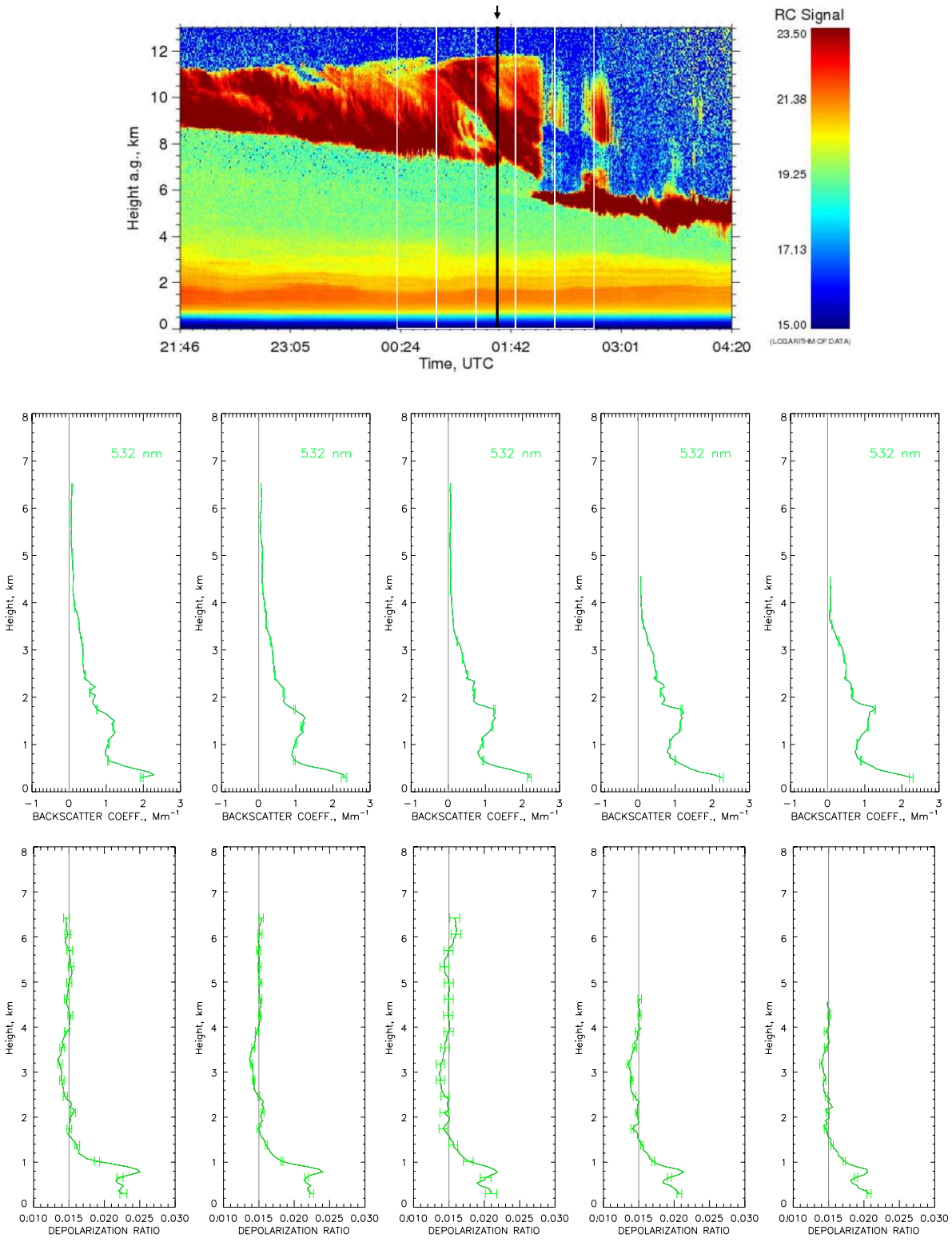

Figure 4.5: Case A measurement performed at Leipzig on 25–26 May 2008, 21.26-04.21 UT in terms of the range-corrected 1064-nm backscatter signal (top). The CALIPSO overpass at 01.33 UT (distance of 42.8 km) is indicated (black line and arrow). 30-min averaging periods are indicated with white boxes, and the corresponding aerosol profiles of the 532-nm backscatter coefficient (middle) and depolarization ratio (bottom) are shown.

resolution is required. Therefore, less averaging is applied, what is consistent with the higher signal-to-noise ratios obtained in clouds as well as with the horizontal resolution of the CALIPSO cloud products. In general, cloud profiles are only stored for Case A observations.

During the Case A measurement at Leipzig on 26 May 2008, a cirrus cloud was present above 7 km height. According to the name convention, for the timeseries around the overpass at 01.33 UT, three 10-min backscatter-coefficient profiles starting at 01.18 UT, 01.28 UT, and 01.38 UT were created and stored with the filenames *le0805260118.cb532*, *le0805260128.cb532*, *le0805260138.b532*. Again, these high-resolved *b-files* contain the depolarization-ratio profiles as well. Fig. 4.6 illustrates the series of cloud profiles.

4.3 Aerosol and cloud feature products – Parts B and C of the database

4.3.1 Feature finding and classification

Parts B and C of the database are established by further exploitation of the Part A products. For each measurement (consisting of a set of profile data) significant features are selected and classified. A combined threshold and gradient method is used for feature finding and boundary determination. For the feature classification, we apply the procedures and tools described in Chapter 3.

4.3.2 Definition of Part B products

Part B of the database assembles layer-mean cloud and aerosol geophysical products. For each layer, the geometrical properties (layer boundaries and geometrical depth), the extensive optical parameters (layer-mean extinction and backscatter coefficients), and the intensive particle parameters are calculated. The intensive parameters do not depend on the absolute concentration of aerosol and cloud particles, but on characteristic properties of an ensemble of scattering particles. Therefore, Part B of the database is the core data set for the development of aerosol and cloud classification schemes and the derivation of conversion factors (see Part C).

First, the geometrical properties of each layer are stored:

- layer bottom height z_{bot},
- layer top height z_{top}.

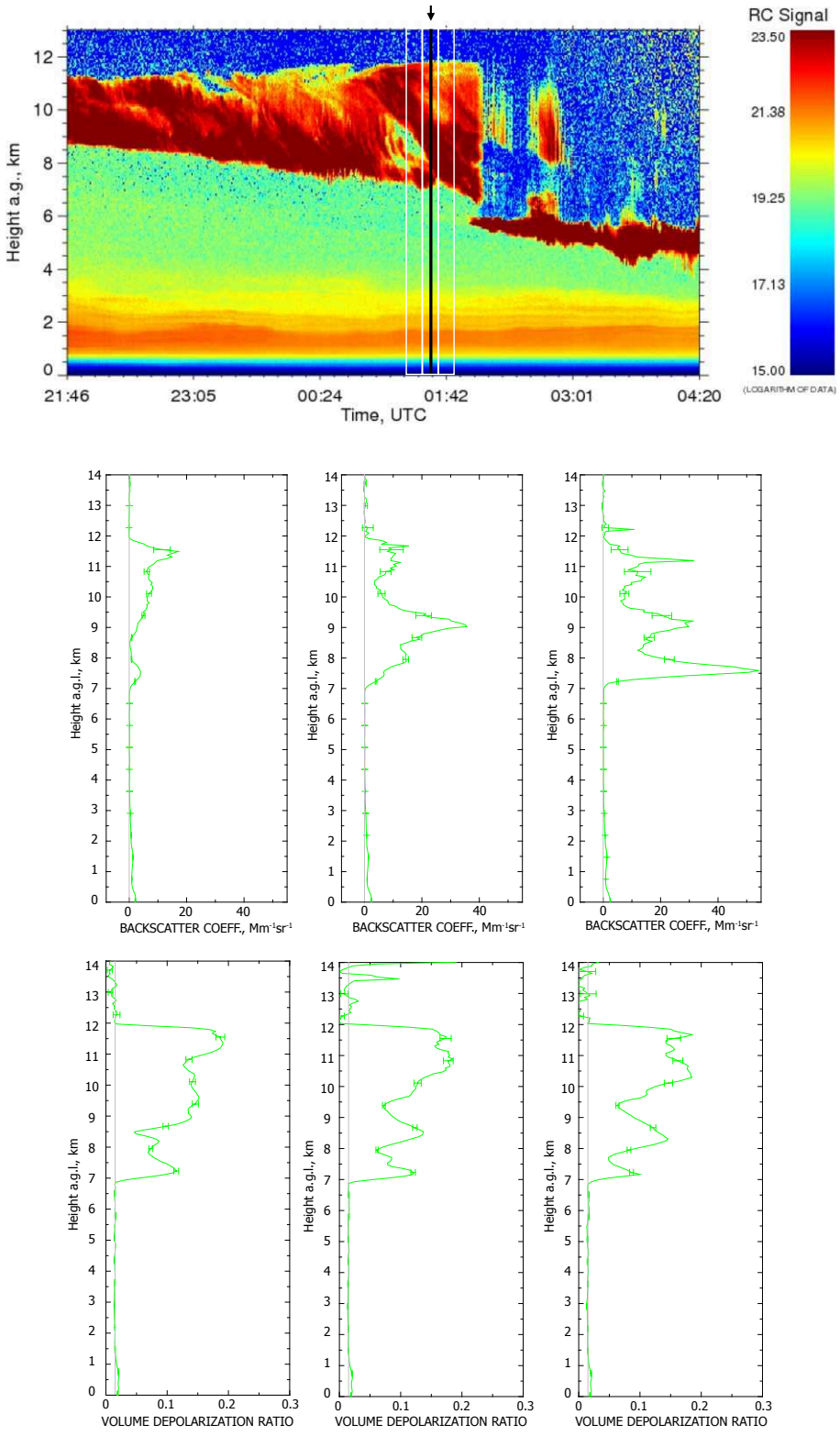

Figure 4.6: Case A measurement performed at Leipzig on 25–26 May 2008, 21.26-04.21 UT in terms of the range-corrected 1064-nm backscatter signal (top). The CALIPSO overpass at 01.33 UT (distance of 42.8 km) is indicated (black line and arrow). 10-min averaging periods are indicated with white boxes, and the corresponding cloud profiles of the 532-nm backscatter coefficient (middle) and depolarization ratio (bottom) are shown.

Second, according to the requirements defined in Chapter 3, layer mean values of the following products are generated:

- 355-nm extinction coefficient, α_{UV},
- 532-nm extinction coefficient, α_{VIS},
- 355-nm backscatter coefficient, β_{UV},
- 532-nm backscatter coefficient, β_{VIS},
- 1064-nm backscatter coefficient, β_{IR},
- 355-nm lidar ratio, S_{UV},
- 532-nm lidar ratio, S_{VIS},
- ratio of the 532-nm lidar ratio to the 355-nm lidar ratio (S–ratio VIS–UV, $s_{\mathrm{VIS-UV}}$),
- 532-to-355-nm extinction ratio (extinction color ratio VIS–UV, $C_{\alpha,\mathrm{VIS-UV}}$),
- 532-to-355-nm extinction-related Ångström exponent (extinction Ångström exponent VIS–UV, $\mathring{a}_{\alpha,\mathrm{VIS-UV}}$),
- 532-to-355-nm backscatter ratio (backscatter color ratio VIS–UV, $C_{\beta,\mathrm{VIS-UV}}$),
- 532-to-355-nm backscatter-related Ångström exponent (backscatter Ångström exponent VIS–UV, $\mathring{a}_{\beta,\mathrm{VIS-UV}}$),
- 1064-to-532-nm backscatter ratio (backscatter color ratio IR–VIS, $C_{\beta,\mathrm{IR-VIS}}$),
- 1064-to-532-nm backscatter-related Ångström exponent (backscatter Ångström exponent IR–VIS, $\mathring{a}_{\beta,\mathrm{IR-VIS}}$),
- 1064-to-355-nm backscatter ratio (backscatter color ratio IR–UV, $C_{\beta,\mathrm{IR-UV}}$),
- 1064-to-355-nm backscatter-related Ångström exponent (backscatter Ångström exponent IR–UV, $\mathring{a}_{\beta,\mathrm{IR-UV}}$),
- 532-nm depolarization ratio, δ_{VIS}.

The lidar ratio is the ratio of the particle extinction to the particle backscatter coefficient measured at $\lambda_0 = 355$ (UV) or 532 nm (VIS):

$$S_{\mathrm{UV,VIS}}(Z, \lambda_0) = \frac{\alpha_{\mathrm{par}}(Z, \lambda_0)}{\beta_{\mathrm{par}}(Z, \lambda_0)} \,. \tag{4.5}$$

We call the ratio of the lidar ratios at 532 and 355 nm the S–ratio and define it as

$$s_{\mathrm{VIS-UV}}(Z) = \frac{S_{\mathrm{par}}(Z, 532\ \mathrm{nm})}{S_{\mathrm{par}}(Z, 355\ \mathrm{nm})}\,. \tag{4.6}$$

Color ratios for extinction and backscattering are defined as the ratio of the particle extinction coefficients measured at 532 and 355 nm (VIS–UV),

$$C_{\alpha,\mathrm{VIS-UV}}(Z) = \frac{\alpha_{\mathrm{par}}(Z, 532\ \mathrm{nm})}{\alpha_{\mathrm{par}}(Z, 355\ \mathrm{nm})}\,, \tag{4.7}$$

the ratio of the particle backscatter coefficients measured at 532 and 355 nm (VIS–UV),

$$C_{\beta,\mathrm{VIS-UV}}(Z) = \frac{\beta_{\mathrm{par}}(Z, 532\ \mathrm{nm})}{\beta_{\mathrm{par}}(Z, 355\ \mathrm{nm})}\,, \tag{4.8}$$

the ratio of the particle backscatter coefficients measured at 1064 and 532 nm (IR–VIS),

$$C_{\beta,\mathrm{IR-VIS}}(Z) = \frac{\beta_{\mathrm{par}}(Z, 1064\ \mathrm{nm})}{\beta_{\mathrm{par}}(Z, 532\ \mathrm{nm})}\,, \tag{4.9}$$

and the ratio of the particle backscatter coefficients measured at 1064 and 355 nm (IR–UV),

$$C_{\beta,\mathrm{IR-UV}}(Z) = \frac{\beta_{\mathrm{par}}(Z, 1064\ \mathrm{nm})}{\beta_{\mathrm{par}}(Z, 355\ \mathrm{nm})}\,. \tag{4.10}$$

Accordingly, the exinction-related (VIS–UV) and backscatter-related Ångström exponents (VIS–UV, IR–VIS, and IR–UV) are calculated as follows:

$$\mathring{a}_{\alpha,\mathrm{VIS-UV}}(Z) = \frac{\ln[\alpha_{\mathrm{par}}(Z, 355\ \mathrm{nm})/\alpha_{\mathrm{par}}(Z, 532\ \mathrm{nm})]}{\ln(532\ \mathrm{nm}/355\ \mathrm{nm})}\,, \tag{4.11}$$

$$\mathring{a}_{\beta,\mathrm{VIS-UV}}(Z) = \frac{\ln[\beta_{\mathrm{par}}(Z, 355\ \mathrm{nm})/\beta_{\mathrm{par}}(Z, 532\ \mathrm{nm})]}{\ln(532\ \mathrm{nm}/355\ \mathrm{nm})}\,, \tag{4.12}$$

$$\mathring{a}_{\beta,\mathrm{IR-VIS}}(Z) = \frac{\ln[\beta_{\mathrm{par}}(Z, 532\ \mathrm{nm})/\beta_{\mathrm{par}}(Z, 1064\ \mathrm{nm})]}{\ln(1064\ \mathrm{nm}/532\ \mathrm{nm})}\,, \tag{4.13}$$

$$\mathring{a}_{\beta,\mathrm{IR-UV}}(Z) = \frac{\ln[\beta_{\mathrm{par}}(Z, 355\ \mathrm{nm})/\beta_{\mathrm{par}}(Z, 1064\ \mathrm{nm})]}{\ln(1064\ \mathrm{nm}/355\ \mathrm{nm})}\,. \tag{4.14}$$

As can be seen from the equations above, we follow the convention used for CALIPSO and define the color ratios so that the value for the longer wavelength is divided by the value for the shorter wavelength. Care must taken when comparing the results with literature data, because the opposite wavelength definition is often used.

Errors of the above-listed parameters are given in the database in terms of one standard deviation of the layer mean value. Atmospheric variability as well as statistical noise present in the primary extinction and backscatter profiles contribute to this error.

Finally, for the classification of features, Part B of the database contains the following information for each aerosol layer in addition:

- aerosol type,
- source region,
- age,
- relative humidity.

In the case of clouds the cloud type (water, ice, mixed-phase) is indicated.

4.3.3 Examples of Part B products

Table 4.1 shows an example of layer products extracted from the lidar profiles measured at Leipzig on 27 May 2008, 20.24-21.30 UT (see Fig. 4.4). All meaningful products are stored, independent on the number and kind of actually available profiles in a height region. In the present case, the complete optical information is available for Layers 2, 3 and 4. A reduced data set is given for the lowest layer. Even if only a single backscatter-coefficient profile is available from a certain station and a certain time, the respective features are identified in terms of their geometrical properties and the mean backscatter coefficient, so that the data can be used in the EARLINET–CALIPSO intercomparison study.

4.3.4 Definition of Part C products

Part C of the database contains conversion factors to relate spaceborne lidar observations with different instruments to each other. The conversion factors are follow-up products from Part B of the database. In principle, no new products are calculated, but the products of Part B are further exploited with special view on the spaceborne lidar products. Part C of the database can only be established on the basis of a sufficient number of Part B entries, i.e. a statistically significant number of observations for each aerosol and cloud type.

For each pre-defined feature type (either aerosol or cloud type) mean values and standard deviations of all extensive and intensive lidar parameters stored in Part B of the database are calculated. In this way, aerosol and cloud type dependent conversion factors are obtained either directly (e.g., color ratios) or by further relating the obtained mean parameters (e.g., color-ratio versus lidar-ratio factor). The following conversion factors are of specific interest to relate ALADIN and ATLID products to CALIPSO observations (see also Chapter 1):

- 532-to-355-nm extinction ratio ($C_{\alpha,\mathrm{VIS-UV}}$),
- 532-to-355-nm backscatter ratio ($C_{\beta,\mathrm{VIS-UV}}$),

Table 4.1: Layer products for four aerosol layers selected from the measurement at Leipzig on 27 May 2008, 20.2421.30 UT (see Fig. 4.4).

Parameter	Unit	Layer 1	Layer 2	Layer 3	Layer 4
z_{bot}	m	0	950	2200	2600
z_{top}	m	950	2200	2600	5000
α_{UV}	$10^{-6}\,\mathrm{m}^{-1}$		49±9	36±1	50±6
α_{VIS}	$10^{-6}\,\mathrm{m}^{-1}$		38±8	31±2	47±5
β_{UV}	$10^{-6}\,\mathrm{m}^{-1}\mathrm{sr}^{-1}$	2.5±1.1	0.83±0.04	0.86±0.03	1.07±0.15
β_{VIS}	$10^{-6}\,\mathrm{m}^{-1}\mathrm{sr}^{-1}$	1.2±0.5	0.73±0.02	0.76±0.02	0.87±0.12
β_{IR}	$10^{-6}\,\mathrm{m}^{-1}\mathrm{sr}^{-1}$		0.65±0.06	0.67±0.07	0.9±0.2
S_{UV}	sr		59±9	42±2	47±3
S_{VIS}	sr		52±10	40±4	54±6
$s_{\mathrm{VIS-UV}}$			0.88±0.05	0.96±0.06	1.16±0.07
$C_{\alpha,\mathrm{VIS-UV}}$			0.77±0.04	0.85±0.05	0.94±0.05
$\mathring{a}_{\alpha,\mathrm{VIS-UV}}$			0.65±0.11	0.4±0.2	0.2±0.1
$C_{\beta,\mathrm{VIS-UV}}$		0.52±0.04	0.88±0.02	0.892±0.007	0.81±0.03
$\mathring{a}_{\beta,\mathrm{VIS-UV}}$		1.64±0.21	0.32±0.05	0.28±0.02	0.52±0.08
$C_{\beta,\mathrm{IR-VIS}}$			0.89±0.07	0.88±0.06	1.03±0.12
$\mathring{a}_{\beta,\mathrm{IR-VIS}}$			0.18±0.12	0.19±0.11	-0.03±0.17
$C_{\beta,\mathrm{IR-UV}}$			0.78±0.06	0.78±0.05	0.83±0.10
$\mathring{a}_{\beta,\mathrm{IR-UV}}$			0.23±0.07	0.23±0.06	0.17±0.11
δ_{VIS}		0.020±0.002	0.043±0.008	0.046±0.003	0.059±0.006

- 1064-to-355-nm backscatter ratio ($C_{\beta,\mathrm{IR-UV}}$),
- ratio of the 532-nm lidar ratio to the 355-nm lidar ratio ($s_{\mathrm{VIS-UV}}$).

Beside the explicite conversion factors, several of the obtained parameters will be of interest for spaceborne lidar algorithm developments in general.

4.3.5 Example of Part C products

Conversion factors are calculated on the basis of statistically significant sets of data for each feature type. An example is presented in Tab. 4.2. Conversion factors for Saharan dust based on the evaluation of 44 dust layers observed at seven EARLINET stations in May 2008 are shown.

Table 4.2: Conversion factors for Saharan dust derived from the evaluation of 44 dust layers observed at seven EARLINET stations in May 2008.

Conversion factor	Mean value and standard deviation
$C_{\alpha,\mathrm{VIS-UV}}$	0.89±0.13
$C_{\beta,\mathrm{VIS-UV}}$	0.92±0.17
$C_{\beta,\mathrm{IR-UV}}$	0.66±0.17
$s_{\mathrm{VIS-UV}}$	0.95±0.19

4.4 Correlation of EARLINET and CALIPSO products – Part D of the database

Part D of the database is dedicated to the comparison of EARLINET and CALIPSO measurements and the results of the correlation analysis. In particular, a selection of EARLINET profiles contained in Part A of the database and aerosol and cloud feature products reported in Part B of the database are compared to CALIPSO Level 2 Profile and Layer products. The corresponding CALIPSO Level 2 products are included in this part of the database. Profiles (backscatter and extinction coefficients) as well as layer products (boundaries, layer-mean backscatter and extinction values) are related. Differences between ground-based and spaceborne data are reported together with the percentage differences with respect to EARLINET observations. The correlative study is carried out in terms of geometrical parameters, such as the difference of cloud and aerosol layer base and top heights, and in terms of optical data, such as difference backscatter coefficient profiles (see Chapter 3).

These quantities are given in the database together with information about the spatial and temporal distance of the spaceborne and ground-based observations and the location of CALIPSO measurements. This allows us to investigate the dependence of EARLINET–CALIPSO differences as a function of temporal and spatial distances through single-point comparisons as well as with multiple-point observations.

4.4.1 CALIPSO products

In order to assure a stand-alone usefulness of the database itself, CALIPSO Level 2 data products are included in the database thanks to an agreement with NASA. Both Level 1 and Level 2 CALIPSO data are available at http://eosweb.larc.nasa.gov/PRODOCS/calipso. For the present study, only CALIPSO Level 2 data products related to Europe and surrounding areas (namely 20°–80° N, −20°–

50° E, see Fig. 4.7), extracted from the original CALIPSO database for EARLINET directly by NASA Langley Research Center Atmospheric Science Data Center, are stored in the database. CALIPSO data are stored in Hierarchical Data Format (hdf), the standard data format for all NASA Earth Observing System (EOS) data products.

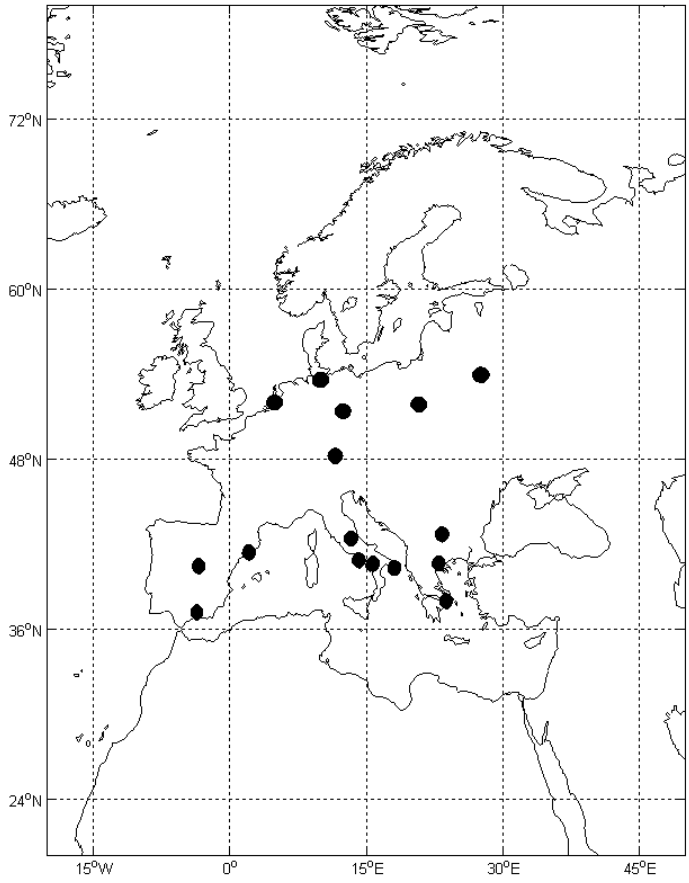

Figure 4.7: Geographical area of the CALIPSO subset data used in the present study. The dots indicate the EARLINET stations.

Level 2 CALIPSO data sets provide geophysical products. In particular, two different kinds of Level 2 data are provided: Level 2 Cloud and Aerosol Layer data and Level 2 Cloud and Aerosol Profile data.

4.4.1.1 Level 2 Layer data

The main products of this kind of files are the optical and geometrical properties of identified atmospheric layers. Four different Level 2 Layer files are produced for each observation:

- Level 2 Layer file for clouds at 1/3 km resolution (raw horizontal resolution),

- Level 2 Layer file for clouds at 1 km horizontal resolution,
- Level 2 Layer file for clouds at 5 km horizontal resolution,
- Level 2 Layer file for aerosol at 5 km horizontal resolution.

The layer identification is performed by means of a complex algorithm that is mainly based on a threshold routine, in which the threshold is altitude dependent. Advanced procedures are used to avoid false alarm due to noise and of course clouds are handled differently from aerosols (higher threshold is used for clouds and thin layers are allowed). A first estimation of the base is the point where a profile is again below the threshold and the slope of the signal is 0. Due to the noise, a better estimation of the base of the layer is obtained as the point at which in a chosen altitude range (that depends on the type of feature, i.e. if it is an aerosol or a cloud layer) the number of values higher than the threshold is lower than 50%. For each layer, the following quantities are reported:

- integrated attenuated backscatter at 532 nm,
- integrated attenuated backscatter at 1064 nm,
- integrated attenuated color ratio,
- integrated volume depolarization ratio.

For each of these quantities, mean, standard deviation, minimum and maximum, centroid and skewness values are also reported.

The integrated attenuated backscatter is defined as:

$$\gamma_{\text{feature}} = \int_{\text{top}}^{\text{base}} \beta_{\text{par}}(Z, \lambda_0) T^2_{\text{par}}(Z, \lambda_0) \mathrm{d}Z \,, \tag{4.15}$$

where $\beta_{\text{par}}(Z, \lambda_0)$ is the particle backscatter coefficient at wavelength λ_0 (532 nm or 1064 nm) at range Z and $T_{\text{par}}(Z, \lambda_0)$ is the transmission term present in the elastic lidar equation due to the particles contained in the atmospheric layer extending between the lidar and the range Z. From CALIPSO raw signals, however, it is not possible to obtain γ_{feature} until particle extinction involved in the transmission term is retrieved. Therefore, approximations are needed. An estimation of the feature integrated attenuated backscatter is possible using the clear-air trapezoid technique (*Vaughan et al.*, 2005). The feature backscatter intensity is characterized in terms of the corrected total attenuated backscatter:

$$B_{\text{feature}} = \frac{\beta'(Z, \lambda_0)}{T^2_{\text{mol}}(Z, \lambda_0) T^2_{\text{O}_3}(Z, \lambda_0)} \,, \tag{4.16}$$

where β' is the attenuated backscatter reported in Level 1 data (*Hostetler et al.*, 2006). The attenuated backscatter is the calibrated CALIOP range-corrected signal obtained after the subtraction of the background:

$$\beta'(Z) = [\beta_{\text{par}}(Z, \lambda_0) + \beta_{\text{mol}}(Z, \lambda_0)] T^2_{\text{par}}(Z, \lambda_0) T^2_{\text{mol}}(Z, \lambda_0) T^2_{\text{O}_3}(Z, \lambda_0) \,, \tag{4.17}$$

where both the total backscatter coefficient and the transmissions term at wavelength λ_0 and range Z are expressed in terms of particle and molecule (and ozone) contributions.

The volume depolarization ratio is defined as the ratio of attenuated backscatter received in the two channels for the detection of perpendicular and parallel backscatter signals with respect to the plane of polarization of the transmitted laser light:

$$\delta_{\mathrm{v}} = \frac{\beta'_{532,\perp}}{\beta'_{532,\parallel}} \,. \tag{4.18}$$

Starting from the definition of the volume depolarization ratio, the integrated volume depolarization ratio is defined as:

$$\delta_{\mathrm{feature}} = \frac{\sum_{k=\mathrm{top}}^{\mathrm{base}} \beta'_{532,\perp}(z_k)}{\sum_{k=\mathrm{top}}^{\mathrm{base}} \beta'_{532,\parallel}(z_k)} \,. \tag{4.19}$$

The attenuated total color ratio is calculated starting from the feature backscatter intensity defined above as:

$$\chi'(Z) = \frac{B_{1064}(Z)}{B'_{532}(Z)} \,. \tag{4.20}$$

It follows that the integrated attenuated total color ratio is:

$$\chi'_{\mathrm{feature}} = \frac{\sum_{k=\mathrm{top}}^{\mathrm{base}} B_{1064}(z_k)}{\sum_{k=\mathrm{top}}^{\mathrm{base}} B_{532}(z_k)} \,. \tag{4.21}$$

Besides all these quantities, Level 2 Layer data contain also additional information about the nature of identified layers, namely:

- feature classification flags,
- CAD score.

The feature classification flags provide information about the feature type (e.g., cloud vs. aerosol vs. stratospheric feature), the feature subtype (kind of aerosol), the layer ice–water phase (clouds only), and the amount of horizontal averaging required for layer detection. Moreover, the CAD score (Cloud–Aerosol Discrimination) provides information on the results obtained for each layer by the CALIOP cloud–aerosol discrimination algorithm (*Liu et al.*, 2005). The CAD algorithm separates clouds and aerosols based on multi-dimensional, altitude-dependent histograms of scattering properties (e.g., intensity and spectral dependence).

4.4.1.2 Level 2 Profile data

The CALIPSO data processing system generates separate sets of profile products for clouds and aerosols. The cloud profile products are reported at a uniform spatial resolution

of 60 m vertically and 5 km horizontally, over a nominal altitude range from 20 km to −0.5 km. The aerosol profile products are reported over a broader altitude range of 30 km to −0.5 km. Profile data for all features detected in the stratosphere are reported in the aerosol profile product. Due to constraints imposed by CALIPSO's on-board data averaging scheme, the vertical resolution of the aerosol profile data varies as a function of altitude. In the tropospheric region between 20 km and −0.5 km, the aerosol profile products are reported at a spatial resolution of 120 m vertically and 40 km horizontally. In the stratospheric region (above 20 km), the aerosol profile products are reported at a spatial resolution of 360 m vertically and 40 km horizontally.

Level 2 Profile data contain the vertical profiles of the following quantities:

- total backscatter coefficient at 532 nm,
- perpendicular backscatter coefficient at 532 nm,
- backscatter coefficient at 1064 nm,
- particle depolarization ratio at 532 nm,
- extinction coefficient at 532 nm,
- extinction coefficient at 1064 nm.

Retrieving optical depth and profiles of extinction and backscatter coefficients from the CALIOP measurements requires an estimate of the lidar ratio. These initial estimates are selected based on the type and subtype of the layer being analyzed and mainly based on AERONET climatological studies and model calculations (*Liu et al.*, 2005; *Young et al.*, 2008; *Cattrall et al.*, 2005). The values used in the current release are reported in Table 4.3. The initial lidar ratio is adjusted, if extinction retrieval leads to a non-physical solution (*Young et al.*, 2008).

However, because of the natural variability of each aerosol species, even for those cases where the aerosol type is correctly identified, the initial lidar ratio represents an imperfect estimate of the layer effective lidar ratio of any specific aerosol layer. The same caveats apply to the mean values used for the initial cloud lidar ratios. Multiple scattering is an important problem affecting the extinction profiles derived from spaceborne lidar measurements (see Chapter 3). Even if this is a severe problem mainly for clouds, the effect has to be taken into account also for optically dense aerosol layers. At the moment, CALIPSO data processing provides a rough multiple scattering correction for cloud profiles, but no multiple-scattering correction is applied to aerosol profiles (*Mark Vaughan, personal communication*). Finally, Level 2 Profile data for clouds contain also ice/water flags, where the cloud phase is determined using a depolarization/backscatter relation, together with temperature and backscatter thresholds (*Liu et al.*, 2005).

Table 4.3: Initial estimates of lidar ratio at 532 and 1064 nm used for CALIPSO extinction and backscatter retrievals for each of the cloud and aerosol layer types and subtypes.

Type	Subtype	Initial 532-nm lidar ratio	Initial 1064-nm lidar ratio
cloud	water	18 sr	N/A
cloud	ice	25 sr	N/A
aerosol	marine	20 sr	45 sr
aerosol	desert dust	40 sr	30 sr
aerosol	polluted continental	70 sr	30 sr
aerosol	clean continental	35 sr	30 sr
aerosol	polluted dust	65 sr	30 sr
aerosol	biomass burning	70 sr	40 sr
stratospheric	all	15 sr	15 sr

4.4.1.3 CALIPSO data files

The CALIPSO Level 2 data described above are stored in Part D of the database without any modification. The files are of the following types:

- **CAL_LID_L2_05kmALay:** contains the CALIPSO Level 2 aerosol layer data with a horizontal resolution of 5 km. These data are used for the aerosol feature comparison.

- **CAL_LID_L2_05kmCLay:** contains the CALIPSO Level 2 cloud layer data with a horizontal resolution of 5 km. These data are used for the cloud feature comparison.

- **CAL_LID_L2_01kmCLay:** contains the CALIPSO Level 2 cloud layer data with a horizontal resolution of 1 km. These data are used for the cloud feature comparison.

- **CAL_LID_L2_333kmCLay:** contains the CALIPSO Level 2 cloud layer data with a horizontal resolution of 1/3 km (full resolution). These data are used for the cloud feature comparison.

- **CAL_LID_L2_40kmAProCal:** contains the CALIPSO calibrated Level 2 aerosol profile data with a horizontal resolution of 40 km. These data are used for the aerosol profile comparison.

- **CAL_LID_L2_05kmCPro:** contains the CALIPSO Level 2 cloud profile data with a horizontal resolution of 5 km. These data are used for the cloud profile comparison.

4.4.2 Definition of Part D products

The correlative study of EARLINET and CALIPSO Level 2 products is performed in terms of geometrical feature parameters and profiles of particle optical properties as well. In Part D of the database, absolute differences between ground-based and corresponding satellite measurements are reported together with the percentage differences with respect to the EARLINET observations, for the comparable parameters.

EARLINET vs. CALIPSO comparisons are classified primarily in Aerosol and Clouds. This choice is related to different temporal and spatial variability of aerosol and cloud fields and, therefore, to the necessity of different approaches for the correlative study of aerosol and clouds. On the other hand, CALIPSO Level 2 data are provided separately and with different vertical and horizontal resolutions for aerosol and clouds.

4.4.2.1 Part D – Aerosol

For the aerosol correlative study, point-to-point absolute and percentage differences are evaluated with respect to CALIPSO aerosol products provided at 5-km horizontal resolution for Level 2 Layer products and 40-km horizontal resolution for Level 2 Profile data for the following quantities:

- top, base and thickness of the layer,
- particle backscatter profile at 532 nm,
- particle backscatter profile at 1064 nm (only for stations operating at 1064 nm),
- particle extinction profile at 532 nm (only for stations with extinction measurements at 532 nm),
- particle depolarization-ratio profile at 532 nm (if available).

Single-point comparisons for aerosol observations are divided into two main categories: boundary layer and free troposphere. Because of the very local nature of the boundary-layer aerosol content, comparison between EARLINET and CALIPSO data are reported only for overpasses within 10 km and/or within 10 min to the EARLINET observation. For free-tropospheric aerosol investigation, different temporal and spatial distances between satellite ground track and ground-based lidar observation are considered:

- overpass within 10 km and 10 minutes,
- overpass within 50 km and 30 minutes,

- overpass within 100 km and 150 minutes.

For the comparison of CALIPSO data with multiple-point observations, statistical analysis is performed on EARLINET measurements collected within each of the identified clusters and CALIPSO data collected over the cluster area. Comparisons are carried out for all parameters reported above, for specific scenarios (such as Saharan dust intrusion over Europe), seasons, and for data acquired during a single satellite cross section over each cluster.

4.4.2.2 Part D – Clouds

For the EARLINET vs. CALIPSO correlative study for clouds, the very high variability of cloud fields in time and space, both on horizontal and vertical scale, has to be considered. Therefore, for the cloud study, vertical-profile comparison does not make sense at all, and for these cases the following quantities are investigated:

- top, base and thickness of the layer,
- particle depolarization ratio at 532 nm (if available).

These differences are investigated also by dividing cases with respect to the cloud type. A first cloud classification in water, mixed-phase, and ice clouds is possible starting from the altitude, because the temperature (and thus the altitude) of the clouds primarily determines the presence of ice and/or water. For mid-latitude regions as Europe, typically clouds below 4 km are water clouds, whereas clouds above 8 km contain only ice, and the 4–8 km altitude range is typical for mixed-phase clouds.

For each cloud type, the dependence of EARLINET–CALIPSO differences are investigated as a function of temporal and spatial distance between the observing points. In particular, point-to-point comparisons are divided in:

- overpass within 10 km and 10 minutes,
- overpass within 50 km and 30 minutes,
- overpass within 100 km and 150 minutes.

Furthermore, the temporal variability is investigated as a function of the horizontal resolution of CALIPSO Level 2 data. For this aim, the overpass within 10 km and 10 minutes is studied using all three different horizontal resolutions of CALIPSO Level 2 Layer products

(1/3, 1, and 5 km). For larger distances, only the 5 km horizontal resolution CALIPSO Level 2 data is used.

As in the case of aerosols, climatological analysis is performed for each of the identified clusters of stations for the multiple-point comparisons. The climatological analysis is performed for each of the three cloud types, and results are achieved in terms of cloud geometrical properties (top, base, and thickness) and intensive properties (depolarization ratio).

4.4.3 Example of Part D products

In the following, a measurement performed at Potenza on 8 July 2008 is presented as an example of comparison between satellite and ground-based measurements. As shown in the DREAM dust forecast image reported in Fig. 4.8, a Saharan dust intrusion was expected over the Mediterranean, Southern Italy, and the Balkans region on this day.

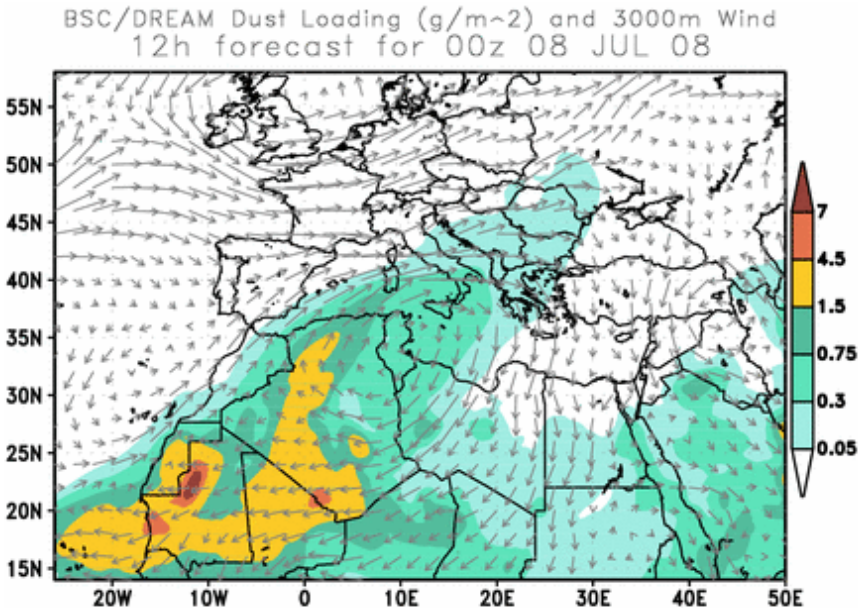

Figure 4.8: Dust-loading forecast by the DREAM model for 8 July 2008 at 00.00 UT.

Fig. 4.9 shows the temporal evolution of the lidar range-corrected signal at 1064 nm measured at Potenza on 8 July 2008. An aerosol layer extending from 3 to 5 km a.s.l. was oberved for almost the whole time interval of the measurement. A very intense aerosol layer was observed at about 2 km a.s.l. at the beginning of the measurement. This layer then went down in altitude and came into contact with the underlying planetary boundary layer (PBL) toward the end of the measurement around 02.50 UT, causing an enriched PBL aerosol load.

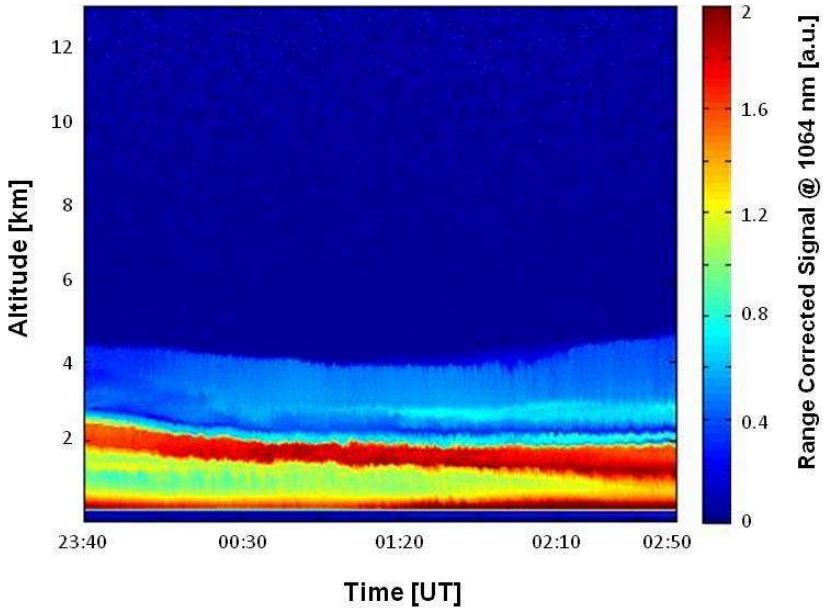

Figure 4.9: Temporal evolution of the lidar range-corrected signal at 1064 nm measured at Potenza on 8 July 2008.

The corresponding CALIPSO cross section of the total attenuated backscatter measured at 532 nm on 8 July 2008 is presented in Fig. 4.10. A large amount of aerosol was detected over the area extending between the Central Mediterranean and Africa (41° N, 13° E–25° N, 10° E). In coincidence with the overpass at Potenza (purple box), an aerosol layer at low altitude ranges was observed. A large spatial variability can be seen in Fig. 4.10 in the cross-section region close to Potenza, with the presence of broken low clouds. Figure 4.11 reports the CALIPSO retrieved Vertical Feature Mask, where the layers indentified as clouds and aerosol can be seen. In particular, it is evident that an aerosol layer reaching up to 5 km is present in almost the whole section of CALIPSO observations.

Figure 4.12 shows the aerosol backscatter profiles measured at 532 and 1064 nm with the EARLINET lidar at Potenza in comparison to the CALIPSO observation for the closest available overpass (about 172 km distance) and temporal coincidence and the corresponding differences profiles. The CALIPSO profiles have a horizontal resolution of 40 km, whereas the ground-based measurement is obtained with an integration time of 2 hours centered around the CALIPSO overpass time at 01.18 UT.

A good agreement in the shape of the profiles is observed above 3 km of altitude, while there are considerable differences at lower altitudes to be ascribed to the horizontal distance between the two observations. In Fig. 4.12, aerosol layer base and top altitudes are reported for both ground-based and spaceborne measurements as horizontal lines. For CALIPSO measurements, layers are highlighted by solid lines, when they are detected along the whole 40-km cross section, and by dotted lines, if they are detected only over a

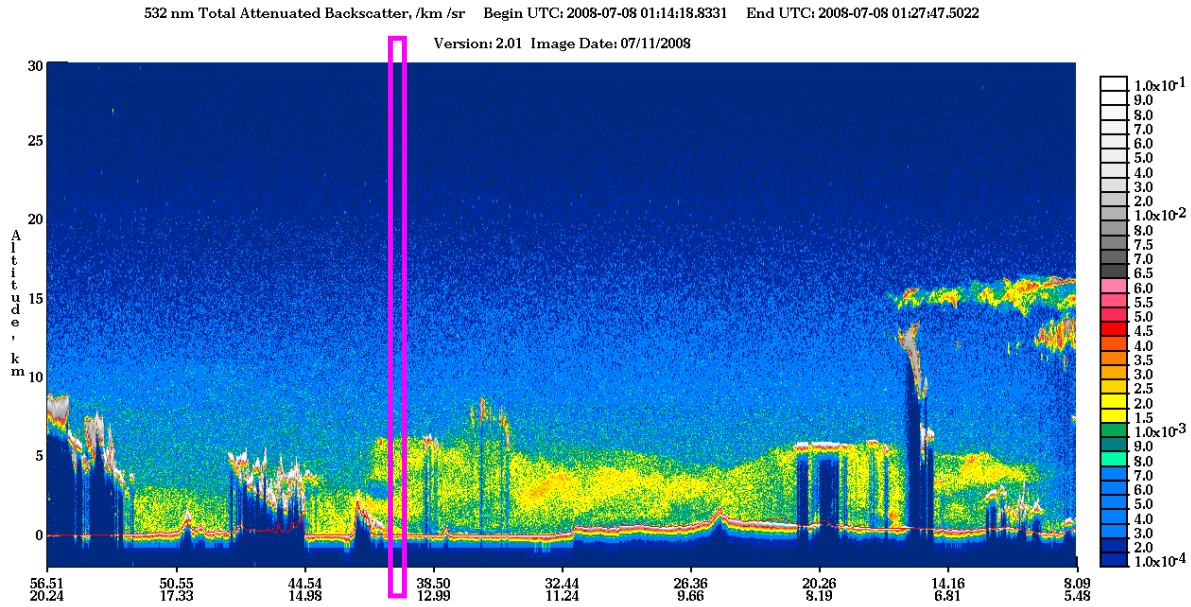

Figure 4.10: Cross section of the total attenuated backscatter measured by CALIPSO at 532 nm on 8 July 2008. The purple box highlights the overpass at Potenza.

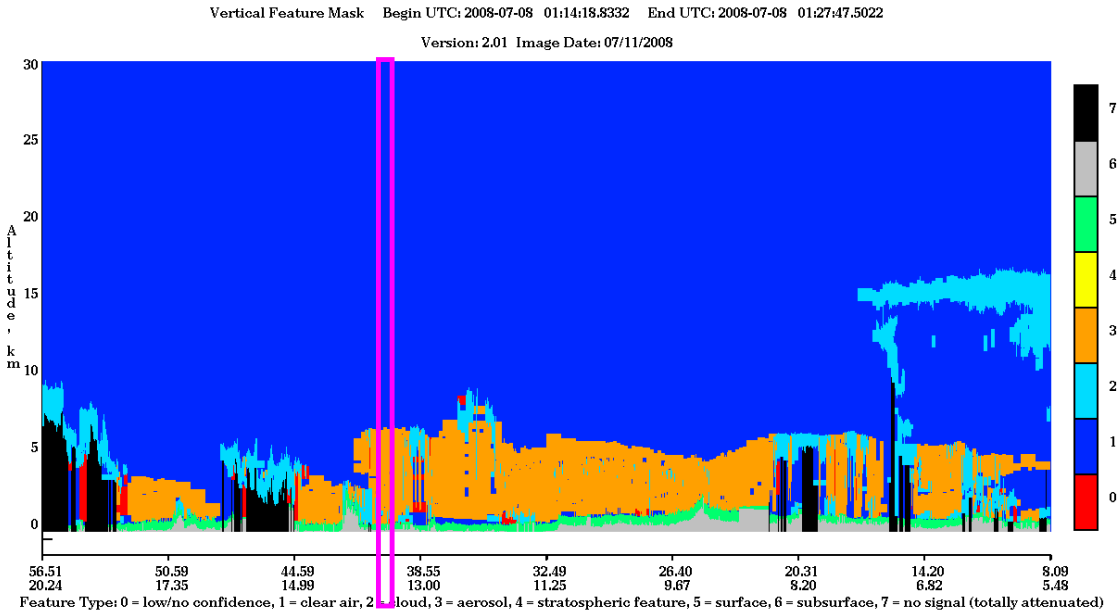

Figure 4.11: Cross section of the Vertical Feature Mask identified by CALIPSO on 8 July 2008. The purple box highlights the overpass at Potenza.

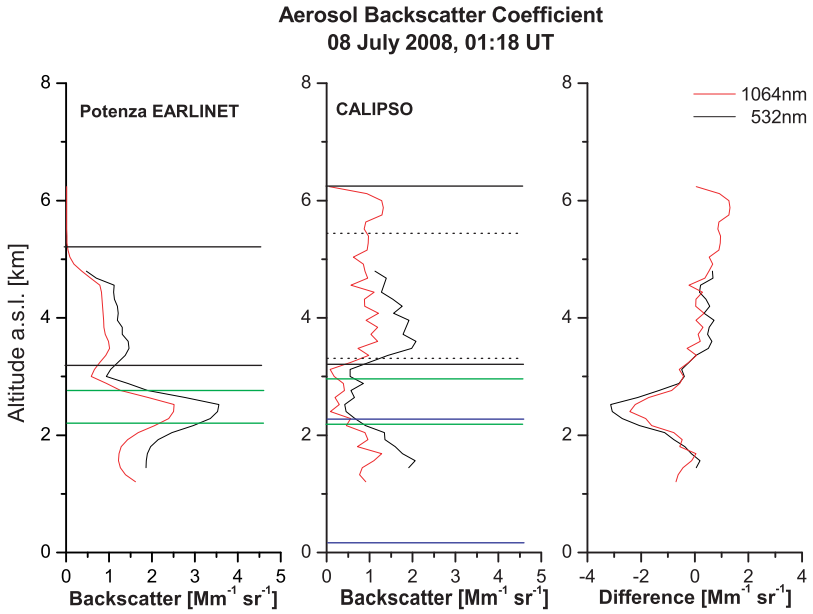

Figure 4.12: Aerosol backscatter coefficients at 532 and 1064 nm measured at Potenza EARLINET station (left) and by CALIPSO (middle) on 8 July 2008, 01.18 UT. Profiles of the differences are reported in the right panel. Top and base of aerosol layers are also indicated for both EARLINET and CALIPSO profiles as horizontal lines (black, green, and blue).

fraction of this distance. Along the whole 40-km pass, CALIPSO detects two aerosol layers extending from 2.2 to 3.0 km and from 3.2 to 6.2 km. Therefore, the feature comparison for this case results in a pretty good agreement of the lofted layer bottom altitudes. In the layer above 3.2 km detected by both systems, a relatively small difference of backscatter coefficients is observed resulting in a mean of 0.41 $Mm^{-1}sr^{-1}$ and 0.26 $Mm^{-1}sr^{-1}$ at 532 and 1064 nm, respectively. These small but not negligible differences are caused by the spatial and temporal variability of aerosol content, together with the horizontal distance between the air volumes sampled.

4.5 Implementation and structure of the database

The long-term aerosol and cloud database contains files, in which the following information is stored: EARLINET profiles in NetCDF format as described in Sec. 4.2.2, CALIPSO Level 2 data products (layers and profiles) for the area 20°–80° N, −20°–50° E in hdf format, EARLINET-CALIPSO difference profiles stored in NetCDF files. The files are administrated with a relational database. This database furthermore contains all results (layer products) retrieved from the EARLINET profiles, in particular the layer-mean feature products (Part B of the database) and the conversion factors (Part C of the database), as well as the EARLINET–CALIPSO layer difference values. In the following, the data handling in the relational database is described in more detail.

4.5.1 Relational database

For the administration of the complex information of all four parts of the database that consist of profile, layer, and single-value data (including errors), a relational database has been set up which is based on open-source software and allows platform-independent access. Currently, the database is implemented on a server which can be accessed from selected, external computers only. The access to the server is granted via secure channels (openVPN). Each channel is dedicated to a single user which is identified by a crypto certificate (key).[2]

PostgreSQL was chosen for the management of the relational database, because it allows a structured object access control management, i.e. different authorization can be provided to different users. The comprehensive PostgreSQL database design and management system pgAdmin III is implemented as the graphical user interface to the database. Figure 4.13 presents a schematic view of the database structure.

4.5.2 Database tables

For the administration of and the work with the database a series of tables is created. Besides the tables that are related to Parts A–D of the database, there are tables with basic information on the stations and the parameters used in the database. A brief description of the tables is given in the following.

Five tables provide basic information on the EARLINET stations, the selected features (aerosol and cloud types) and aerosol source regions, the optical data and feature properties used in the data evaluation:

[2]The finalized database can be transferred to any other server with any kind of access.

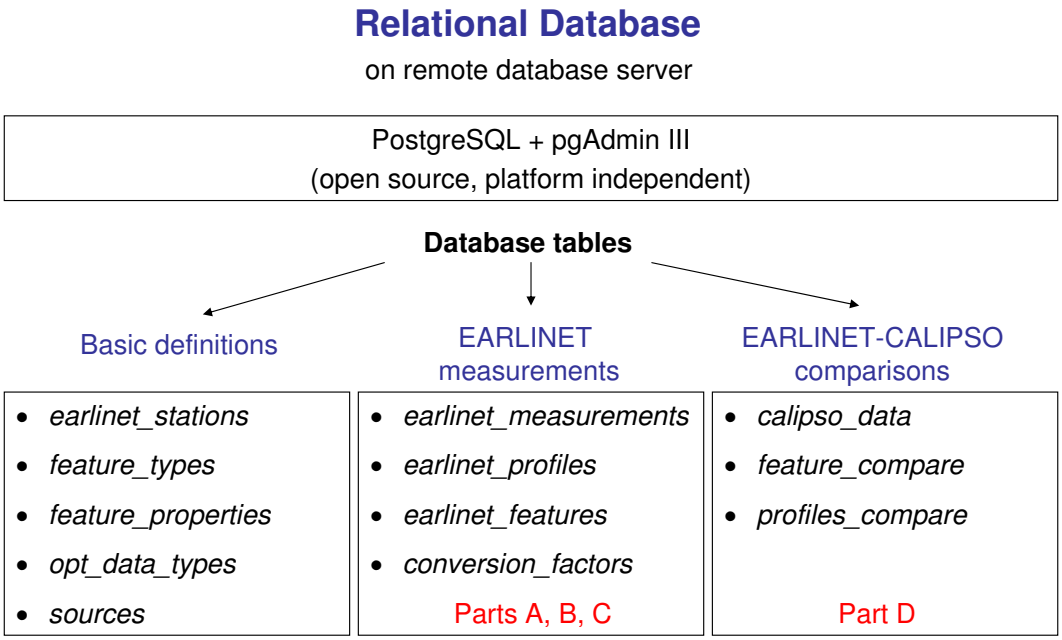

Figure 4.13: Structure of the relational database for aerosol and cloud products.

- *earlinet_stations*: In this table information on the EARLINET stations is given. The stations are identified by their station ID (see Tab. 2.1). The full station name (site, country), the name of the institution operating the station, the name of the PI and his/her e-mail address, latitude, longitude, height above sea level, the cluster to which the station belongs, and the abbreviation of the institution are provided.

- *feature_types*: This table provides the list of features selected in the study to characterize the different aerosol and cloud types and other features. Each feature type has an ID number. Aerosol and cloud features are distinguished. The following list is used:

Feature ID	Feature Name	Cloud	Aerosol
0	unknown feature	FALSE	FALSE
1	clear air	FALSE	FALSE
2	unknown aerosol	FALSE	TRUE
3	**stratospheric aerosol**	FALSE	TRUE
4	**clean marine**	FALSE	TRUE
5	**dust**	FALSE	TRUE
6	**polluted continental**	FALSE	TRUE
7	**clean continental**	FALSE	TRUE
8	*dust and smoke*	FALSE	TRUE
9	**smoke**	FALSE	TRUE
10	unknown cloud	TRUE	FALSE
11	**stratospheric cloud**	TRUE	FALSE
12	**cirrus**	TRUE	FALSE
13	**mixed-phase cloud**	TRUE	FALSE
14	**water cloud**	TRUE	FALSE
15	*pollution and dust and marine*	FALSE	TRUE
16	*pollution and smoke*	FALSE	TRUE
17	*pollution and marine*	FALSE	TRUE
18	*dust and marine*	FALSE	TRUE
19	*dust and marine and smoke*	FALSE	TRUE
20	*clean continental and marine*	FALSE	TRUE
21	*clean continental and dust and marine*	FALSE	TRUE
22	*clean continental and dust*	FALSE	TRUE
23	*pollution and marine and smoke*	FALSE	TRUE
24	*clean continental and marine and smoke*	FALSE	TRUE
25	*marine and smoke*	FALSE	TRUE
26	*pollution and dust and marine and smoke*	FALSE	TRUE
27	*pollution and dus*t	FALSE	TRUE
28	*pollution and dust and smoke*	FALSE	TRUE
29	**volcanic**	FALSE	TRUE

The basic cloud and the pure aerosol types are indicate in bold. Mixtures of aerosols are given in italic. Only mixtures which have indeed been found in the analysis are listed.

- *feature_properties*: In this table the feature properties are listed. Each feature property has an ID number and a short name. It is indicated whether the property is a conversion factor and whether it is available as a CALIPSO product. The following properties are considered:

Property ID	Feature Property	Conversion Factor	CALIPSO Product
1	feature bottom height	FALSE	TRUE
2	feature top height	FALSE	TRUE
3	feature depth	FALSE	TRUE
4	$\gamma_{\text{feature,VIS}}$	FALSE	TRUE
5	$\gamma_{\text{feature,IR}}$	FALSE	TRUE
6	χ'_{feature}	FALSE	TRUE
7	δ_{feature}	FALSE	TRUE
8	$C_{\alpha,\text{VIS}-\text{UV}}$	TRUE	FALSE
9	$C_{\beta,\text{VIS}-\text{UV}}$	TRUE	FALSE
10	$s_{\text{VIS}-\text{UV}}$	TRUE	FALSE
11	$C_{\beta,\text{IR}-\text{VIS}}/S_{\text{UV}}$	TRUE	FALSE
12	β_{UV}	FALSE	FALSE
13	β_{VIS}	FALSE	FALSE
14	β_{IR}	FALSE	FALSE
15	α_{UV}	FALSE	FALSE
16	α_{VIS}	FALSE	FALSE
17	S_{UV}	FALSE	FALSE
18	S_{VIS}	FALSE	FALSE
19	$\mathring{a}_{\alpha,\text{VIS}-\text{UV}}$	FALSE	FALSE
20	$\mathring{a}_{\beta,\text{VIS}-\text{UV}}$	FALSE	FALSE
21	$\mathring{a}_{\beta,\text{IR}-\text{VIS}}$	FALSE	FALSE
22	$C_{\beta,\text{IR}-\text{VIS}}$	FALSE	FALSE
23	δ_{VIS}	FALSE	FALSE
24	$\mathring{a}_{\beta,\text{IR}-\text{UV}}$	FALSE	FALSE
25	$C_{\beta,\text{IR}-\text{UV}}$	FALSE	FALSE
26	feature bottom calculation height	FALSE	TRUE
27	feature top calculation height	FALSE	TRUE

- *opt_data_types*: This tables lists the types of optical data used in the comparison of EARLINET and CALIPSO data:

Data Type ID	Optical Data Type
1	attenuated backscatter
2	backscatter coefficient
3	extinction coefficient
4	depolarization ratio
5	lidar ratio

- *sources*: This table lists the aerosol source regions which are considered in the study. It is indicated whether the source region is within Europe or whether the transport regime is intercontinental.

Source ID	**Source Region**	**Intercontinental**
1	Atlantic Ocean	TRUE
2	North Sea	FALSE
3	Baltic Sea	FALSE
4	Mediterranean	FALSE
5	Western Sahara	TRUE
6	Central Sahara	TRUE
7	Eastern Sahara	TRUE
8	Central Europe	FALSE
9	Southwestern Europe	FALSE
10	Southern Europe	FALSE
11	Southeastern Europe	FALSE
12	Eastern Europe	FALSE
13	Arctic	TRUE
14	North America	TRUE
15	Northern Europe	FALSE
16	Western Europe	FALSE
17	Europe	FALSE
18	Siberia	TRUE
20	Arabian Peninsula	TRUE

  In addition to the single source regions listed above, the table allows combinations of source regions in order to describe the origin of mixed aerosols.

Four tables administrate the EARLINET measurements. They are related to parts A, B, and C of the database.

- *earlinet_measurements*: The table gives information on each individual EARLINET measurement. It lists the measurement ID and the station ID (see Tab. 2.1), identifies Case A/B/C measurements, the day number in the CALIPSO cycle, and nighttime/daytime measurements. In addition, the table logs the status of the evaluation of these data with respect to parts B, C, and D of the database.

- *earlinet_profiles*: This table administrates Part A of the database. It lists all files (extinction and backscatter+depolarization profiles) provided by the EARLINET stations in terms of measurement ID, filename (styymmddnnn.twv), profile ID, start

and stop time of the measurement, zenith angle, receiver field of view, and wavelength.

Furthermore, this table is used to log the status of the files of Part A of the database. It is indicated when the data have been uploaded and whether the data are finalized or not. As long as data are not finalized, they can be re-evaluated. After finalization, no changes to the data are possible.[3] All files are quality checked and set to be valid or invalid. In this way, data which are found to be of low quality or useless can be excluded from further use.

- *earlinet_features*: This table represents Part B of the database. It contains the properties of all features (layers) selected from the profiles listed in *earlinet_profiles*. The measurement ID, profile(s) ID, feature ID, feature type ID (according to *feature_types*), source ID (according to *sources* if the feature is an aerosol), mean relative humidity (for aerosol), age (for aerosol), feature property ID (according to *feature_properties*) are listed together with the mean value and the standard deviation of the feature property.

- *conversion_factors*: This table represents Part C of the database. It contains the conversion factors and statistical information for selected feature types. The feature ID (according to *feature_types*) and the conversion factor ID (according to *feature_properties* with Conversion Factor = TRUE) are given together with mean value, standard deviation, median, maximum, minimum, and skewness of the conversion factors.

Three tables belong to Part D of the database. They relate the EARLINET measurements with the CALIPSO data.

- *calipso_files*: This table administrates the CALIPSO data. A CALIPSO file ID, the CALIPSO file name, horizontal resolution, and data release version are listed. Furthermore, it is indicated whether the file contains cloud or aerosol, nighttime or daytime, and layer or profile data.

- *feature_compare*: This table, together with table *profiles_compare*, administrates Part D of the database. The table provides the absolute and relative differences between CALIPSO and EARLINET layer data. Information is listed in terms of EARLINET feature ID, CALIPSO file ID, CALIPSO feature ID, CALIPSO first and last profile ID, CALIPSO time, CALIPSO latitude and longitude, CALIPSO horizontal average, distance in space and time between EARLINET and CALIPSO measurements, feature property ID (according to *feature_properties* with CALIPSO Product

[3]When the database is made public, all data will be in the finalized status.

= TRUE), absolute and relative difference of the feature property, CALIPSO feature classification flag, and CALIPSO CAD score.

- *profiles_compare*: This table provides the list of files of Part D of the database with the profiles of absolute and relative differences between CALIPSO and EARLINET Level 2 data. Information is given in terms of EARLINET profile ID, CALIPSO file ID, CALIPSO start and stop time, CALIPSO longitude and latitude, distance in space and time between EARLINET and CALIPSO measurements, names of the files containing the absolute and relative difference profiles, and the type of compared optical data (according to *opt_data_types*).

4.5.3 Exploitation tools

As mentioned before, standard exploitation and visualization tools are available for NetCDF data. The same holds for the hdf format in which the CALIPSO data are stored. Tools for extracting and displaying CALIPSO data are provided at http://eosweb.larc.nasa.gov/PRODOCS/calipso/table_calipso.html.

Within the relational database, any kind of search functions can easily be executed and any pre-defined parameters can be related to each other by SQL statements. The relational database is also accessible with external programs by SQL statements and can thus be implemented in automated algorithms. These functions of the relational database can be used for further exploitation of the database products. They are also available after the end of the project, when the database will be delivered for further use.

Any data can be exported from the database into user-defined external files for further exploitation or visualization. Preferably, a standard format such as NetCDF would be used, so that again standard visualization tools, e.g. ncBrowse, can be applied.

Chapter 5

Aerosol and cloud classification from ground-based measurements

In this chapter we illustrate the aerosol and cloud classification schemes on the basis of case studies selected from the long-term ground-based lidar observations at 16 EARLINET stations. Section 5.1 deals with the aerosol classification. Geophysical properties of six pure aerosol types are studied in detail:

- Marine aerosol
- Mineral dust
- Polluted continental aerosol
- Continental background aerosol
- Biomass-burning aerosol (smoke)
- Stratospheric (volcanic) aerosol

In addition, we discuss the most important mixtures of different aerosol types:

- Mineral dust and marine aerosol
- Polluted continental aerosol, mineral dust, and marine aerosol
- Polluted continental and marine aerosol
- Polluted continental aerosol and smoke

The cloud classification scheme, which considers water, ice, and mixed-phase clouds, is discussed in Section 5.2.

5.1 Aerosol classification

5.1.1 Marine aerosol

5.1.1.1 Marine aerosol source regions

Source regions of marine aerosol which might be detected at EARLINET stations are:

- the North Atlantic/North Sea region,
- the Baltic Sea,
- the Mediterranean Sea,
- the Black Sea.

As discussed in Chapter 3, only a part of the EARLINET stations might be directly influenced by marine air (see Fig. 5.1). Most of these stations (Barcelona, Granada, Naples, Athens, Thessaloniki, Hamburg) also represent densely populated areas, so that undisturbed measurements of clean oceanic aerosols are quite unlikely. The orographic situation with very specific coastal circulation pattern complicates the observational conditions in addition. Barcelona measurements, for instance, often show a complex vertical layering and wave structures. The stations of Cabauw and Lecce are located in flat, rural environments and might be better suited for the observation of marine aerosols. In any case, the identification of marine aerosols requires specific care. Within the 18-month measurement period, clean marine air could be identified for a few measurement cases only. In most circumstances, marine air was mixed with other aerosols such as pollution or dust.

5.1.1.2 Case study: Granada, 2 August 2009

Figure 5.2 presents one of the few occassions when very low lidar ratios as typical for marine aerosols have been observed at an EARLINET station. The measurement was performed at Granada on 2 August 2009. As seen from the FLEXPART transport simulation in Fig. 5.3, the layer obtained above the local planetary boundary layer between 2570 and 3930 m was directly advected from the Atlantic Ocean. The airmass traveled close to the ocean surface and had not been in contact with land during the past four days. Thus most likely, even if lofted, the layer is dominated by marine aerosol particles.

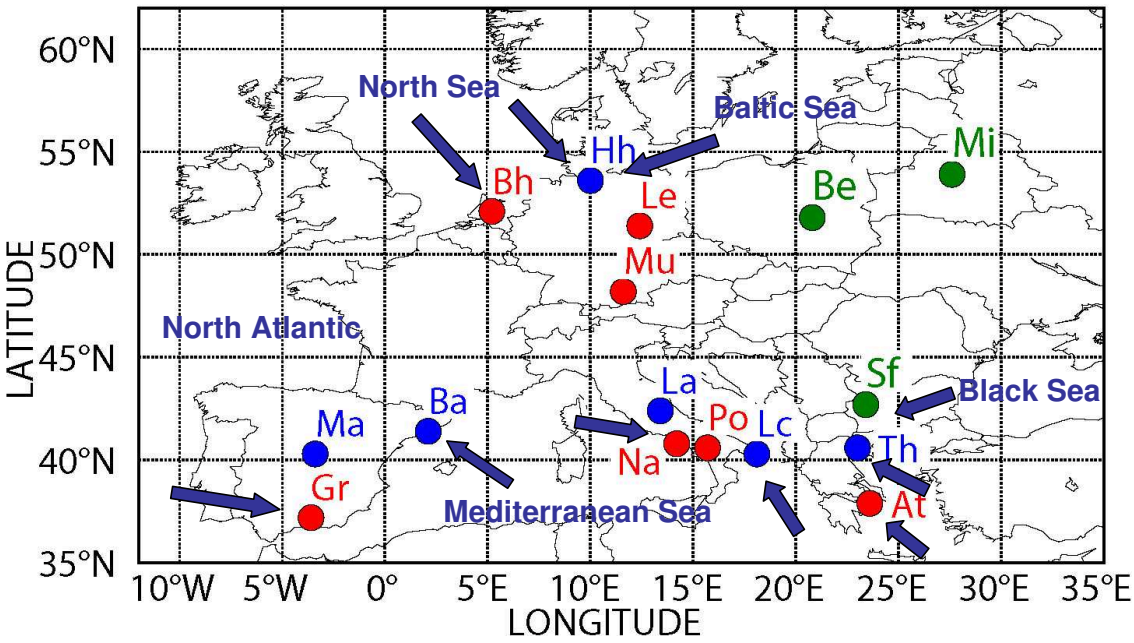

Figure 5.1: Source regions of marine aerosols around Europe and EARLINET stations at which direct advection of marine air is expected.

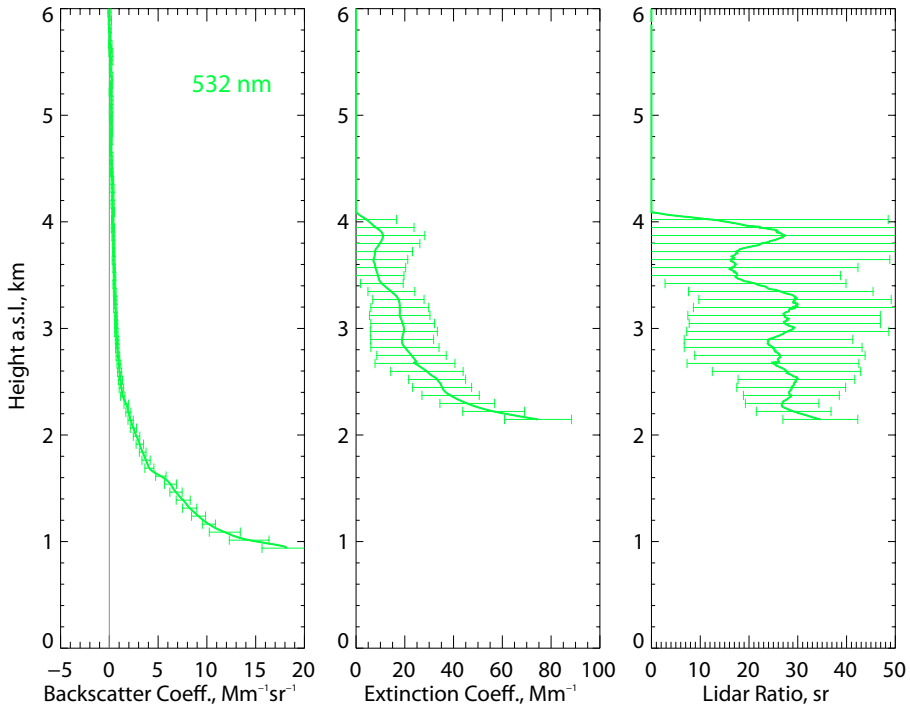

Figure 5.2: Profiles of backscatter coefficient, extinction coefficient, and lidar ratio at 532 nm measured at Granada on 2 August 2009, 03.09–03.39 UT.

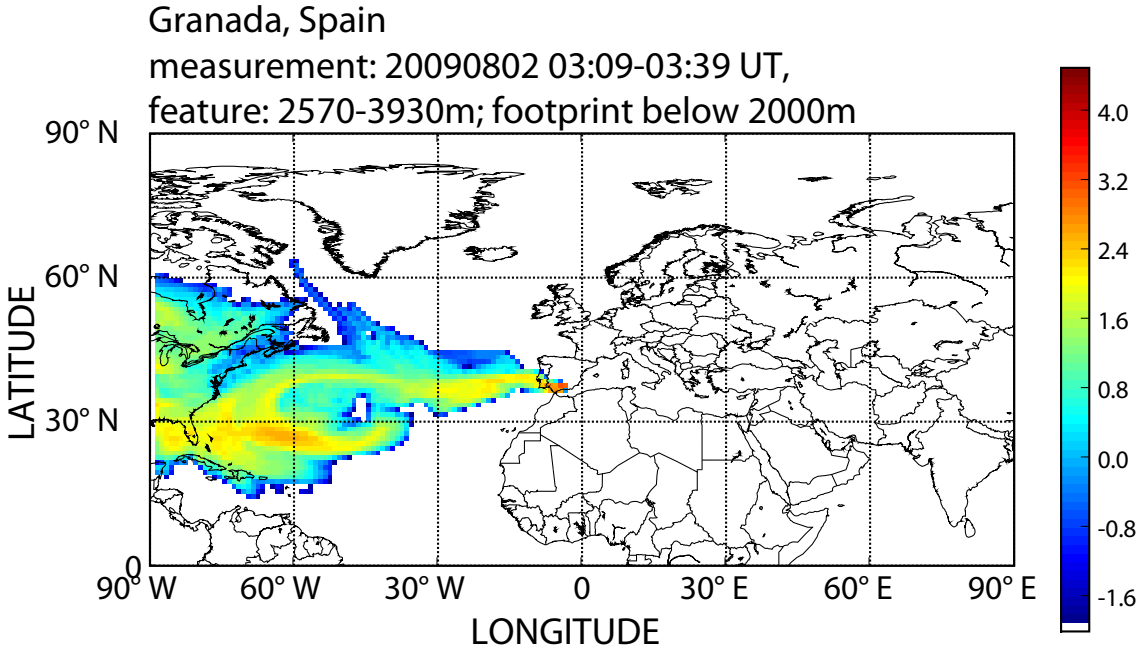

Figure 5.3: FLEXPART footprint for airmasses traveling below 2000 m height and arriving at Granada between 2570 and 3930 m height at 03.39 UT on 2 August 2009. The colors represent the logarithm of the integrated residence time in a grid box in seconds for 10-day integration time.

5.1.2 Mineral dust

5.1.2.1 Dust source regions

In Chapter 3, we suggested to distinguish different source regions in the dust characterization. Western, Central, and Eastern Sahara were introduced as preliminary dust source areas. In the following, we refine this classification with the help of recent studies on dust source activation and results from transport modeling.

Fig. 5.4 shows the results of a study on dust source activation (*Schepanski et al.*, 2007). The authors investigated IR images of Meteosat Second Generation for March 2006 - February 2007. The study underlines that the major dust source of the Sahara is the Bodele depression in the Lake Chad Basin (middle red-encircled area). Other important active areas are connected to the foothills of mountainous regions in Southern Algeria, Northern Mali, and Western Niger (left red-encircled area) and the foothills of the Red Sea Mountains in Sudan (right red-encircled area). As already suggested by other authors (*Prospero et al.*, 2002), the dust originates from the sediments of fine soil mobilized in geographical lows and foothills where dry (paleo) lakes and rivers (wadis) exist.

The findings by *Schepanski et al.* (2007) very well coincide with our suggested dust source regions. Based on the identified active areas, we can refine the boundaries of these regions. As can be seen from Fig. 5.5, a separation along the 10° E and 25° E meridians is a useful approach. Thus we define the source regions for Saharan dust in this study as follows:

- Western Sahara: all African areas north of 10° N and west of 10° E,
- Central Sahara: all African areas north of 10° N and between 10° and 25° E,
- Eastern Sahara: all African areas north of 10° N and east of 25° E.

As an example for the classification of Saharan dust, we present a measurement taken at Leipzig on 30 May 2008 during an intense Saharan dust episode (see next section). Fig. 5.6 shows the time-height contour plot of the 1064-nm range-corrected signal. The dust layer extended to a height of approximately 5.5 km in the morning of this day. The white box indicates the time and height range for which a FLEXPART transport simulation was performed (see Chapter 3). The result of transport modeling is shown in Fig. 5.7. The footprint represents airmasses which traveled below 2000 m height and arrived at Leipzig between 3150 and 5310 m height at 09.00 UT on 30 May 2008. The model output is given in terms of the integrated residence time in a grid box. The integration time used here is 10 days. With the help of this model result, the respective layer is classified as dust from the Western Sahara in the database.

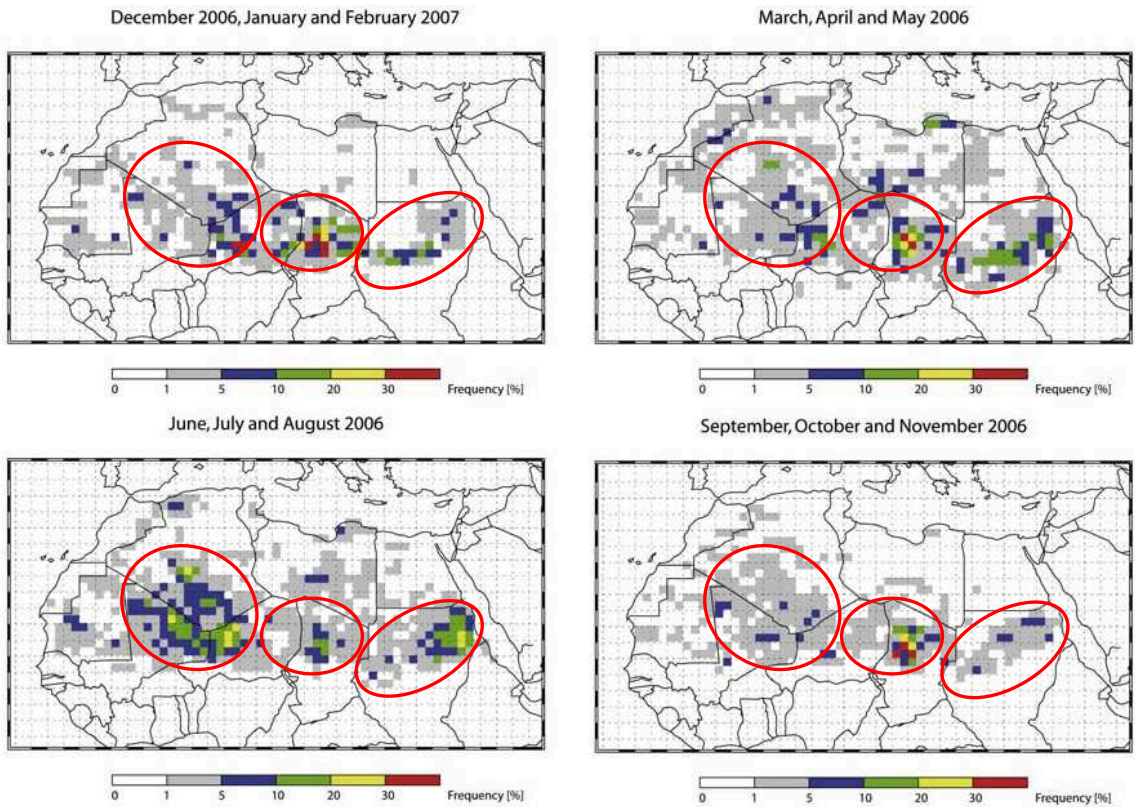

Figure 5.4: Seasonal frequencies (relative number of days) of dust source activation on a $1^o \times 1^o$ grid, derived from MSG IR difference composite images for March 2006 to February 2007 (taken from *Schepanski et al.* (2007)). Major dust source regions considered for the present study are encircled in red.

5.1.2.2 Case study: 15–31 May 2008

In the second half of May 2008, two major Saharan dust outbreaks determined the aerosol conditions over a large part of Europe. The event of May 26–30, 2008, was one of the most intense dust events in Europe ever observed with lidar. Fig. 5.8 and 5.9 show the dust forecast from the DREAM model for the periods 15–22 and 24–31 May 2008, respectively.

The period covers a full CALIPSO cycle and respective EARLINET Case A and B measurements. In addition, Case C alerts were given especially for the Central Mediterranean (CM), Eastern Mediterranean (EM), and Central European (CE) clusters for the periods 15–20 and 26-30 May 2008. EARLINET stations reported 30 Case A, 15 Case B, and 63 Case C measurements for the entire period. This intensive observational phase has been investigated in detail and results are presented in the following as well as in Sec. 7.3 and in Chapter 7. The case is also discussed in the publication by *Pappalardo et al.* (2010).

Even if dust had a major influence on the aerosol conditions, each single measurement

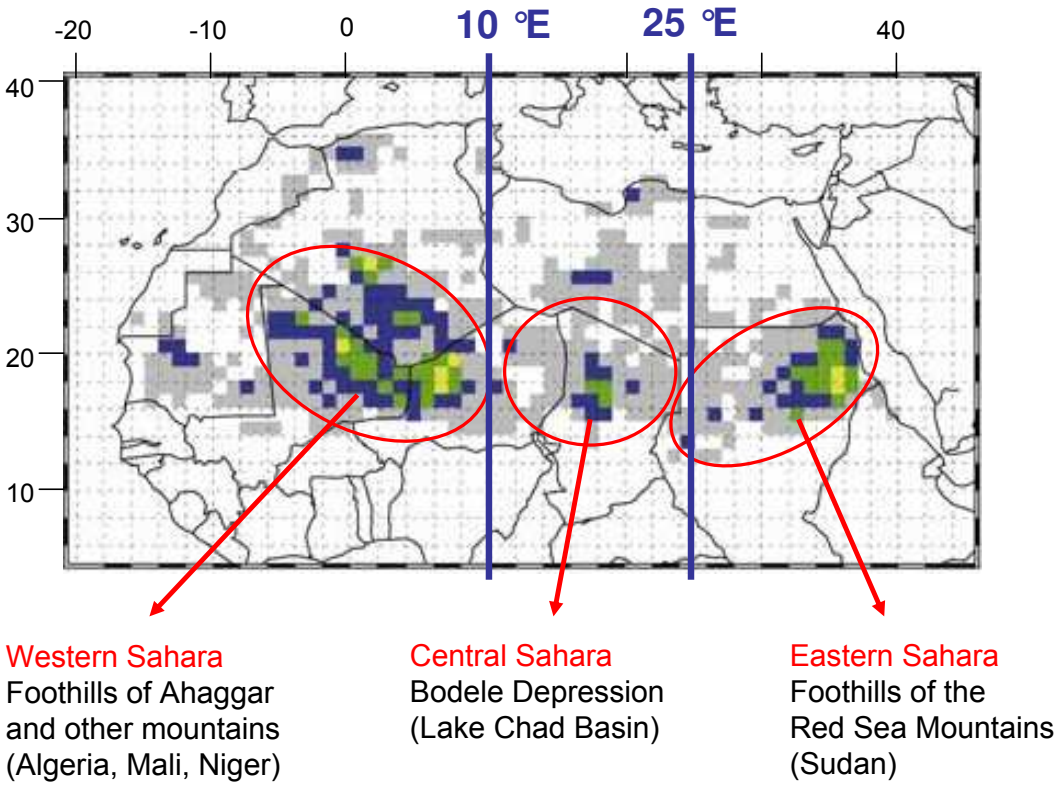

Figure 5.5: Definition of dust source regions based on the study by *Schepanski et al.* (2007). The 10° E and 25° E meridians are taken as the boundaries between the three major source regions.

must be investigated in detail and the origin of each feature must be clarified. Continental pollution is almost always present in the lower troposphere over Europe. Transport modeling and the lidar results are used to distinguish pure dust, mixtures of dust, and other aerosol types. Examples are presented below.

Figure 5.10 shows the DREAM forecast for 27-30 May, 00.00 UT, together with maps indicating the CALIPSO overpasses on these days. The major dust plume stretched from Africa over Italy toward Germany most of the time. CALIPSO crossed the central part of the dust plume during a night-time overpass on 28 May and during a night-time and a daytime overpass on 30 May. Case A observations for these overpasses were performed in L'Aquila on 28 May, in Belsk, Potenza, and Napoli on 30 May at night, and in Hamburg and Maisach on 30 May during daytime, together with a Case B observation in Leipzig.

The high spatial and temporal variability of the dust plume becomes visible in the CALIPSO as well as in the EARLINET observations. Fig. 5.11 presents a sample of backscatter-coefficient profiles taken at Leipzig, L'Aquila, and Potenza, i.e. along the north-south axis of the major dust plume, from 26 to 30 May 2008. The main dust layer stretched up to 6 km height typically. Maximum backscatter-coefficient values were around

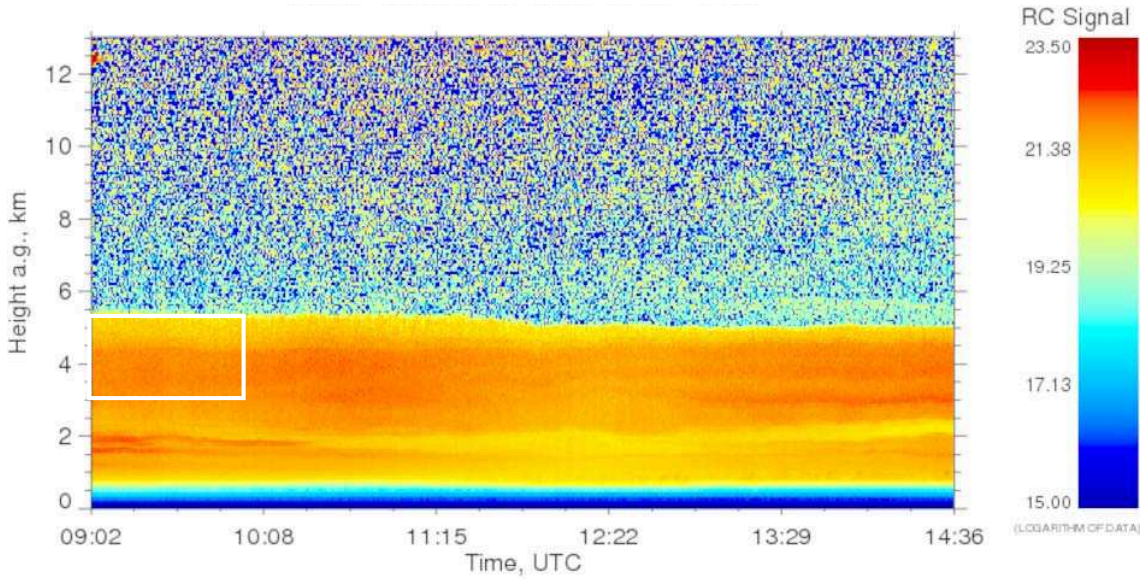

Figure 5.6: Time–height contour plot of the range-corrected 1064-nm signal measured at Leipzig between 09.02 and 14.36 UT on 30 May 2008. The white box indicates time and height range for which the FLEXPART transport simulation was performed (see Fig. 5.7).

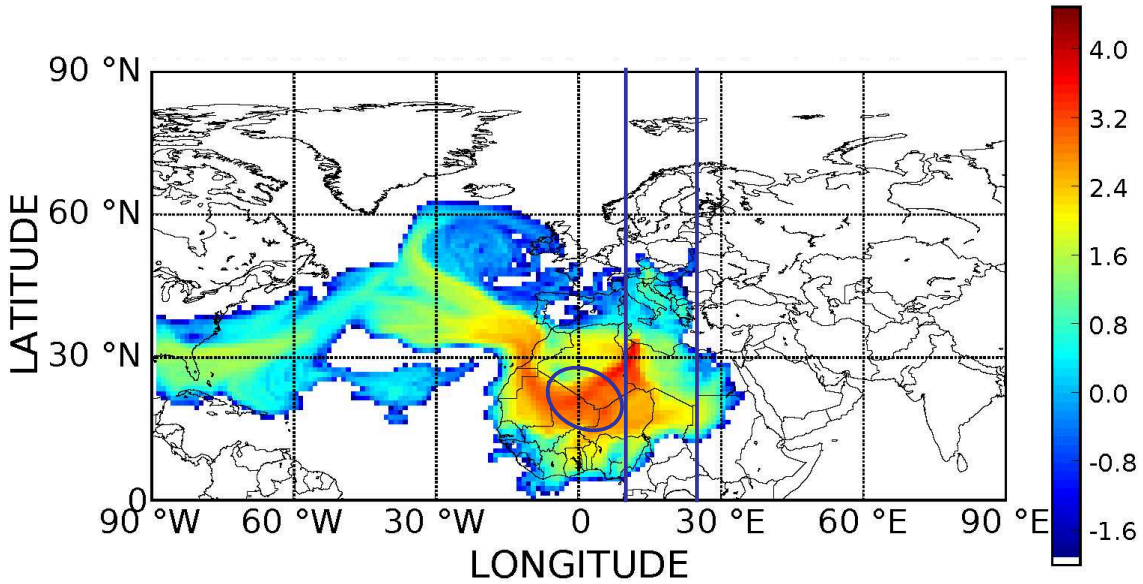

Figure 5.7: FLEXPART footprint for airmasses traveling below 2000 m height and arriving at Leipzig between 3150 and 5310 m height at 09.00 UT on 30 May 2008. The colors represent the logarithm of the integrated residence time in a grid box in seconds for 10-day integration time. The boundaries of source regions identified in Fig. 5.4 and 5.5 are indicated.

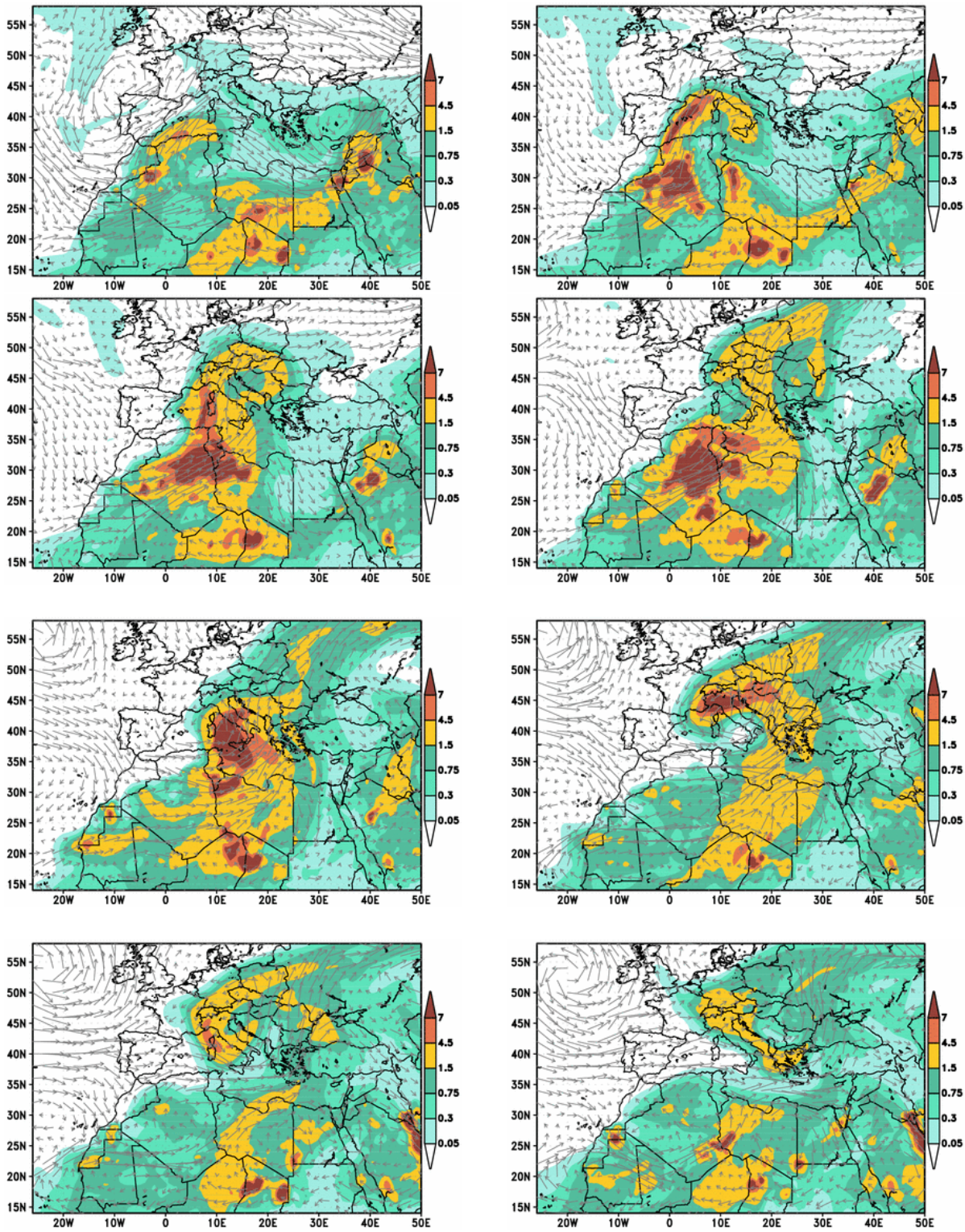

Figure 5.8: Saharan dust episode over North Africa and Southern/Central Europe as forecast with the DREAM model from 15 May (upper left) to 22 May 2008 (lower right). Shown is the 0-h forecast at 12.00 UT of each day in terms of column dust load in g/m^2 (colored) together with the 3000-m wind field (arrows).

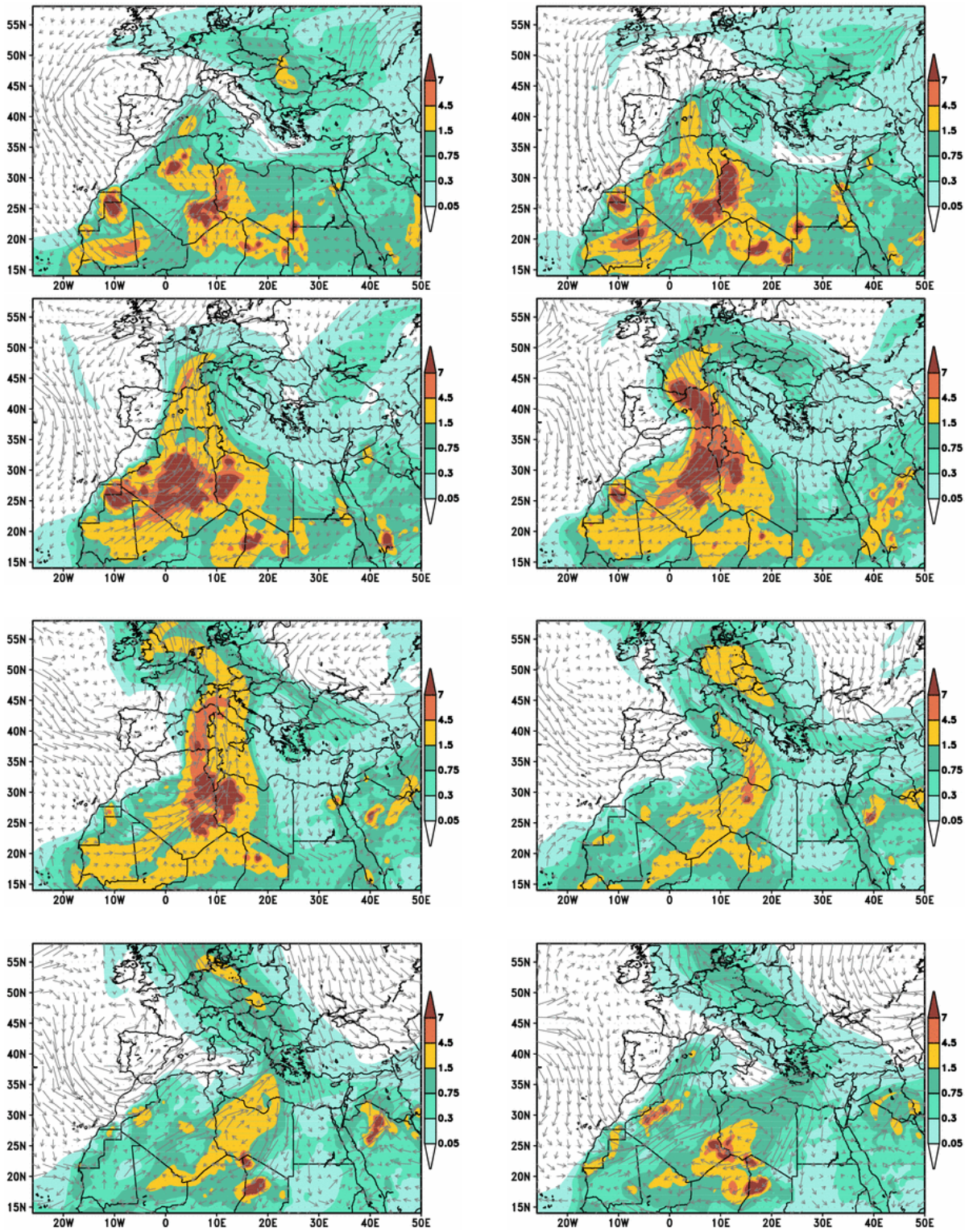

Figure 5.9: Saharan dust episode over North Africa and Southern/Central Europe as forecast with the DREAM model from 24 May (upper left) to 31 May 2008 (lower right). Shown is the 0-h forecast at 12.00 UT of each day in terms of column dust load in g/m^2 (colored) together with the 3000-m wind field (arrows).

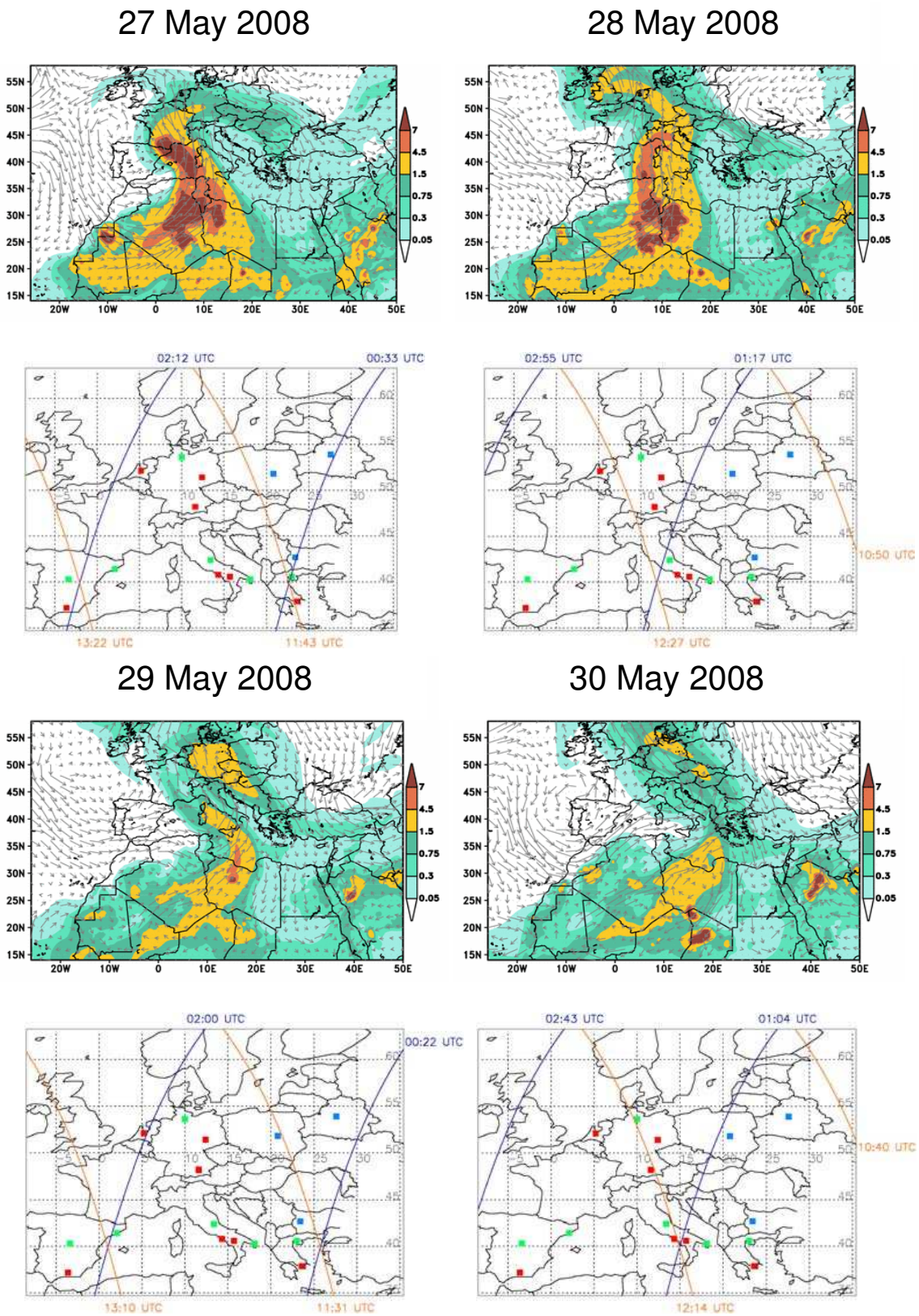

Figure 5.10: DREAM forecast for 27-30 May 2008, 00.00 UT together with maps indicating the CALIPSO overpasses on the same days.

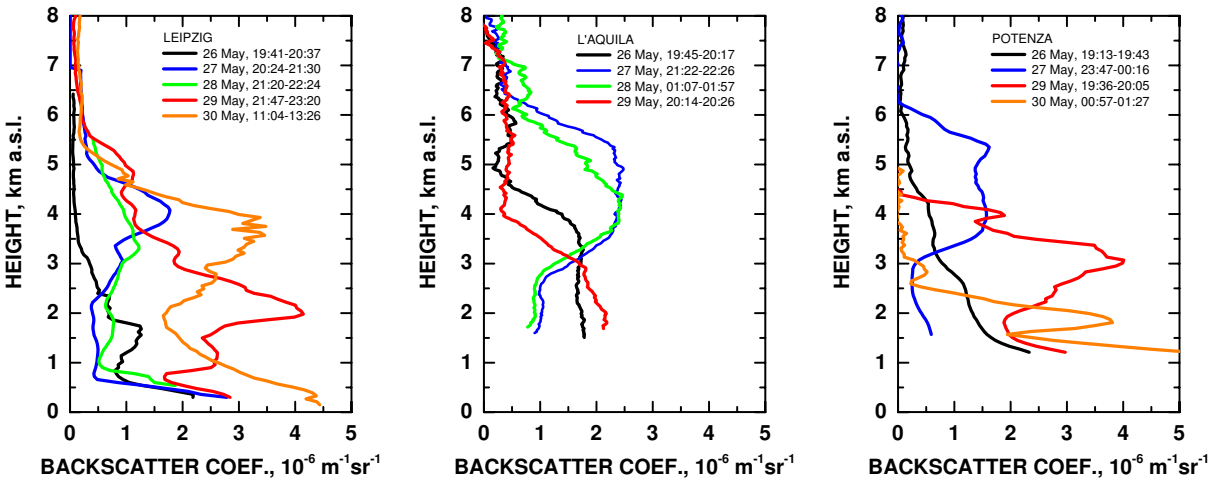

Figure 5.11: Backscatter-coefficient profiles measured at the EARLINET stations Leipzig (532 nm), L'Aquila (355 nm), and Potenza (532 nm) during the major Saharan dust outbreak in the period 26-30 May 2008.

0.002-0.004 $km^{-1}sr^{-1}$, corresponding to extinction coefficients of 0.1-0.4 km^{-1}. The optical depth reached values of 1-1.5 in the center of the plume, which is also confirmed by AERONET observations at several European sites in this period. Fig. 5.12 shows the CALIPSO cross section for the night-time overpass on 28 May in terms of the 532-nm total attenuated backscatter and the vertical feature mask (Version 2 data release). The dust plume stretching toward Europe is encircled and the location of L'Aquila EARLINET station (La) is indicated. Fig. 5.13 shows the direct intercomparison of the backscatter-coefficient profiles measured from ground at L'Aquila and from CALIPSO (Version 2) in horizontal distances of 48, 75, and 67 km. Under consideration of the spatial and temporal inhomogeneity, indicated by the successive CALIPSO profiles, a very good agreement of the L2 aerosol profiles is obtained. It must be mentioned here that the L'Aquila lidar operates at 355 nm. Normally, a direct comparison with the CALIPSO 532-nm profiles is not possible. However, as shown below, Ångström exponents of dust are close to zero, i.e. the wavelength dependence is negligible here.

Figures 5.14 and 5.15 present a respective approach for the CALIPSO daytime overpass on 30 May. The 532-nm total attenuated backscatter coefficient shows high and mid-level clouds over the Alps, i.e. above and south of the EARLINET station at Maisach (Ms). Cirrus clouds are also present over Northern Germany (EARLINET station Hamburg, Hh). The dust plume is indicated again by a red circle in Fig. 5.14. However, from the vertical feature mask (Version 2) it can be seen that most of the plume is classified as cloud. Obviously, this is a misclassification caused by the high backscatter and depolarization values of dust at relatively high latitudes. North of 50° N, outside of the so-called dust belt, the CALIPSO cloud-aerosol discrimination algorithm forces the identification of

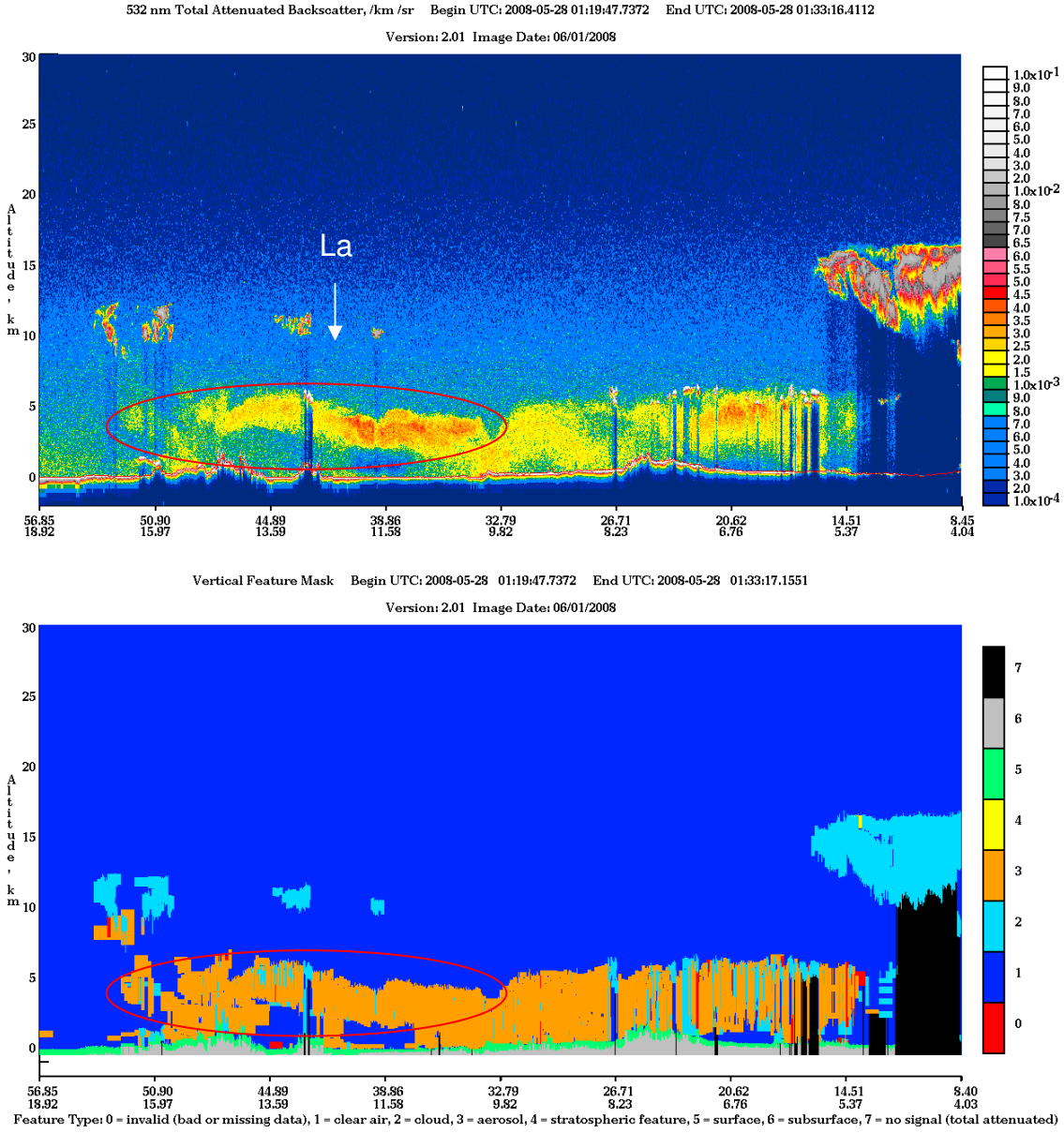

Figure 5.12: CALIPSO cross sections of 532-nm total attenuated backscatter and the vertical feature mask (Version 2 data release) for the overpass at 01.19–01.33 UT on 28 May 2008. The dust plume stretching toward Central Europe is encircled and the location of L'Aquila EARLINET station is indicated (figures taken from http://www-calipso.larc.nasa.gov/products/lidar/browse_images/show_calendar.php).

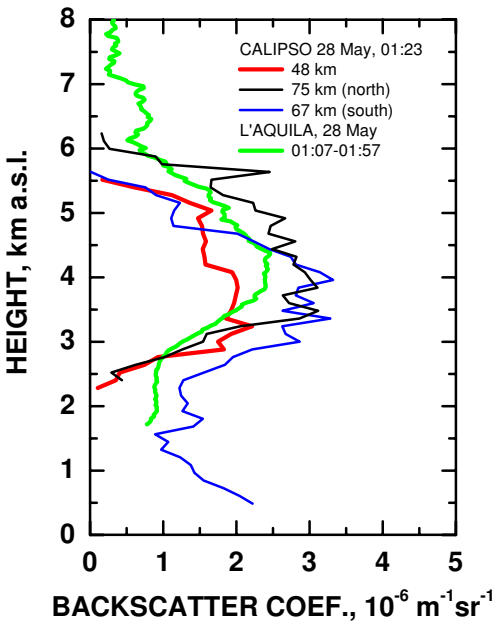

Figure 5.13: Backscatter-coefficient profile (355 nm) taken at L'Aquila EARLINET station during the CALIPSO night-time overpass on 28 May 2008 and corresponding backscatter-coefficient profiles (532 nm) derived from CALIPSO measurements (Version 2) in the vicinity of L'Aquila.

polar ice clouds instead of dust. Both features cause very similar signatures (*Liu et al.*, 2009). Measurements at Leipzig between 9 and 15 UT did not show any clouds, and during the 24-h observations in Hamburg cirrus clouds above 8 km height were detected only. The satellite image shown in Fig. 5.16 underlines the nearly cloud-free conditions for the CALIPSO overpass (yellow line). The three EARLINET stations are indicated as well (red circles). As a consequence of the classification, only few CALIPSO L2 aerosol data are available for the intercomparison. One profile taken about 130 km to the north of Maisach fits quite well to the gro und-based measurement at this site (see Fig. 5.15). It can also be seen that the dust load toward the north, where the misclassification is found, was much higher, as indicated by the Leipzig and Hamburg profiles.

The measurement case has been re-investigated after the release of CALIPSO Version 3 data. As mentioned before, improved aerosol and cloud classification schemes were implemented for the new data release. The CALIPSO Version 3 vertical feature mask together with the cloud and aerosol classification is presented in Fig. 5.17. Some improvements for the lower part of the dust plume can be seen. However, the major part of the dust plume is still identified as an ice cloud, with some water at the base, for the entire cross section north of 50° N.

For the dust period in May 2008, we selected 44 layers from measurements taken at

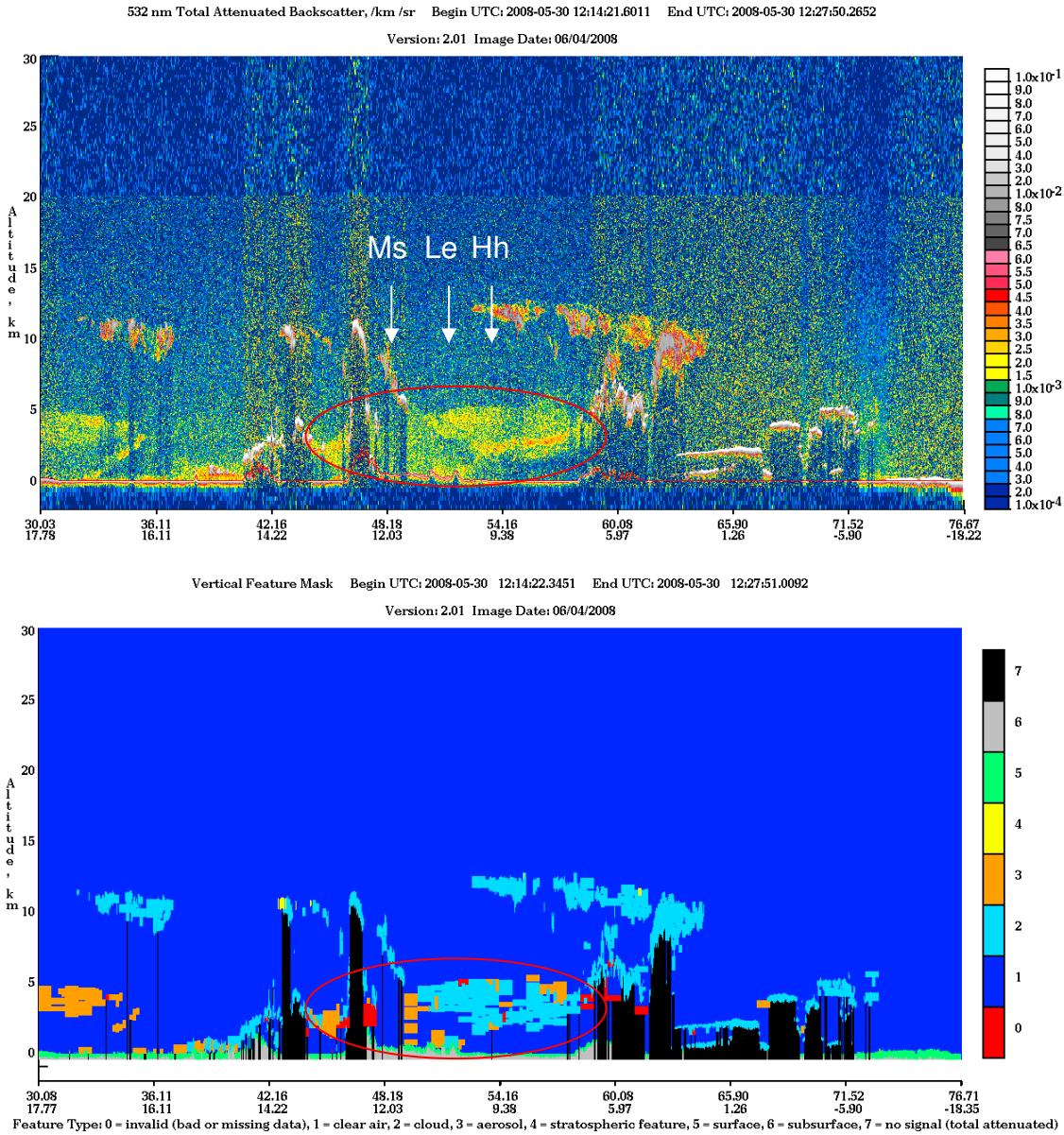

Figure 5.14: CALIPSO cross sections of 532-nm total attenuated backscatter and the vertical feature mask (Version 2 data release) for the overpass at 12.14–12.27 UT on 30 May 2008. The dust plume over Central Europe is encircled and the location of Maisach, Leipzig, and Hamburg EARLINET stations is indicated (figures taken from http://www-calipso.larc.nasa.gov/products/lidar/browse_images/show_calendar.php).

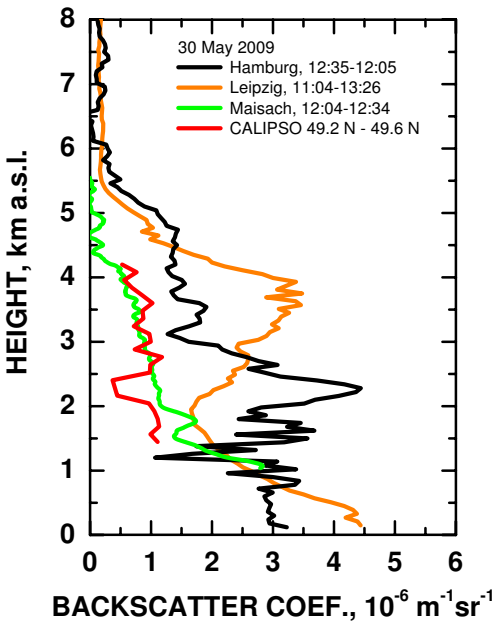

Figure 5.15: Backscatter-coefficient profiles (532 nm) taken at the EARLINET stations Hamburg, Leipzig, and Maisach during the CALIPSO daytime overpass on 30 May 2008 and corresponding backscatter-coefficient profile (532 nm) derived from CALIPSO measurements approximately 130 km to the north of Maisach.

Leipzig (CE), Maisach (CE), Hamburg (CE), L'Aquila (CM), Napoli (CM), Potenza (CM), Athens (EM), Thessaloniki (EM), Sofia (EM), Belsk, and Minsk. These layers were identified either as pure Saharan dust or mixtures of dust with other aerosol types. From the layer-mean data, mean optical parameters were calculated for each station. Table 5.1 summarizes the results of the statistical analysis for pure dust. We obtained typical lidar ratios of pure dust of 59 ± 13 sr and 57 ± 5 sr at 355 and 532 nm, respectively. The extinction-related and backscatter-related Ångström exponent were of the order of 0.26–0.34, which corresponds to color ratios of 0.84–0.92. The values are in very good agreement with previous findings at EARLINET stations and with measurements in the Sahara during SAMUM–1 (see Chapter 3). Again, the discrepancy to the lidar ratio used in the CALIPSO retrievals is noted.

5.1.2.3 Influence of multiple scattering on dust observations from space

In order to investigate the reasons of the discrepancies obtained between the CALIPSO dust model and the ground-based observations from EARLINET and SAMUM we have performed additional comparisons and theoretical studies. In a first step, we focussed on observations performed in pure dust in the Saharan dust plume over Southern Morocco and Cape Verde, because we have detailed airborne *in situ* measurements together with

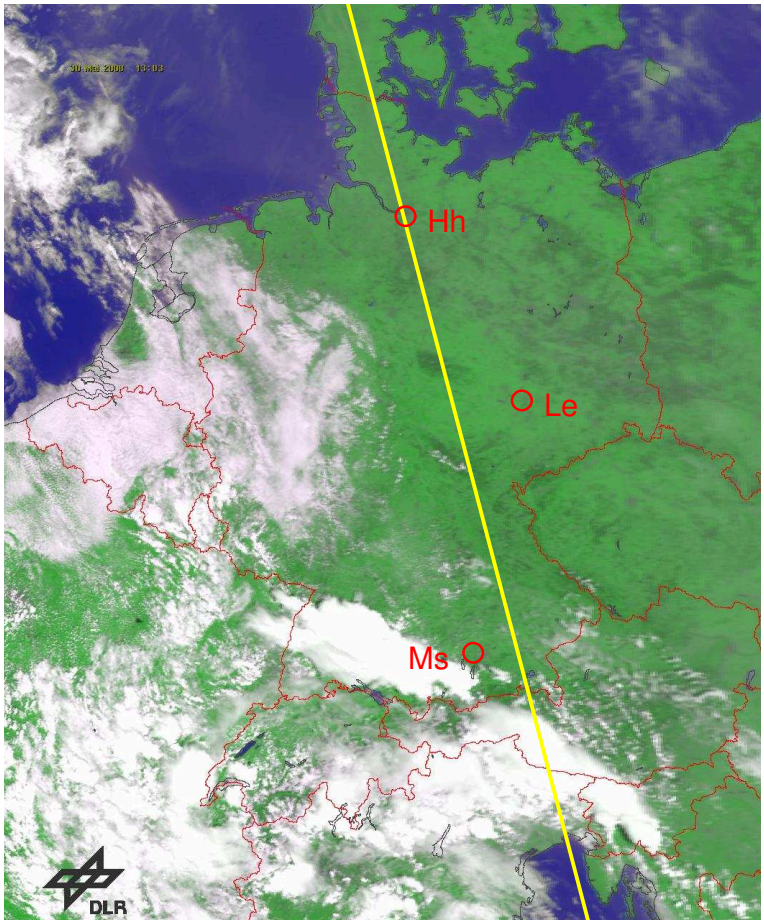

Figure 5.16: Satellite image of Germany at 13.08 UT on 30 May 2008 (taken from http://imkhp2.physik.uni-karlsruhe.de/m̃uehr/satpicsf/noaa/Central_Europe/2008/). The CALIPSO track for the overpass at 12.14–12.27 UT is indicated with a yellow line. The red circles show the location of the EARLINET stations of Hamburg (Hh), Leipzig (Le), and Maisach (Ms).

lidar observations from the SAMUM campaigns. The *in situ* measurements over Southern Morocco revealed effective particle radii between 1.2 and 6.8 μm (*Weinzierl et al.*, 2009). It could be shown that this particle size leads to a considerable influence of multiple scattering on the spaceborne observations. Atmospheric attenuation is reduced by 10%–40% in optically dense dust plumes. In the CALIPSO retrieval of backscatter coefficients, the atmospheric attenuation is corrected with the help of *a priori* lidar ratios from the look-up table. It was found, that the value of 40 sr used for dust represents an effective value that accounts well for the reduced attenuation caused by multiple scattering. Therefore, CALIPSO backscatter retrievals work well and comparisons with ground-based observations show good agreement. In contrast, if extinction values are calculated by multiplying the backscatter values with the effective lidar ratio, a systematic underestimation of extinction, and thus optical depth, by 10%–40% is caused. This could be avoided, if a true

Table 5.1: Mean properties of Saharan dust derived from observations at seven EARLINET stations in May 2008.

Parameter	Mean value and standard deviation
Lidar ratio at 355 nm	59±13
Lidar ratio at 532 nm	57±5
Extinction-related Ångström exponent (532 nm/355nm)	0.34±0.4
Backscatter-related Ångström exponent (532 nm/355nm)	0.26±0.38
Backscatter-related Ångström exponent (1064 nm/532nm)	0.32±0.47
Extinction-related color ratio (532 nm/355nm)	0.89±0.13
Backscatter-related color ratio (532 nm/355nm)	0.92±0.17
Backscatter-related color ratio (1064 nm/532nm)	0.84±0.21

mean lidar ratio of 55 sr would be used for the extinction calculation. Details of the study can be found in the paper by *Wandinger et al.* (2010).

Differences between extinction coefficients derived from CALIPSO observations and measured by EARLINET stations are frequently observed for Saharan dust. An example of a measurement taken at Granada on 5 July 2008 is presented in Fig. 5.18. Dust was observed in different layers up to about 6 km height. The lidar ratio measured from ground is again larger than the CALIPSO *a priori* value, especially in the layer between 4.2 and 5.2 km height, that could be traced back to the Western Sahara. The difference of the extinction coefficients in this layer is 20% larger than the difference of the backscatter coefficients. As explained in the next section, dust over Europe is often mixed with other aerosols. To what extent multiple-scattering effects are modified by the mixing remains to be investigated.

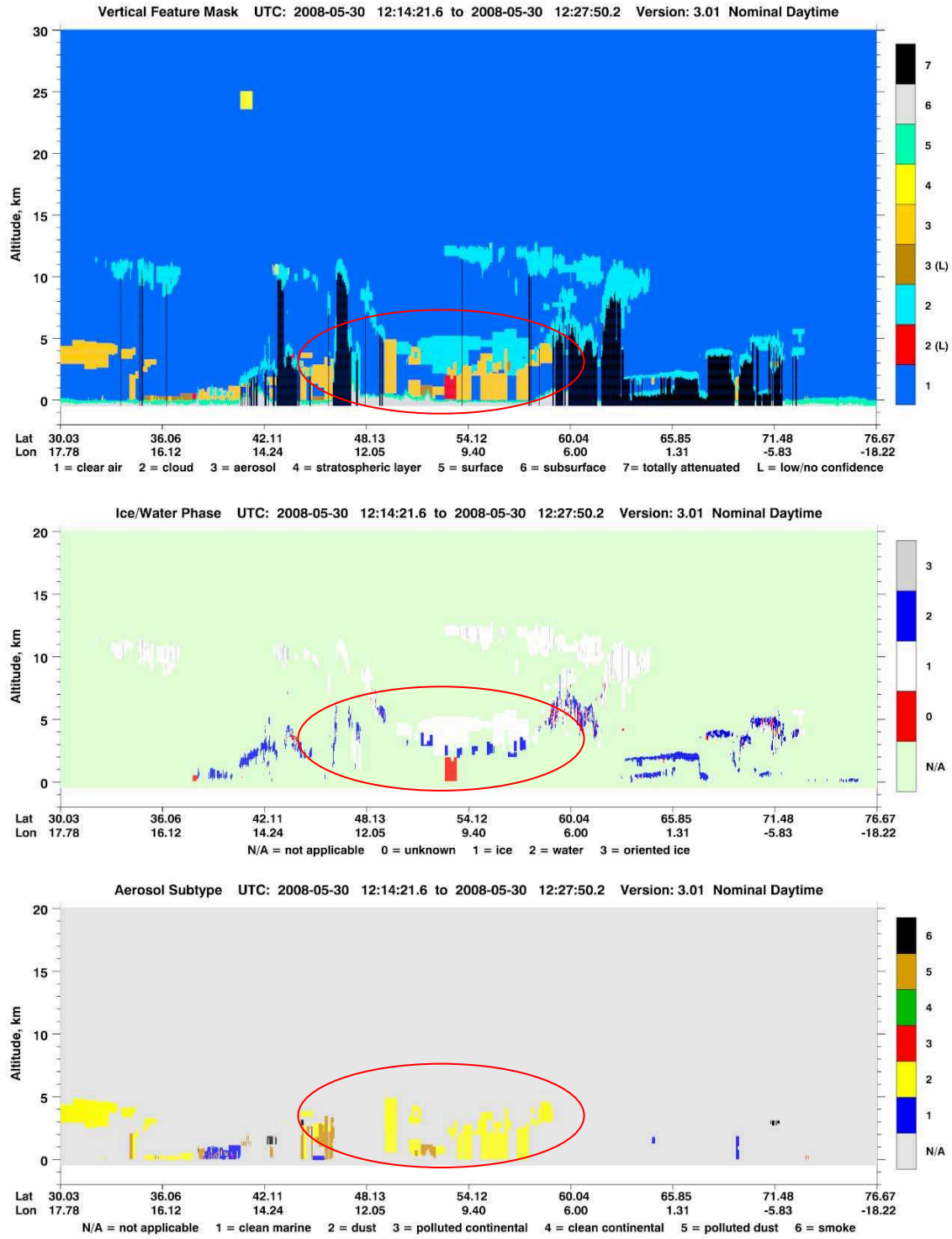

Figure 5.17: CALIPSO vertical feature mask, cloud type, and aerosol type (Version 3 data release) for the overpass at 12.14–12.27 UT on 30 May 2008. The dust plume over Central Europe is encircled (figures taken from http://www-calipso.larc.nasa.gov/products/lidar/browse_images/show_calendar.php).

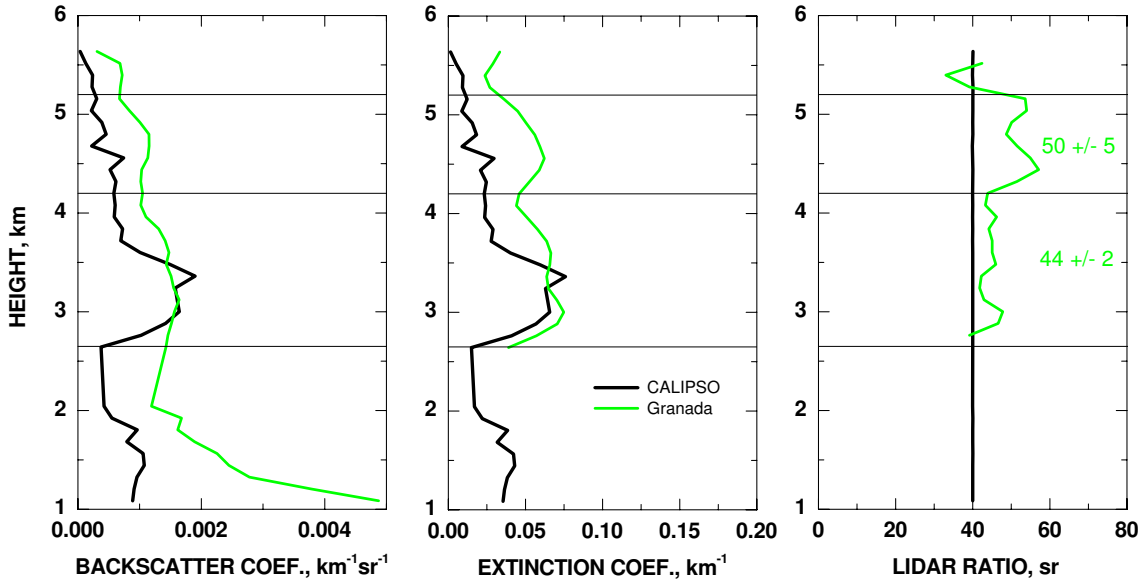

Figure 5.18: Backscatter coefficient, extinction coefficient, and lidar ratio at 532 nm measured at Granada on 5 July 2008, 02.17–02.47 UT, and taken from CALIPSO Version 2 data for the overpass at 02.27 UT. Two dust layers are indicated by horizontal lines.

5.1.3 Polluted continental aerosol

5.1.3.1 Anthropogenic source regions in Europe

Polluted continental aerosol obtained with EARLINET is mainly related to the emission of particulate matter and aerosol precursor gases in different European source regions. Fig. 5.19 shows emission maps of CO, SO_x, $PM_{2.5}$ (particle mass for particle diameter <2.5 μm), and PM_{coarse} (coarse particle mass) for the year 2005 as provided by EMEP (Co-operative Programme for Monitoring and Evaluation of the Long-range Transmission of Air Pollutants in Europe, see http://www.ceip.at). The EMEP emission inventory can be linked with the FLEXPART model in order to study the transport of polluted air from specific source regions to the EARLINET observational sites.

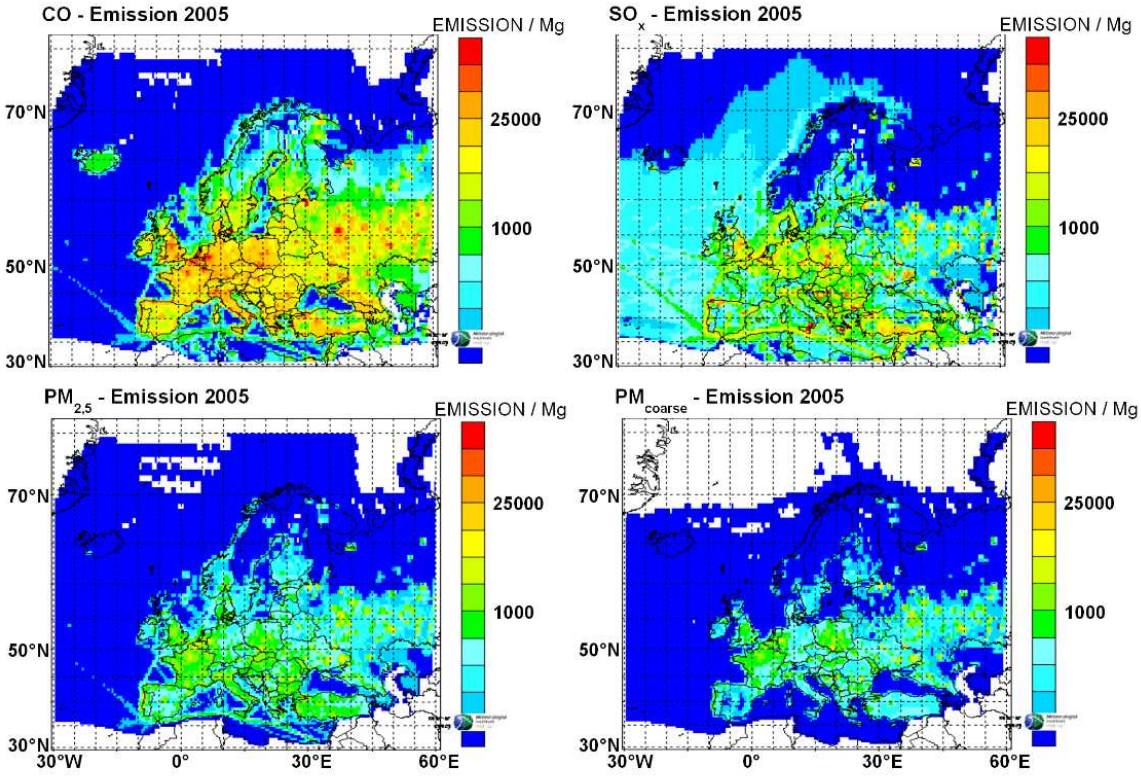

Figure 5.19: European emissions of CO, SO_x, $PM_{2.5}$, and PM_{coarse} for the year 2005 as provided by EMEP.

Based on the EMEP emission inventory and on the distribution of EARLINET stations within Europe, we propose to distinguish European source regions according to Fig. 5.20 as follows:

- Central Europe (mainly including Germany, BeNeLux, Eastern France, Czechia, Slovakia, northern parts of Switzerland, Austria, and Hungary),

- Northern Europe (mainly including Scandinavia and Northern Russia),
- Eastern Europe (mainly including Russia, Ukraine, Belarus, the Baltic States, and Eastern Poland),
- Western Europe (mainly including Great Britain and Western France),
- Southwestern Europe (mainly including Spain and Portugal),
- Southern Europe (mainly including Italy and the surrounding islands, southern parts of Switzerland),
- Southeastern Europe (mainly including the Balkans, Greece, and Turkey).

In this way, local pollution in Central, Eastern, Southeastern, Southern, and Southwestern Europe can be directly related to the respective EARLINET measurement stations and clusters (see Chapter 2). In addition to the areas defined in Fig. 5.20, extra-European

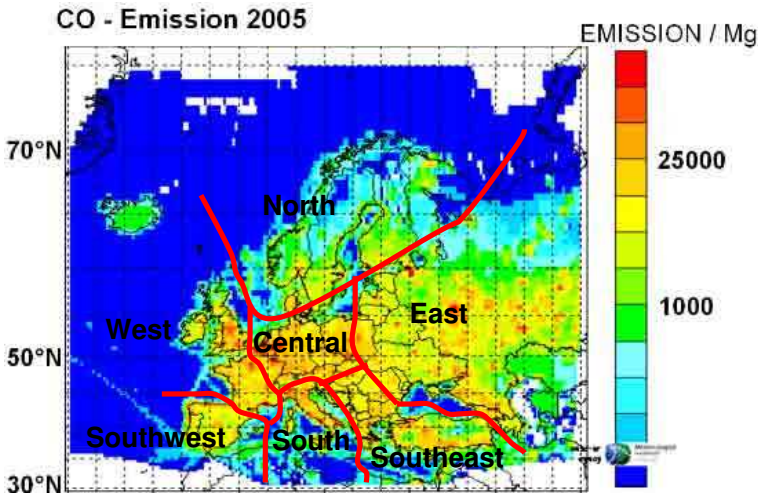

Figure 5.20: Definition of European source regions for polluted continental aerosol. The boundaries are overlayed on the EMEP emission map of CO in 2005.

source regions are considered, because polluted continental aerosols can also be transported in lofted layers from outside toward Europe. In particular, EARLINET has observed anthropogenic pollution from North America and arctic haze in the past.

5.1.3.2 Case study: Cabauw, 13 May 2008

Figure 5.21 shows profiles obtained at Cabauw on 13 May 2008. This measurement was taken a couple of days before the big dust event described in the previous section. High

aerosol load up to 3.5 km can be seen. Large Ångström exponents and lidar ratios, particularly in the uppermost layer, indicate the presence of small particles. Ångströms exponents of 1.4–1.6 and lidar ratios of 68–70 sr were found in the aerosol layer between 2.5 and 3.2 km height.

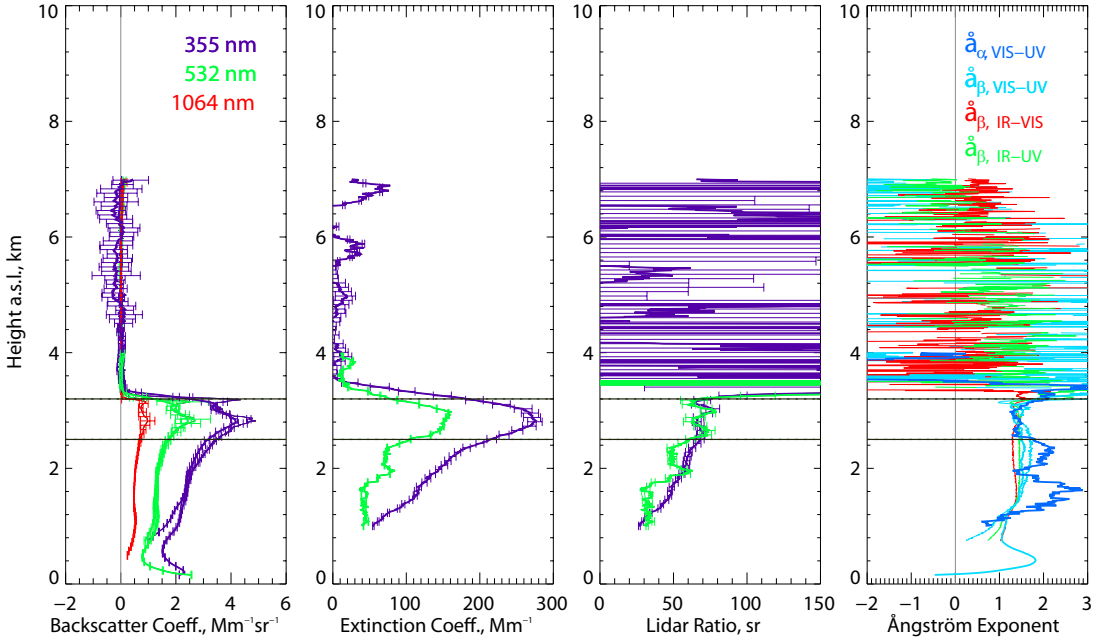

Figure 5.21: Profiles of backscatter and extinction coefficients, lidar ratios, and Ångström exponents from the measurement taken at Cabauw on 13 May 2008, 00.01-01.23 UT. Aerosol is observed up to 3.5 km. Data above are corrupted by noise.

Figure 5.22 shows FLEXPART transport simulation results for airmasses arriving at Cabauw betweeen 2.5 and 3.2 km at 01.23 UT on 13 May 2008. Again, only air parcels that touched the height range below 2000 m within the last 10 days are considered. The footprint shows that the airmass circled above Northern and Central Europe for a longer time and thus could take up pollution over industrialized areas.

5.1.4 Continental background aerosol

5.1.4.1 Definition of continental background aerosol

An aerosol layer is defined as continental background aerosol when the aerosol load (optical depth, mean backscatter coefficient) is low compared with the average aerosol load at the observing station. Continental background aerosols are normally observed when particulate pollution has been removed from the atmosphere through precipitation events or when clean airmasses arrive from remote, less-polluted areas, e.g., from Northern or

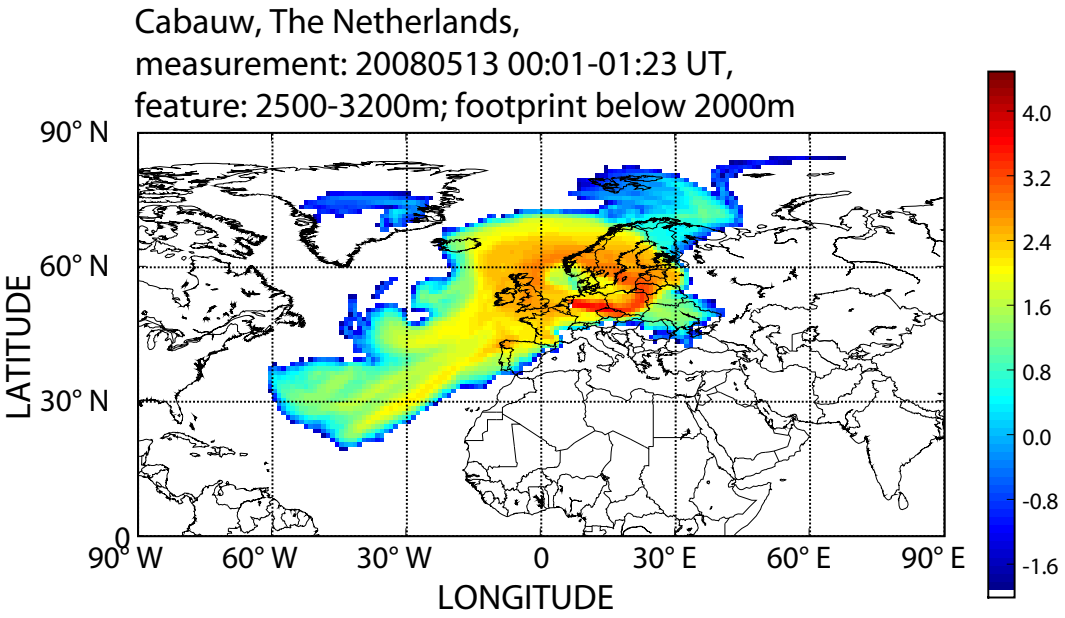

Figure 5.22: FLEXPART footprint for airmasses traveling below 2000 m height and arriving at Cabauw between 2500 and 3200 m height at 01.23 UT on 13 May 2008. The colors represent the logarithm of the integrated residence time in a grid box in seconds for 10-day integration time.

Northeastern Europe. Typically, no specific sources can be related to such aerosol layers. Nevertheless, the advection scheme indicated by the FLEXPART simulation is recorded in the database following the aerosol source regions defined for polluted continental aerosol.

5.1.4.2 Case study: Minsk, 27 May 2008

An example for continental background conditions is presented in Fig. 5.23. The CALIPSO Case A observation was performed at Minsk on 27 May 2008. At Minsk, the period from May 26 to 31 was characterized by low optical depths of <0.15 in the visible wavelength range as can be seen from respective AERONET observations (see http://aeronet.gsfc.nasa.gov). Minsk was only marginally influenced by the Saharan dust outbreak of this period described above. 532-nm backscatter coefficients were ≤ 1 Mm^{-1}sr^{-1} in the well developed planetary boundary layer up to about 2.4 km height and <0.3 Mm^{-1}sr^{-1} above.

Figure 5.24 shows the FLEXPART transport simulation results for airmasses arriving at Minsk betweeen 1050 and 2400 m at 00.58 UT on 27 May 2008. Again, only air parcels that traveled in height ranges below 2000 m within the last 10 days are considered. The footprint clearly shows the advection of airmasses from areas in Northern and Eastern Europe with low emissions of particulate matter and aerosol precursor gases (see also

Fig. 5.19).

5.1.5 Biomass-burning aerosol (smoke)

5.1.5.1 Smoke source regions

Europe is influenced by different smoke sources. As explained in Chapter 3, long-range transported aerosol from boreal forest fires in North America and Siberia can be obtained as well as smoke from local crop-burning fires. Fig. 5.25 shows a selection of 10-day MODIS maps of active fires for the northern hemisphere in the period May 2008 to April 2009. The fire season in northern midlatitudes lasts from March to October. Major fire activity is observed from July–September, especially in the croplands of the Ukraine (north of the Black Sea) and around the Mediterranean. The mediterranean clusters EM and CM are mainly influenced by these fires. In springtime, a fire belt stretches from the Ukraine along Southern Siberia toward the Pacific Ocean. Westerly winds predominate the transport of the smoke, which can thus be obtained over Europe in most cases only after several days of transport via the Pacific, North America, and the Atlantic. Boreal forest fires in the Northern US and Canada are mainly active in the summer months and often cause free-tropospheric aerosol layers arriving with westerly winds over Europe as well.

In accordance with the MODIS maps of active fires, we distinguish between European and extra-European smoke sources and define the major source regions as follows.

Extra-European smoke source regions:

- North America,
- Siberia,
- North Africa (especially the coast line along the Mediterranean Sea).

European smoke source regions:

- Eastern Europe (especially the Ukraine and the surrounding area north of Black Sea),
- Southeastern Europe (especially the Balkans, including Greece),
- Southern Europe (especially Southern Italy),
- Southwestern Europe (Iberian Peninsula),
- Remaining parts of Europe (Central and Northern Europe).

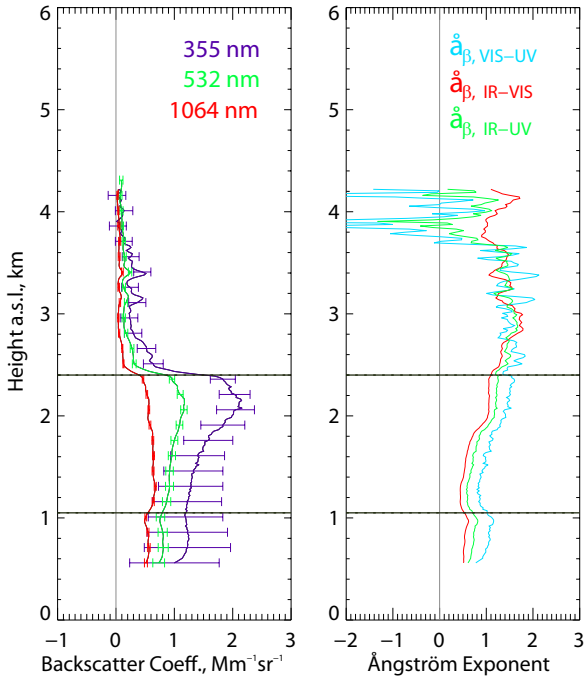

Figure 5.23: Backscatter coefficients (left) and corresponding Ångström exponents (right) obtained at Minsk from 00.24–00.58 UT on 27 May 2008.

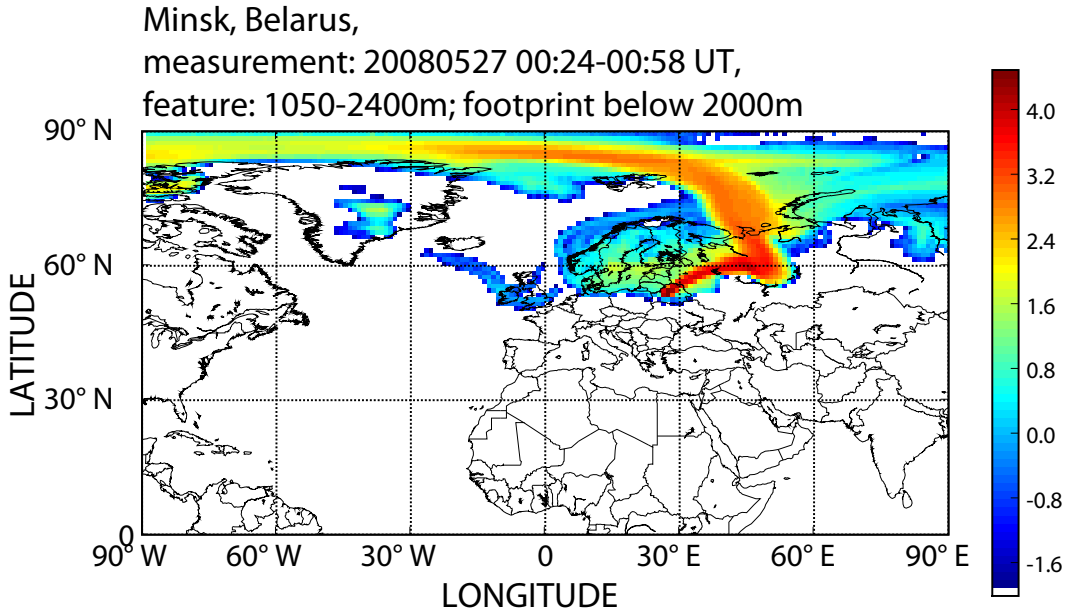

Figure 5.24: FLEXPART footprint for airmasses traveling below 2000 m height and arriving at Minsk between 1050 and 2400 m height at 00.58 UT on 27 May 2008. The colors represent the logarithm of the integrated residence time in a grid box in seconds for 10-day integration time.

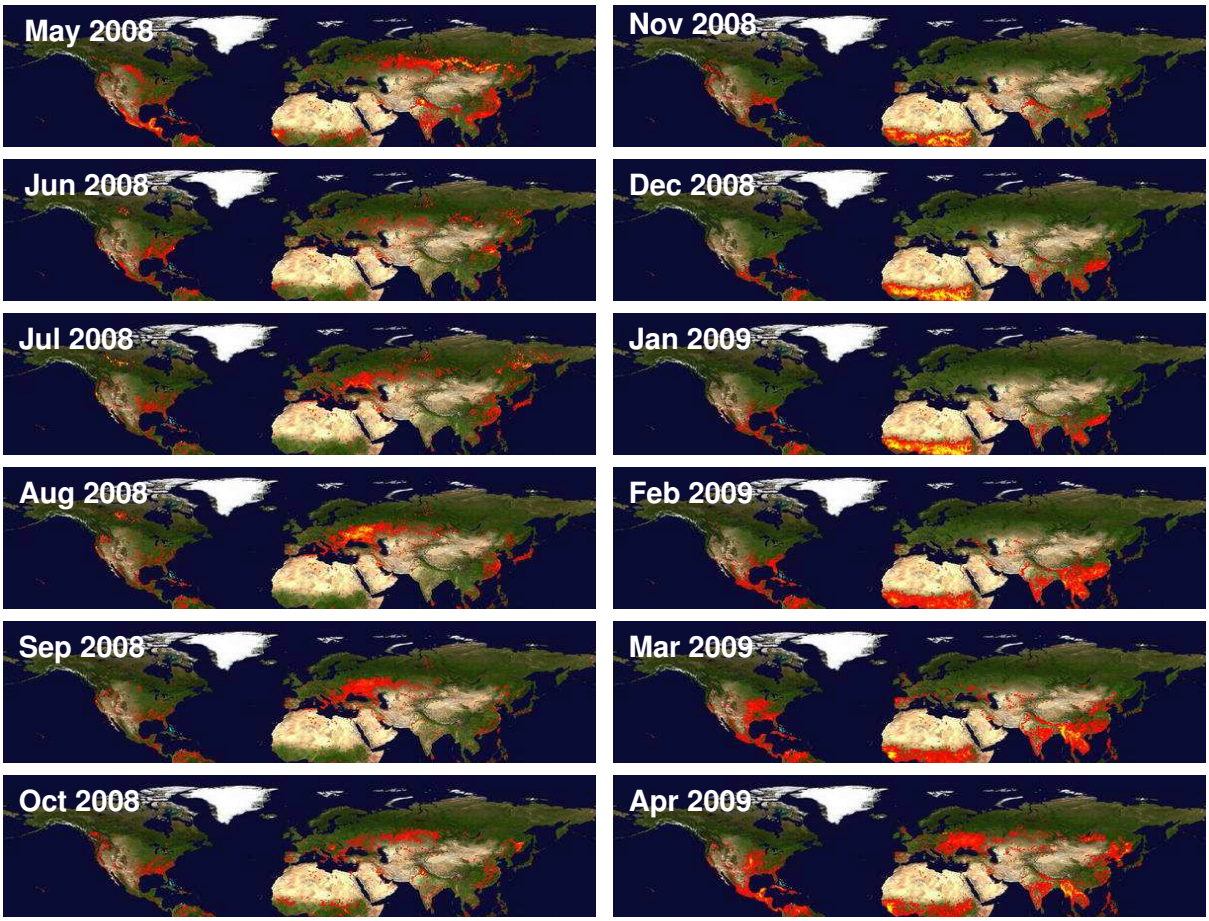

Figure 5.25: Selection of 10-day MODIS maps of active fires (red and yellow dots) for the northern hemisphere in the period May 2008 to April 2009.

5.1.5.2 Case studies

Several periods with fresh biomass-burning smoke layers were observed at the stations of the EM cluster in the summer seasons of 2008 and 2009. In the following, we present the most prominent events measured at Athens and Thessaloniki. Fig. 5.26 shows the 10-day MODIS maps of active fires for the period of 29 July – 18 August 2008. Several fire sources are visible in the vicinity of the EARLINET stations in Greece, but also in general on the Balkans, north of the Black Sea, and in Southern Italy.

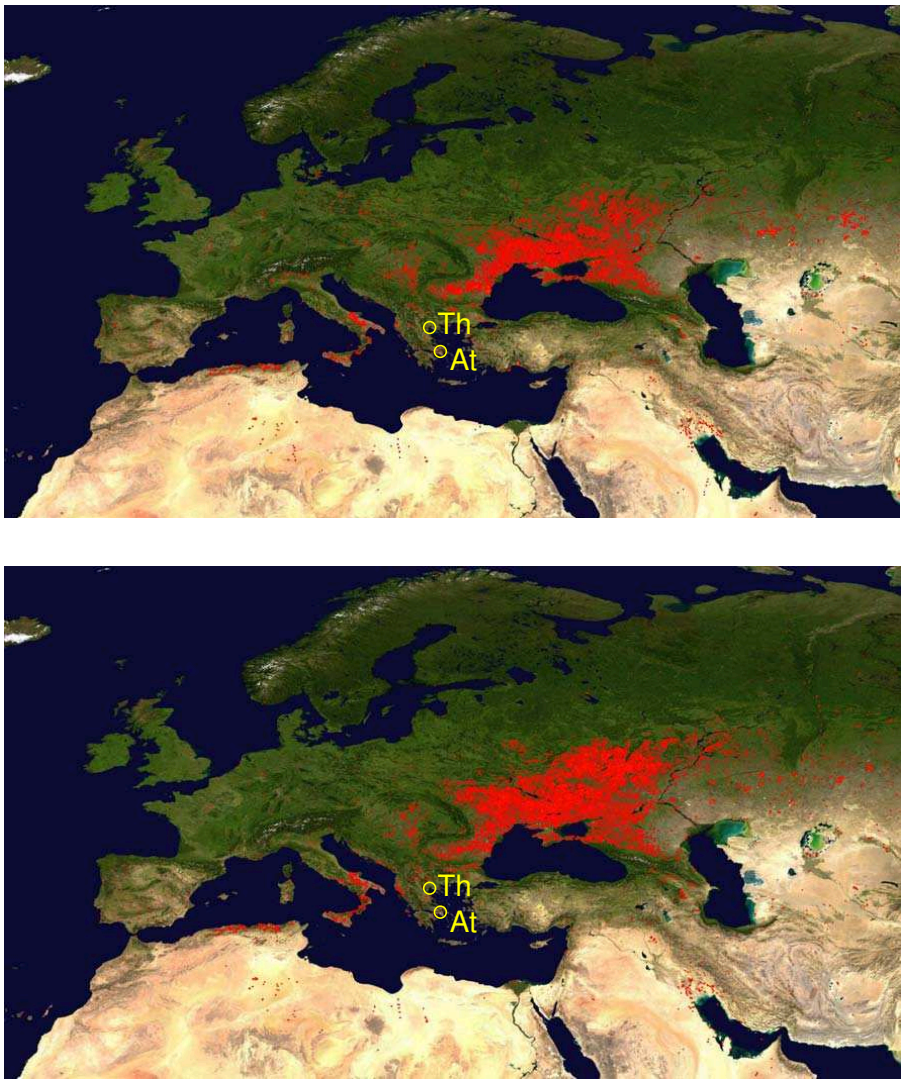

Figure 5.26: MODIS map of active fires (red spots) for the period 29 July – 7 August 2008 (upper panel) and 8–17 August 2008 (lower panel). The EARLINET stations of Athens (At) and Thessaloniki (Th) are indicated.

Thessaloniki, 30 July 2008

The first measurement example is a Case A observation at Thessaloniki on 30 July 2008. Profiles derived for the period 00.58–01.28 UT are shown in Fig. 5.27. A lofted layer with a maximum at 2 km height reaching up to about 3.7 km height was observed. High lidar ratios of 50–80 sr at both 355 and 532 nm and high extinction-related and backscatter-related Ångström exponents of 1.5–2 were determined. Northerly flows dominated over Greece. None of the models indicated dust transport from the Sahara. As the FLEXPART simulations in Fig. 5.28 show the airmass was advected over the regions with high fire activity north and west of the Black Sea toward Thessaloniki at low heights and within 72 hours prior to the measurement.

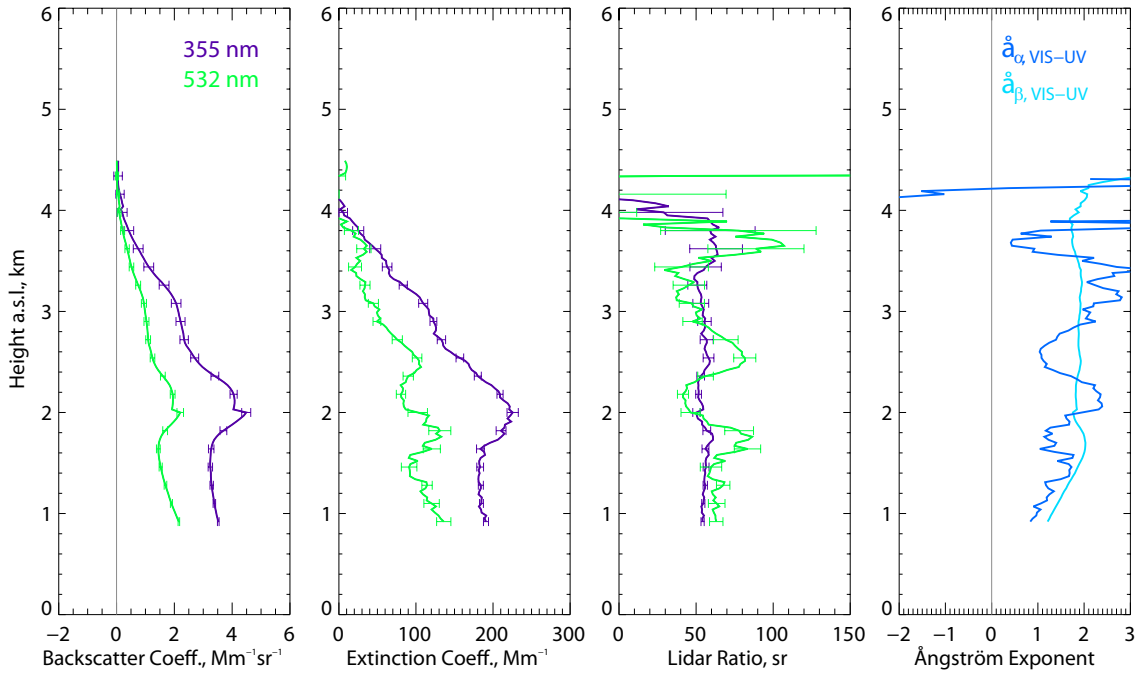

Figure 5.27: Profile data from the measurement taken at Thessaloniki on 30 July 2008, 00.58–01.28 UT.

The corresponding CALIPSO cross sections of the 532-nm attenuated backscatter and the aerosol classification mask are shown in Fig. 5.29. The location of Thessaloniki is indicated. Indeed smoke dominates in the CALIPSO aerosol typing, especially in the upper part of the layer. Dust, polluted dust, and clean marine aerosol are indicated in the vicinity as well. The typing is rather inhomogeneous and reflects the complicated situation commonly found in the Mediterranean.

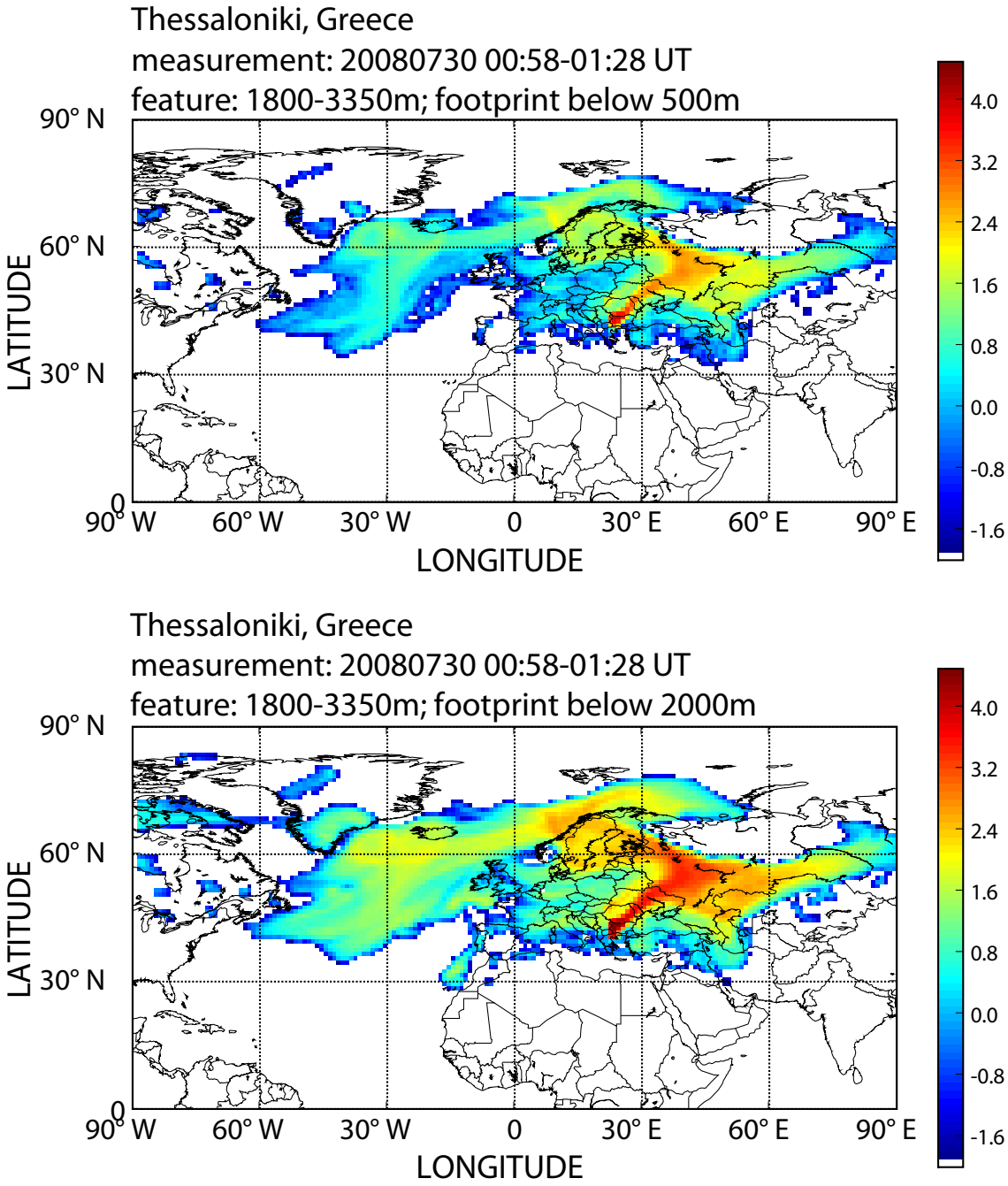

Figure 5.28: FLEXPART footprint for airmasses traveling below 500 m (upper panel) and 2000 m height (lower panel) and arriving at Thessaloniki between 1800 and 3350 m height at 01.28 UT on 30 July 2008. The colors represent the logarithm of the integrated residence time in a grid box in seconds for 10-day integration time.

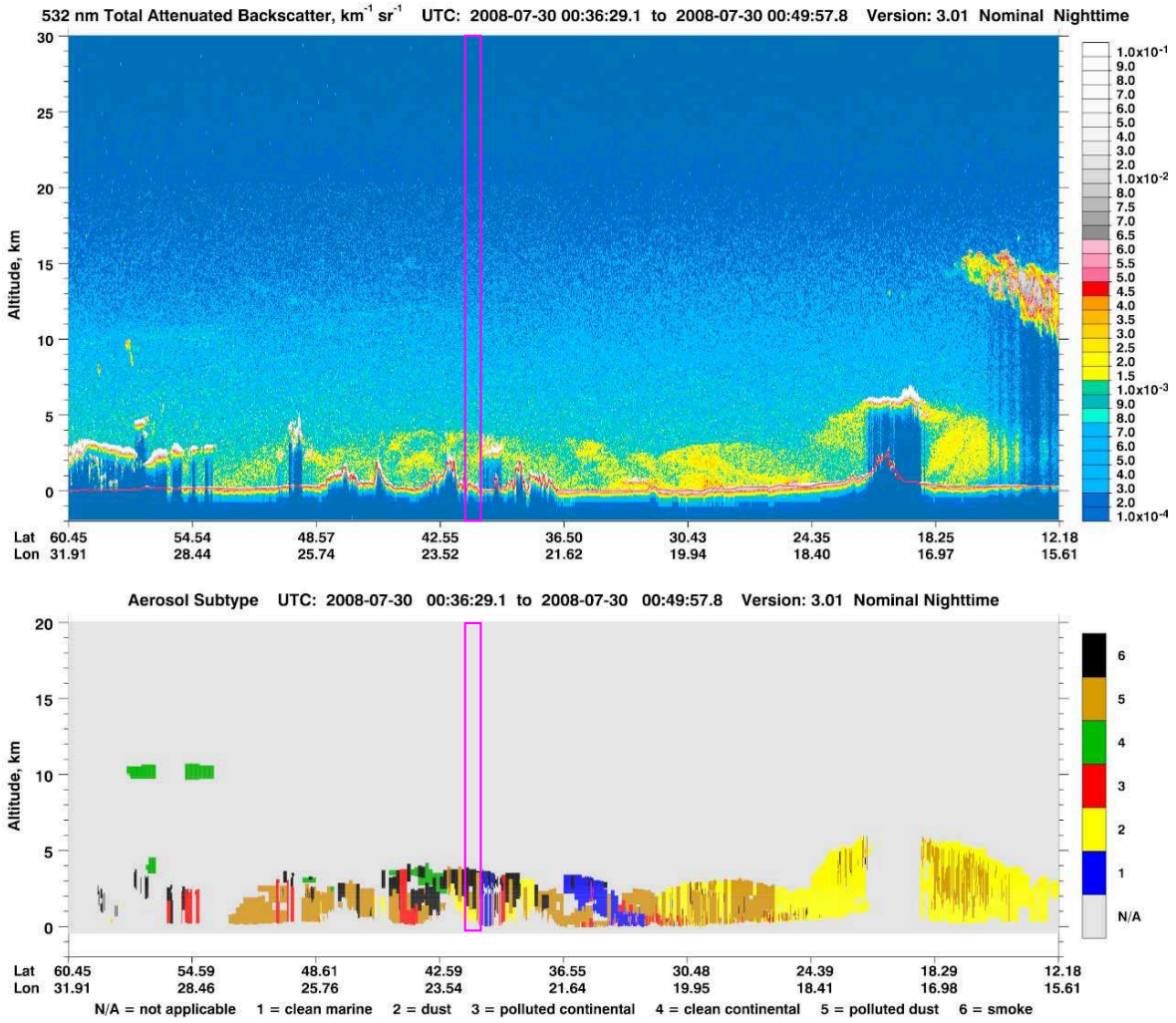

Figure 5.29: CALIPSO cross sections of 532-nm total attenuated backscatter and aerosol classification mask (Version 3 data release) for the overpass at 00.36–00.50 UT on 30 July 2008. The magenta box indicates the location of the corresponding EARLINET observation at Thessaloniki (figures taken from http://www-calipso.larc.nasa.gov/products/lidar/browse_images/show_calendar.php).

Athens, 7–8 August 2008

An example for the observation of smoke in Athens is presented in Fig. 5.30 and 5.31. A long-term lidar observation lasting from 7–9 August 2008 is shown in terms of the time–height contour plot of the range-corrected 1064-nm signal in Fig. 5.30. The diurnal cycle of the local planetary boundary layer is clearly visible below about 2 km height. In addition, an inhomogeneous lofted layer was observed between 2 and 5 km height, which was clearly separated from the PBL most of the time. Profiles derived for the night of 7–8 August 2008, 00.21–00.50 UT, are shown in Fig. 5.31.

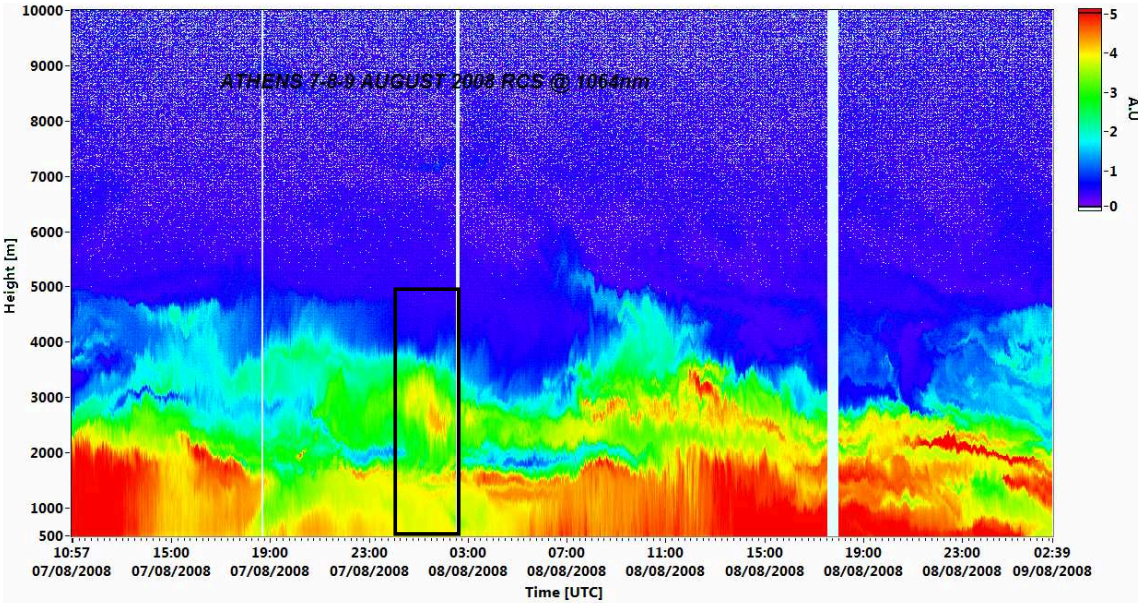

Figure 5.30: Time–height contour plot of the range-corrected 1064-nm signal measured at Athens between 10.57 UT on 7 August and 02.39 UT on 9 August 2008. The black box indicates the period for which profiles were evaluated (see Fig. 5.31).

Fig. 5.32 shows the FLEXPART transport simulation results for airmasses arriving at Athens betweeen 2100 and 3800 m at 00.50 UT on 8 August 2008. Air parcels that touched the height range below 500 and 2000 m within the last 10 days are shown in the upper and lower panels, respectively. The simulations clearly indicate the Balkans and Northern Greece in particular as the major source region of the observed aerosol layer.

The measurement at Athens in this night was a Case A observation. The corresponding CALIPSO cross sections of the 532-nm attenuated backscatter and the aerosol classification mask are shown in Fig. 5.33. The location of Athens is indicated. Smoke in the upper part of the layer and polluted dust in the lower part dominate in the CALIPSO typing near Athens. Clean marine aerosol is indicated in the vicinity as well.

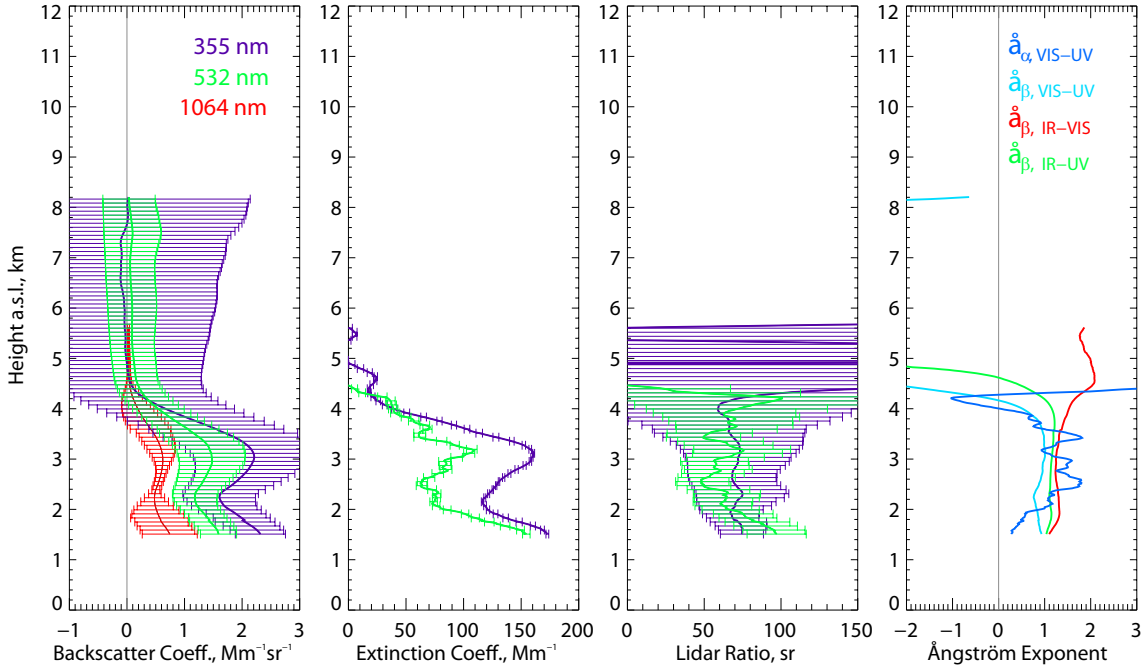

Figure 5.31: Profile data from the measurement taken at Athens on 8 August 2008, 00.21–00.50 UT. The intensive parameters are disturbed by noise above 4 km.

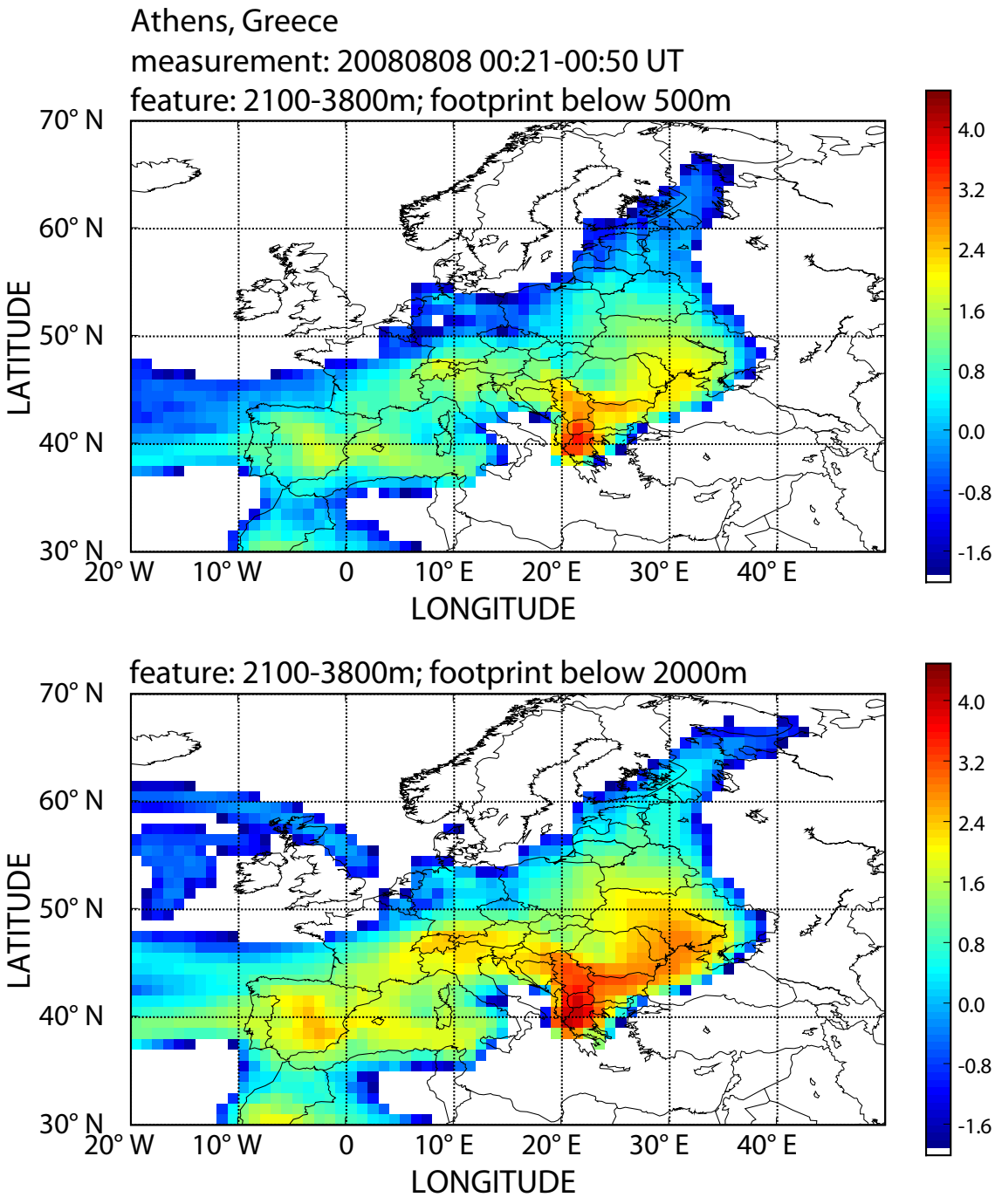

Figure 5.32: FLEXPART footprint for airmasses traveling below 500 m (upper panel) and 2000 m height (lower panel) and arriving at Athens between 2100 and 3800 m height at 00.50 UT on 8 August 2008. The colors represent the logarithm of the integrated residence time in a grid box in seconds for 10-day integration time.

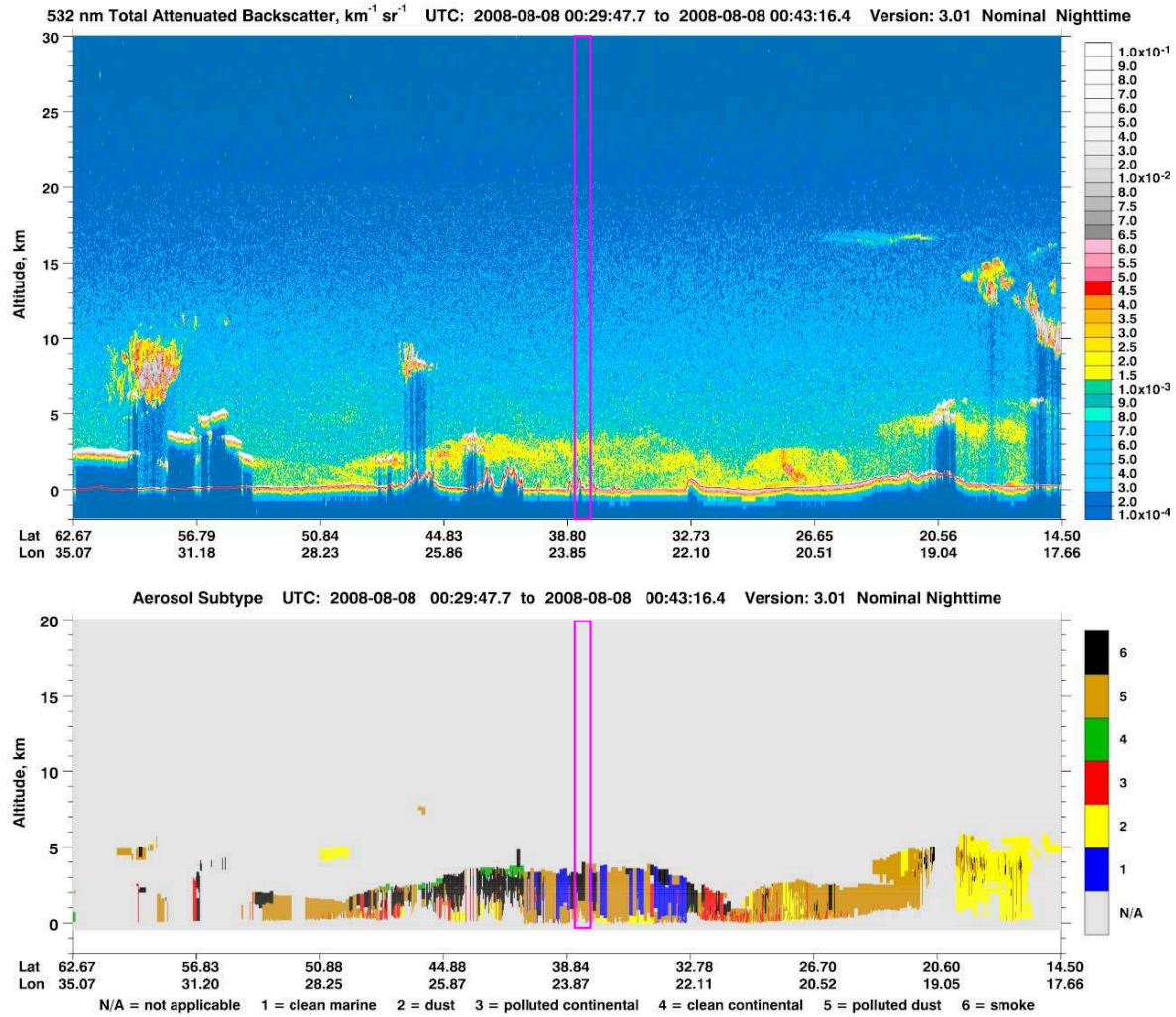

Figure 5.33: CALIPSO cross sections of 532-nm total attenuated backscatter and aerosol classification mask (Version 3 data release) for the overpass at 00.29–00.43 UT on 8 August 2008. The magenta box indicates the location of the corresponding EARLINET observation at Athens (figures taken from http://www-calipso.larc.nasa.gov/products/lidar/browse_images/show_calendar.php).

Thessaloniki, 14–15 August 2008

A further example is again a Case A observation at Thessaloniki. Profiles derived for the period 23.58 UT on 14 August to 00.27 UT on 15 August 2008 are shown in Fig. 5.34. Aerosol layers up to about 3.3 km height were observed. Again high lidar ratios of 50–80 sr at both 355 and 532 nm and high extinction-related and backscatter-related Ångström exponents of about 2 were found. The FLEXPART simulations shown in Fig. 5.35 indicate the advection of airmasses from the Black Sea at all heights.

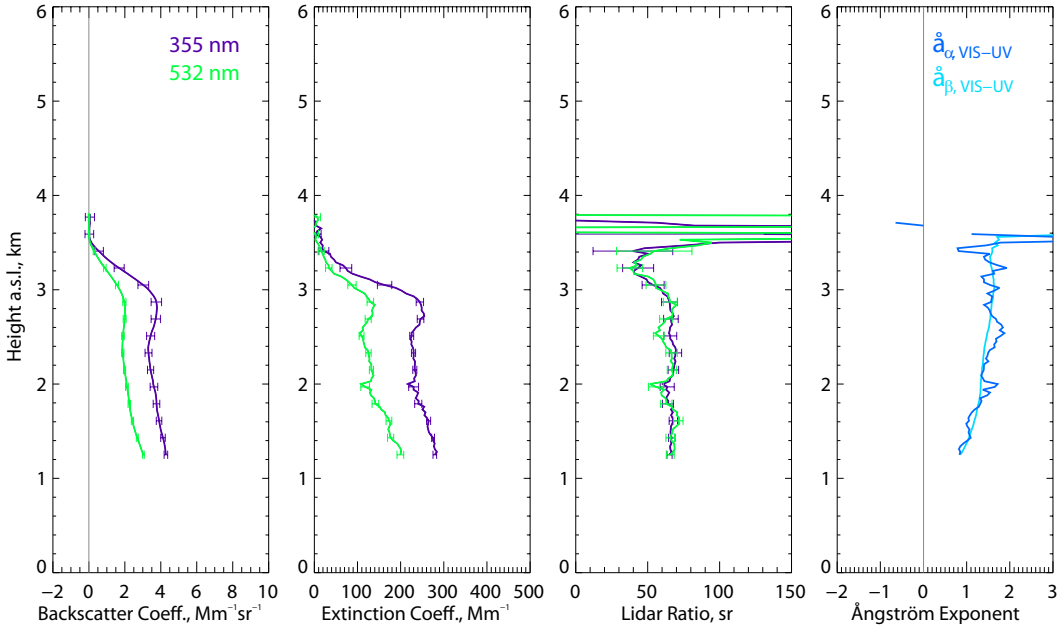

Figure 5.34: Profile data from the measurement taken at Thessaloniki on 14–15 August 2008, 23.58–00.27 UT.

The corresponding CALIPSO cross sections of the 532-nm attenuated backscatter and the aerosol classification mask are shown in Fig. 5.36. The location of Thessaloniki is indicated. Also in this case, smoke is classified together with dust, polluted dust, and clean marine aerosol in a rather inhomogeneous way.

For all smoke cases and CALIPSO comparisons presented in this section, the FLEXPART simulations clearly show that the influence of Saharan dust can be excluded. Nevertheless, CALIPSO classifies large parts of the aerosol in the surrounding of the EARLINET stations as polluted dust. As can be seen from Fig. 3.2 polluted dust is selected over non-desert surfaces when the depolarization ratio is between 0.075 and 0.2. As discussed before, such high depolarization can only be caused by large, non-spherical particles. Presumably, large soil and ash particles which are brought into the atmosphere by the fires are responsible for the high depolarization ratios and the respective classification of the aerosol as polluted dust.

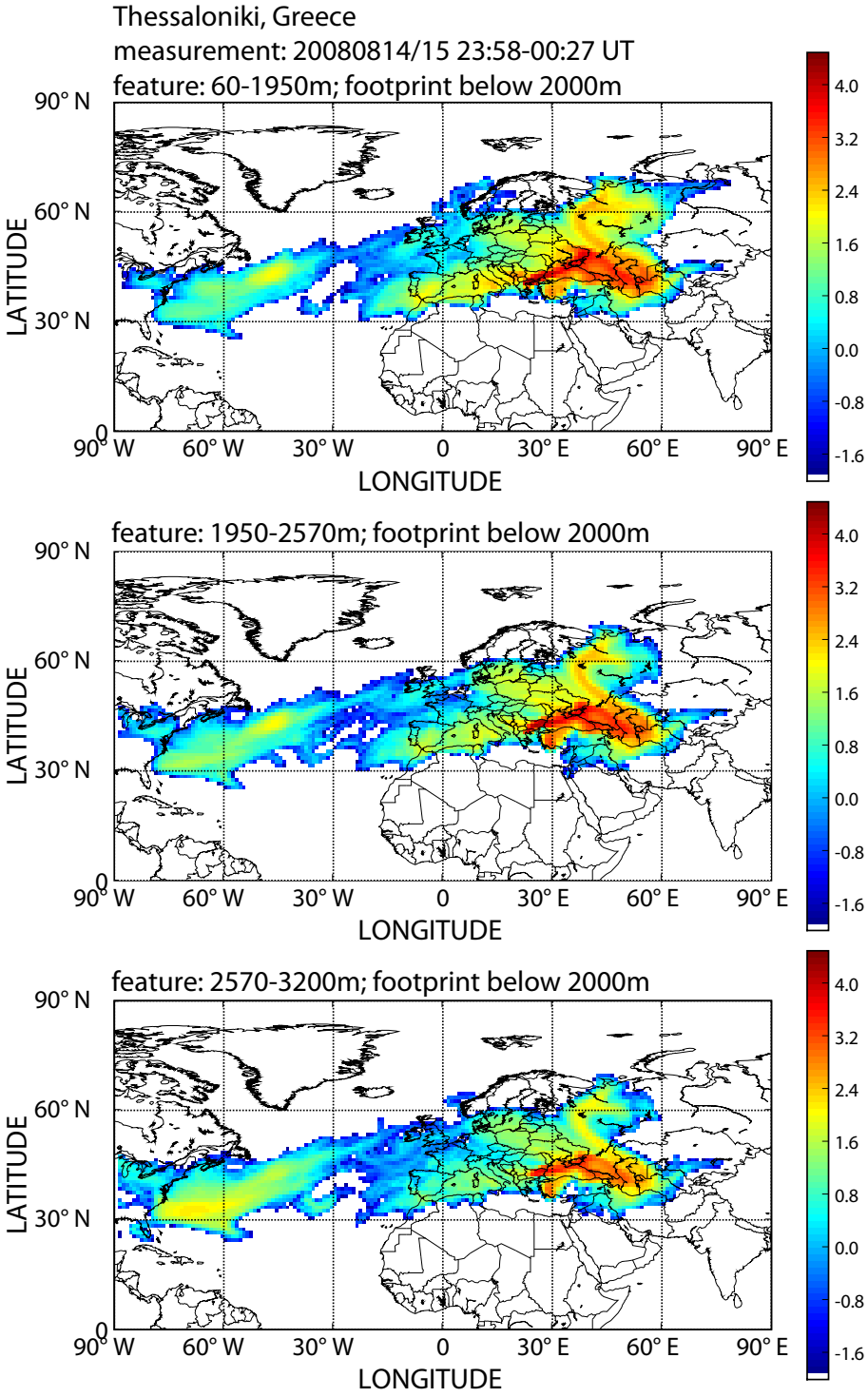

Figure 5.35: FLEXPART footprint for airmasses traveling below 2000 m and arriving at Thessaloniki between 60 and 1950 m (upper panel), 1950 and 2570 m (middle panel), and 2570 and 3200 m (lower panel) at 00.27 UT on 15 August 2008. The colors represent the logarithm of the integrated residence time in a grid box in seconds for 10-day integration time.

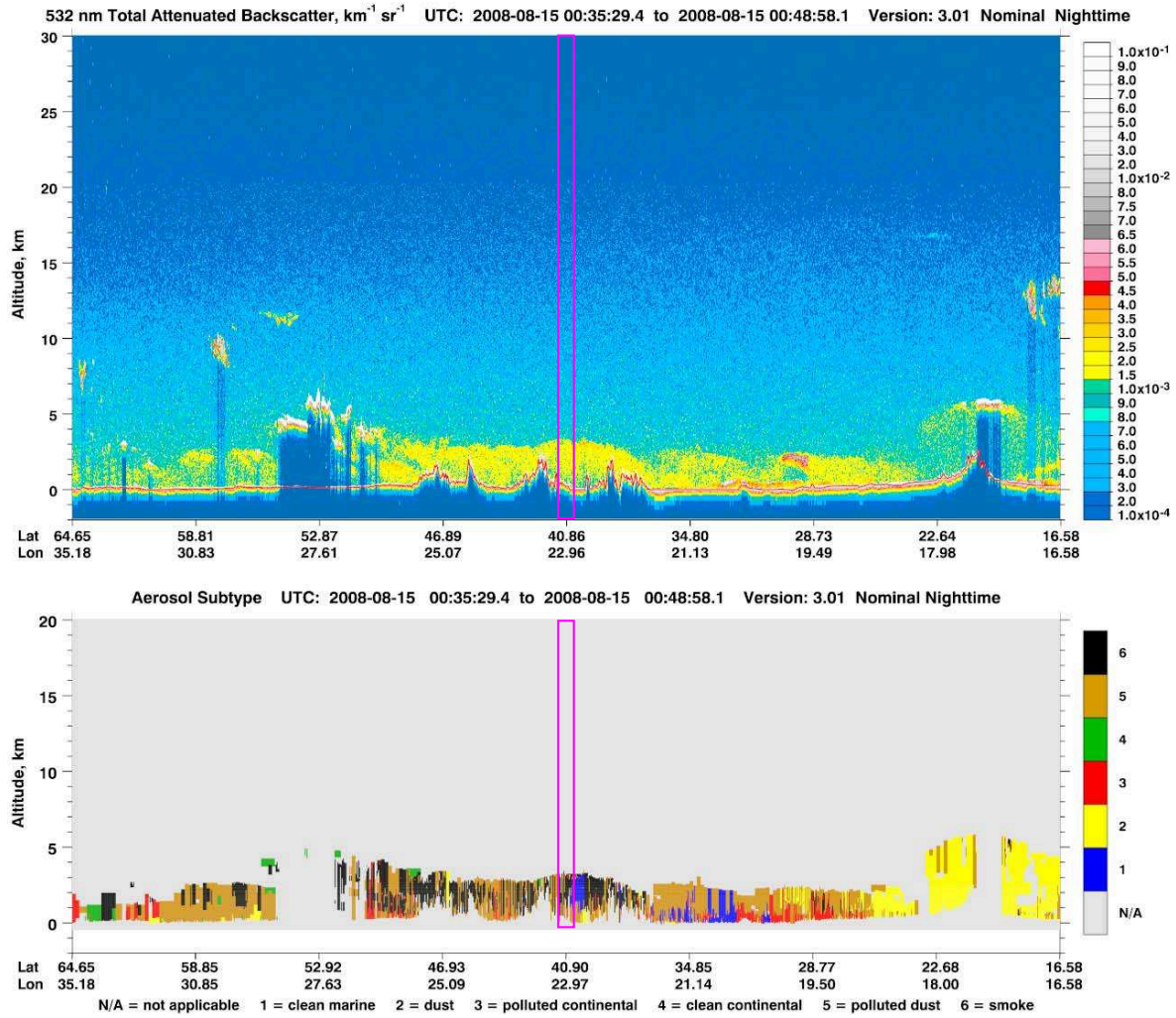

Figure 5.36: CALIPSO cross sections of 532-nm total attenuated backscatter and aerosol classification mask (Version 3 data release) for the overpass at 00.35–00.49 UT on 15 August 2008. The magenta box indicates the location of the corresponding EARLINET observation at Thessaloniki (figures taken from http://www-calipso.larc.nasa.gov/products/lidar/browse_images/show_calendar.php).

Athens, 25 August 2009

As the final example we present an observation from Athens on 25 August 2009. In the summer of 2009, large wild fires occured in the forests around Athens. Fig. 5.37 shows an image from MODIS on Terra taken on 24 August 2009, where a large smoke plume is visible. Fig. 5.38 and 5.39 present the measurement results from the following night in terms of the time-height contour plot of the range-corrected 1064-nm signal and the profiles for the time period from 02.00–03.12 UT. An intense smoke plume arrived in Athens at 3.5 km height around 20 UT. In the course of the night, the plume stretched over a height range from about 1.5 to 4.5 km. Very high lidar ratios of 70–100 sr and Ångström exponents of the order of 1.5 were measured.

Figure 5.37: Terra MODIS image of the Athens area with a large smoke plume taken on 24 August 2009. The location of the EARLINET Athens station (At) is indicated.

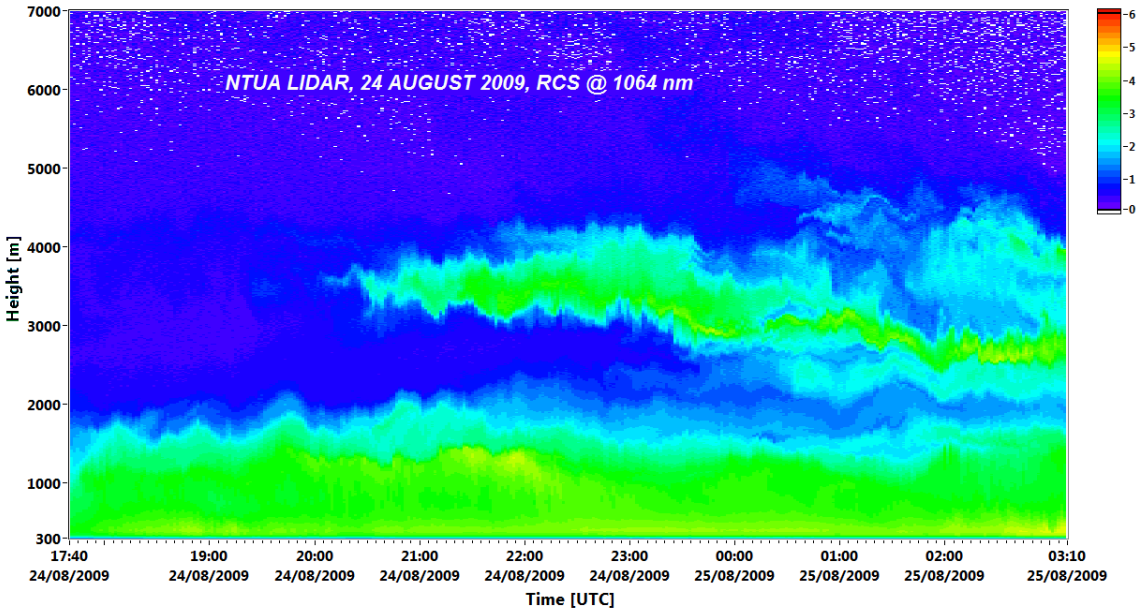

Figure 5.38: Time–height contour plot of the range-corrected 1064-nm signal measured at Athens between 17.40 UT on 24 August and 03.10 UT on 25 August 2009.

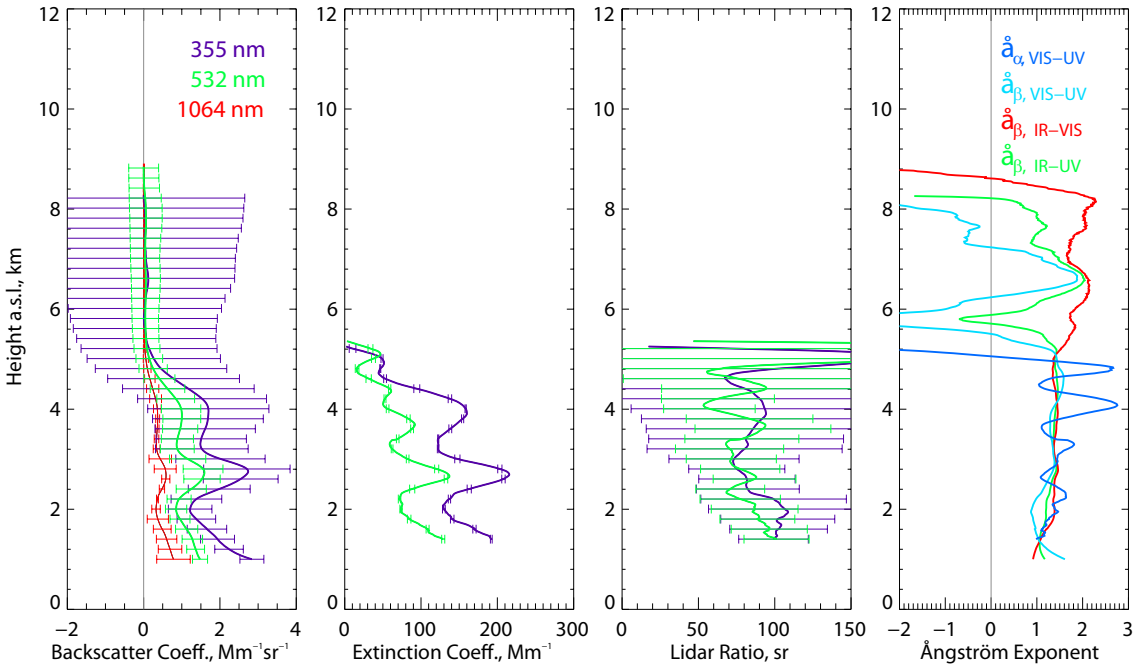

Figure 5.39: Profile data from the measurement taken at Athens on 25 August 2009, 02.00-03.10 UT.

5.1.6 Stratospheric aerosol

5.1.6.1 Sources of stratospheric aerosol

Beginning in July 2008, EARLINET observed increased aerosol load in the upper troposphere and lower stratosphere caused by increased volcanic activity in the North Pacific region. Several major volcanic eruptions occurred between July 2008 and October 2009. Table 5.2 lists the active volcanoes together with the start date of the eruption and the reported height of the ash plume[1]. These volcanoes belong to the so-called Ring of Fire and are located in Alaska, the Aleutian Islands, the Kuril Islands and Kamtchatka as shown in Fig. 5.40.

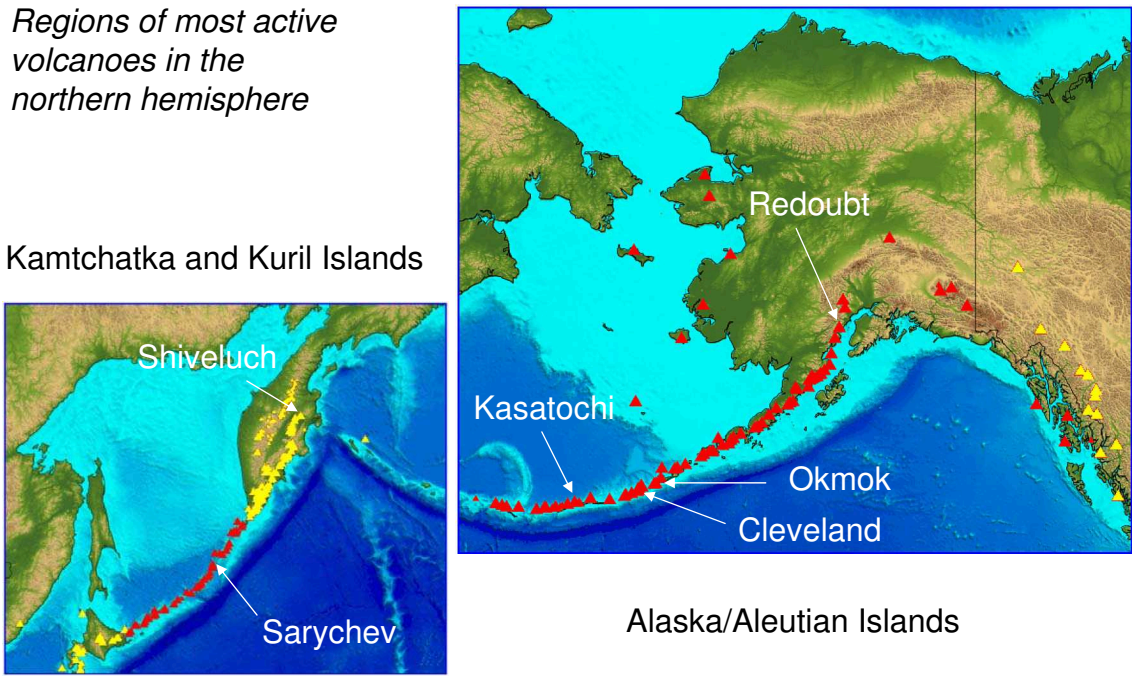

Figure 5.40: Location of eruptive volcanoes active between July 2008 and July 2009 (source: The Smithsonian's Global Volcanism Program, http://www.volcano.si.edu/).

The injection and transport of aerosol layers in the upper troposphere and lower stratosphere from these volcanoes can be seen in CALIPSO browse images of attenuated backscatter. In the following, we show measurement examples taken at Leipzig between July 2008 and December 2009.

[1]The height of the ash plume is an indication of the eruption strength. It should be noted, however, that ash has a relatively short lifetime and usually is not transported over long distances. Volcanic aerosols in the stratosphere and upper troposphere are mainly secondary aerosols which are produced from sulfur-containing precursor gases. During an eruption gases are emitted into larger heights than ash, and volcanic aerosol layers can occur in much larger heights than the reported ash plume.

Table 5.2: Major volcanic eruptions in the northern hemisphere from July 2008 to July 2009 (source: The Smithsonian's Global Volcanism Program, http://www.volcano.si.edu/).

Volcano	Start date of eruptions	Stop date of eruptions	Estimated ash plume height	Coordinates
Okmok	12 Jul 2008	19 Aug 2008	15200 m	53.4 N, 168.1 W
Cleveland	21 Jul 2008	12 Aug 2008	7600 m	52.8 N, 169.9 W
	2 Jan 2009	2 Jan 2009	6000 m	
	2 Oct 2009	2 Oct 2009	6000 m	
Kasatochi	7 Aug 2008	8 Aug 2008	13700 m	52.2 N, 175.5 W
Bezymianny	19 Aug 2008	19 Aug 2008	9000 m	56.0 N, 160.6 W
Shiveluch	13 Sep 2008	22 Jan 2009	8800 m	56.6 N, 161.4 E
	6 Mar 2009	29 Apr 2009	8000 m	
	6 Jun 2009	16 Jul 2009	8100 m	
	10 Sep 2009		15000 m	
Kliuchevskoi	8 Dec 2008	16 Jan 2009	8200 m	56.6 N, 161.4 E
Redoubt	22 Mar 2009	12 Apr 2009	19800 m	60.5 N, 152.7 W
Sarychev	13 Jun 2009	16 Jun 2009	12000 m	48.1 N, 153.2 E

5.1.6.2 Measurement examples

In summer 2008, after the Okmok and Kasatochi eruptions, several EARLINET stations reported increased aerosol load in the tropopause region and the lower stratosphere. A major event could be observed in Leipzig on 21 August 2009. As shown in Fig. 5.41 an aerosol layer between 7 and 12 km was present. Trajectory analysis and transport calculations indicate the arrival of aerosols from the Kasatochi eruption. Signatures between 7.5 and 10 km were strong enough to allow the determination of spectral backscatter and extinction coefficients, lidar ratios, and Ångström exponents. The volume depolarization ratio clearly shows non-depolarizing aerosol particles and proves the absence of ice clouds. In contrast to other aerosol types, the lidar ratio shows a strong wavelength dependence with values around 60 sr in the UV and 30 sr in the visible wavelength range. First attempts to invert microphysical particle properties indicated the presence of very small particles with effective radii around 0.1 μm in the volcanic aerosol layers.

Whereas particles in the troposphere are efficiently removed through cloud and precipation processes, aerosols injected into the stratosphere can stay there for months or even years. Fig. 5.42 shows the comparison of backscatter profiles measured after the Kasatochi eruption at Leipzig in August 2008 and in January 2009. The stratospheric aerosol con-

tribution remained almost constant over this time. The aerosol layer near the tropopause had been observed throughout the year since July 2008. This becomes also visible from Fig. 5.43, where a series of profiles measured between 28 July 2008 and 1 April 2009 is shown. On 1 April 2009 the plume injected by the eruption of Mt. Redoubt arrived at the Leipzig site and caused a sudden increase of aerosol load near the tropopause.

The eruptions of Sarychev Peak in the Kuril Islands, which started on 12 June 2009 and continued throughout June and July 2009, injected new aerosol into the stratosphere. Isolated stratospheric layers between the tropopause and 22 km height were frequently observed by several EARLINET stations in July and August 2009. Fig. 5.44 shows an observation taken at Leipzig on 16 July 2009 with layers at about 12, 15, and 17.5 km height. The very faint layer at 22 km intensified during the day and was clearly visible in the evening measurement on 16 July 2009 (not shown). The respective CALIPSO overpass is presented in Fig. 5.45. The stratospheric layers are visible in the browse image of the 532-nm attenuated backscatter and are partly identified in the CALIPSO vertical feature mask.

Finally, in Fig. 5.46 we present an overview of aerosol observation in the upper troposphere and lower stratosphere (ULTS) during the years 2008–2009. The 532-nm particle optical depth, given at the bottom of Fig. 5.46, is computed from the 1064-nm backscatter coeffcients integrated from the bottom to the top of the identified UTLS aerosol layers. The integrated backscatter coefficients have been converted to 532 nm by assuming a backscatter-related Ångström exponent of 1.05. Finally, multiplication by a factor of 38 sr (lidar ratio) provides a good estimate of the 532-nm particle optical depth. Both conversion factors, 532-nm lidar ratio and 532-nm-to-1064-nm backscatter-related Ångström exponent are mean values of all multiwavelength Raman lidar observations of volcanic layers in the UTLS region in 2008 and 2009.

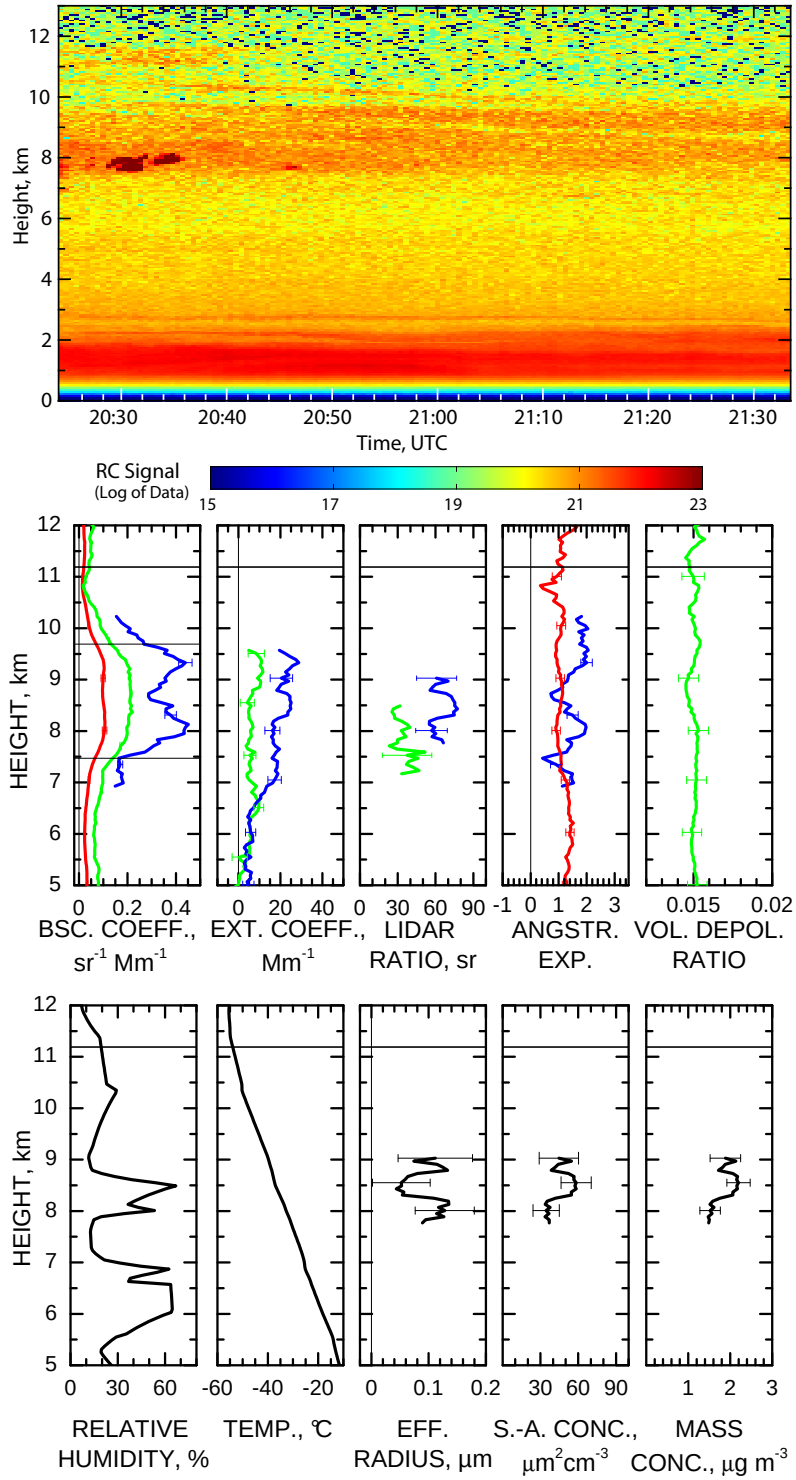

Figure 5.41: Measurement of volcanic aerosol (above 7 km) from the Kasatochi eruption taken at Leipzig on 21 August 2008 (20.27–21.34). The upper panel shows the time–height contour plot of the range-corrected signal at 1064 nm. The middle panels present the lidar profiles and lower panels radiosonde measurements of temperature and humidity and microphysical particle properties inverted from the multiwavelength lidar observations (adapted from *Mattis et al.* (2010)).

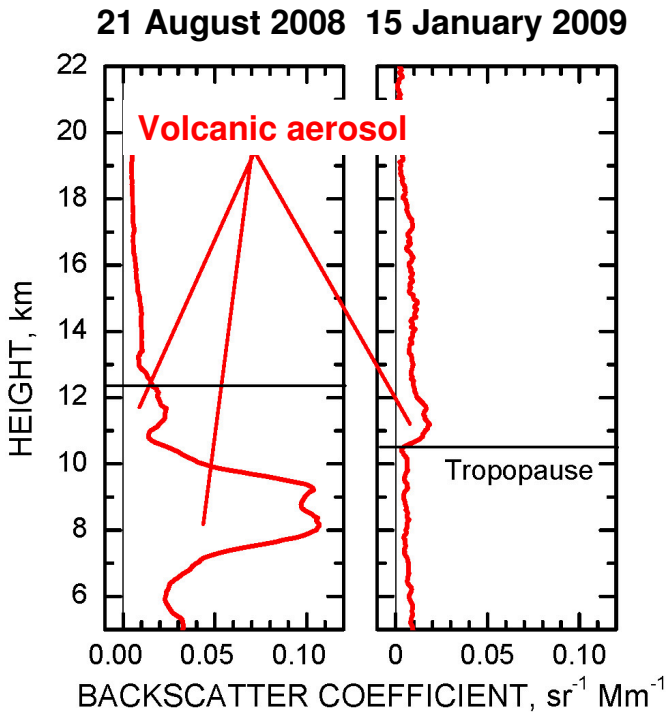

Figure 5.42: Comparison of 1064-nm backscatter profiles measured at Leipzig after the Kasatochi eruption on 21 August 2008 and on 15 January 2009.

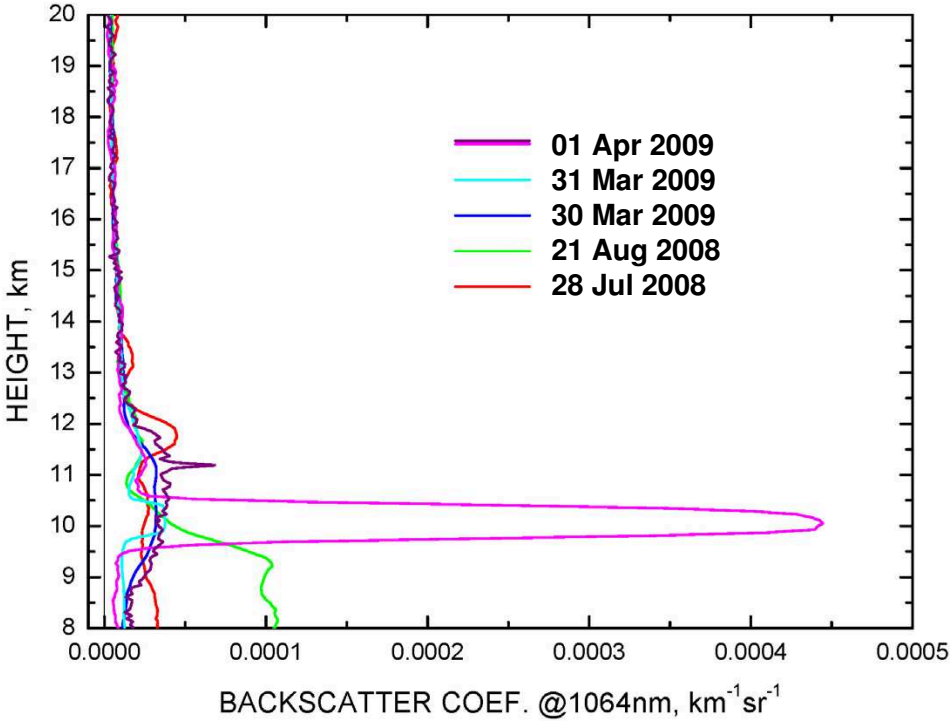

Figure 5.43: 1064-nm backscatter profiles measured at Leipzig between 28 July 2008 and 1 April 2009.

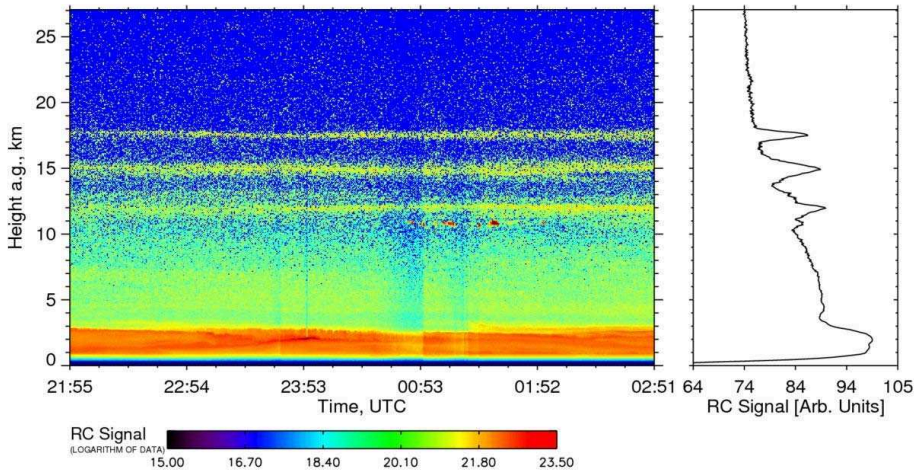

Figure 5.44: Time–height contour plot of the range-corrected 1064-nm signal measured at Leipzig between 21.55 on 15 July and 02.51 UT on 16 July 2009. The right graph shows the signal averaged over the entire measurement period. The corresponding CALIPSO overpass was at 01.37 UT (see below).

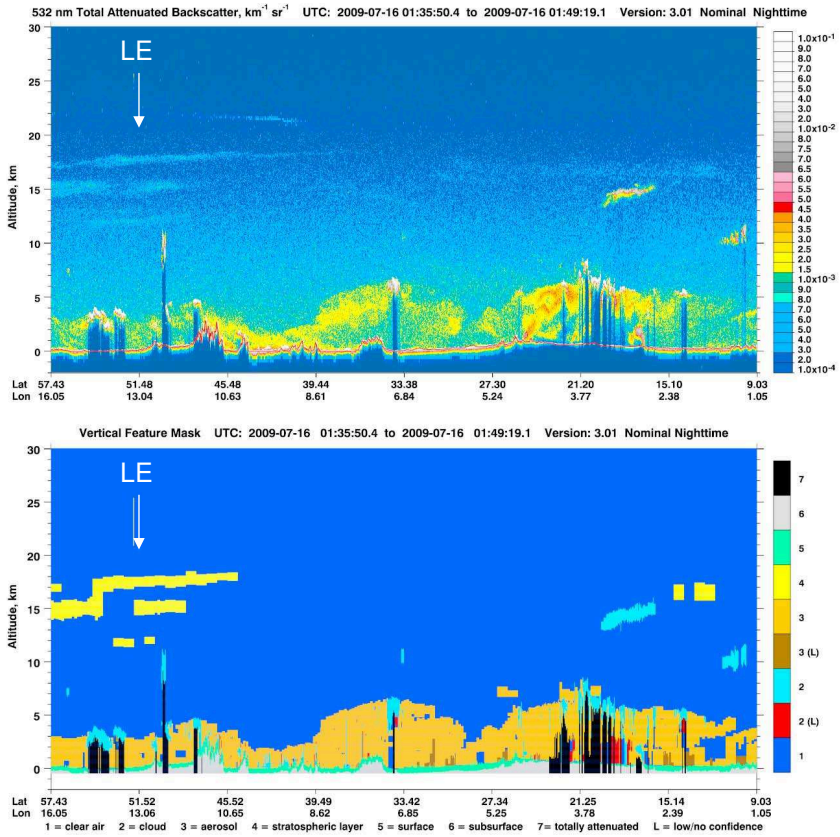

Figure 5.45: CALIPSO cross sections of 532-nm total attenuated backscatter and the vertical feature mask (Version 3 data release) for the overpass at 01.35–01.49 UT on 16 July 2009. The location of Leipzig EARLINET station is indicated (figures taken from http://www-calipso.larc.nasa.gov/products/lidar/browse_images/show_calendar.php).

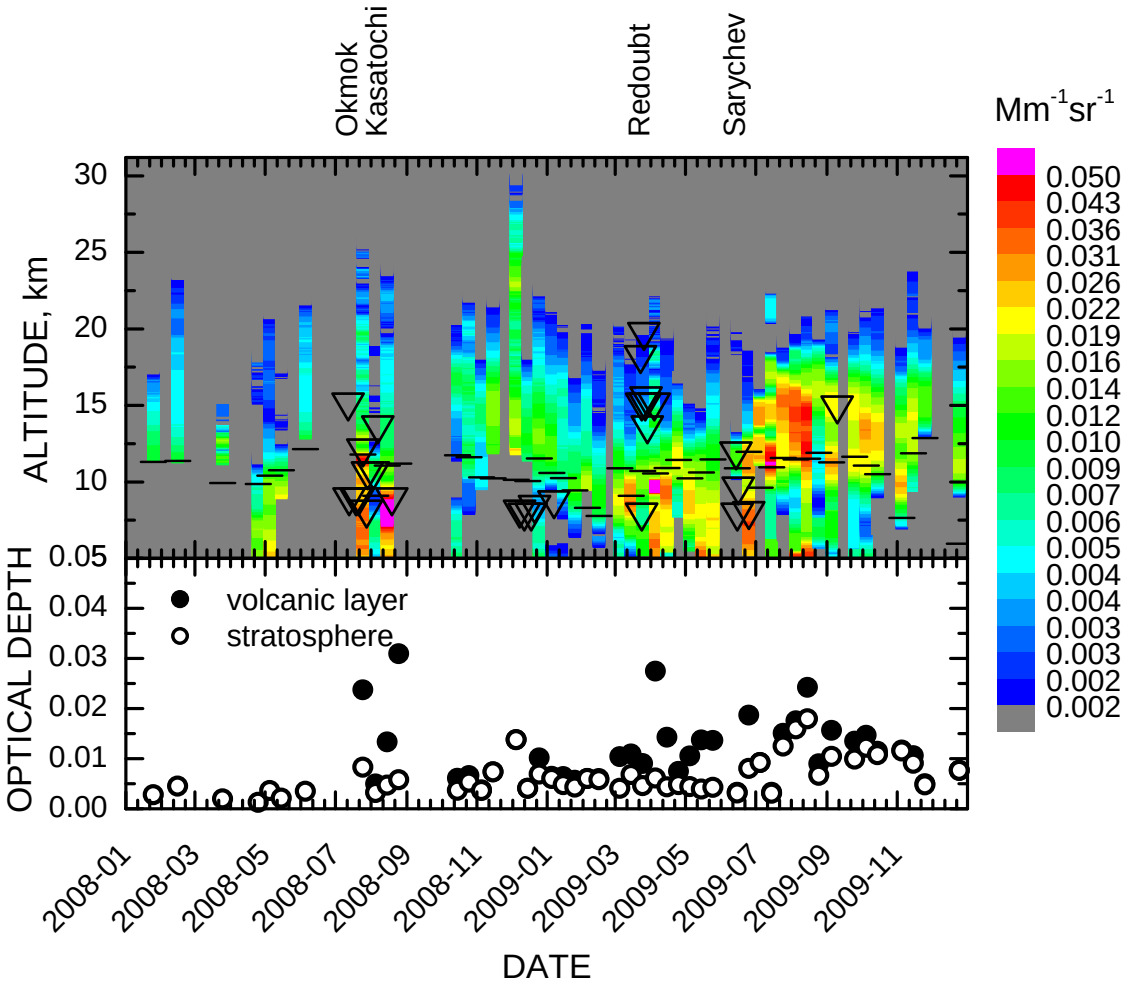

Figure 5.46: Time series of aerosol layers in the ULTS region in terms of 10-day mean profiles of the backscatter coefficient at 1064 nm. Black horizontal bars indicate the tropopause height in the individual observations. Triangles show the plume top heights of the different volcanic eruptions listed in Table 5.2. The particle optical depth at 532 nm (bottom) is computed for the entire volcanic aerosol layer (solid circles) and for the stratosphere (above the tropopause) only. The date is given in the format YYYY-MM (adapted from *Mattis et al.* (2010)).

5.1.7 Aerosol mixtures

5.1.7.1 Occurrence of aerosol mixtures

During the development of an aerosol classification scheme for the present study, it turned out that mixtures of different aerosols play an important role over the European continent. Even if we can follow the CALIPSO typing scheme for the pure aerosol types, we found that a better differentiation of their different states of mixing is necessary. The mixing occurs because of the relatively long pathways of airmasses across different aerosol source regions before the detection over the European continent. For instance, when dust is transported at low altitudes from the Sahara toward Europe, it is mixed with other aerosols from local or regional sources. This situation is often observed at EARLINET stations in the Mediterranean. Here, dust can be mixed with marine aerosol over the sea, but also with anthropogenic pollution and smoke in the densely populated coastal areas. Sea-salt particles are large and non-absorbing, whereas smoke and pollution aerosol consist of relatively small particles and show a considerable absorption. Thus mixing of either marine aerosol or absorbing aerosol or both with dust may result in quite different optical properties.

As mentioned before, the only mixture of aerosol considered in the CALIPSO retrievals is the so-called polluted dust, i.e. a mixture of dust with pollution or smoke. The CALIPSO polluted dust model does not consider mixtures of dust with marine aerosol. The mixing of marine aerosol with continental pollution or smoke plumes is also not taken into account. In the following, we present several case studies to demonstrate the occurrence of such kind of aerosol mixtures over Europe.

5.1.7.2 Dust and marine aerosol: Potenza, 8 July 2008

A measurement example for a mixture of dust with marine aerosol is presented in Fig. 5.47. The measurement was performed at Potenza on 8 July 2008, 00.19–02.26 UT. The profiles show two distinct aerosol layers above the PBL (1.75 km.). The first one is centered at 2.5 km., the second one extends from 3.2 to 4.6 km. In the lower layer between 2.1 and 2.6 km mean lidar ratios of 43±2 sr and 41±4 sr are found at 355 and 532 nm, respectively. The extinction-related Ångström exponent in the 355–532-nm range is 0.65±0.08, and the backscatter-related Ångström exponents are 0.51±0.19 and 0.50±0.02 in the 355–532-nm and the 532–1064 nm range, respectively.

Figure 5.48 shows results of FLEXPART transport simulations for both layers. The layers are traced back to Northwestern Africa. From the time-resolved simulation (not shown), it can be seen that the airmass was above the Western Sahara more than three days before the observation. During the last three days it traveled along the coastlines of Morocco

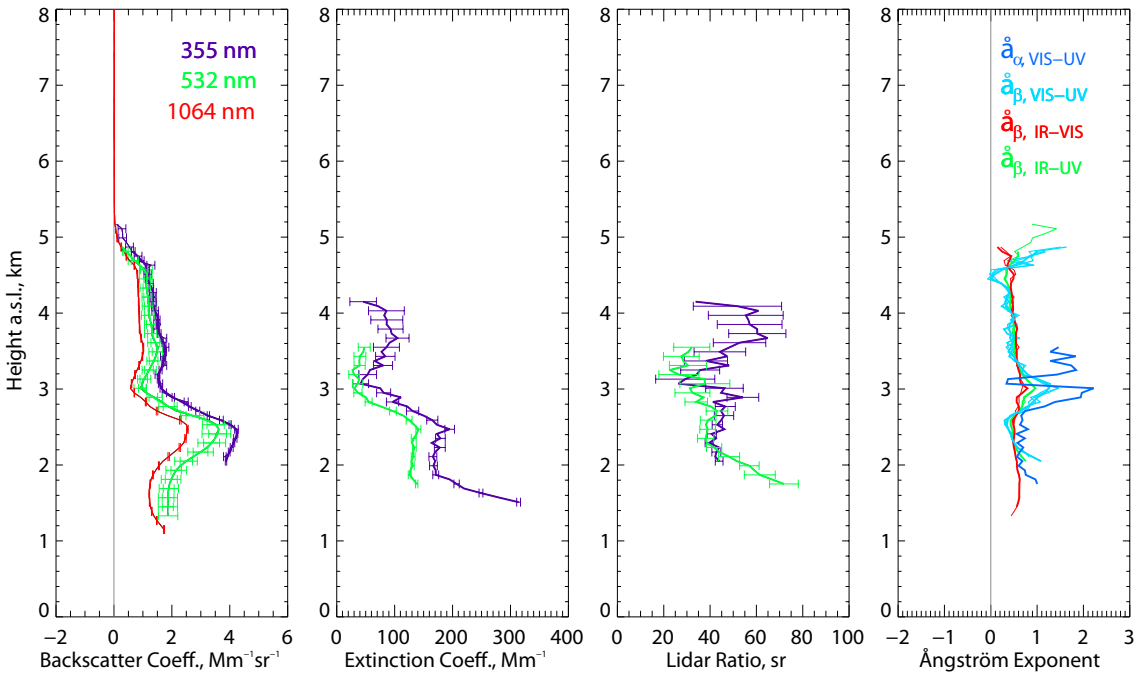

Figure 5.47: Profile data from the measurement taken at Potenza on 8 July 2008, 00.19–02.26 UT.

and Algeria before it crossed the Mediterranean. In addition, part of the airmass arrived directly from the North Atlantic. Thus in both layers an influence of marine aerosol is very likely. The optical data support this finding. Lidar ratios are smaller and Ångström exponents are larger than typically measured in pure dust.

As mentioned above, such kind of mixing of dust with marine aerosol is often observed over the Mediterranean. The CALIPSO definition of polluted dust does not fit to such mixtures, because the marine aerosol has a low lidar ratio of the order of 25 sr and thus decreases the lidar ratio of mixed dust compared to the one of pure dust. In contrast, the lidar ratio of polluted dust in the CALIPSO look-up table is 65 sr at 532 nm compared to 40 sr for pure dust.

5.1.7.3 Pollution, dust, and marine aerosol: Leipzig, 26 May 2008

Figure 5.49 shows profiles obtained at Leipzig on 26 May 2008 during a nighttime CALIPSO overpass (Case A). The measurement was taken during the period of strong dust load over Europe (see Sec. 5.1.2). However, the optical signatures do not indicate a strong influence of large mineral dust particles. Depolarization ratios are very low, and the extinction and backscatter coefficients exhibit a strong wavelength dependence resulting in relatively large Ångströms exponents and indicating the presence of small particles.

Figure 5.50 shows FLEXPART transport simulation results for airmasses arriving at

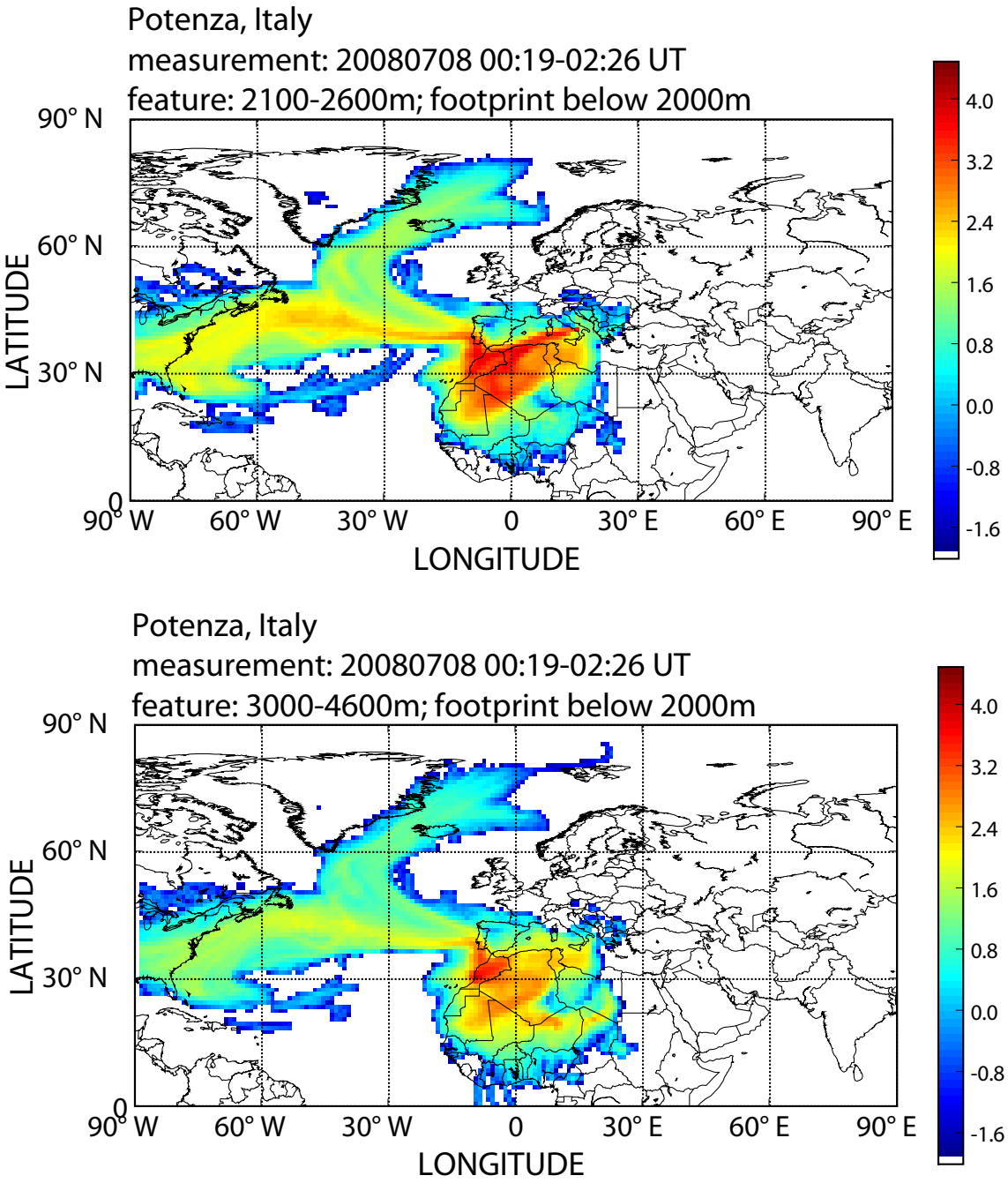

Figure 5.48: FLEXPART footprint for airmasses traveling below 2000 m height and arriving at Potenza between 2.1 and 2.6 km height (upper panel) and 3.2 and 4.8 km height (lower panel) at 02.26 UT on 8 July 2008. The colors represent the logarithm of the integrated residence time in a grid box in seconds for 10-day integration time.

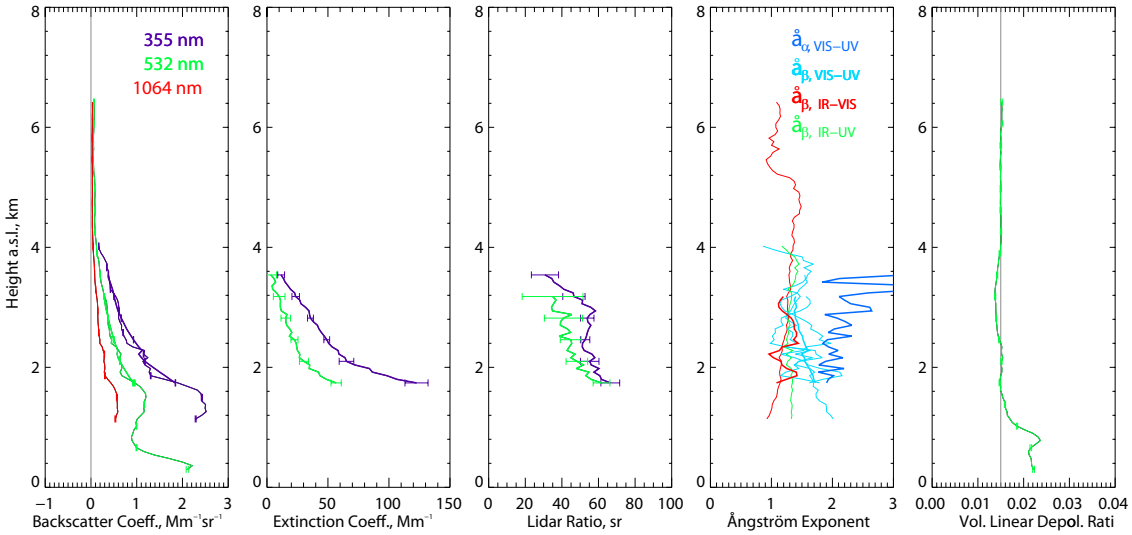

Figure 5.49: Profile data from the measurement taken at Leipzig on 26 May 2008, 00.00-01.54 UT.

Leipzig betweeen 1.8 and 2.34 km and 2.34 and 3 km, respectively, at 01.54 UT on 26 May 2008. Again, only air parcels that touched the height range below 2000 m within the last 10 days are considered. The footprints indicate that a larger part of the airmass traveled over the North Atlantic and a smaller part came from the Sahara. Aerosol uptake over the Mediterranean and Central Europe and thus a considerable influence of European pollution on the observed aerosol conditions at Leipzig on that day is very likely as well. A mixture of pollution with dust and marine aerosol was most probably obtained.

5.1.7.4 Pollution and marine aerosol: Potenza, 23–24 June 2008

An occassion of mixing of pollution with marine aerosol is presented in Fig. 5.51. The measurement was taken at Potenza on 23 June 2008. Aerosol layers up to 3–4 km were present. The variation of lidar ratios and Ångström exponents indicates a layering of different aerosol types or mixtures. A FLEXPART transport simulation for the layer around 2 km height is presented in Fig. 5.52. A long pathway of the airmass over the North Atlantic and Central Europe is indicated. The final advection toward Potenza occurred from the east over the Adriatic Sea. Thus we can expect a mixture of European pollution with some marine aerosol.

5.1.7.5 Pollution and smoke: Athens, 29–30 July 2008

Finally, we show the mixing of pollution and smoke which is a typical situation in Greece in the summer season. As shown in Sec. 5.1.5, the Greek EARLINET stations frequently

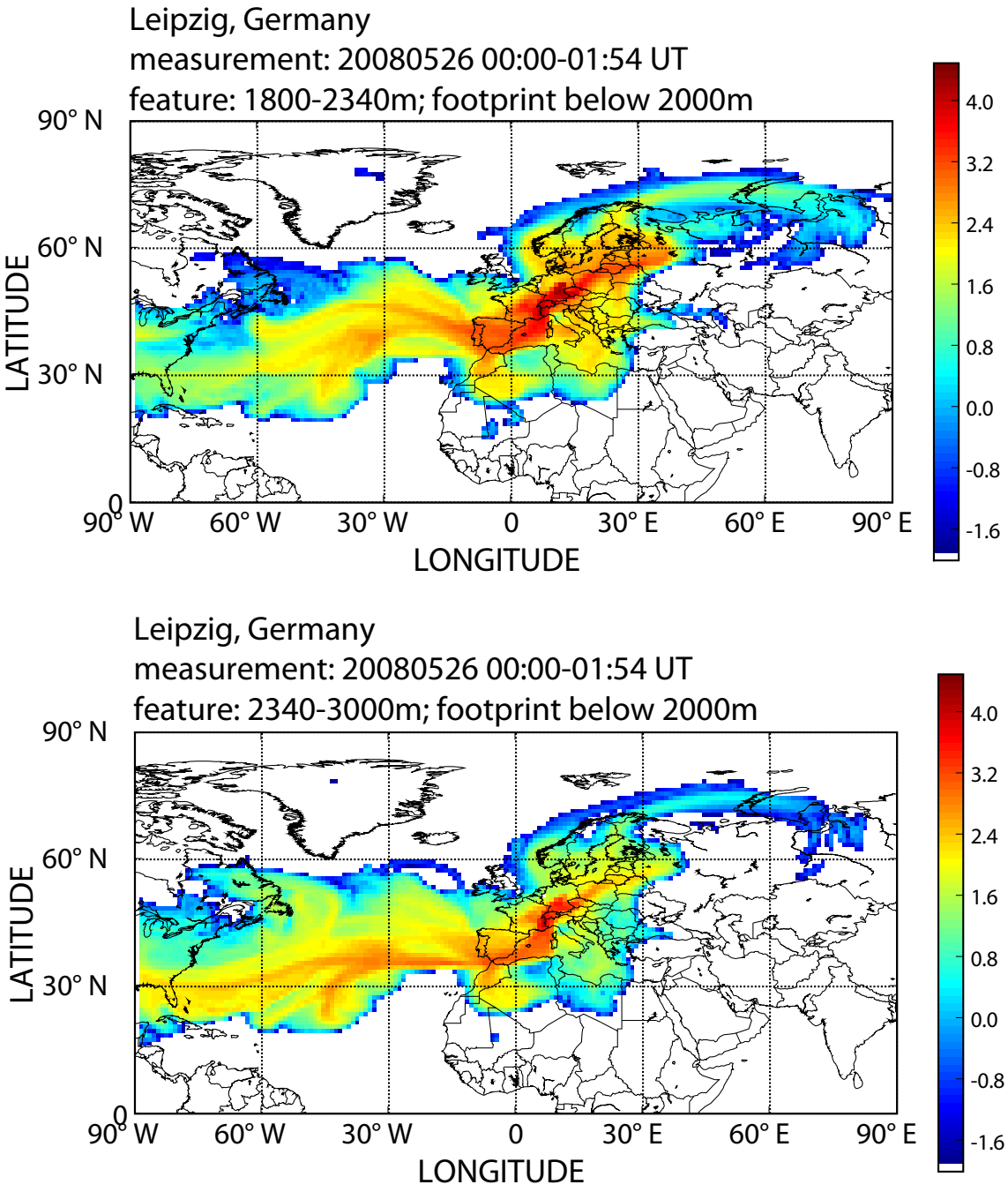

Figure 5.50: FLEXPART footprint for airmasses traveling below 2000 m height and arriving at Leipzig between 1.8 and 2.34 km height (upper panel) and 2.34 and 3 km height at 01.54 UT on 26 May 2008. The colors represent the logarithm of the integrated residence time in a grid box in seconds for 10-day integration time.

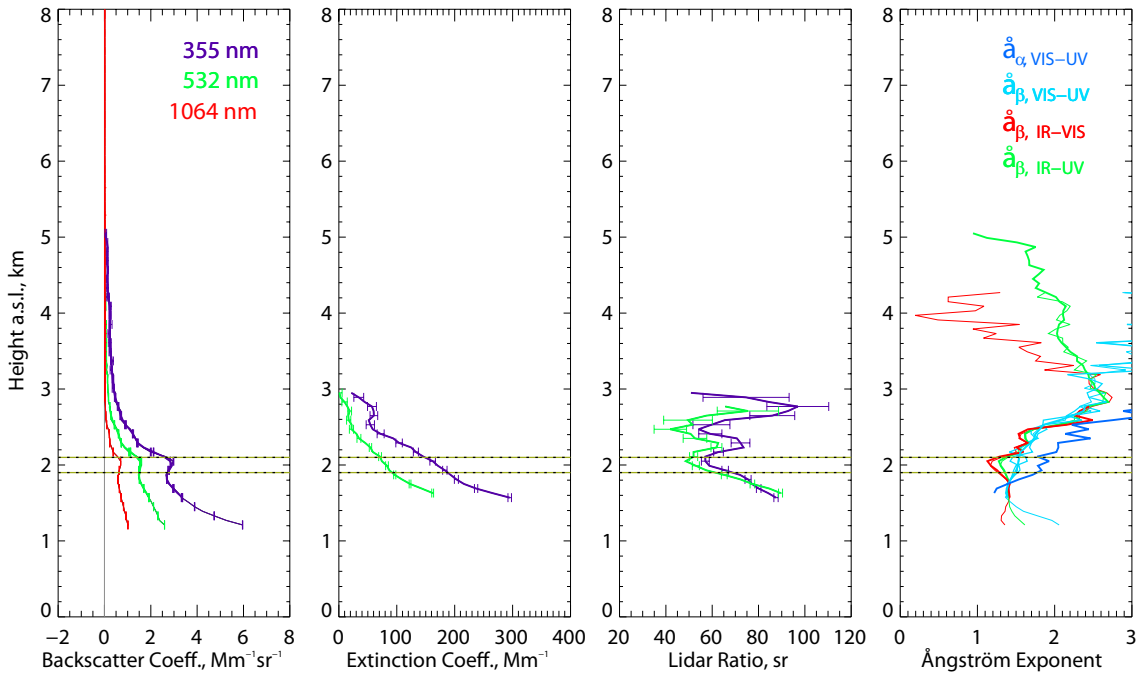

Figure 5.51: Profile data from the measurement taken at Potenza on 23–24 June 2008, 23.35-02.36 UT.

observe smoke from local and regional fires in July and August. At the same time, the metropolitan areas of Athens and Thessaloniki suffer from heavy pollution and photochemical smog. Sometimes, the smoke plumes are well separated as shown in Sec. 5.1.5, but often the smoke is mixed into the PBL which typically reaches up to 2–3 km in summer. Fig. 5.53 shows the profiles from the upper part of the PBL at Athens in the night from 29 to 30 July 2008. High lidar ratio and large Ångström exponents were found.

The respective FLEXPART transport simulation is presented in Fig. 5.54. The typical flow pattern from the north over the regions with active fires is observed (see Sec. 5.1.5). In such cases, when no isolated smoke layer can be identified, the aerosol is classified as a mixture of smoke and continental pollution.

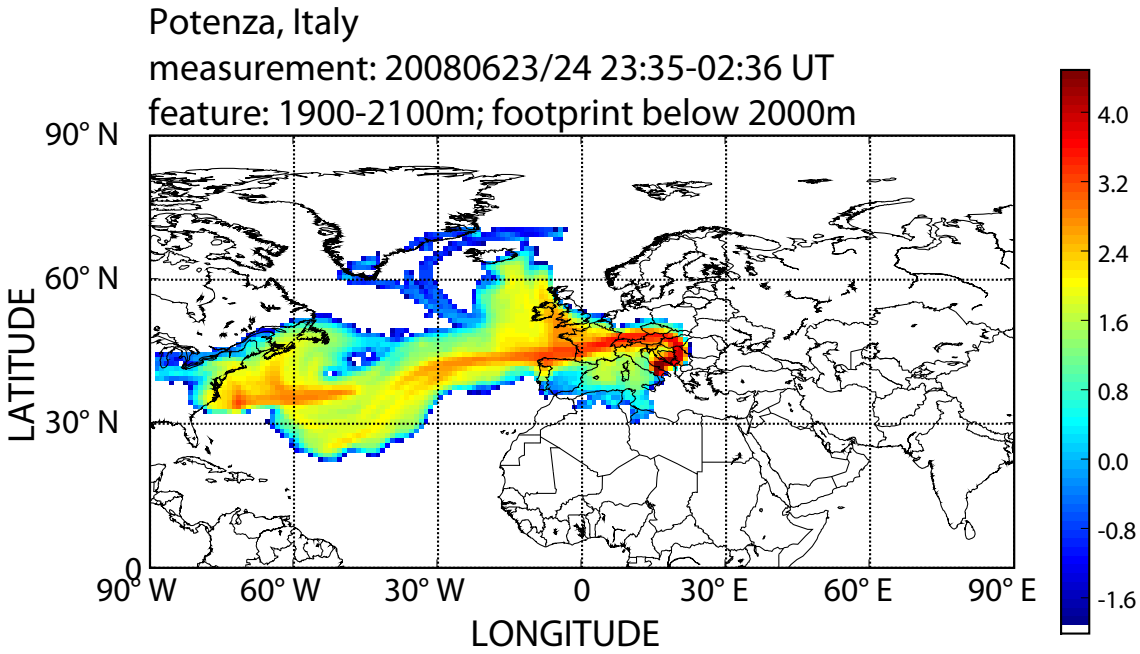

Figure 5.52: FLEXPART footprint for airmasses traveling below 2000 m height and arriving at Potenza between 1.9 and 2.1 km height at 02.36 UT on 24 June 2008. The colors represent the logarithm of the integrated residence time in a grid box in seconds for 10-day integration time.

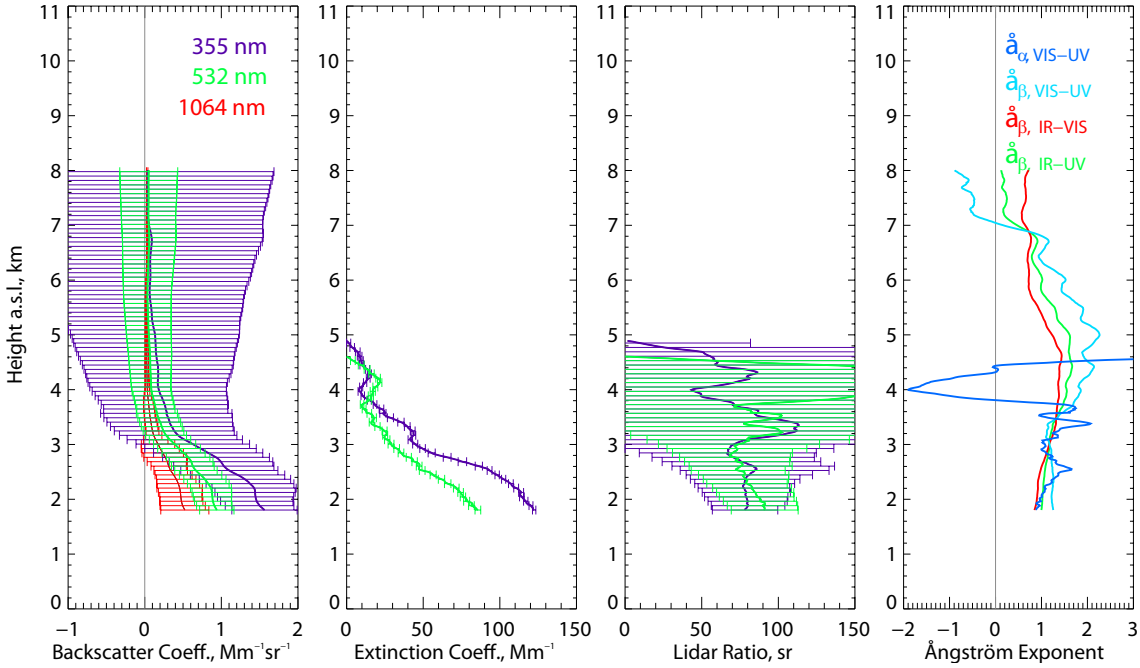

Figure 5.53: Profile data from the measurement taken at Athens on 29–30 July 2008, 22.32-00.29 UT.

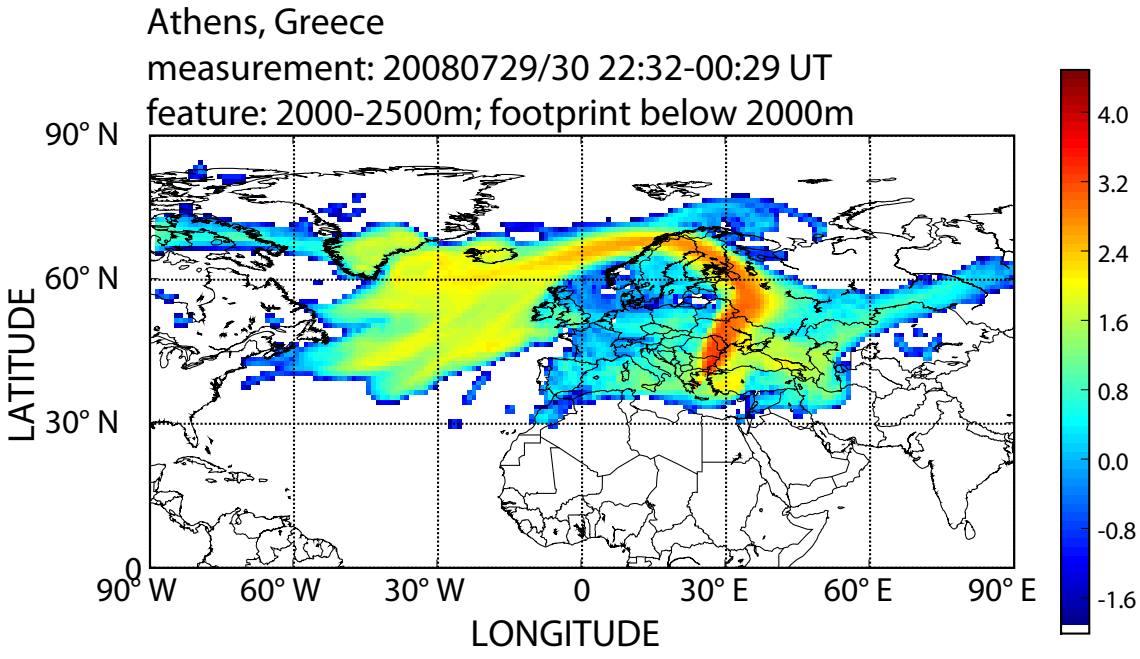

Figure 5.54: FLEXPART footprint for airmasses traveling below 2000 m height and arriving at Athens between 2 and 2.5 km height at 00.29 UT on 30 July 2008. The colors represent the logarithm of the integrated residence time in a grid box in seconds for 10-day integration time.

5.2 Cloud classification

Figure 5.55 shows an example of an EARLINET measurement during which all types of clouds defined for this study, i.e. water, mixed-phase and ice clouds, could be observed. The Case A measurement was taken at Granada EARLINET station on 22 January 2009. Together with the time-height contour plot a temperature profile is presented in Fig. 5.55.

Ice and water can co-exist in the atmosphere between 0 and −35 °C. Typically, <10% and >90% of the clouds contain ice at temperatures of −5 and −25 °C, respectively. These threshold values are indicated in the plot of the temperature profile in Fig. 5.55. In agreement with the temperature profile, the clouds in the height range of 3 to 6 km show the typical signature of mixed-phase clouds. For instance, a layer consisting mainly of liquid water occurs in the beginning of the measurement at 5.5 km altitude. This layer is optically dense and not penetrated by the laser beam. Ice crystals fall out of this layer and appear as faint structures below the liquid-water layer. In the course of the measurement, water clouds appear at the top of the PBL between 1 and 2 km height. They could not be penetrated most of the time after 2.10 UT. Ice clouds were observed between 7.5 and 11 km height, when the laser beam could reach the upper troposphere.

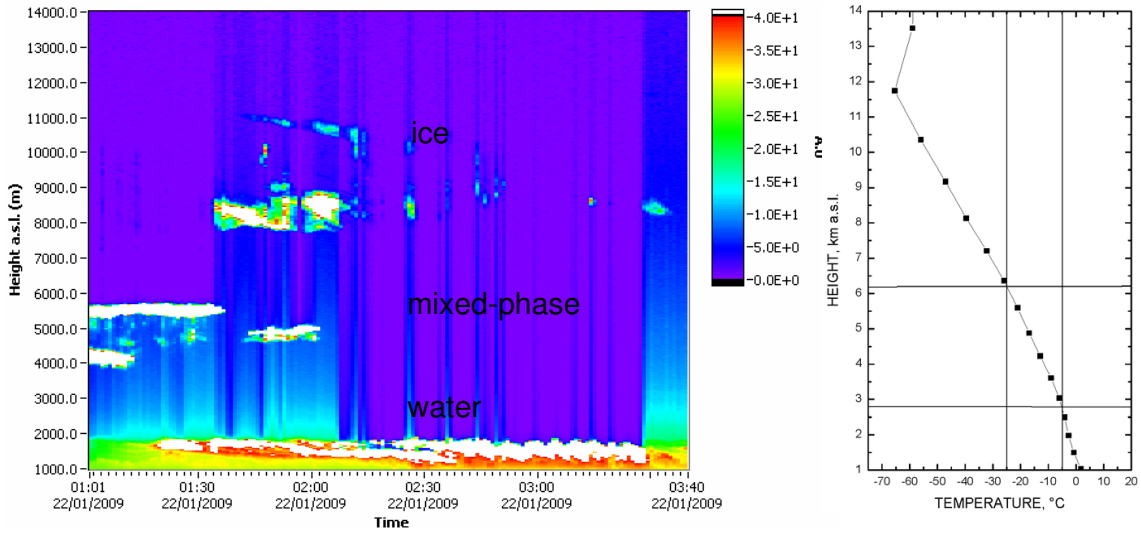

Figure 5.55: Time-height contour plot of the range-corrected signal at 1064 nm for the measurement taken at Granada on 22 January 2009 and corresponding temperature profile. Water clouds (below 3 km), mixed-phase clouds (between 3 and 6 km), and ice clouds (above 7 km) occurred in the course of the measurement.

As a second example, we present a case study of a cirrus observation taken at at Leipzig on 26 May 2008. Above the aerosol layers (see previous section), a cirrus cloud was observed at the Leipzig EARLINET station during the CALIPSO overpass at 01.33 UT. In Fig. 5.56 and 5.57 we present a comparison with the CALIPSO cloud observation.

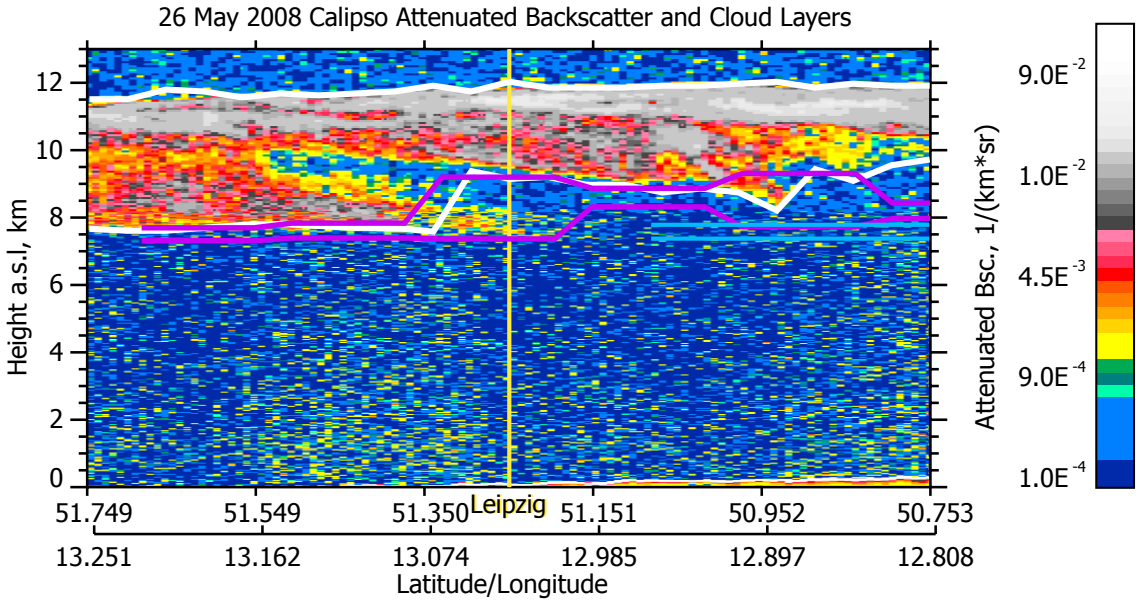

Figure 5.56: Browse image of the CALIPSO 532-nm attenuated backscatter coefficient with overlayed cloud boundaries from the the CALIPSO L2 5-km cloud layer product.

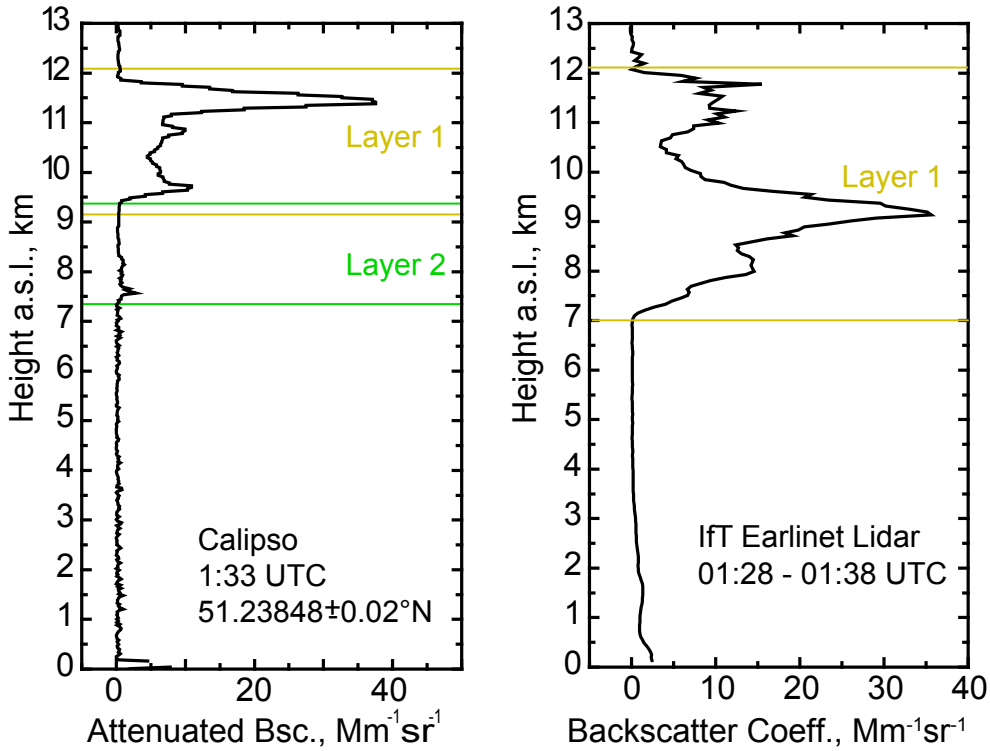

Figure 5.57: Comparison of the CALIPSO 532-nm attenuated backscatter profile (left) and the EARLINET 532-nm backscatter coefficient profile (right) taken during the correlative observation at Leipzig on 26 May 2008. The cloud layers identified by the CALIPSO cloud algorithm and from the EARLINET data evaluation are indicated.

Fig. 5.56 shows a browse image of the CALIPSO 532-nm attenuated backscatter coefficient with overlayed cloud boundaries from the CALIPSO L2 5-km cloud layer product. The cirrus cloud is well identified. According to the inhomogeneous structure of the cloud base (fall streaks), the cloud is subdivided into two or even three layers depending on the actual shape along the cross section. Nevertheless, as can be seen from Fig. 5.57, the uppermost and lowermost boundaries of the cloud as obtained from ground and from space agree incredibly well, even though the distance between the observations was about 40 km. In Section 7.3.5, we present further examples of cloud observations with EARLINET and CALIPSO.

Chapter 6

Optical properties and conversion factors of major aerosol types

In this chapter we discuss statistical findings derived from the long-term aerosol and cloud database established within this study. Mean optical properties and conversion factors for pure aerosol types and typical mixtures of aerosols resulting from the observations at 16 EARLINET stations are presented. Sec. 6.1 provides an overview on the frequency of occurrence of pure aerosol types and aerosol mixtures as obtained from the analysis of several hundreds of aerosol layers investigated in detail so far. Optical properties and conversion factors for pure aerosol types are presented in Sec. 6.2. The findings for mixed aerosols are discussed in Sec. 6.3. A further assessment of the statistical results is provided in Sec. 6.4.

6.1 Occurrence of pure aerosol types and aerosol mixtures

The statistical results presented in this chapter are based on an in-depth investigation of more than 400 aerosol layers selected from measured profiles provided by 16 EARLINET stations, with focus on the high-sophisticated stations (see Sec. 2.2). Each measurement has been inspected regarding quality (e.g., noise level) and the occurrence of distinct aerosol layers. For each selected layer, a FLEXPART transport simulation was performed to determine its origin, transport path, and age. The DREAM and NAAPS models together with MODIS fire maps and other tools (see Sec. 3.5) were used to cross-check the sources and to assign a pure aerosol type or an aerosol mixture for each layer, in the way discussed for several examples in Chapter 5.

In Fig. 6.1 the frequency of occurrence of the different pure and mixed aerosol types is shown. In 28% of the cases, a pure aerosol type was assigned. For the remaining 72%, a mixing of different aerosol types could not be excluded. For the pure aerosol types (see Fig. 6.1b), the majority is defined as polluted or clean continental aerosol. 21% of the layers were identified as Saharan dust and 11% as smoke. Clean marine conditions were found for 5% of the pure-type fraction (i.e. 1.4% of all layers) only. 6% of the layers of the pure-type fraction occurred in the stratosphere. Stratospheric aerosol has been discussed in detail already in Sec. 5.1.6 and is not further considered in this chapter, where we focus on tropospheric aerosols. In principle, all kind of mixtures of pure tropospheric aerosol types can occur over Europe as the analysis shows (see Fig. 6.1c). Predominantly, the mixed aerosols contain pollution and/or dust. The mixture of dust, pollution, and marine aerosol is most frequently obtained. This can be explained with the large number of measurements contributed by stations in the Mediterranean.

Even if clean marine aerosol is found seldomly, a marine influence cannot be excluded for many cases. It is caused by typical transport pattern from the North Atlantic or from the Sahara over the Mediterranean Sea toward Europe. Fig. 6.2 shows that for 76% of the layers a marine influence has at least to be taken into account. Pollution and dust occur in 59% and 53% of the layers, respectively, in either pure or mixed state. It should be noted that, with the tools applied here, it is estimated whether the presence of a certain aerosol type is likely or not. It is not possible to determine the absolute contribution of different aerosol types to a mixture.

In the following, we present mean optical properties and the respective conversion factors calculated for the pure aerosol types (Sec. 6.2) and a selection of mixtures (Sec. 6.3). For each of the pure types and aerosol mixtures considered in Fig. 6.1, there were at least six individual layers available in the database which contribute to the statistics. Mixtures with lower occurrence were sampled in the category “other” in Fig. 6.1c. On average, 25 layers contribute to the statistical values for each type.

6.2 Optical properties of pure aerosol types

Table 6.1 summarizes mean values and their standard deviation of extensive and intensive optical properties for the pure tropospheric aerosol types. Missing numbers are due to the limited number of observations at high-sophisticated stations. As mentioned, clean marine conditions are rarely found over Europe. Clean continental aerosol is mainly observed over remote sites (e.g., Belsk, Minsk) where no high-sophisticated stations are located. The list of optical data in Tab. 6.1 also contains the conversion factors (indicated in bold) introduced in Sec. 4.3.4, i.e. those parameters which are relevant to relate observations

a)

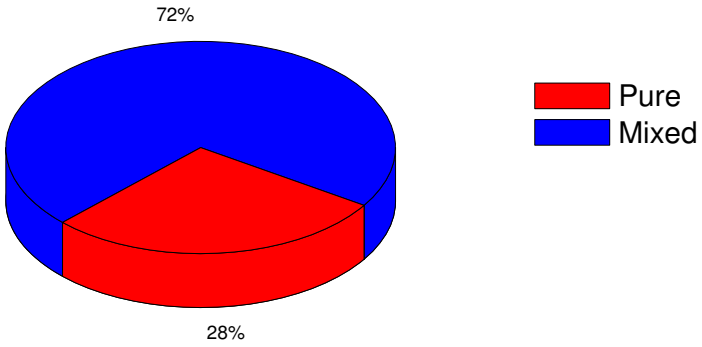

b)

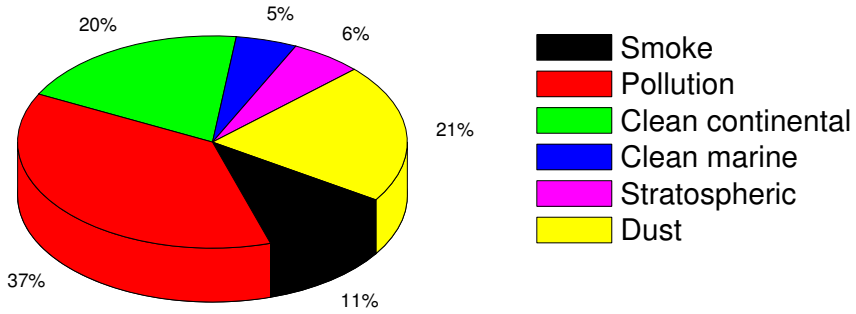

c)

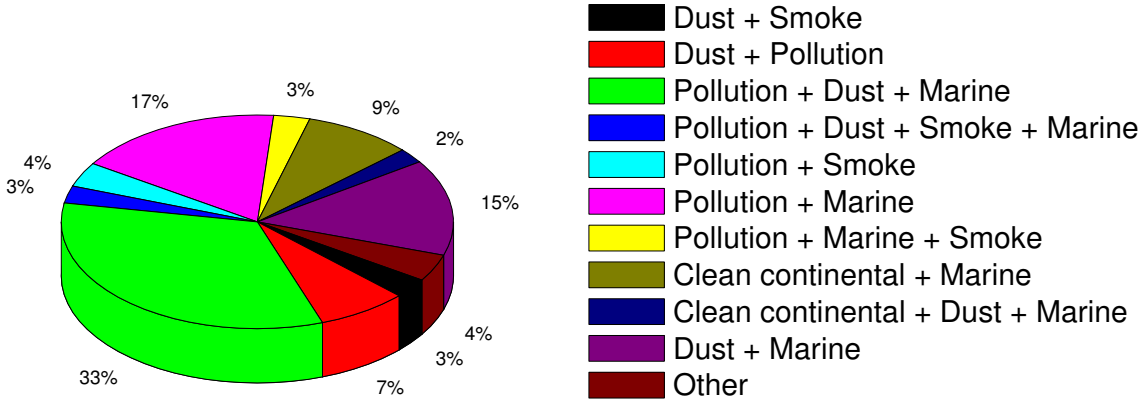

Figure 6.1: Frequency of occurrence of pure and mixed aerosol types as obtained from the aerosol-layer analysis: a) fraction of layers containing either pure or mixed aerosols, b) distribution of smoke, pollution, clean continental, clean marine, and dust aerosol within the fraction of pure aerosol types, c) distribution of different mixtures within the fraction of mixed aerosols.

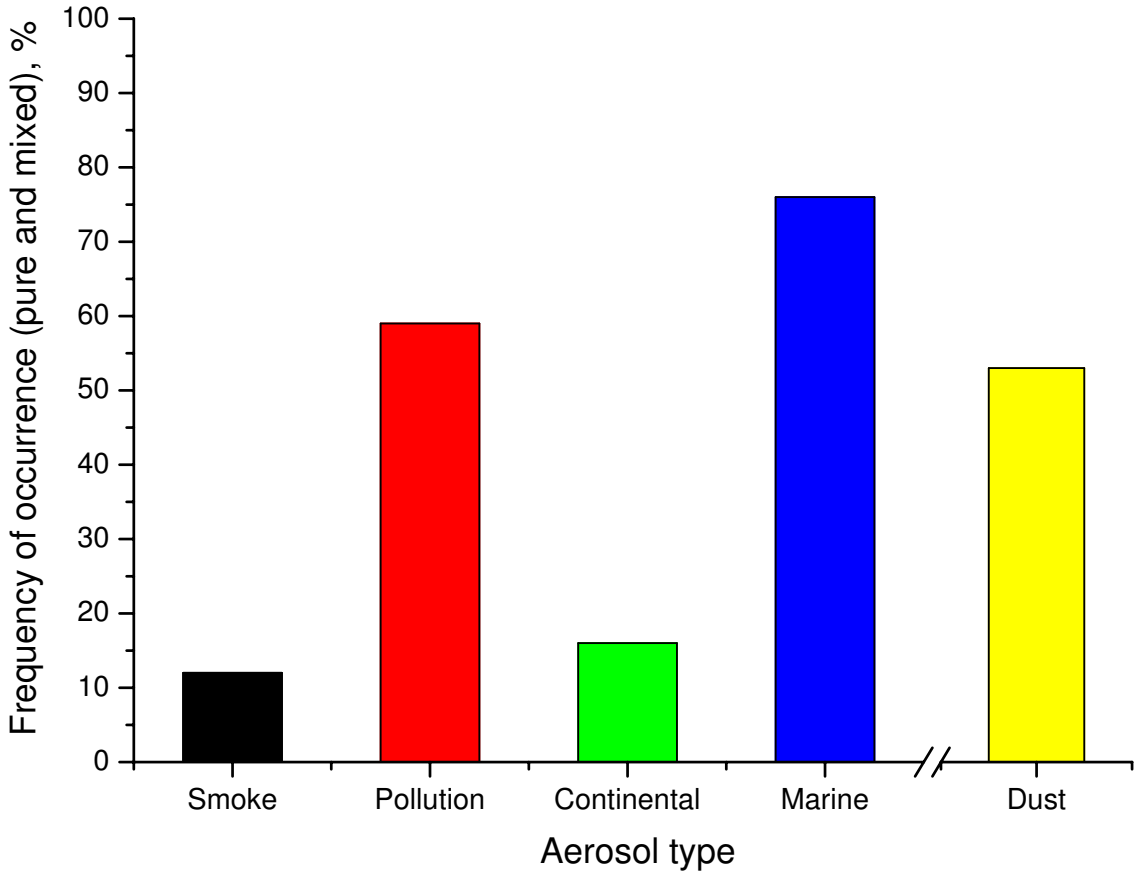

Figure 6.2: Frequency of occurrence of the aerosol types smoke, pollution, continental, marine, and dust in pure and mixed states.

with different instruments (CALIOP, ALADIN, ATLID) to each other. Fig. 6.3 illustrates the findings for lidar ratios and Ångström exponents and shows in addition to mean values and standard deviation also the median as well as the minimum and maximum values.

In general, the results fit well into the picture of aerosol typing as discussed in Chapters 3 and 5. Highest lidar ratios and Ångström exponents are obtained for smoke, indicating small and highly absorbing particles, followed by the values for pollution. The dust lidar ratios are 57.7±10.8 and 56.6±5.4 sr at 355 and 532 nm, respectively, and agree very well with the findings of SAMUM–1 in the Saharan source region (*Tesche et al.*, 2009b). Again, the discrepancy to the CALIPSO dust lidar ratio is noticed. The S–ratio plot (lower left panel in Fig. 6.3) shows that there is no indication for a significant wavelength dependence of the lidar ratio between 355 and 532 nm for any of the aerosol types. Ångström exponents are of the order of 1.5 for smoke and pollution and <0.5 for dust and marine aerosol. They are also in good agreement with the literature values (see Sec. 3.2).

The variability of the parameters has both natural and technical reasons. Because of the limited number of observations, single outliers, which may be caused by misclassification

Table 6.1: Mean values and standard deviation of extensive and intensive optical properties for the pure aerosol types marine, dust, pollution, clean continental, and smoke. Conversion factors as defined in Sec. 4.3.4 are indicated in bold.

Parameter, unit	Marine	Dust	Pollution	Clean continental	Smoke
α_{UV}, $10^{-6}\,\mathrm{m}^{-1}$		69.9±31.8	131.1±79.3		149.2±72.8
α_{VIS}, $10^{-6}\,\mathrm{m}^{-1}$		56.6±27.9	77.0±39.4		81.6±39.3
β_{UV}, $10^{-6}\,\mathrm{m}^{-1}\mathrm{sr}^{-1}$	0.85±0.80	1.29±0.63	1.80±1.25	1.26±0.48	2.15±1.22
β_{VIS}, $10^{-6}\,\mathrm{m}^{-1}\mathrm{sr}^{-1}$	0.56±0.57	1.06±0.61	1.31±1.16	0.81±0.43	1.14±0.61
β_{IR}, $10^{-6}\,\mathrm{m}^{-1}\mathrm{sr}^{-1}$	0.54±0.36	0.79±0.60	0.36±0.36	0.56±0.41	0.33±0.18
S_{UV}, sr		57.7±10.8	69.9±19.3		78.1±16.5
S_{VIS}, sr		56.6±5.4	66.6±19.6		74.1±12.5
$\mathbf{s}_{\mathrm{VIS-UV}}$		**0.95±0.19**	**1.02±0.11**		**0.95±0.05**
$\mathbf{C}_{\alpha,\mathrm{VIS-UV}}$		**0.89±0.13**	**0.57±0.09**		**0.55±0.05**
$\mathring{a}_{\alpha,\mathrm{VIS-UV}}$		0.34±0.40	1.40±0.35		1.49±0.25
$\mathbf{C}_{\beta,\mathrm{VIS-UV}}$	**0.80±0.14**	**0.89±0.14**	**0.55±0.05**	**0.63±0.12**	**0.55±0.07**
$\mathring{a}_{\beta,\mathrm{VIS-UV}}$	0.50±0.42	0.32±0.31	1.51±0.21	1.19±0.53	1.50±0.32
$C_{\beta,\mathrm{IR-VIS}}$	0.87±0.04	0.83±0.18	0.37±0.07	0.59±0.17	0.41±0.03
$\mathring{a}_{\beta,\mathrm{IR-VIS}}$	0.28±0.04	0.32±0.39	1.48±0.31	0.82±0.42	1.28±0.11
$\mathbf{C}_{\beta,\mathrm{IR-UV}}$		**0.65±0.13**	**0.20±0.06**	**0.39±0.19**	**0.24±0.03**
$\mathring{a}_{\beta,\mathrm{IR-UV}}$		0.42±0.26	1.53±0.34	0.97±0.46	1.30±0.10
δ_{VIS}		0.08±0.04	0.03±0.03	0.04±0.03	

or measurement errors, still have a large influence. This kind of scattering in the data can be reduced by increasing the number of observations in the database. Further discussion of the data is provided in Sec. 6.4.

6.3 Optical properties of aerosol mixtures

Mean values and their standard deviation of extensive and intensive optical properties for a selection of aerosol mixtures are given in Table 6.2. Mixtures with the highest frequency of occurrence were chosen (see Fig. 6.1c). Again, the conversion factors are indicated in bold. A visualization for the lidar ratios and Ångström exponents is provided in Fig. 6.4.

Looking at the mean or median values, one can clearly see the influence of the different pure aerosol types. When smoke or pollution contributes to the mixture, lidar ratios and Ångström exponents are normally higher. The presence of marine aerosol decreases the

Table 6.2: Mean values and standard deviation of extensive and intensive optical properties for different mixtures of dust, pollution, smoke, and marine aerosol. Conversion factors as defined in Sec. 4.3.4 are indicated in bold.

Parameter, unit	Dust and smoke	Dust and pollution	Dust and pollution and marine	Dust and marine	Pollution and marine
α_{UV}, $10^{-6}\,\mathrm{m}^{-1}$	60.8±25.1	77.1±40.4	99.8±71.6	103.9±61.1	72.4±62.2
α_{VIS}, $10^{-6}\,\mathrm{m}^{-1}$	49.0±28.6	71.8±27.6	113.3±86.4	96.2±63.0	41.5±32.2
β_{UV}, $10^{-6}\,\mathrm{m}^{-1}\mathrm{sr}^{-1}$	1.59±1.21	1.45±0.87	2.05±1.70	2.19±1.63	1.54±1.09
β_{VIS}, $10^{-6}\,\mathrm{m}^{-1}\mathrm{sr}^{-1}$	0.82±0.45	1.20±0.79	1.60±1.71	1.69±1.34	1.14±1.50
β_{IR}, $10^{-6}\,\mathrm{m}^{-1}\mathrm{sr}^{-1}$	0.41±0.23	0.67±0.46	0.66±0.66	1.02±0.80	0.49±0.39
S_{UV}, sr	67.3±9.6	63.1±6.9	53.0±13.9	46.7±12.4	47.3±10.7
S_{VIS}, sr	66.0±14.0	71.6±13.0	53.1±14.7	47.1±8.0	43.6±14.4
$\mathbf{s}_{\mathrm{VIS-UV}}$	**1.04±0.14**	**1.12±0.19**	**0.92±0.22**	**1.17±0.25**	**0.86±0.31**
$\mathbf{C}_{\alpha,\mathrm{VIS-UV}}$	**0.82±0.13**	**0.76±0.12**	**0.69±0.26**	**0.87±0.12**	**0.73±0.29**
$\mathring{a}_{\alpha,\mathrm{VIS-UV}}$	0.48±0.33	0.73±0.38	1.09±0.95	0.38±0.30	0.85±0.86
$\mathbf{C}_{\beta,\mathrm{VIS-UV}}$	**0.67±0.21**	**0.79±0.19**	**0.78±0.31**	**0.79±0.19**	**0.72±0.36**
$\mathring{a}_{\beta,\mathrm{VIS-UV}}$	1.15±0.94	0.72±0.57	0.71±0.62	0.65±0.47	1.01±0.89
$C_{\beta,\mathrm{IR-VIS}}$	0.53±0.17	0.59±0.12	0.61±0.18	0.77±0.12	0.49±0.18
$\mathring{a}_{\beta,\mathrm{IR-VIS}}$	1.01±0.54	0.80±0.32	0.78±0.42	0.40±0.21	1.10±0.43
$\mathbf{C}_{\beta,\mathrm{IR-UV}}$	**0.40±0.28**	**0.49±0.09**	**0.40±0.17**	**0.65±0.22**	**0.36±0.22**
$\mathring{a}_{\beta,\mathrm{IR-UV}}$	1.04±0.74	0.67±0.17	0.87±0.33	0.44±0.25	1.05±0.45
δ_{VIS}		0.15±0.11	0.14±0.12	0.05±0.01	0.07±0.04

lidar ratios. Smallest Ångström exponents are found for the mixture of dust and marine aerosol, where both components contribute relatively large particles. Also for the aerosol mixtures, there is no evidence that the lidar ratio has a strong wavelength dependence. The variability of the data is higher than for the pure types. This finding is not surprising because the amount of single components in a mixture varies from case to case. Also the identification of certain mixtures is rather difficult, and misclassifications can easily happen.

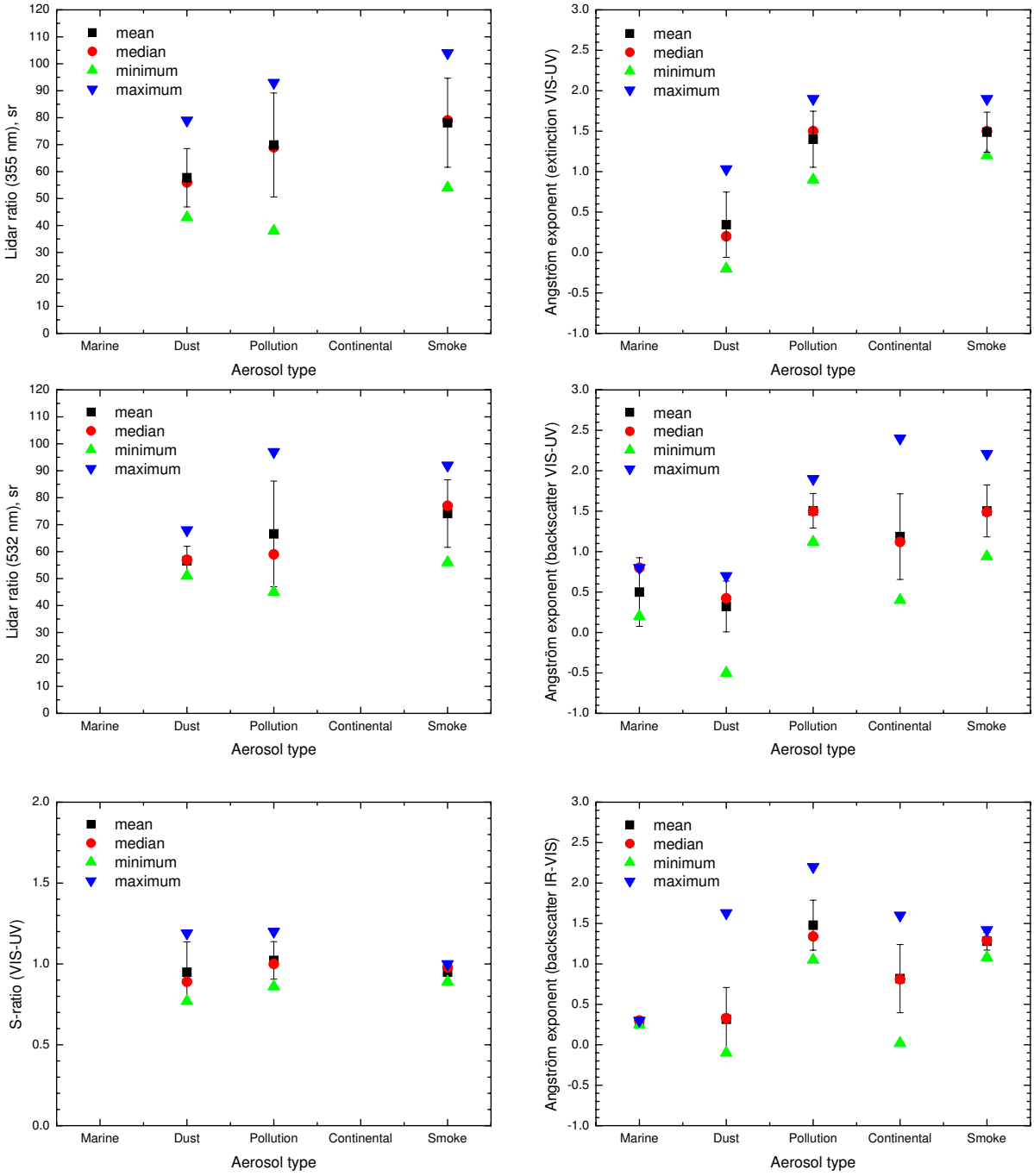

Figure 6.3: Lidar ratio at 355 nm (upper left) and 532 nm (middle left) and 532-to-355-nm S–ratio (lower left), extinction-related (upper right) and backscatter-related Ångström exponents in the UV-VIS (middle right) and VIS-IR wavelength range (lower right) for pure aerosol types. Mean values and standard deviation, median, maximum, and minimum values are indicated.

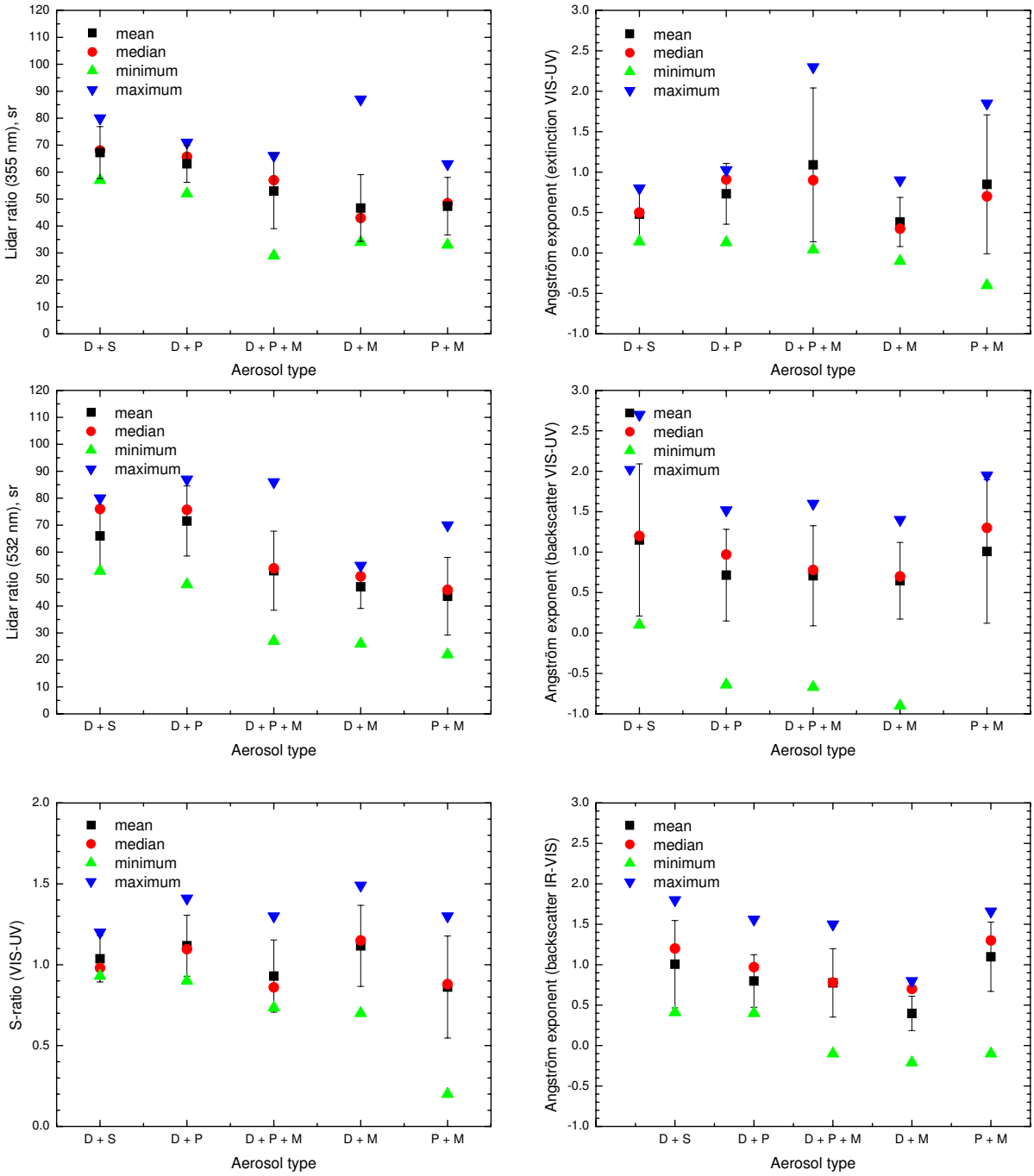

Figure 6.4: Lidar ratio at 355 nm (upper left) and 532 nm (middle left) and 532-to-355-nm S–ratio (lower left), extinction-related (upper right) and backscatter-related Ångström exponents in the UV-VIS (middle right) and VIS-IR wavelength range (lower right) for aerosol mixtures (D+S = Dust and Smoke, D+P = Dust and Pollution, D+P+M = Dust and Pollution and Marine, D+M = Dust and Marine, P+M = Pollution and Marine). Mean values and standard deviation, median, maximum, and minimum values are indicated.

6.4 Discussion and assessment

The statistical exploitation of 400 aerosol layers from the long-term database already provides a valuable insight into the benefits and limits of aerosol typing schemes for space-borne lidar missions. One of the core results is presented in Fig. 6.5. This plot shows a two-dimensional distribution of aerosol types in terms of the 1064-to-532 nm color ratio as measured with CALIOP versus the 355-nm-lidar ratio as measured with ATLID. Big color dots stand for the pure aerosol types, whereas smaller dots represent the mixtures discussed in the previous section. Colored lines indicate which pure types contribute to the mixtures. For marine aerosol, a fixed value of 25 sr for the lidar is taken from the literature because of the lack of data in the database.

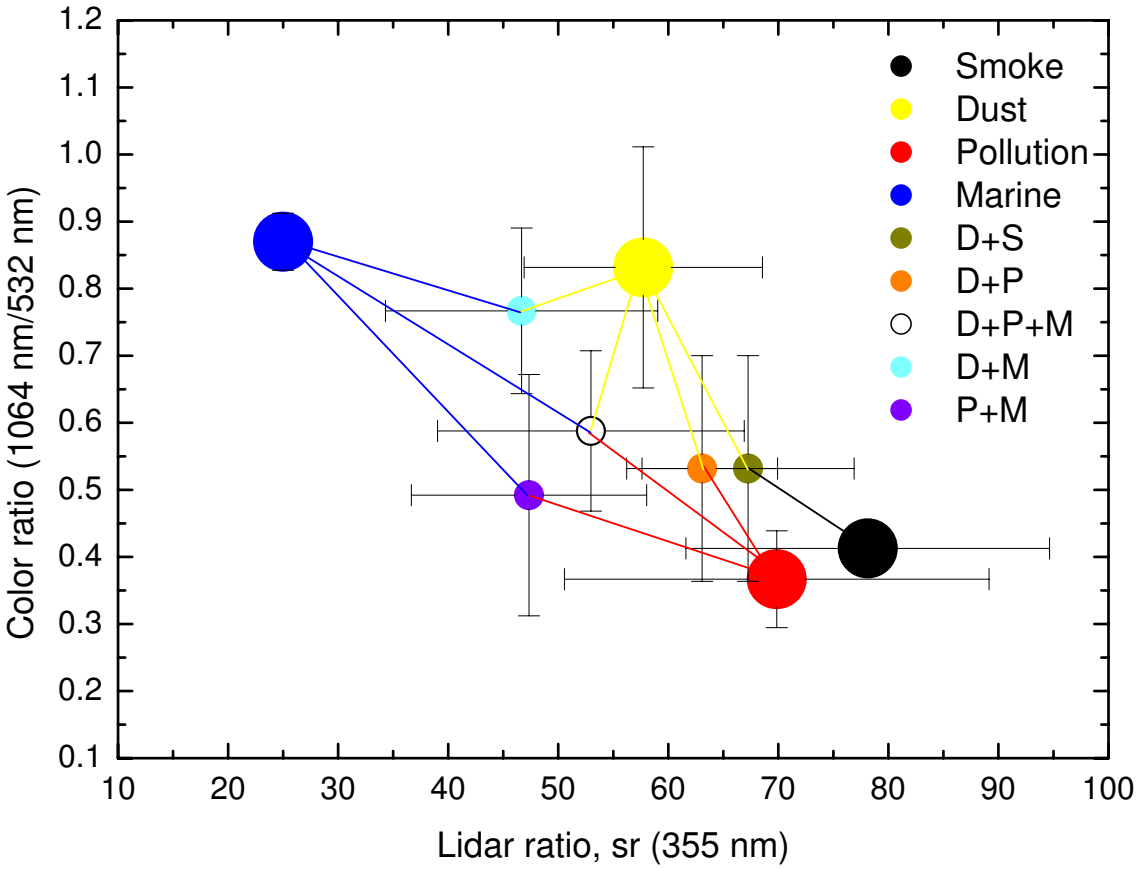

Figure 6.5: Relation between color ratio (1064/532 nm) as measured with CALIOP and lidar ratio at 355 nm as measured with ATLID for pure and mixed aerosol tpyes derived from the long-term database. The lidar ratio of marine aerosol is set to the literature value of 25 sr because of the lack of data from the present study.

A very interesting result which becomes clear from Fig. 6.5 is that the pure types of smoke, dust, pollution, and marine aerosol define the corner points of this two-dimensional

distribution and that all mixtures lie on nearly straight connecting lines between their constituents. Such a clear behavior is not necessarily expected, because particles can be mixed in different ways, externally or internally. In the case of internal mixtures, the individual properties of the constituents are not conserved and optical parameters may completely change. For instance, when discussing the aging (and thus mixing) of dust during transport, it is often assumed that soluble substances (e.g., sea salt or organic matter) condensate on the dust particles and produce a coating. In such a case the particles would grow, change their absorption properties, and probably lose their non-spherical shape, so that it is not very likely that the optical parameters of the mixture remain on a straight line in between those of the constituents. If we can neglect the internal mixing and presume the dominance of external mixing when airmasses cross different source regions, we can work with probability density functions to describe the state of mixing of the aerosol, i.e. we can define "trajectories" between pure aerosol types in a multi-dimensional parameter space on which the mixtures occur.

With only one of the two intensive optical parameters shown in Fig. 6.5, a clear aerosol typing is not possible. With the color ratio (i.e. CALIOP-like instruments), aerosols with a strong coarse particle mode (dust and marine aerosol) can be distinguished from aerosols with a dominating fine particle mode (smoke and pollution). In terms of the lidar ratio (i.e. ATLID-like instruments) the different types spread a bit better, but only the marine aerosol is clearly separated from the other types. Thus it is very important to consider the particle depolarization ratio as an additional intensive parameter that can help in the classification.

In the present study we used the volume depolarization ratio (see Eq. (4.4)) provided by a few stations to distinguish spherical and non-spherical scatterers. In Tab. 6.1 and 6.2 a few numbers are given. However, the volume depolarization is a rather qualitative measure and not suitable for a distinct aerosol typing, because it describes the depolarizing properties of the scattering volume containing both air and particles. In clouds, where molecular scattering is negligible, the volume depolarization ratio is well suited to distinguish between ice crystals and droplets. For aerosols, we need the particle depolarization ratio, i.e. the depolarization ratio corrected for molecular scattering. Measurements of the particle depolarization ratio are not trivial and require a careful instrument characterization and a specific calibration (*Freudenthaler et al.*, 2009). For the further discussion, we also have to make clear that we speak about the linear depolarization, i.e. the emission of linearly polarized laser light and the detection of the components that are parallel and cross-polarized with respect to the plane of the laser polarization (in contrast to circular polarization as used for ALADIN, see also Chapter 9).

The particle depolarization ratio is not an EARLINET standard product yet and only few measurements with well-calibrated systems are available. Therefore, we briefly discuss

values from the literature in order to complete the discussion on aerosol typing. Large efforts to measure the particle depolarization ratio have been made during the SAMUM campaigns (*Freudenthaler et al.*, 2009; *Tesche*, 2011; *Groß et al.*, 2011). For pure mineral dust, values of 0.31±0.03 and 0.26±0.06 at 532 and 355 nm, respectively, were found in the Saharan source region during SAMUM–1 (*Freudenthaler et al.*, 2009). Very similar values were observed in the fresh ash plume of Eyjafjallajökull (*Ansmann et al.*, 2010). For marine aerosol and smoke obtained at Cape Verde during SAMUM–2 the typical values were 0.03 and 0.05, respectively (*Groß et al.*, 2011). Especially for the purpose of aerosol typing, *Sakai et al.* (2010) measured linear depolarization ratios of mineral, sea-salt, and ammonium-sulfate particles in the laboratory. They found values of 0.39±0.04 for large and 0.17±0.03 to 0.14±0.03 for small Asian and Saharan dust particles. Dry sea salt, which occurs at humidities below 45% only, showed values of 0.08±0.01. In the liquid state, the number dropped to 0.01±0.001. The same value was found for liquid ammonium-sulfate particles.

It can be seen that only large mineral particles as contained in desert or soil dust and ash generate a considerable light depolarization, which can be used to distinguish this kind of material from other aerosols. By knowing the depolarization properties of these particles, it is even possible to quantify their contribution to a two-component mixture, as it has been demonstrated for mixtures of dust and smoke (*Tesche et al.*, 2009a) and volcanic ash and sulfate (*Tesche et al.*, 2011).

Figure 6.6 illustrates the location of dust, smoke, pollution, and marine aerosol in the three-dimensional space of the intensive particle properties color ratio (1064/532 nm), lidar ratio (355 nm), and depolarization ratio. For the latter parameter, typical values of 0.30, 0.05, 0.03, and 0.01 are assumed for dust, smoke, marine aerosol, and pollution, respectively. A wavelength dependence is not considered (although a small wavelength dependence has been found for dust, see above). The projections into the x–z and y–z planes show the two-dimensional parameter spaces of ATLID and CALIOP, respectively. It can be seen that with both lidar types, primarily three groups of aerosols are clearly discriminable: dust (and ash, not shown), marine aerosol, and pollution/smoke. A clear discrimination of pollution and smoke is difficult. Here, we also have to keep in mind that smoke and pollution properties are quite variable and that we show only mean values for Europe. The properties of smoke change in dependence of the fire type (smoldering or flaming) and of the transport time (see also Sec. 3.2). The properties of anthropogenic pollution are obviously different in highly industrialized regions of Europe and North America with their strong environmental regulations and in Southeast Asia (*Franke et al.*, 2003; *Cattrall et al.*, 2005). Nevertheless, threshold values to distinguish small and highly absorbing particles (higher lidar ratio, smaller color ratio) from coarser and less-absorbing particles (smaller lidar ratio, higher color ratio) can be introduced. The major conclusion

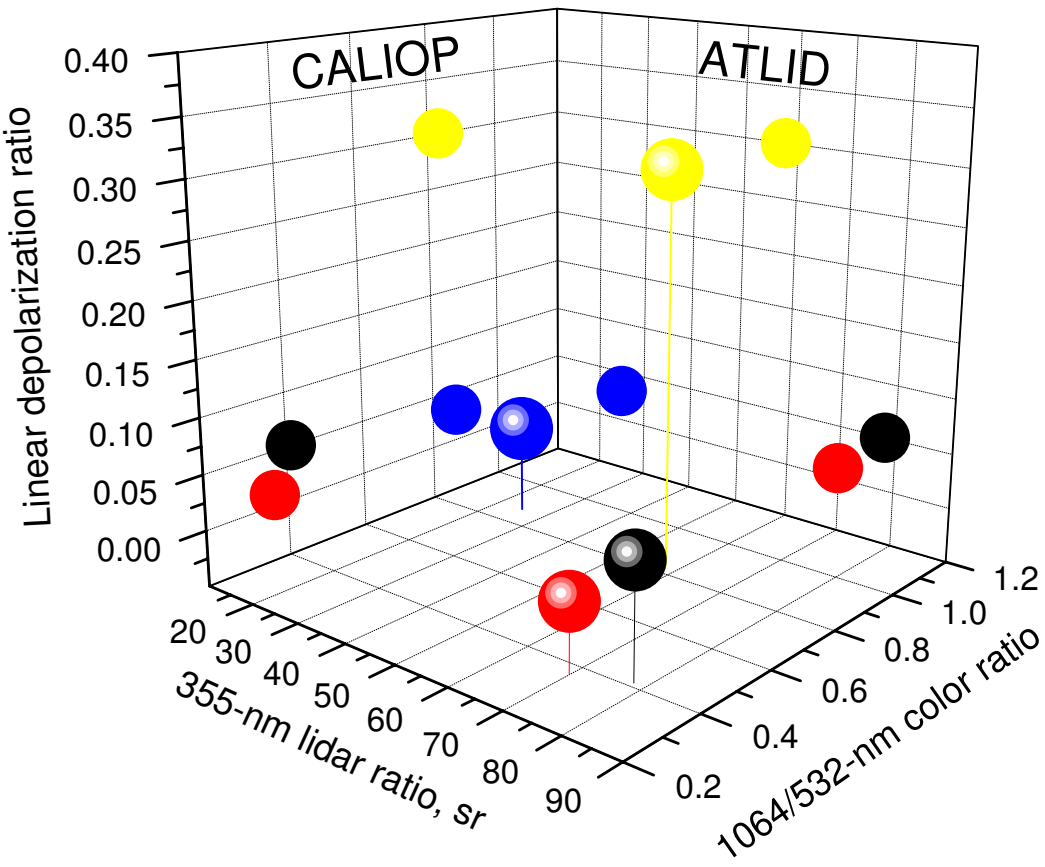

Figure 6.6: Three-dimensional relation between color ratio (1064/532 nm), lidar ratio at 355 nm, and linear depolarization ratio for the pure aerosol types (marine – blue, dust – yellow, pollution – red, smoke – black). The two-dimensional projections into the x–z and y–z planes show the separation of aerosol types as seen by ATLID and CALIOP, respectively. Because of the lack of data from the present study, the lidar ratio of marine aerosol and linear depolarization ratios are taken from the literature.

from Fig. 6.6 is that it is possible to apply a common aerosol typing scheme to CALIOP and ATLID data and thus to harmonize the long-term observations with both instruments by applying respective conversion factors, as derived in this study, for the major aerosol types.

Chapter 7

Representativeness study

In this chapter, we discuss the representativeness of CALIPSO aerosol and cloud measurements through comparisons with EARLINET ground-based reference points. The representativeness study reported in this chapter is based on the use of CALIPSO L2 Version 2 data products. After a short introduction, the overall methodology for the representativeness study is presented. In Section 7.3 examples of the representativeness study for specific scenarios (such as Saharan dust intrusion over Europe), for seasons, for each identified cluster of EARLINET stations, and for each identified type of cloud are reported.

7.1 Introduction

The high variability both in space and time of tropospheric aerosols is the main cause of the high uncertainty about radiative forcing related to tropospheric aerosols and their interaction with clouds *Forster et al.* (2007). In particular, before CALIPSO launch, information on high-resolution global vertical profiles of aerosol and clouds were missing. Therefore, vertical gradients are typically not considered in the models resulting in a uncertainty on particle (aerosol and clouds) distribution. For the first time, it is possible to investigate the 4-dimensional distribution of aerosols and clouds on a global scale thanks to the high-resolution vertical profiles provided by CALIOP, the lidar onboard CALIPSO. However, because of the small footprint and the revisit time of 16 days, how well these CALIOP measurements represent the atmospheric conditions of a surrounding area over a longer time is an important issue to be investigated. An integrated study of CALIPSO and EARLINET correlative measurements opens new possibilities for spatial (both horizontal and vertical) and temporal representativeness investigation of polar-orbit satellite measurements also in terms of revisit time. In fact, EARLINET provides well-established high-quality data that can be considered as a reference point for aerosol studies. In addition, the geographical distribution of EARLINET stations over Europe allows us to in-

vestigate a large variety of different aerosol contents in the free troposphere and the local planetary boundary layer (e.g. *Matthias et al.*, 2004; *Pappalardo et al.*, 2004b; *Wandinger et al.*, 2004; *Mona et al.*, 2006; *Amiridis et al.*, 2008; *Papayannis et al.*, 2008).

7.2 Approach of the representativeness study

For the representativeness study, the geophysical products stored in the long-term aerosol and cloud database are used. In particular, comparisons of ground-based and satellite measurements at different temporal and spatial distances contained in Part D of the database are the backbone for the representativeness study (see Section 4.4). Part D tables contain the information on the EARLINET and CALIPSO products correlation analysis related to a selection of EARLINET and CALIPSO profiles (contained in Part A and Part D of the database, respectively) and aerosol and cloud feature products as observed by EARLINET (Part B of the database) and CALIPSO (Part D of the database).

Following the measurements strategy established for the ESA–CALIPSO study (see Section 2.4), EARLINET correlative measurements are performed at single stations in correspondence of CALIPSO overpass within 100 km (Case A measurements, simultaneously with stations in the same cluster (Case B measurements) and for large scales at stations in different clusters during interesting additional cases like Saharan dust intrusions and forest fires (Case C measurements)). In this way, the horizontal distance between CALIPSO and EARLINET selected stations covers a large interval: 0–100 km for Case A with almost 60% of the cases within 50 km, 120–750 km for Case B with almost 70% of the cases within 500 km, and also larger distances for Case C measurements. This allows us to investigate the variability on different horizontal scales, from regional to continental. Records of measurements lasting 150 minutes allows us to investigate the temporal variability of aerosol/clouds fields.

Two different approaches for the correlation study are used according to the actual strategy for the correlative measurements: a point-to-point comparison, in which each EARLINET observation is compared with the corresponding CALIPSO overpass measurement, and a multiple-point approach for different scenarios such as long-range aerosol transport, in which multiple-point observations are compared to appropriate horizontal averages along the satellite cross section. In particular, the spatial variability of aerosol/cloud fields is investigated through CALIPSO–EARLINET differences for almost simultaneous measurements performed at different relative horizontal distances (from 0 to 750 km with Case A and B measurements and larger distances with Case C measurements). The 150-minute time series of measurements performed during Case A measurements allow the study of the temporal variability independent of the spatial variability. Finally, observations of long-range transport over Europe provide information on the variability on larger

horizontal scales and within different time intervals. In these situations, the variability can be particularly high both in terms of geometrical and optical properties (e.g. *Papayannis et al.*, 2008; *Mona et al.*, 2006; *Wang et al.*, 2008; *Villani et al.*, 2006). Therefore, point-to-point comparisons would be not sufficient and a specific subset of CALIPSO data related to Europe and surrounding areas has to be considered.

Furthermore, the large database collected during the ESA–CALIPSO study allows climatological and statistical analysis for each identified cluster of EARLINET stations, for specific scenarios (such as Saharan dust intrusion over Europe), seasons, and for each type of identified cloud (water, mixed-phase and ice clouds), in terms of geometrical and optical properties.

7.3 Examples of approach for representativeness study

7.3.1 Specific scenario: Saharan dust outbreak, 26–31 May 2008

The observational period of 26–31 May 2008 has been chosen for a first correlation analysis for both single-point and multiple-point observations as a period with a large number of performed measurements. In fact, during these days 15 Case A, 7 additional Case B measurements, and 56 additional Case C measurements were performed because of the Saharan dust alert distributed to the EARLINET stations (see also Section 5.1.2.2). At the moment, 420 EARLINET files are on the database for this period corresponding to 46 of the measurements reported above, providing a significant ground-based database for illustrating the representativeness study strategy.

Dust coming from the Western and Central Sahara was forecast over the Central and Eastern Mediterranean reaching also Central Europe by the DREAM model for this period. On these days, a large amount of aerosol was detected by CALIPSO over Africa and a dust plume over Europe was observed at altitudes between the ground and 5–6 km a.s.l. For cases like this one, there is a high horizontal variability both in geometrical and optical aerosol layer properties, because of the horizontal extension of the aerosol source, as can be seen in an example of the CALIPSO cross section of the total attenuated backscatter measured at 532 nm in this period and reported in Figure 7.1.

From the ground-based point of view, it is clear that at a fixed observational point a significant temporal variability of geometrical features as well as of the their optical properties is observed. An example of the temporal evolution of the lidar range-corrected signal at 1064 nm measured at Potenza on 29–30 May 2008, 19.36–02.50 UT, is reported in Figure 7.2.

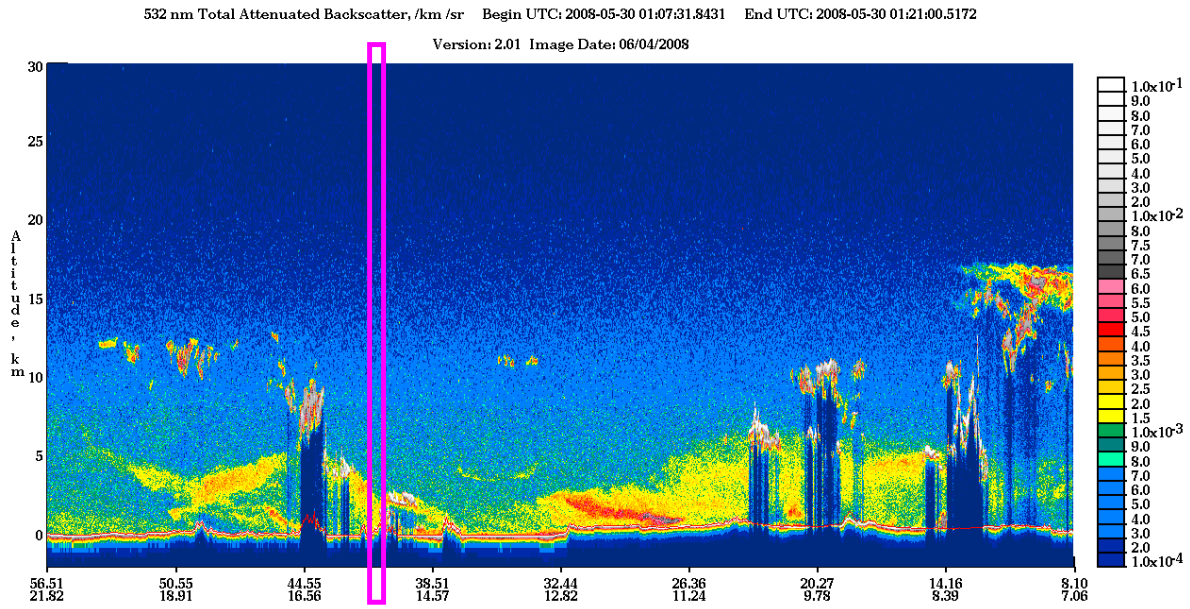

Figure 7.1: Cross section of the total attenuated backscatter measured by CALIPSO at 532 nm on 30 May 2008. The purple box highlights the overpass at Potenza.

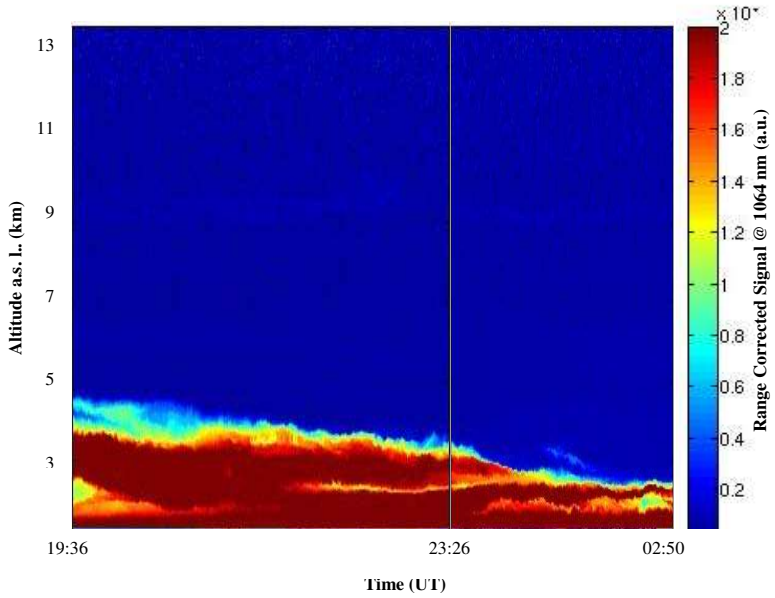

Figure 7.2: Temporal evolution of the lidar range-corrected signal at 1064 nm measured at Potenza on 29–30 May 2008.

Figure 7.3 shows vertical profiles of the aerosol backscatter and extinction coefficients at 532 nm as almost simultaneously measured at CNR–IMAA Potenza EARLINET station

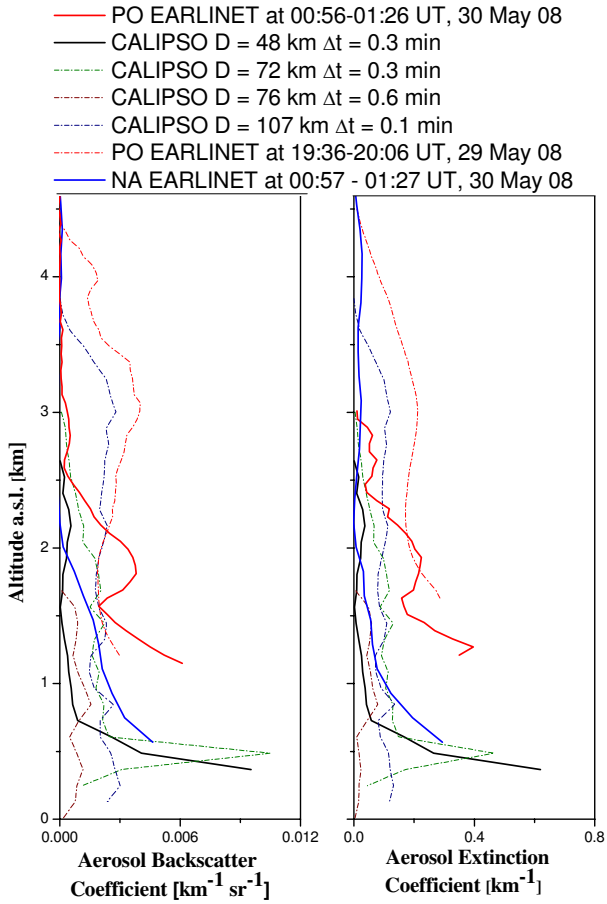

Figure 7.3: Aerosol backscatter (left panel) and extinction coefficient (right panel) at 532 nm measured at Potenza (PO) and Naples (NA) EARLINET stations and obtained from CALIPSO observations at different horizontal distance from Potenza lidar station for the 29–30 May 2008 night-time case.

and CALIOP at different horizontal distances. Additional profiles measured at CNR-IMAA at different times are reported to provide information about the temporal variability. Profiles measured at Naples EARLINET station are also reported in order to provide information related to a larger horizontal distance between independent observations (Naples is about 130 km north-west of Potenza). For the closest and simultaneous measurements, reported in Figure 7.3 as solid lines, large differences are observed for both aerosol backscatter and extinction coefficients also in terms of the vertical layering structure as observed by CALIPSO and by the two ground-based stations. Differences observed in almost simultaneous CALIPSO measurements (dotted lines) are also a consequence of the horizontal inhomogeneity of the aerosol field. There seems to be a better agreement for the aerosol backscatter coefficient between the CALIPSO observation related to an

horizontal distance of about 107 km from Potenza (dotted blue line) and the Potenza measurement on 29 May evening (dotted red line) corresponding to a temporal shift from the CALIPSO observation of 320 min. This corresponds to a wind speed of about 5.6 m/s in agreement with the typical wind speed of 5–10 m/s observed over Potenza at 2–5 km a.s.l. A similar agreement is not observed for the corresponding aerosol extinction coefficient. However, it has to be considered that CALIPSO extinction measurements are strongly affected by the assumptions on the lidar ratio needed for the retrieval and this can lead to the observed differences.

The absolute differences between ground-based and spaceborne data and the percentage differences with respect to the EARLINET observations included in Part D of the ESA–CALIPSO database are used to study the horizontal and temporal variability for the considered Saharan dust case. In particular, we focus on the backscatter coefficient at 532 nm in the following since it is a primary product of CALIPSO and is available from most of the EARLINET participating stations, so that a larger data set can be used. Comparisons within 100 km (Case A measurements) and different time shift are used to study the temporal variability of the aerosol field, while almost simultaneous measurements (within 10 minutes from the CALIPSO overpass) at different horizontal distances are selected in order to study the spatial variability.

7.3.1.1 Comparisons within 100 km and different time shifts

Starting from the distance in time and space reported in Part D of the database, all differences profiles related to spaceborne vs ground-based lidar horizontal distance below 100 km (Case A measurements) are selected and classified based on the time shift between the two observations. Figure 7.4 reports the mean differences of observed backscatter coefficient for different time shifts. In Figure 7.4a, time shifts lower than 10, 30, 60, 120, and 720 minutes are considered. Figure 7.4b reports the mean differences of observed backscatter coefficient calculated from 10 available difference profiles for the class $\Delta t <$ 10 min, 11 for $\Delta t <$ 30min, 15 for 30 min $< \Delta t <$ 60 min, 13 for 60 min $< \Delta t <$ 120 min, and 26 for 120 min $< \Delta t <$ 720 min.

Apart from the 0–2 km where typically local aerosol content is present, differences seem to do not significantly change when larger time shifts are considered. In the first 2 km of altitude, Figure 7.4a shows that the mean differences decrease with the increase of the time shift. However, mean difference profiles, as reported in 7.4b, show a more clear separation between time shifts shorter and longer that 30 minutes. In particular, the largest mean differences are observed below about 2 km of altitude, with mean values of 0.008 $km^{-1}sr^{-1}$ and 0.005 $km^{-1}sr^{-1}$ for the 10 and 30 minutes time shifts respectively, while smaller mean differences are found for larger time shifts, -0.003 $km^{-1}sr^{-1}$ for 30 min

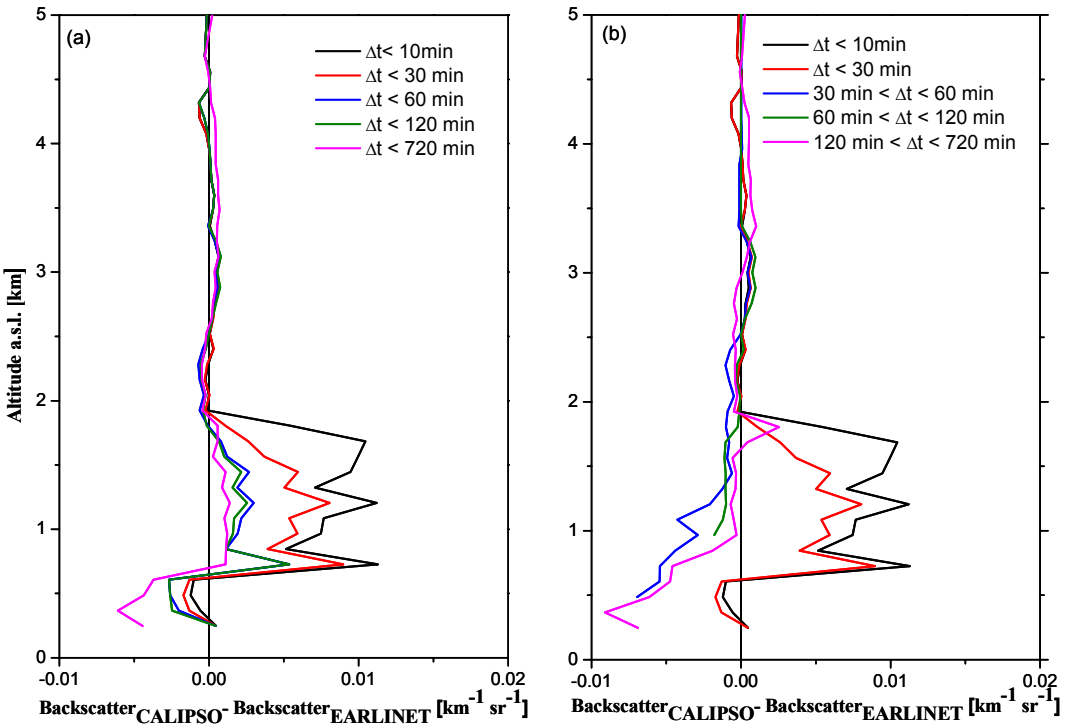

Figure 7.4: Mean difference profiles ($\text{Backscatter}_{\text{CALIPSO}}$–$\text{Backscatter}_{\text{EARLINET}}$) at 532 nm as obtained by averaging over 26-31 May 2008 cases with a spaceborne vs ground-based lidar horizontal distance below 100 km and divided in five time-shift (Δt) classes: time shifts lower than 10, 30, 60, 120 and 720 minutes.

$< \Delta t <$ 60 min and -0.001 $\text{km}^{-1}\text{sr}^{-1}$ for both 60 min $< \Delta t <$ 120 min and 120 min $< \Delta t <$ 720 min. In the free troposphere, above 2 km of altitude, the mean differences profiles do not change significantly with the time shifts, with values ranging between 0.00005 and 0.0001 $\text{km}^{-1}\text{sr}^{-1}$. Smaller mean differences, observed for altitudes below 2 km and for time shifts larger than 30 minutes are due to the presence of both positive and negative differences, which means that the CALIPSO and EARLINET observations, for this event, are less correlated for time shifts larger than 30 minutes.

Considering that the profile structures as seen by CALIPSO and EARLINET are similar, we can, for a more quantitative study, compare the count distributions of CALIPSO and EARLINET backscatter-coefficient measurements for these classes with different time shifts. This can be done using the corresponding CALIPSO and EARLINET profiles contained in Part A and Part D of the database and related to the difference profiles through the relational database itself. Figure 7.5 shows one example of count distribution for the backscatter coefficient measured at 532 nm by CALIPSO and EARLINET with 100 km as maximum horizontal distance and 10 minutes as maximum time shift between the two observations. The median values of the two datasets are in good agree-

ment (0.0005 $km^{-1}sr^{-1}$ and 0.0006 $km^{-1}sr^{-1}$ for CALIPSO and EARLINET observations, respectively). The good agreement between the two distributions is evident also from Figure 7.5 and it can be quantified through the linear correlation coefficient of the two count distributions that is 0.9 for this case.

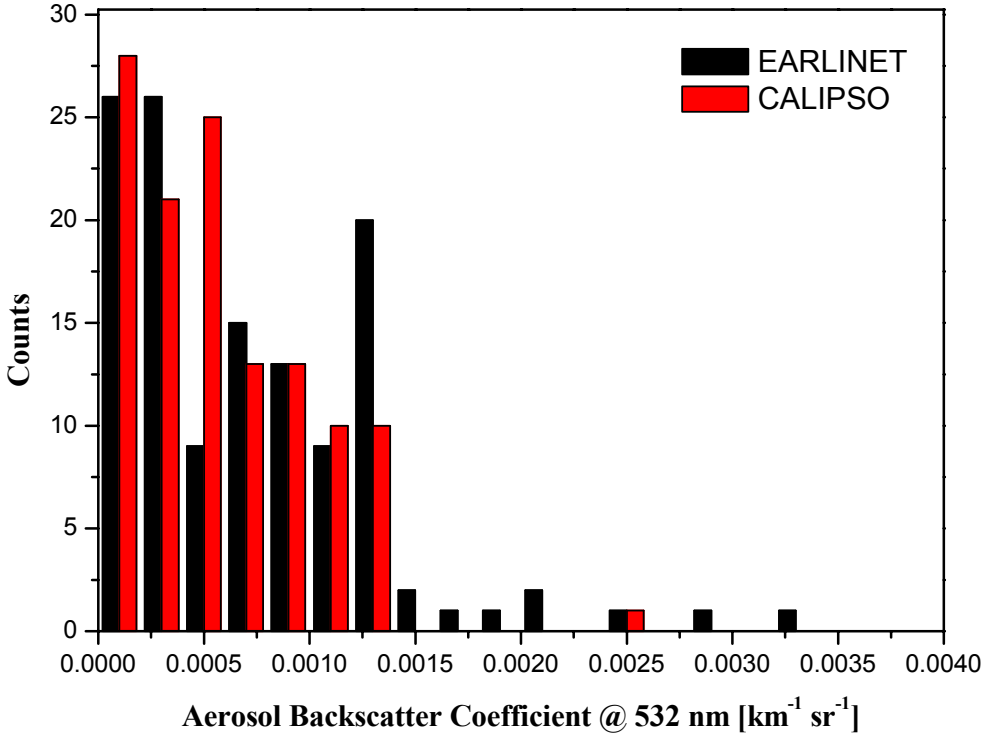

Figure 7.5: Count distribution of EARLINET and CALIPSO measured values of aerosol backscatter coefficient at 532 nm for distances lower than 100 km and 10 minutes.

Figure 7.6 reports the behavior of the correlation coefficient between CALIPSO and EARLINET backscatter count distributions as a function of the maximum considered time shift between the two observations. Figure 7.6a reports the correlation coefficient for the time shift classes of Δt lower than 10, 30, 60, 120, and 720 minutes (corresponding to what is shown in Figure 7.4a). Figure 7.6b reports the correlation coefficient for the time shift classes $\Delta t < 10$ min, $\Delta t < 30$ min, 30 min $\leq \Delta t < 60$ min, 60 min $\leq \Delta t < 120$ min, and 120 min $\leq \Delta t < 720$ min.

In both figures it is clear that the correlation coefficient decreases with the increase of the time shift. However, in Figure 7.6b, a sharper drop is observed. In particular, the correlation coefficient remains around 0.9 for time shifts up to 30 minutes and decreases to 0.76 for 30 min $\leq \Delta t < 60$ min, 0.56 for 660 min $\leq \Delta t < 120$ min, and 0.57 for 120 min $\leq \Delta t < 720$ min. Therefore, for time shifts larger than 30 minutes the two observations are not correlated, what implies that on a spatial scale of 100 km the aerosol time variability for this event is of the order of 30 minutes.

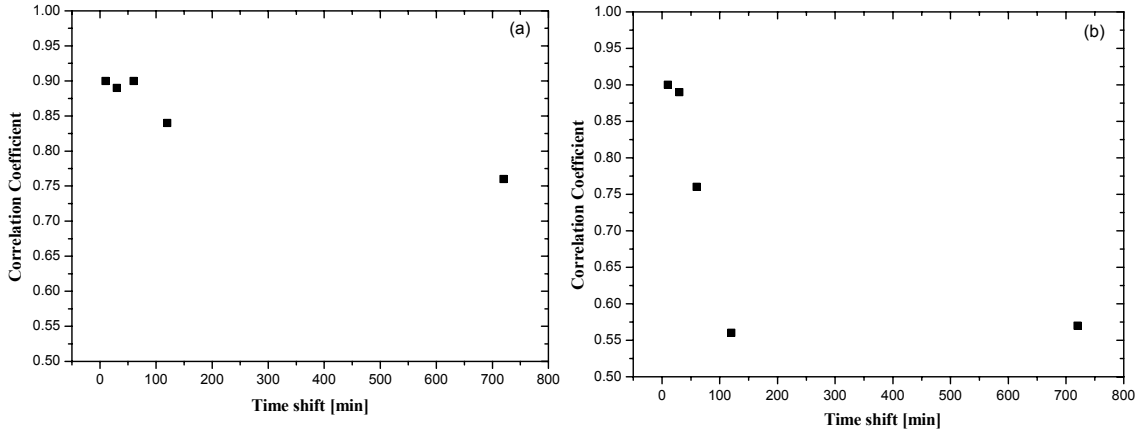

Figure 7.6: Correlation coefficient between CALIPSO and EARLINET backscatter count distributions for horizontal distances lower than 100 km as a function of the maximum considered time shift between the two observations. a) Correlation coefficient for the time shift classes lower than 10, 30, 60, 120 and 720 minutes. b) Correlation coefficient for the time shift classes $\Delta t < 10$ min, $\Delta t < 30$ min, 30 min $\leq \Delta t < 60$ min, 60 min $\leq \Delta t < 120$ min, and 120 min $\leq \Delta t < 720$ min.

7.3.1.2 Comparisons within 10 minutes and different horizontal distances

While in the previous section, the temporal variability has been investigated, here the spatial variability is studied by means of almost simultaneous measurements (within 10 minutes from the CALIPSO overpass) at different horizontal distances. As previously in this study, difference profiles and spatial-temporal distance information reported in Part D of the ESA–CALIPSO database are used and the related EARLINET and CALIPSO profiles are compared. Following the measurements plan, during CALIPSO overpass above one EARLINET station also other stations included in the same cluster perform measurements. In addition, for the event considered here, 56 additional measurements are performed by the network as Case C measurements allowing to collect a large data set of EARLINET measurements within 10 minutes and 2000 km (considered here as maximum distance for the comparisons) of the CALIPSO overpass. This large data set of almost simultaneous measurements allows us to investigate the spatial variability in eight classes of horizontal distances (D) lower than 100, 200, 300, 400, 500, 1000, 1500, and 2000 km (Figure 7.7a) and for $D < 100$ km, 100 km$\leq D < 200$ km, 200 km$\leq D < 300$ km, 300 km$\leq D < 400$ km, 400 km$\leq D < 500$ km, 500 km$\leq D < 1000$ km, 1000 km$\leq D < 1500$ km, and 1500 km$\leq D < 2000$ km (Figure 7.7b). In Figure 7.7b, the mean difference profile has been calculated from 10 available difference profiles for the class $D < 100$ km, 20 for 100 km$\leq D < 200$ km, 34 for 200 km$\leq D < 300$ km, 23 for 300 km$\leq D < 400$ km, 25 for 400 km$\leq D < 500$ km, 103 for 500 km$\leq D < 1000$ km, 98 for 1000 km$\leq D < 1500$ km,

and 106 for 1500 km$\leq D <$ 2000 km.

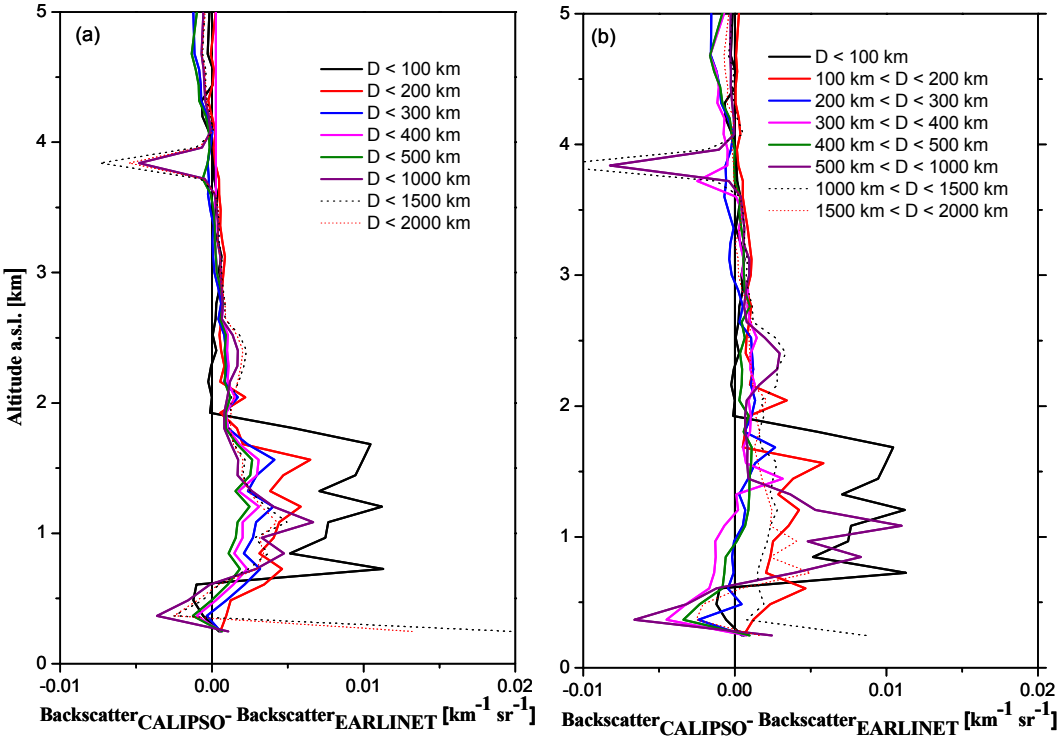

Figure 7.7: Mean difference profiles (Backscatter$_{\text{CALIPSO}}$–Backscatter$_{\text{EARLINET}}$) at 532 nm as obtained averaging over 26–31 May 2008 cases with a spaceborne vs ground-based lidar time shift lower than 10 minutes and divided in 8 horizontal distances (D) classes from 100 km to 2000 km.

As in the case of comparisons within 100 km and different time shifts, also here differences seem to not significantly change with horizontal distance. In the first 2 km of altitude, while in Figure 7.7a it is not possible to identify a behavior as function of the horizontal distance, in Figure 7.7b the mean difference profiles for horizontal distances within 200–500 km are much lower with respect to the other cases.

The correlation coefficient between CALIPSO and EARLINET backscatter count distributions is reported in Figure 7.8 as a function of the horizontal distances between the two observations. Figure 7.8a reports the correlation coefficient for horizontal distances (D) lower than 100, 200, 300, 400, 500, 1000, 1500, and 2000 km. Figure 7.8b reports the correlation coefficient for $D <$ 100 km, 100 km$\leq D <$ 200 km, 200 km$\leq D <$ 300 km, 300 km$\leq D <$ 400 km, 400 km$\leq D <$ 500 km, 500 km$\leq D <$ 1000 km, 1000 km$\leq D <$ 1500 km, and 1500 km$\leq D <$ 2000 km.

We observe in both figures a strong dependence on the horizontal distance with a decrease of the correlation coefficient with the increase of the horizontal distance. However,

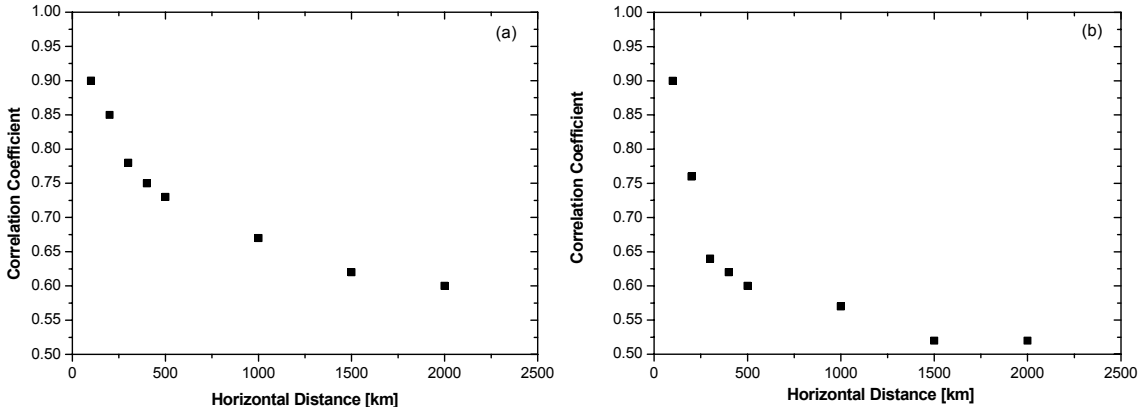

Figure 7.8: Correlation coefficient between CALIPSO and EARLINET backscatter count distributions for time shifts lower than 10 minutes reported as a function of the horizontal distance (D) between the two observations, a) for D lower than 100, 200, 300, 400, 500, 1000, 1500 and 2000 km and b) for $D < 100$ km, 100 km $\leq D <$ 200 km, 200 km $\leq D <$ 300 km, 300 km $\leq D <$ 400 km, 400 km $\leq D <$ 500 km, 500 km $\leq D <$ 1000 km, 1000 km $\leq D <$ 1500 km, and 1500 km $\leq D <$ 2000 km.

a sharper decrease is observed in Figure 7.8b where the correlation coefficient drops from 0.9 for a distance of $<$ 100 km to 0.76 for distances between 100 and 200 km. The correlation coefficient continues to decrease with the increase of the horizontal distance between the CALIPSO and EARLINET observations. This statistical analysis performed as function of spatial and temporal differences between CALIPSO and EARLINET observations provides an estimate of the spatial and temporal scale of the event under study.

7.3.1.3 Comparisons with different time and horizontal distances

While in the previous sections the temporal and the spatial variability have been investigated, here the strategy for studying the vertical variability is introduced. Here all CALIPSO and EARLINET backscatter-coefficient values measured at a maximum distance of 2000 km and with time shifts of $\leq$12 hours between the two observations are considered. In total we have about 75000 backscatter values available for this comparison.

Figure 7.9 shows count distributions of CALIPSO and EARLINET backscatter-coefficient data at 532 nm for all the available data. A good agreement is found for median values ($\text{Backscatter}_{\text{CALIPSO}} = 0.0011$ km^{-1}sr^{-1} and $\text{Backscatter}_{\text{EARLINET}} = 0.0012$ km^{-1}sr^{-1}) with a reasonable correlation coefficient of 0.86.

Count distributions of aerosol backscatter values measured by CALIPSO and EARLINET within 12 hours and 2000 km are studied for different altitudes and reported in Figure 7.10 for the altitude ranges 1–2 km (a), 2–3 km (b), and 4–5 km (c). In the first altitude range

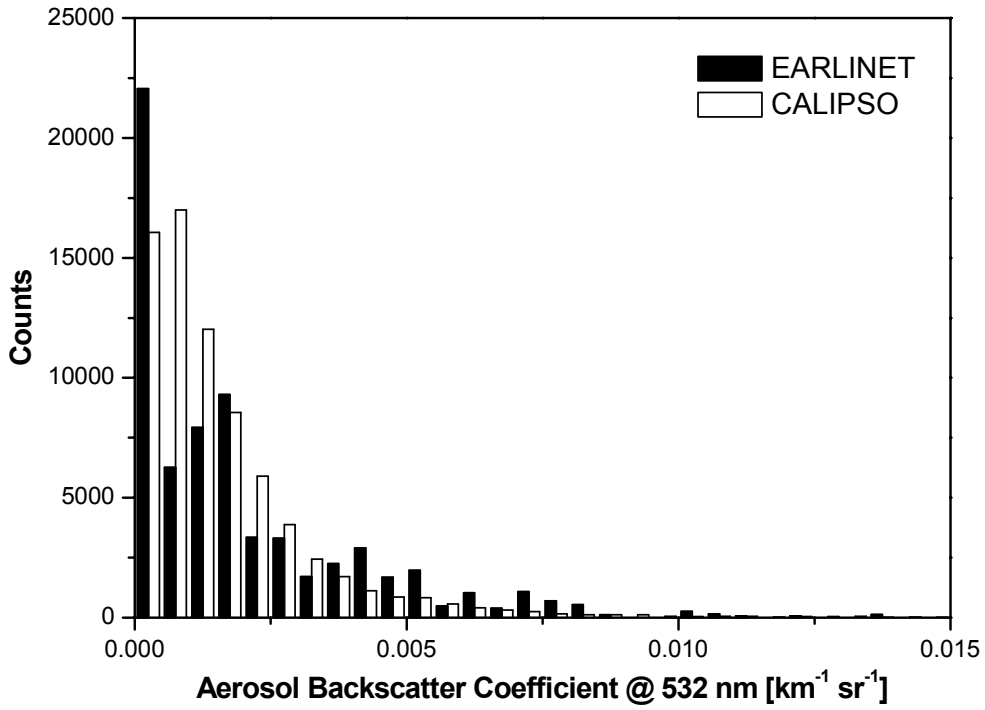

Figure 7.9: Count distributions of aerosol backscatter measured by CALIPSO and EARLINET within 12 hours and 2000 km of distance between the two measurements.

(1–2 km), the correlation between the two distributions is not very good as expected because of the more significant influence of the local boundary-layer aerosol. In the altitude range 2–3 km, a much better agreement is observed with a correlation coefficient of 0.92. This result is consistent with the expected behavior of such a major Saharan dust event extended on a continental scale. In the altitude range 4–5 km, we observe differences in both shape and values of the distributions. The observed differences still need to be investigated, also with view on geometrical properties of the detected layers. As mentioned before, CALIPSO Level 2 profiles only report values in identified layers. Therefore, for low aerosol load some backscatter data might be missing if the layer has not been identified. On the other hand, very large aerosol load can be misclassified as clouds and excluded from the Level 2 aerosol database. Hence both of these characteristics of the CALIPSO Level 2 aerosol data base should be taken into account when investigating spatial and temporal variability.

In the future, starting from all the available CALIPSO and EARLINET profiles, a complete analysis will allow climatological and statistical studies, in terms of geometrical and optical properties for each identified cluster of EARLINET stations, for specific scenarios (such as Saharan dust intrusions over Europe), for seasons, and for different aerosol and cloud types.

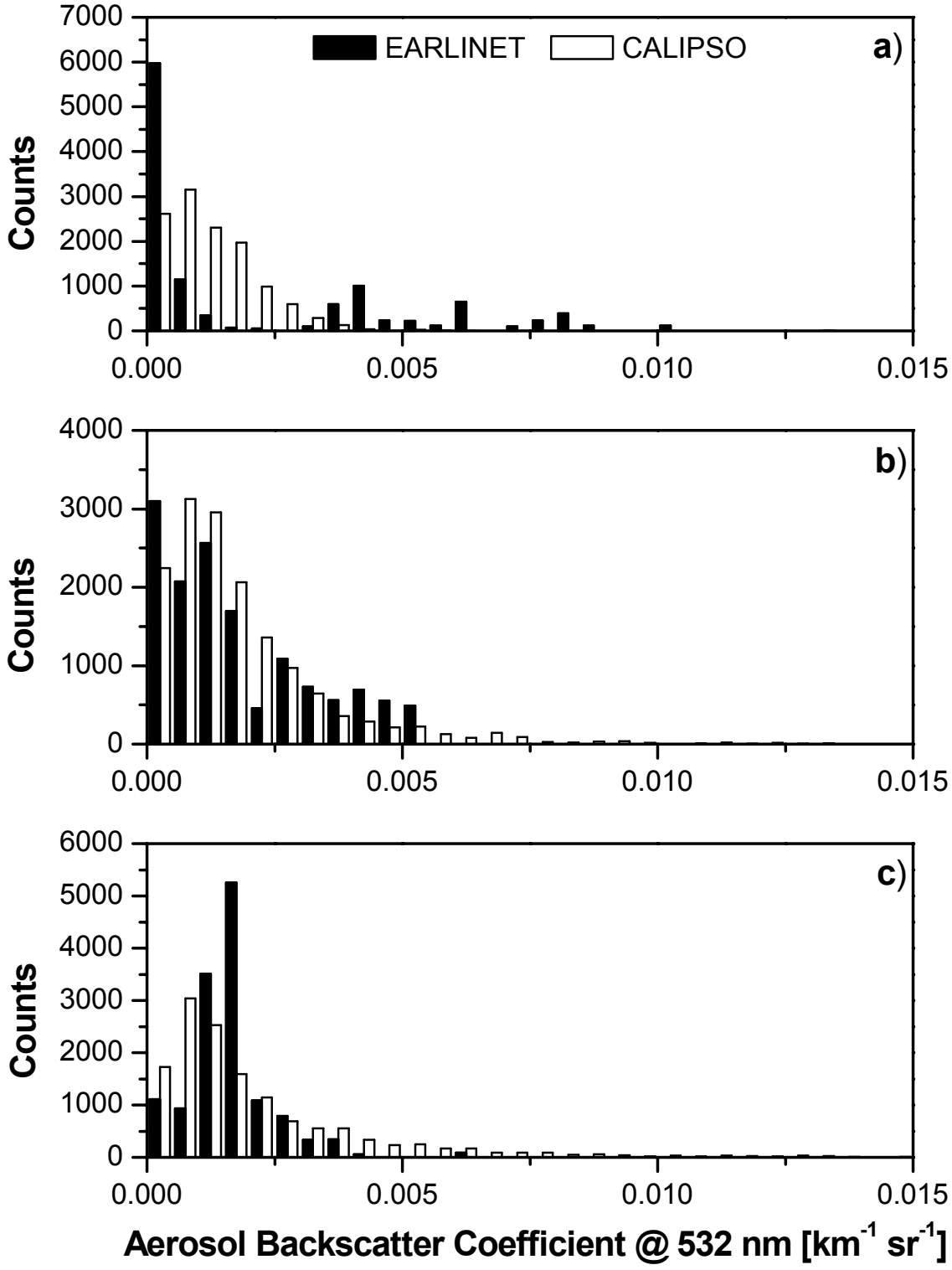

Figure 7.10: Count distributions of aerosol backscatter measured by CALIPSO and EARLINET within 12 hours and 2000 km of distance between the two measurements for three different altitudes ranges: a) 1–2 km, b) 2-3 km, and c) 4–5 km.

7.3.2 Central Mediterranean Cluster, 8 July 2008

On 8 July 2008 high-pressure conditions have favoured good correlative measurements in the CM cluster. No specific alert for Saharan dust or other events was sent for this day. Figure 7.11 shows the profiles of the aerosol backscatter coefficient at 532 nm as measured at the Napoli EARLINET station (NA) in coincidence with the CALIPSO overpass on

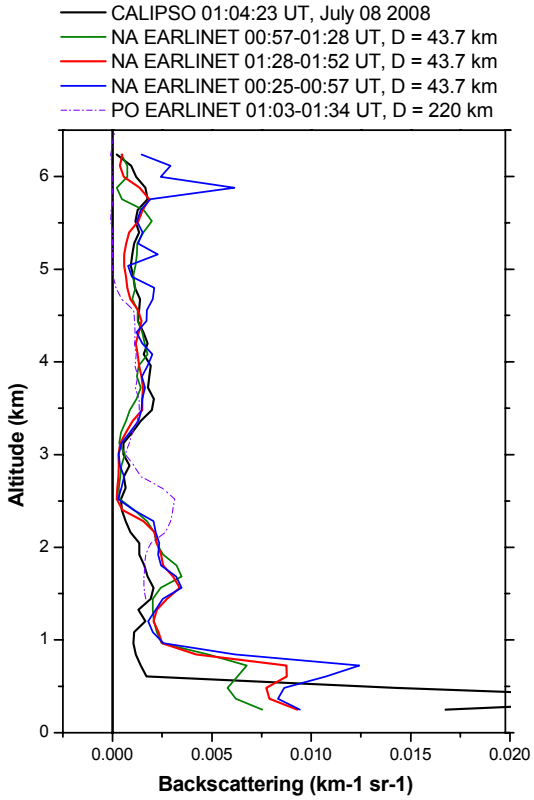

Figure 7.11: Aerosol backscatter (left panel) and extinction coefficient (right panel) at 532 nm measured at Naples (NA) and Potenza (PO) EARLINET stations and obtained from CALIPSO observations at different horizontal distance from Napoli lidar station for the 8 July 2008 night-time case.

8 July 2008 at 01:04:23 UT. In the figure also other backscatter profiles as measured at the Napoli ground-based station at different time shifts with respect to the CALIPSO overpass are reported together with the profile measured at the Potenza EARLINET station (PO) closest in time (about 130 km distance from Napoli). A good agreement between all ground-based observations and CALIPSO is observed above 3-km of altitude. This indicates pretty stable atmospheric conditions. At lower altitudes the structures as seen from CALIPSO and Napoli stations are similar, larger differences have been found at these low altitudes from the Potenza observation.

All difference profiles related to spaceborne vs ground-based observations have been se-

lected and classified for different horizontal distances and for different time shifts between the two observations. Figure 7.12 reports the correlation coefficient between CALIPSO and EARLINET backscatter count distribution as a function of horizontal distance for a time shift lower than 30 minutes. Good correlation is found for horizontal distances from 200 km up to 500 km.

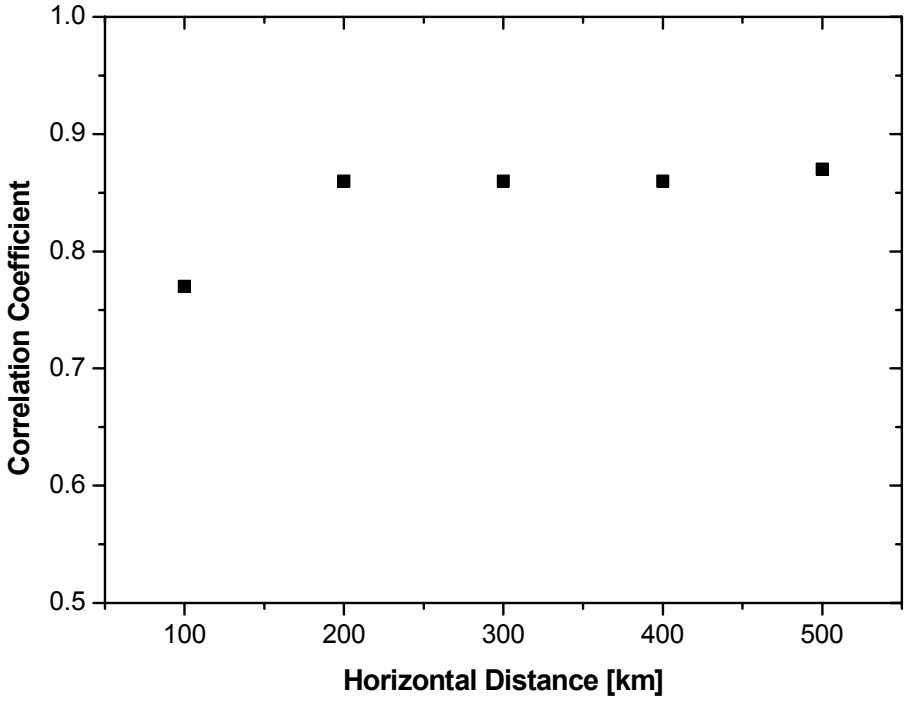

Figure 7.12: Correlation coefficient between CALIPSO and EARLINET backscatter count distribution as a function of horizontal distance for time shifts lower than 30 minutes.

Figure 7.13 reports the correlation coefficient between CALIPSO and EARLINET backscatter count distribution as a function of horizontal distance for a time shift 30 min$\leq$ Δt $<$ 60 min. In this case relatively good correlation is found for horizontal distances up to 200 km. Starting from all the available data, the analysis has been performed for different altitude levels (Figure 7.14).

7.3.3 Climatological study

CALIPSO has been acquiring data since June 2006 and at the same time EARLINET stations started performing correlative measurements for CALIPSO data full exploitation. These data allow the investigation of the aerosol and cloud content over Europe in a climatological sense. Seasonal statistical analysis is possible from CALIPSO and EARLINET data. Space vs ground-based comparisons are carried out with a point-to-point as well

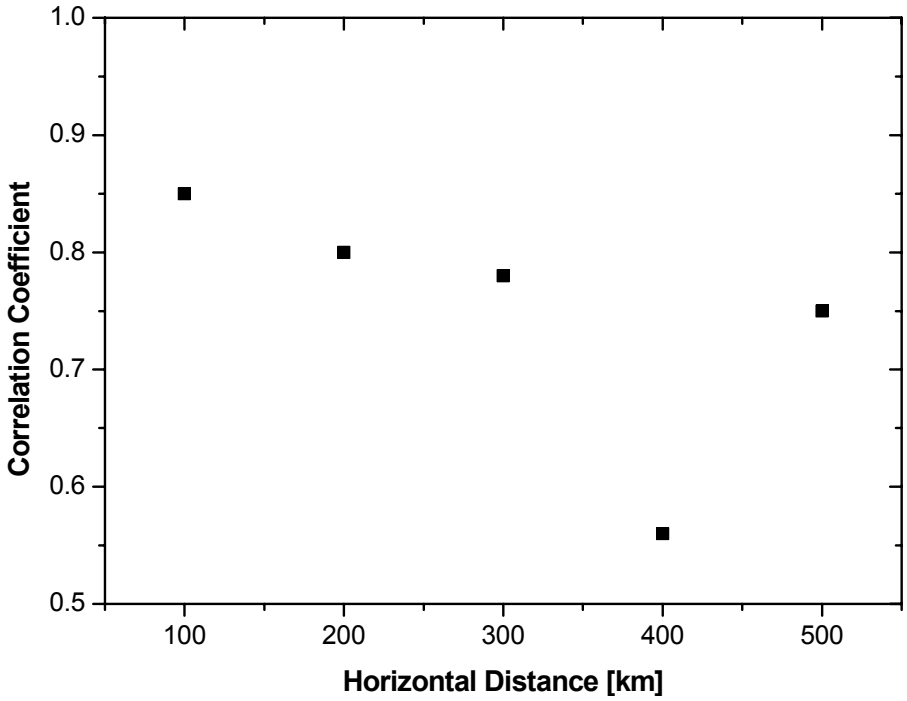

Figure 7.13: Correlation coefficient between CALIPSO and EARLINET backscatter count distribution as a function of horizontal distance for time shifts 30 min$\leq \Delta t <$ 60 min.

as a multiple-point approach. A point-to-point comparison based on Case A overpasses is essential to understand if CALIPSO measurements are representative of corresponding EARLINET station area in a climatological sense and if there are "systematic" deviations due to assumptions needed in the CALIPSO retrievals. A multiple-point comparison performed on areas of the four clusters will extend the representativeness study, in a climatological sense, to larger areas.

A first example of this kind of study is reported in the following. Two stations with different characteristics are selected for an example of comparison on seasonal behavior starting from Case A measurements: Leipzig as a continental Central European station and Potenza as a Mediterranean station. EARLINET data collected also before the ESA–CALIPSO study are used taking advantage on the previous EARLINET experience on CALIPSO correlative study. On the other hand, Version 3 of CALIPSO Level 2 Aerosol Profile data are currently not available yet. Therefore, data of Version 2.02 are used. For each overpass, only the CALIPSO profile closest in time and space is selected. The backscatter coefficient at 532 nm is considered in this example, because it is a primary product of CALIPSO and there is a large number of data available from EARLINET stations.

Figure 7.15 reports the count distributions of backscatter values at 532 nm measured during the CALIPSO overpasses by CALIOP and by EARLINET Leipzig station in spring,

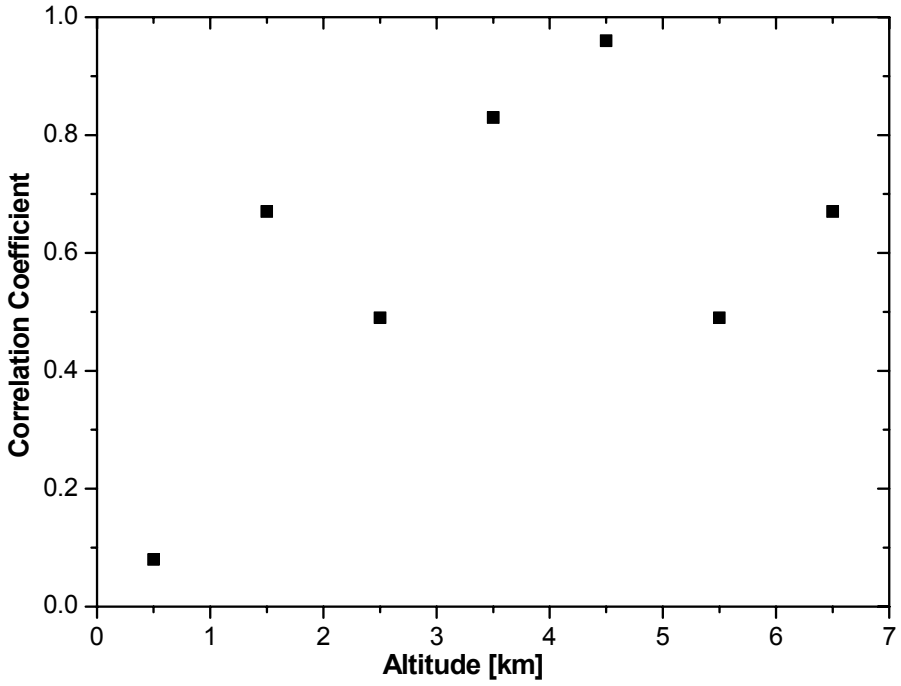

Figure 7.14: Correlation coefficient between CALIPSO and EARLINET backscatter count distribution as a function of altitude for all the available comparison data (within 2000 km and 720 minutes).

summer, and autumn. The bad weather conditions and the presence of low clouds limit the number of correlative ground-based measurements and the availability of aerosol profiles, so that the comparison for the winter season is not possible at the moment. During spring a good agreement is found. In particular for this period it results that the occurrence of backscatter values, collected in the layers identified by CALIPSO as aerosol layers, is higher for small backscatter values and decreases as backscatter increases. However, in satellite data as well as in EARLINET data it is evident a peak in the occurrences for values around 0.00125 $km^{-1}sr^{-1}$. In summer, the agreement is less good but this could be related to the limited data available for this period. For autumn, there is some agreement for values below 0.002 $km^{-1}sr^{-1}$, in fact the two distributions decrease fast with the increase of observed backscatter values, but in CALIPSO data many large values in backscatter are collected. This is probably due to a misclassification of some layers.

The same kind of study has been carried out also for Potenza station. Figure 7.16 reports for this station the backscatter count distributions for the different seasons. Also for Potenza during the winter too few cases have been collected due to low clouds and bad weather conditions. At this station, a good agreement is obtained for summer season, when the distribution of backscatter values has a long tail with a large number of occurrences of values as high as 0.003 $km^{-1}sr^{-1}$, corresponding to the occurrences of dust

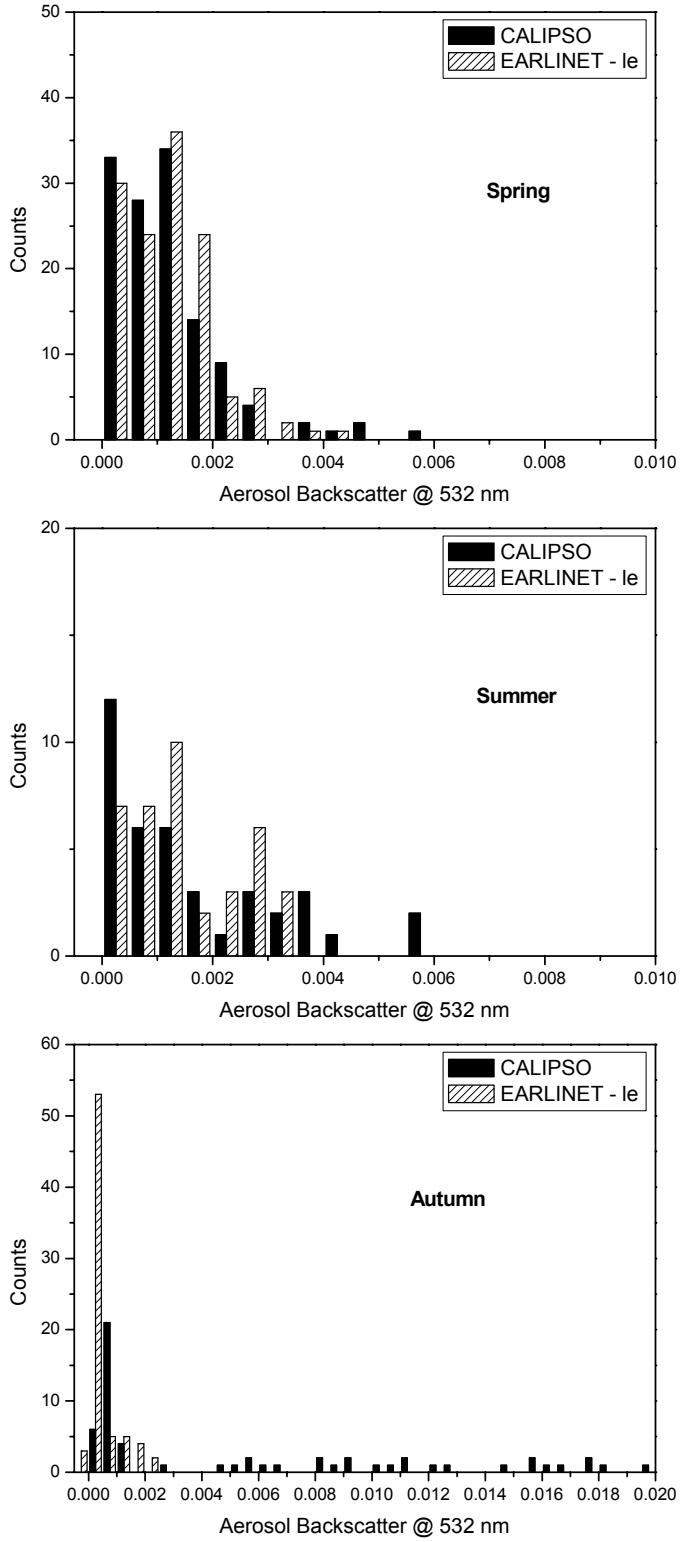

Figure 7.15: Count distributions of values of aerosol backscatter coefficient at 532 nm measured during spring, summer, and autumn at Leipzig EARLINET station and by CALIPSO (Case A measurements).

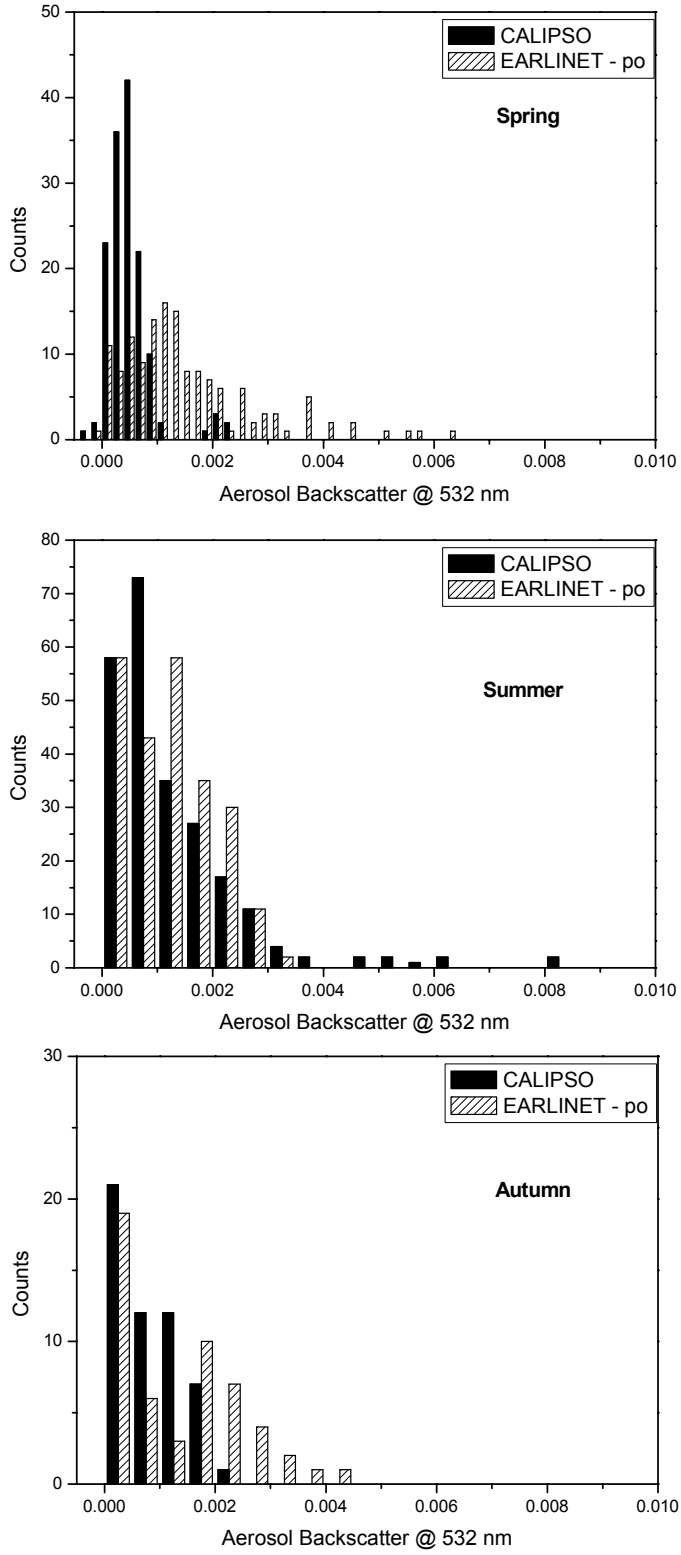

Figure 7.16: Count distributions of values of aerosol backscatter coefficient at 532 nm measured during spring, summer, and autumn at Potenza EARLINET station and by CALIPSO (Case A measurements).

coming over Potenza from the Sahara region (*Mona et al.*, 2006). For both autumn and spring, there is a satisfactory agreement below 0.002 $km^{-1}sr^{-1}$ for the distribution shape. However, EARLINET data show a higher occurrence for backscatter values larger than 0.002 $km^{-1}sr^{-1}$. These values are related to low altitudes (within the PBL), where a larger difference with CALIPSO data is expected because of the high variability of the aerosol at these altitudes (*Mona et al.*, 2009).

7.3.4 Single-point representativeness study

Representativeness study related to CALIPSO measurements, polar 16-day cycle orbit, needs for an investigation of the variability of aerosol and cloud fields on the whole considered area (in our case Europe) as well as locally. For these aims, backscatter coefficients measured by CALIOP and EARLINET lidars are compared following multiple-point and single-point approaches: on large area considering more ground-based lidars (see the approach reported in Section 7.3) for investigating mean temporal-spatial variability scales over Europe, and on a single station for a local study. In the following, an example of the single-point representativeness study is reported. All ground-based backscatter profiles measured at Granada from the beginning of the ESA–CALIPSO study until the last available CALIPSO Level 2 aerosol profile are considered. The un-availability of CALIPSO profiles for the whole duration of the ESA–CALIPSO project obviously limits this kind of study because it does not allow seasonal investigation and reduced the number of available comparisons.

In order to study variability length scale, in space and time, of the aerosol field, Case A, B, and C measurements performed at Granada are considered and compared to CALIPSO ones. In particular, comparisons within 100 km (Case A) and different time shifts are used to study the temporal variability, while almost simultaneous measurements (within 10 minutes) at different horizontal distances allows the study of spatial variability. Aerosol backscatter coefficient profiles at 532 nm are compared since the backscatter profile is a primary product of CALIPSO.

Figure 7.17 reports the count distribution for the aerosol backscatter coefficient values measured by EARLINET Granada station and CALIPSO within a distance of 10 minutes and 100 km (Case A). Backscatter values are almost confined below 0.003 $km^{-1}sr^{-1}$ for both platforms, even if there is a low occurrence of backscatter values around 0.004 $km^{-1}sr^{-1}$ observed by CALIOP and not observed at Granada EARLINET station. This could be due to fact that the closest overpass for this station is at about 64 km distance and therefore the low altitude aerosol content (and backscatter) can significantly change at these distances. A devoted study based on a long database of EARLINET data collected at stations with lower distances to CALIPSO overpasses could significantly

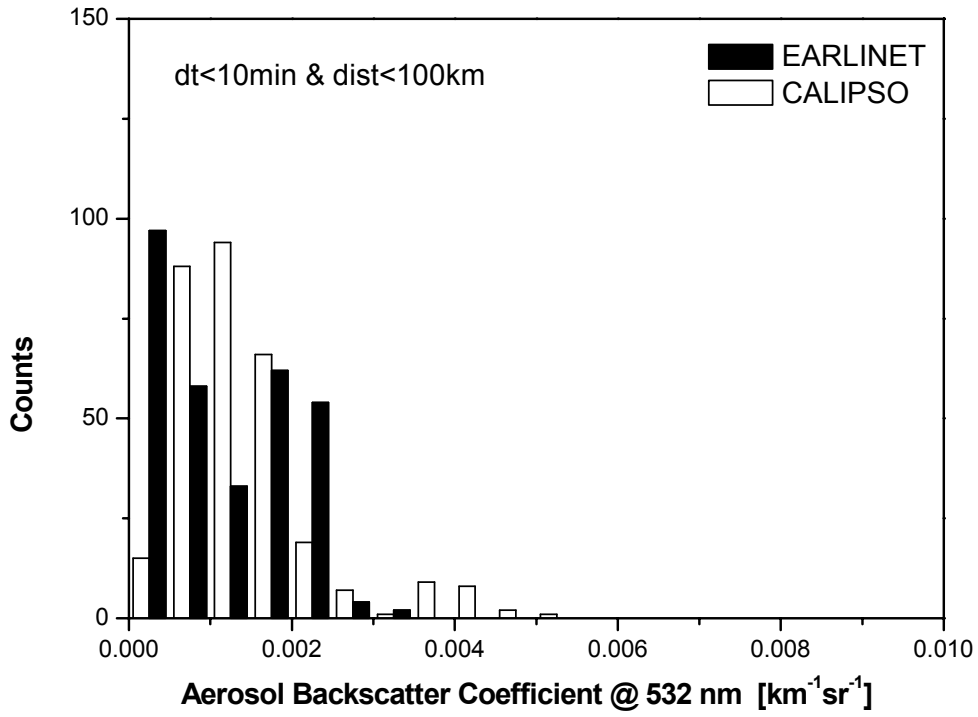

Figure 7.17: Count distributions of EARLINET and CALIPSO measured values of aerosol backscatter at 532 nm for distances lower than 100 km and 10 minutes.

improve the short distance variability investigation.

Figures 7.18 and 7.19 report the aerosol backscatter count distributions for short time (space) distance and large horizontal (temporal) distance: 10 minutes and 2000 km (720 minutes and 100 km). These large-distance comparisons highlight big differences both for shape and observed values, in particular for far away observations at almost coincident time.

Figure 7.20 reports the behavior of the correlation coefficient between CALIPSO and EALINET backscatter count distributions for different horizontal distance and a maximum of 10 minutes as the time shift. As for the Saharan dust related Case C measurements in Summer 2008, there is a strong dependence on the horizontal distance of the correlation coefficient, as expected. However, in this case a sharp decrease is observed at a larger horizontal distance (around 500 km instead of 250 km) and the variation in the correlation coefficient is smoother here. Finally and more important, correlation coefficient values are below 0.7 even for the shorter distances. This could be ascribed to the different atmospheric conditions we are considering here in comparison to Section 7.3. Here all available comparisons for Granada are considered, i.e., long-range-transport aerosol events as well as low aerosol content and local aerosol cases are considered. Therefore, this latter comparison is much more influenced by the distances between the measurements. In addition,

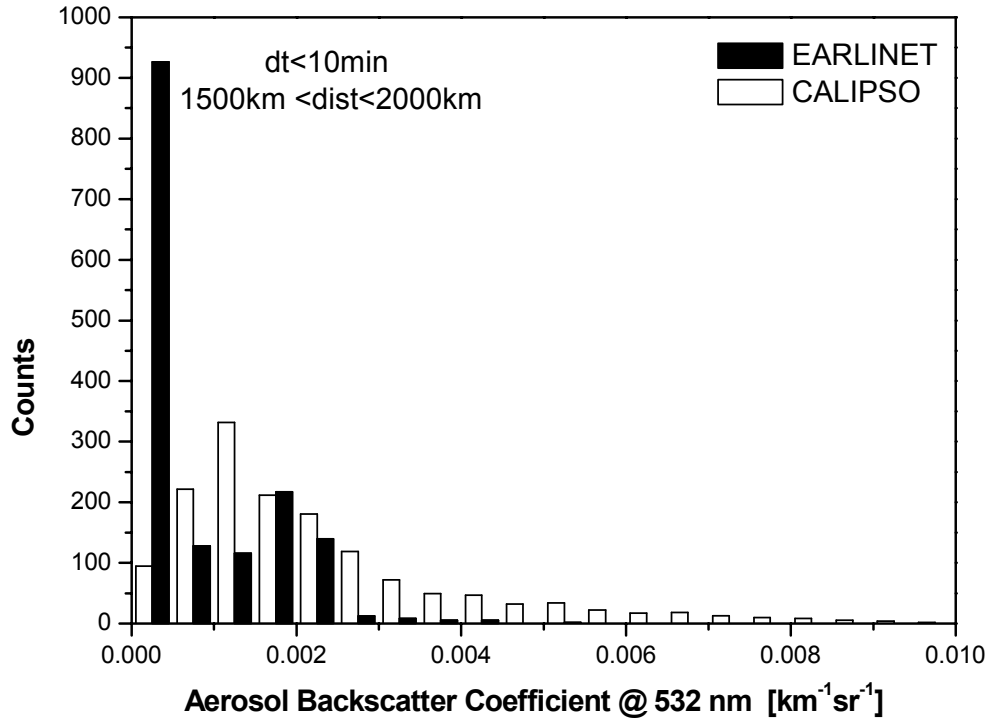

Figure 7.18: Count distributions of EARLINET and CALIPSO measured values of aerosol backscatter at 532 nm for distances lower than 2000 km and 10 minutes.

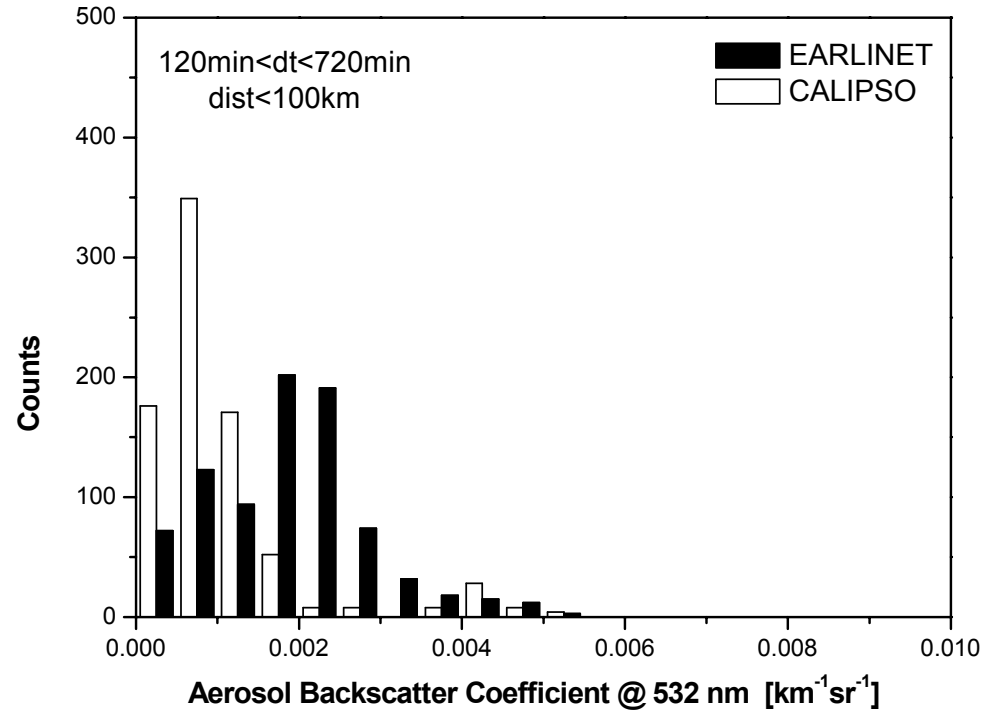

Figure 7.19: Count distributions of EARLINET and CALIPSO measured values of aerosol backscatter at 532 nm for distances lower than 100 km and 720 minutes.

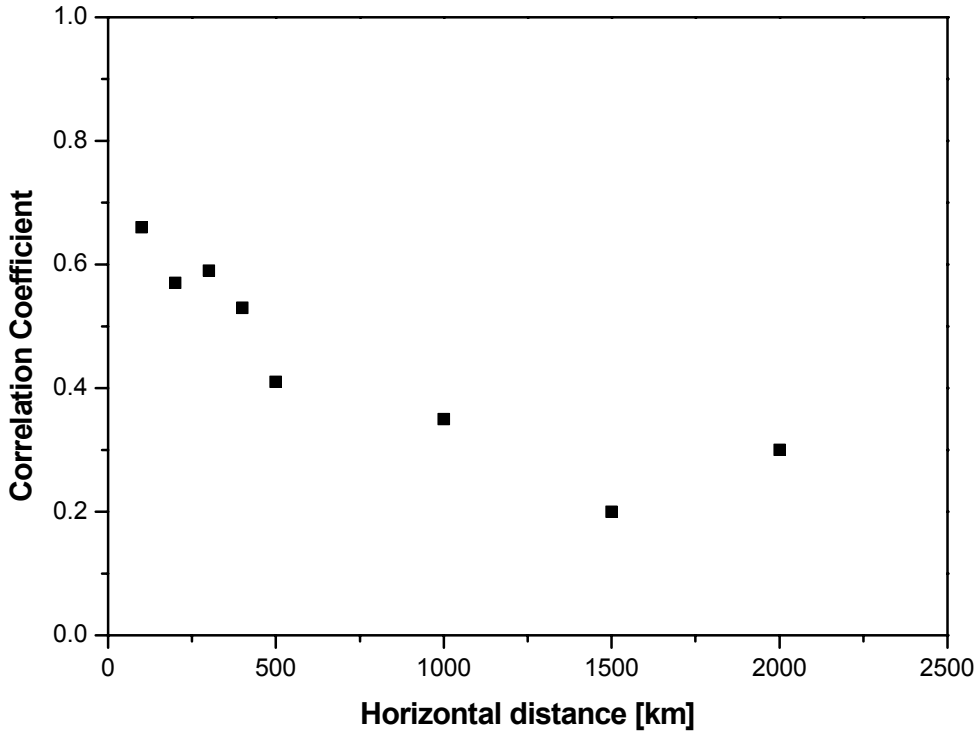

Figure 7.20: Correlation coefficient between CALIPSO and EALINET backscatter count distributions for time shift lower than 10 minutes and different horizontal distance ranges: $D < 100$ km, 100 km $\leq D < 200$ km, 200 km $\leq D < 300$ km, 300 km $\leq D < 400$ km, 400 km $\leq D < 500$ km, 500 km $\leq D < 1000$ km, 1000 km $\leq D < 1500$ km, and 1500 km $\leq D < 2000$ km.

the multiple-point study reported in Section 7.3, considering all involved stations, provides in some sense an average on the whole investigated area and therefore is less sensitive to local differences.

A slight dependence on the time shift is evidenced by the behavior of the correlation coefficient as a function of the time shift when a maximum horizontal distance of 100 km is considered (see Figure 7.21). This could indicate that aerosol variability is much more sensitive to horizontal distance than to time shift. Obviously this kind of result is strictly related to the considered station and its location and the relative location of the CALIPSO track in the station proximity.

7.3.5 Cloud variability study

CALIPSO provides vertical layering of clouds with high vertical and temporal resolution, allowing the study of cloud variability in terms of distribution as well as of optical properties. On the other hand, EARLINET was specifically devoted to the investigation of

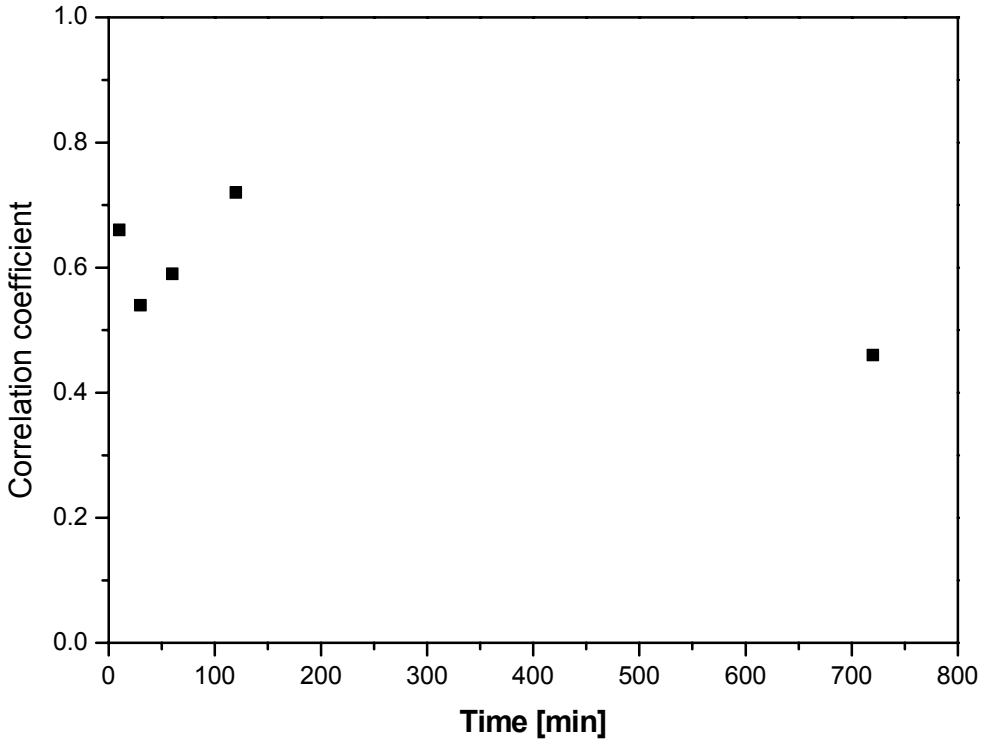

Figure 7.21: Correlation coefficient between CALIPSO and EARLINET backscatter count distributions for horizontal distances lower than 100 km and different time shift classes $\Delta t < 10$ min, $\Delta t < 30$ min, 30 min $\leq \Delta t < 60$ min, 60 min $\leq \Delta t < 120$ min, and 120 min $\leq \Delta t < 720$ min.

aerosols. Apart from cirrus clouds, clouds are removed from EARLINET profiles, because the EARLINET database is an aerosol optical properties database. For the aims of the ESA–CALIPSO study, a cloud file format has been defined within EARLINET and related files are uploaded and stored in a different database. Evaluating cloud optical properties in a quantitative way is a big effort for EARLINET: quality assurance exercises were performed within the network for aerosol optical properties retrieval. This is not the case for cloud evaluations. Therefore, cloud cases need careful checks. In the following examples of comparisons between CALIPSO and EARLINET cloud observations are reported for cirrus and water clouds observed at Granada. Comparisons are performed in terms of top and base of the identified layer. For each case, CALIPSO measurements within 100 km from Granada and as close as possible in time to the ground-based lidar measurements are considered. Spatial variability is investigated thanks to the different CALIPSO observations collected within these constraints. Temporal variability instead is studied taking advantage of the availability of more backscatter-coefficient profiles provided by Granada station for each selected cloud case.

7.3.5.1 Ice clouds

Figure 7.22 shows top and base altitude of a cirrus cloud as identified by CALIPSO and EARLINET lidar on November 10, 2008, in daytime conditions. Short lines indicate

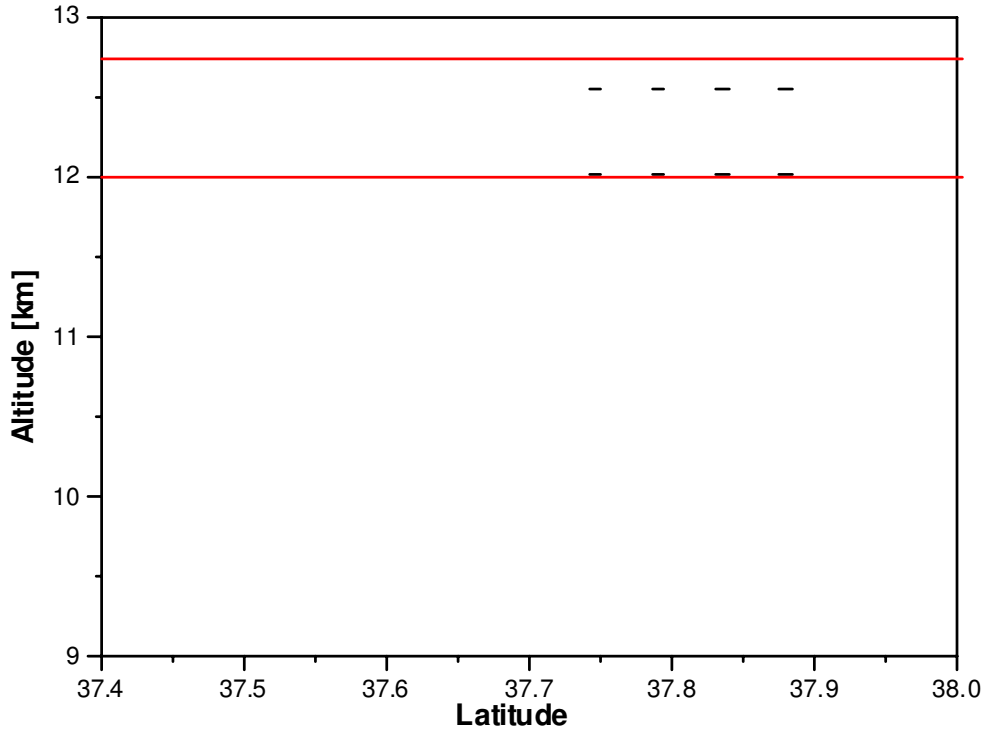

Figure 7.22: Top and base of a cloud layer identified by CALIPSO (short lines) and Granada EARLINET station on 10 November 2008, 13.32 UT. CALIPSO data are reported as a function of latitude. EARLINET 10-minute integrated data are related to the closest CALIPSO overpass (about 86 km).

CALIPSO cirrus boundary altitudes and are reported as a function of the latitude. Red lines instead indicate top and base of the cirrus as identified by Granada EARLINET measurements corresponding to the CALIPSO closest overpass. Granada EARLINET measurements are provided with 10 minutes as temporal resolution and, therefore, extend over the whole CALIPSO observational time period reported in Figure 7.22. The minimum horizontal distance between the two observations is about 86 km. Starting from the three backscatter profiles measured at Granada the following base and top heights are identified: 12.1±0.1 km and 12.67±0.04 km, indicating a small temporal variability in this case. On the other hand, a 20-km horizontal averaging was needed in the CALIPSO retrieval for the identification of this cirrus cloud extending between 12.0 and 12.55 km. Finally, the CALIPSO algorithm correctly identified this layer as an ice cloud.

Figure 7.23 reports a similar comparison related to a cloud observed on 10 November 2008, but during night-time. Over three 10-minutes profiles, a 0.6 km thick cirrus cloud

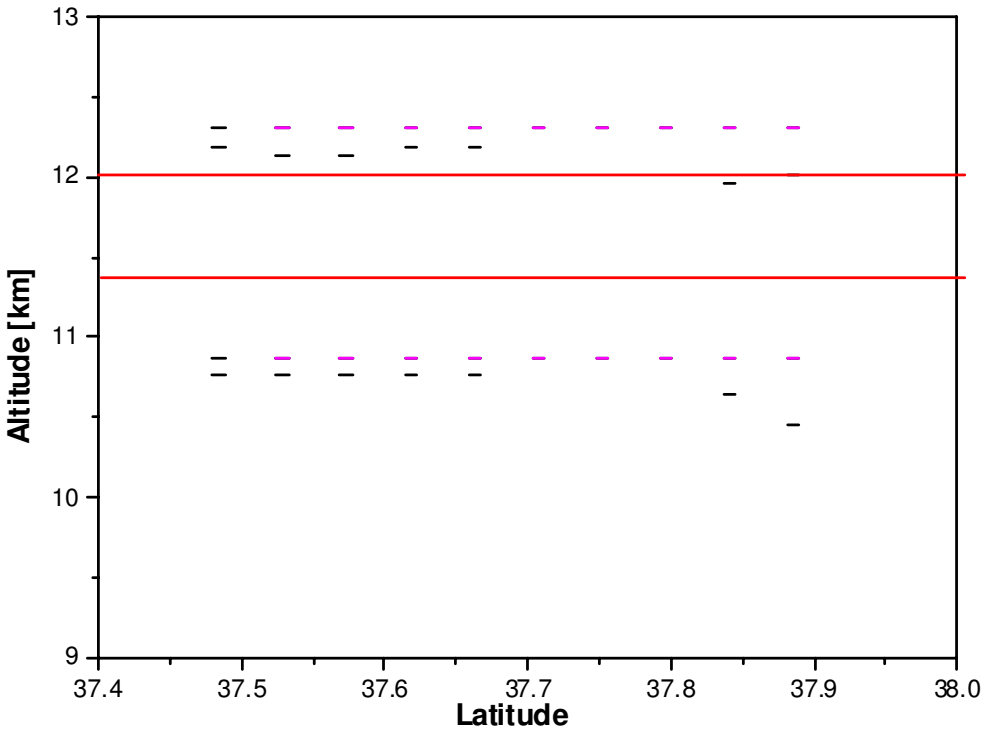

Figure 7.23: Top and base of a cloud layer identified by CALIPSO (short lines) and Granada EARLINET station on 10 November 2008, 2.29 UT. CALIPSO data are reported as a function of latitude. EARLINET 10-minute integrated data are related to the closest CALIPSO overpass (about 68 km).

was observed at Granada with base and top heights of 11.4±0.1 km and 11.98±0.03 km, respectively. The CALIPSO feature finder algorithm for this scene identified often two layers (pink and black short lines in the figure). These two layers often overlap and are typically obtained with different horizontal averaging. The first layer identified with 80 km of horizontal averaging extends between 10.9 and 12.0 km, the second one instead is obtained with a 5–20 km horizontal average and extends between 10.7±0.1 km and 12.1±0.1 km. A clear inconsistency is highlighted by this example: if one could expect that different horizontal averages will result in different identification of the layer in terms of top and base, on the other hand a larger horizontal average should lead to a better signal-to-noise ratio and therefore top (base) of the layer should be equal or at least higher (lower) than what is observed with lower horizontal averaging. Moreover, the two layers are reported in the CALIPSO Level 2 Layer files as distinct layers, but they clearly are physically the same layer.

A more complex case is shown in Figure 7.24. In this case, more spatial variability is observed as demonstrated by the scattering of the top and base altitudes reported in Figure 7.24 for the two layers identified by CALIPSO (pink and black short lines). Typically,

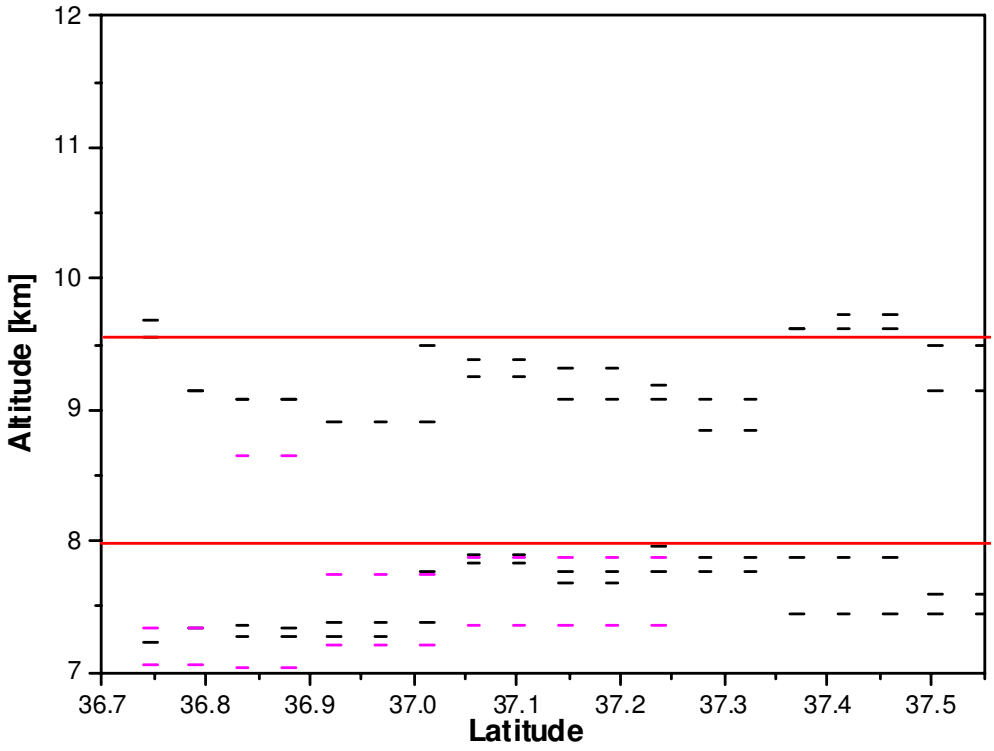

Figure 7.24: Top and base of a cloud layer identified by CALIPSO (short lines) and Granada EARLINET station on 6 August 2008, 2.28 UT. CALIPSO data are reported as a function of latitude. EARLINET 10-minute integrated data are related to the closest CALIPSO overpass (about 73 km).

two layers are identified by CALIPSO and, on average, top and base are 9.3±0.3 km and 7.8 ±0.5 km and 7.7±0.3 km and 7.2±0.1 km, respectively. The high variability is highlighted by the large standard deviation observed in the top and base identified by CALIPSO and at the Granada station, where, over 30 minutes, a mean top of 9.5±0.2 km and a mean base of 8.6±0.6 km were observed. A good agreement between the satellite and ground-based measurements is found, if this spatio-temporal variability is taken into account. For this case, the most extended cloud layer (9.3–7.7 km) has been identified with 5 km horizontal averaging, while a coarser resolution is needed for the identification of the thin cirrus layer present in the 7.2–7.8 km altitude range.

As demonstrated by the previous example, cirrus clouds are typically largely variable both in time and space. Therefore, it is clear that comparing measurements taken at large horizontal distances, as in the case of CALIPSO overpasses over Granada (the closest is at about 64 km), does not always lead to useful results. Figure 7.25 reports one example of extreme difference between EARLINET and CALIPSO observations. At Granada EARLINET site a thin stable cirrus cloud was observed between 12.70 and 12.81 km height (standard deviation of top and base over 30 minutes of observation is

about 0.015 km). On the other hand, CALIPSO found, on average, a thicker cirrus cloud layer extending from 11.1±0.3 km to 11.9±0.1 km, even if additional layers were identified in the considered part of the track (100 km maximum distance from Granada).

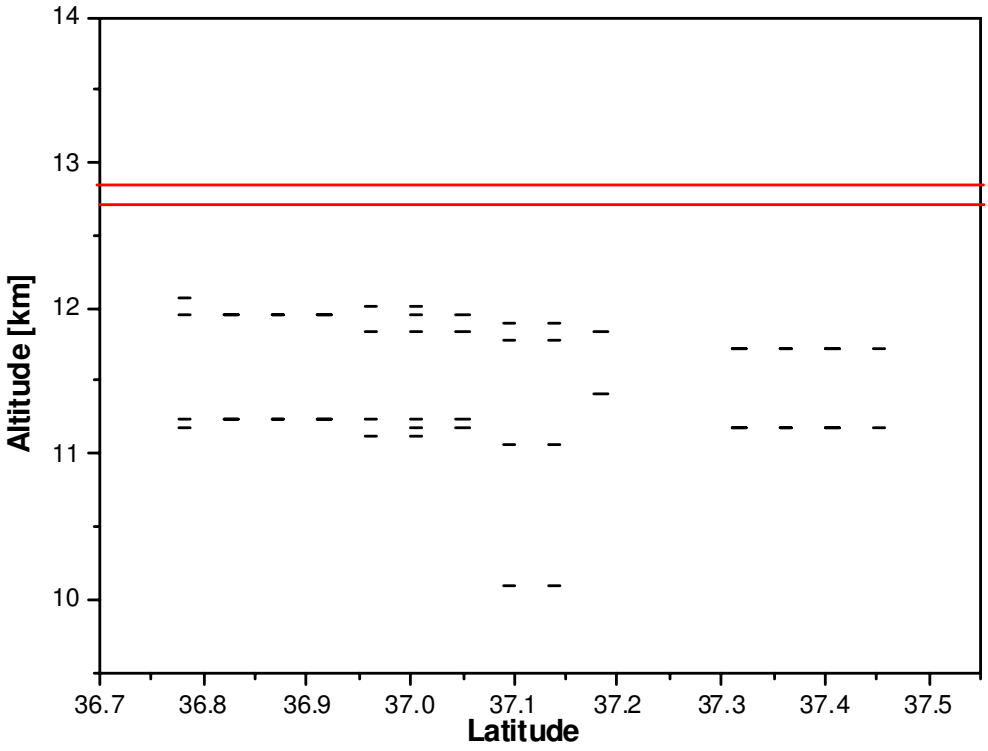

Figure 7.25: Top and base of a cloud layer identified by CALIPSO (short lines) and Granada EARLINET station on 2 May 2008, 13.30 UT. CALIPSO data are reported as a function of latitude. EARLINET 10-minute integrated data are related to the closest CALIPSO overpass (about 69 km).

7.3.5.2 Water clouds

An example of a water cloud is reported in Figure 7.26. On average, there is a good agreement between the base altitudes observed by CALIPSO and Granada EARLINET station: 4.7±0.2 km and 4.5±0.1 km, respectively. A top height of 5.5±0.3 km is found by CALIPSO, while the top height information from EARLINET Granada station is missing, because the cloud was not completely penetrated. The layer has been correctly classified as water cloud from CALIPSO. It was identified as sub-type altostratus opaque water cloud for most of the considered track section (72%).

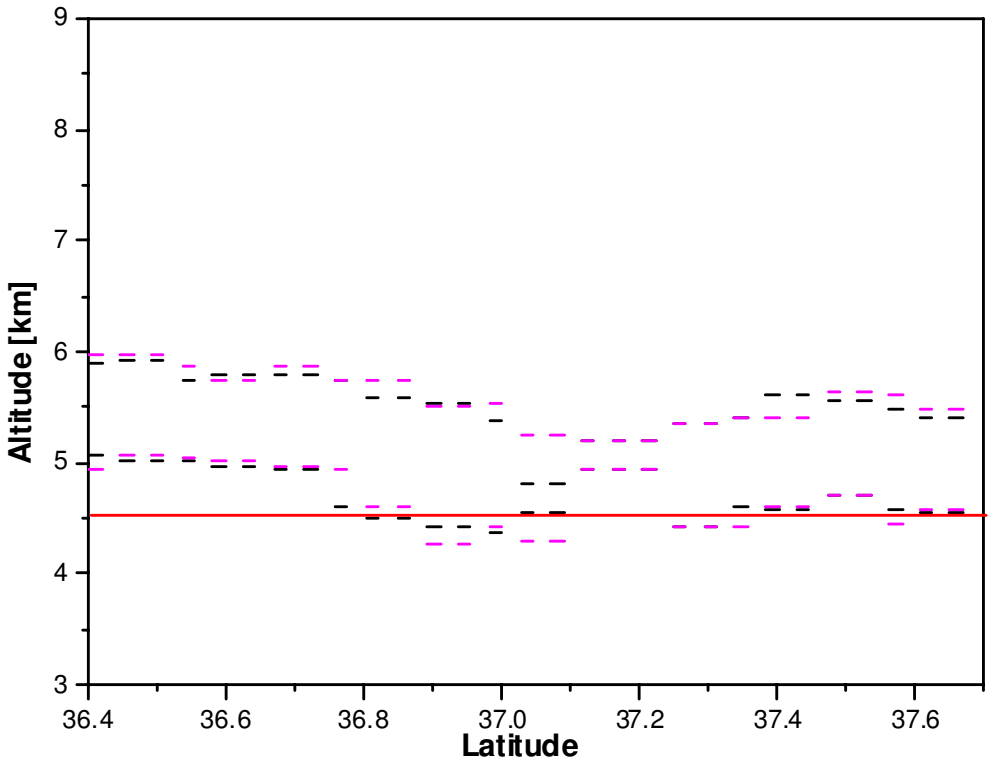

Figure 7.26: Top and base of a cloud layer identified by CALIPSO (short lines) and Granada EARLINET station on 19 November 2008, 2.23 UT. CALIPSO data are reported as a function of latitude. EARLINET 10-minute integrated data are related to the closest CALIPSO overpass (about 64 km).

Chapter 8

Comparison of CALIPSO Version 2 and Version 3 data releases

8.1 CALIPSO Version 3.01 data release

The Version 3.01 (V3) of CALIPSO data was released in May 2010. Apart from specific points regarding the data format, three main improvements with respect to the Version 2 (V2) are included into this new version of data.

1. The Cloud Aerosol Discrimination algorithm is now based on a 5-dimensional probability density function against the 3-dimensional function applied for Version 2.
2. A new procedure is included in V3 for improving the profiling in the PBL through adjustment of PBL altitude.
3. Finally and most important, the Level 2 profile products, i.e. the profiles of particle optical properties, are provided for Version 3 at a horizontal resolution of 5 km instead that of 40 km of the previous versions. In this way, Level 2 profile and layer products are provided at the same horizontal resolution now.

The Version 3.01 dataset covers the periods 13 June 2006 – 16 February 2009 and 17 March 2009 to present. The maturity level of backscatter and extinction coefficient profiles reported in the Version 3.01 release is assessed as provisional, i.e. data products have been compared with a limited set of independent measurements and obvious errors have been repaired since Version 2.01. In this context, a preliminary dataset of Version 3 data (first week of January 2007 and last week of August 2007) was provided at the beginning of April 2010 to scientific groups, and EARLINET among this, working with CALIPSO data. Anyway, backscatter and extinction products are still provisional, so that NASA strongly

encourages users to take into account the numerous data quality flags and uncertainty estimates that were not available in prior releases.

Both the structure and content of the Version 3 products is significantly different from previous releases. In the following, a short summary reports the main algorithm improvements, new quantities included in the Version 3 files and differences in format. All these differences called for a revision and restyling of all routines originally developed within the current study for reading CALIPSO data and for efficiently compare and store information about EARLINET and CALIPSO corresponding layer and profile products. In addition, the larger size of Level 2 products in the Version 3.01 release posed main technical issues about the storing of the CALIPSO data subset provided to EARLINET directly from NASA. A new archive compatible with the new data size has been realized at CNR–IMAA.

8.1.1 Algorithm improvements

Cloud Aerosol Discrimination Algorithm

The cloud-aerosol discrimination (CAD) score, which is reported in the 1-km and 5-km layer products, and now in Version 3 also for the 5-km cloud and aerosol profile products, provides a numerical confidence level for the classification of layers by the CALIOP cloud-aerosol discrimination algorithm. The CAD algorithm separates clouds and aerosols based on multi-dimensional histograms of scattering properties (e.g., intensity and spectral dependence) as a function of geophysical location. In the current release (Version 3), the CAD algorithm uses newly developed five-dimensional (5D) probability density functions (PDFs), rather than the three-dimensional (3D) PDFs used in previous versions. In addition to the parameters used in the earlier 3D version of the algorithm (layer-mean attenuated backscatter at 532 nm, layer-integrated attenuated backscatter color ratio, and altitude), the new 5D PDFs also include feature latitude and the layer-integrated volume depolarization ratio. Enhancements made to incorporate the 5D PDFs used in Version 3 release are described in *Liu et al.* (2010). Because of the better separation between clouds and aerosols in the 5D space, the 5D CAD algorithm significantly improves the reliability of the CAD scores. In particular, the 5D algorithm has been designed in order to address the following issues existing for V2 data (*Liu et al.*, 2010):

- Dense aerosol layers (primarily very dense dust and smoke over and close to the source regions), which are sometimes labelled as cloud in the V2 release;
- Because the V2 CAD algorithm used a latitude-independent set of 3D PDFs, a class of optically thin clouds encountered in the polar regions that can extend from the surface to several kilometers were sometimes misclassified as aerosols.

- Correct classification of heterogeneous layers is difficult. An example of a heterogeneous layer would be an aerosol layer that is vertically adjacent to a cloud or contains an embedded cloud, but which is nonetheless detected by the feature finder as a single entity in the V2 release. By convention, heterogeneous layers should be classified as clouds.

- The noise in the signal, multiple scattering effects, or artificial signal enhancements can cause identification of "pseudo-features" which are neither cloud nor aerosol and are distributed outside of the cloud and aerosol clusters in the PDF space. A small CAD score is assigned in the V3 CAD algorithm in order to better identify these outlier features.

Notwithstanding great improvements in cloud-aerosol discrimination are expected thanks to this 5D algorithm, it is recognized that some misclassification may still occur (*Liu et al.*, 2010). For example, when moderately dense dust layers are occasionally transported to high latitudes, where cirrus clouds can be present even in the low altitudes, they may be misclassified (an example has been presented in Sec. 5.1.2.2). This is also the case for volcanic aerosol injected into the high altitudes that may have a large cross-polarized backscatter signal and thus may be misclassified as cloud.

Multiple Scattering

The multiple scattering profiles, $\eta_{532}(z)$ and $\eta_{1064}(z)$, are specified at each wavelength according to layer type and subtype. Values range between 0 and 1; 1 corresponds to the limit of single scattering only, with smaller values indicating increasing contributions to the backscatter signal from multiple scattering.

Validation comparisons indicate that the multiple-scattering factor of $\eta_{532}(z) = 0.6$ used in Version 2 for ice cloud is an appropriate value and the same value is used in Version 3. The multiple-scattering factor for water clouds has been improved in Version 3 with respect to previous releases. Based on Monte Carlo simulations of multiple scattering, a value of $\eta_{532}(z) = 0.6$ appears to be appropriate for semitransparent water clouds (instead of the value of 1 applied before this release). For denser water clouds (optical depth >1), multiple scattering cannot be properly accounted for in the current retrieval algorithm and retrieval results are unreliable. No changes have been implemented regarding multiple-scattering effects on aerosol optical properties and multiple-scattering factors for both wavelengths are set to unity.

Aerosol Base Extender Algorithm

This algorithm has been introduced into the Version 3 processing to improve the quality of the CALIPSO retrievals of aerosol optical depth (AOD) (*Vaughan et al.*, 2010). This

is because the CALIPSO data products only report extinction profiles—and hence, only calculate optical depths—in those regions where features are detected. Thus the AOD reported by CALIPSO depends critically on an accurate determination of layer boundaries, combined with the ability to accurately differentiate between clouds and aerosol and to correctly recognize different aerosol species. In the Version 3 processing, an intermediate step is inserted: the initial classification is now followed by an assessment of the lowest layers within each column. If the lowest layer is an aerosol and a) the layer is not opaque (i.e., the surface was detected below); b) the initial layer base is within some minimum distance of the surface (2.5 km for the Version 3 processing); c) the 532-nm integrated attenuated backscatter in the region between the initial base altitude and the top of the surface echo is positive, then the estimate of the layer base altitude is revised downward to a point three range bins (∼90 m) above the top of the surface spike. The extinction and optical properties retrievals are conducted immediately after the conclusion of the base readjustment procedure.

Cloud and Aerosol Optical Depths

The reliability of cloud and aerosol optical depths reported in the V3 data products is considerably improved over the V2 release. The maturity level of optical depth is passed from beta (early release) for V2 to provisional for V3. Several algorithm improvements and bugs fixes factored into the decision to upgrade the maturity level. Among these were the addition of the aerosol layer base extension algorithm, which greatly improves AOD estimates in the PBL, and several significant improvements to the code responsible for rescaling the attenuated backscatter coefficients in lower layers to compensate for the beam attenuation that occurs when traversing transparent upper layers.

Cloud Ice/Water Phase Discrimination

As already mentioned in Sec. 3.3, the cloud phase algorithm used in Version 2 has been replaced with a new, completely different algorithm. The V3 algorithm classifies detected cloud layers as water, randomly-oriented ice (ROI), or horizontally-oriented ice (HOI) based on relations between depolarization, backscatter, and color ratio (*Hu et al.*, 2009). These classifications have not yet been rigorously validated, which is difficult, but many of the obvious artifacts found in the V2 data have been eliminated. Accordingly, the new feature classification flag for clouds is:

0 = unknown/not determined,
1 = randomly oriented ice,
2 = water,
3 = horizontally oriented ice.

Finally, some bugs in the cloud clearing code have been fixed and daytime calibration procedures have been improved (*Vaughan et al.*, 2010; *Powell et al.*, 2010).

8.1.2 New parameters

Profile products now report also **Column Optical Depth** (and associated uncertainty) of all clouds, aerosol, or stratospheric layers within a 5-km column. The optical depths are obtained by integrating the 532-nm cloud/aerosol/stratospheric extinction profiles, reported in these profile products. For aerosols and stratospheric layers the optical depth is provided at both 532 and 1064 nm wavelengths. The same quantities are included also in the 5-km layer products (both aerosol and clouds). Additionally, profile products contain also the **Column Integrated Attenuated Backscatter at 532 nm**.

The 5-km products report in the Version 3 a new parameter called **Column Feature Fraction**, the fraction of the 5-km horizontally averaged profile, between 30 km and the surface, which has been identified as containing a feature (i.e., either a cloud, an aerosol, or a stratospheric layer).

Pressure and **Temperature** at base and top of each identified layer are given in layer products at 5-km horizontal resolution. The mid-layer pressure is also included.

The **Layer Base Extended Flags** describe the initial classification state of the lowest layer.

In Version 3 **Particulate Depolarization Ratio** is reported in 5-km layer and profile data.

Ice Water Content and the associated uncertainty are now included in the 5-km cloud layer product.

Particulate Color Ratio (integrated within identified layers, uncertainties and statistics within the layer themselves) are instead included in the Version 3 aerosol layer products.

Uncertainty estimates are now provided for all profile data derived from the Level 1 lidar attenuated backscatter data (extinction, backscatter, perpendicular backscatter and particulate depolarization ratio).

The new **Atmospheric Volume Description (AVD)** flags are reported in Version 3 profile products. These are derived from the standard feature classification flags reported elsewhere in the CALIPSO vertical feature mask and layer products. The information provided in bits 1–13 in the AVD flags is identical to that provided in all versions of the scene classification flags, and thus these bits will have a uniform interpretation across all variants of the CALIPSO data products. However, the information provided by bits 14–16 has been revised to better reflect the reporting needs of the profile products. In addition to providing the averaging required for feature detection, bits 14–16 in the AVD also indicate whether features were detected at sub 5-km resolution within any 5 km $\times$ 60 m AVD range bin.

For each identified layer, a single extinction QC (quality control) flag summarizes the final state of the solution attempt. Each extinction QC flag is stored as a 16-bit integer, where each bit represents a binary flag value. The extinction QC flags are currently being reported only in the 5-km cloud and aerosol layer products. Within the profile products, the extinction QC flags for any layer are replicated as necessary to span the full vertical extent of the layer.

Atmospheric volume description, CAD score, and extinction QC [532/1064] are all profile descriptive flags that are stored in the Level 2 Version 3 profile products. Ideally, each profile descriptive flag would be an array of the size [no. of altitude bins, no. of profiles] with each array element providing a complete description of the range-resolved atmospheric state. However, because the range resolution of the Level 1 profile data below ∼8.3 km is 30 m, and because the feature-finder, scene classification, and extinction algorithms all operate at this finer spatial resolution, providing a genuinely complete description of the atmospheric state for each 60 m Level 2 range bin requires that the profile descriptive flags be stored as 3D arrays of the size [no. profiles, no. altitude bins, 2]. The first dimension, [: , : , 1], corresponds to the standard altitude array of the profile products. Thus, below 8.3 km, the first dimension contains the descriptive flags of the higher of the two full resolution (30 m) bins that comprise the single 60 m bin reported in the profile products. Meanwhile, below 8.3 km, the second dimension [: , : , 2] contains the descriptive flags for the lower of the two 30 m range bins. Above 8.3 km, where the range resolution of the Level 1 data is 60 m or greater, the descriptive flags for each single 60 m (or 180 m) range bin are replicated in both array elements.

8.1.3 Differences in data format

In particular, the aerosol profile products have been completely restructured, and now are reported on the same 5-km spatial grid as the cloud profile products. The horizontal resolution of the cloud and aerosol profile products is now identical to the horizontal resolution of the 5-km cloud and aerosol layer products, thus enabling a one-to-one match between the layer optical properties and the profile data.

Adopting this approach eliminates the 40-km horizontal averaging step that was applied for the Version 2.01 release, yielding the following additional benefits to users:

(a) aerosol profile products are reported at the same spatial resolution as the aerosol layer products, so that one-to-one matching of layers and profiles will now be possible;

(b) horizontal smearing/mixing of different aerosol types (e.g., dust, smoke, etc.) within individual profile altitude resolution element is eliminated;

(c) extinction coefficients from high-quality retrievals will no longer be averaged with those from low-quality retrievals (although there may be occasional exceptions to this rule at some vertical boundaries between different layers of aerosol types within the lower troposphere (−0.5 km to ∼8.3 km)).

The profile times and latitude/longitude coordinates are now reported identically in the 5-km profile products and the 5-km layer products. In Version 2, each of these parameters was recorded in two separate fields, which provided the first (start) and last (stop) values. The Version 3 profile products use a single field with dimensions $N \times 3$. The three elements reported for each record contain, respectively, the first (start), midpoint, and last (stop) values associated with each 5-km (15-shot) averaged profile. New in Version 3.01 is also that the layer extinction QC flags are reported on a profile-by-profile basis.

8.2 Differences and improvements in CALIPSO L2 Version 3 against L2 Version 2 data on the basis of case studies

In the following, an example of comparison between an EARLINET measurement and corresponding CALIPSO Version 2 and Version 3 profiles is reported. Starting from the subset provided by NASA in April 2010 (two weeks of test data), the case of 25 August 2007 overpass over Potenza has been selected. According to the DREAM model forecast and backward trajectories analysis, a Saharan dust intrusion occurred on this day with layers extending from the surface up to 6–6.5 km height.

Figure 8.1 shows aerosol optical properties as measured by the Potenza EARLINET station and as retrieved by CALIPSO with Version 2 and Version 3 at the closest overpass (about 79 km and 1 minute distance). CALIPSO Version 3 profiles of optical properties are averaged over 40 km in order to compare them to the Version 2 data.

Thanks to the adjustment in the PBL definition included in the V3 retrievals, V3 backscatter profiles look more reasonable than V2 profiles: V3 profiles strongly increase in the lowest altitudes toward the surface. In addition, some points are added close to the surface in the V3 profiles. V3 profiles differ from corresponding V2 ones also for the middle altitude range. In particular, the aerosol backscatter and extinction coefficient profiles at 532 nm are lower for V3 than for V2. The opposite is observed for the profiles at 1064 nm. The observed differences increase with the decrease of the altitude, reaching around 1.5 km 20%, 28%, and 10% for aerosol backscatter at 532 nm, backscatter at 1064 nm, and extinction at 532 nm.

Both V2 and V3 profiles are significantly higher than the corresponding EARLINET profiles. First of all, this can be attributed to the spatial distance, but noise effects on the 5-km profiles can influence the mean profiles shown here as well (see discussion below). In addition, lidar-ratio assumptions performed for the CALIPSO retrieval of optical properties play a role. For this case, a mean value around 65 sr is measured by EARLINET in the most intense part of the desert dust layer (2–3 km) and a lower value around 50 sr is observed in the 3.5–4.5 km altitude range. The CALIPSO feature classification algorithm correctly identifies this as a case of dust and therefore used for the retrieval the corresponding fixed lidar-ratio values of 40 sr at 532 nm and of 30 and 55 sr at 1064 nm for V2 and V3, respectively. The different lidar ratios at 1064 nm used in the V2 and V3 retrievals cause the increasing deviation of the CALIPSO backscatter profiles toward the ground (see middle panel of Fig. 8.1). The lidar ratio of 40 sr used to convert the 532-nm CALIPSO backscatter (left panel of Fig. 8.1) to the extinction profile (right panel of Fig. 8.1) lead to a smaller difference between the CALIPSO and EARLINET extinction profiles compared to the backscatter profiles.

Figure 8.2 reports the eight 5-km profiles of the V3 which were averaged for obtaining the 40-km profiles to be compared with the V2 data (shown in Fig. 8.1). The high level of noise affecting this 5-km profiles is clear. In addition, one of the eight aerosol backscatter and extinction profiles at 532 nm strongly differs from the others. The same is not true for the aerosol backscatter at 1064 nm, so that this cannot be related to atmospheric factors as the aerosol content variability. It is more likely that the retrieval performed on the data with so low signal-to-noise ratio (SNR) produces this strange result. The noise peaks can pretend an optical depth which the algorithm tries to correct for, although it is not there. Once a positive bias is produced at a certain height, the effect builds up toward the ground, because of the integration procedure in the attenuation correction. It is obvious that such single erroneous profiles can also stronlgy bias horizontal averages and influence comparisons on larger scales.

8.3 Representativeness study using Version 3 CALIPSO data products

Version 3 could in principle permit the investigation of satellite measurements representativeness on a shorter horizontal scale thanks to the better horizontal resolution with respect to the Version 2 (5 km against 40 km). The same approach applied on Version 2 data and reported in Chapter 7 is here applied to the Version 3 dataset for the 25–31 May 2008 case. These are the differences in terms of input data with respect to the analysis reported above:

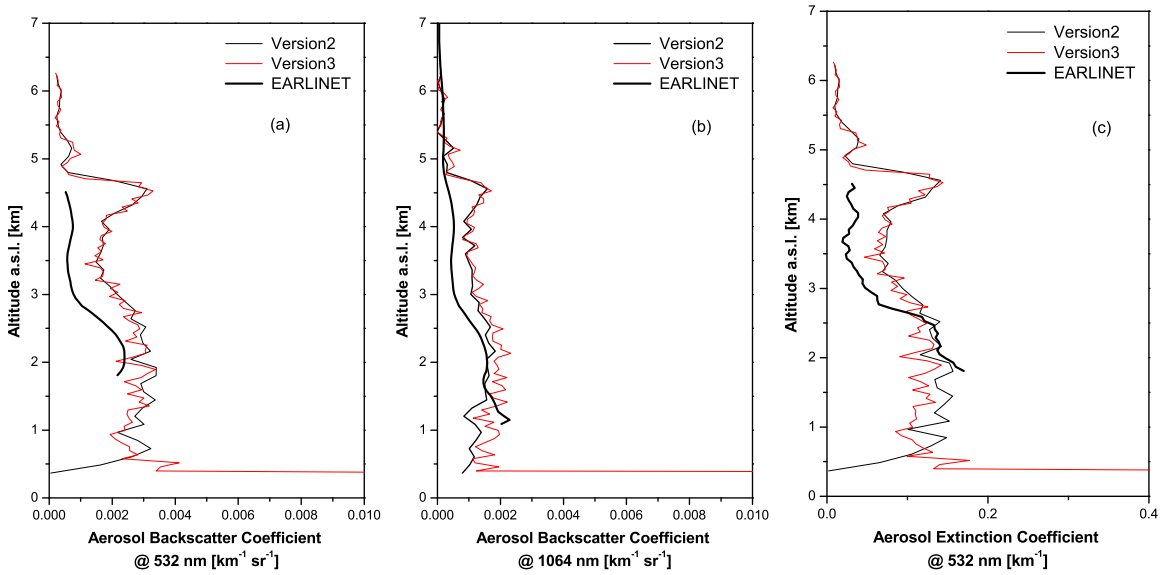

Figure 8.1: Aerosol optical properties as measured on 25 August 2007 by EARLINET (thick lines) and CALIPSO V2 (black lines) and V3 (red lines). EARLINET profiles are obtained as temporal average from 00.04–02.04 UTC on 25 August 2007. CALIPSO profiles correspond to acquisition at 01.05 UTC at a distance of 78.55 km from the Potenza EARLINET site.

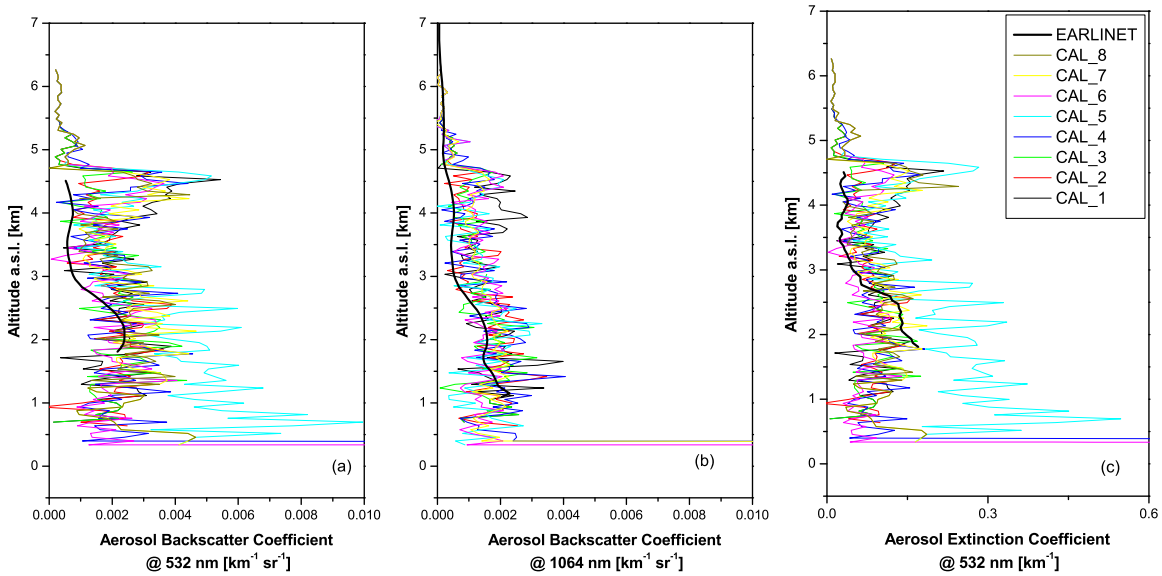

Figure 8.2: Original 5-km profiles provided in CALIPSO Version 3 subset for Potenza overpass 01.05 UTC on 25 August 2007. EARLINET profiles (00.04–02.04 UTC on 25 August 2007) are reported as thick black lines.

- More EARLINET profiles are now available.
- CALIPSO data for 26 May 2008 are now available for Version 3 (there are not corresponding V2 data for the EARLINET subset).
- CALIPSO data have now a resolution of 5 km (40 km in the V2).
- CALIPSO profiles are extended in vertical range coverage (i.e. not only within identified aerosol layers).

All these factors contribute to an increase of the number of data available for the comparison with EARLINET data and the representativeness study. In particular, the availability of 5-km profiles for CALIPSO results directly in a factor of 8 for the number of profile comparisons to be considered for the study and to be uploaded on the relational database (here multiplied by 2, because absolute and relative difference files are to be uploaded). The maximum distance both in terms of space and time has been reduced with respect to the V2 study because of this multiplying factor, in order to obtain a more efficient database. The number of comparisons in terms of aerosol backscatter-coefficient profiles at 532 nm (the most abundant) available with the current EARLINET database for this Saharan dust case is 11552, when maximum distances of 2000 km and 720 minutes are considered. The representativeness study reported in Sec. 7.3 demonstrates that for this intense dust case the correlation between the backscatter count distributions observed by EARLINET and CALIPSO decreases to values around 0.5 for distances of about 1000 km (at maximum time distance of 10 minutes) and 120 minutes (at horizontal distances lower than 100 km). A threshold of 0.5 for the correlation is certainly a signature of no physical correlation between the two measurements. Therefore, maximum distances of 100 km and 240 minutes are considered for the Version 3 study. Regardless of this restriction in terms of spatio-temporal distance, the number of available comparisons is still considerably high: 16427 profile comparisons are collected, preserving the same order of magnitude of comparison used for the V2 data representativeness study.

At the end of the ESA–CALIPSO study, a total of 137 EARLINET profiles are available for this specific event. In particular, there are 51 backscatter profiles at 532 nm collected at the following stations: Athens, Belsk, Hamburg, Leipzig, Minsk, Maisach, Naples, and Potenza. A homogeneous dataset of input files is needed for the representativeness study in order to avoid misleading results. In the following study, only data obtained with the typical 30 minutes temporal average or with a temporal average shorter than one hour are used. This means that the longer-averaged EARLINET profiles, really useful for the multiwavelength characterization of aerosol layers and thus for the conversion factors, are here disregarded. As exercise on this point, we found (not shown here) that the inclusion of these profiles will lead to unfeasible results in terms of correlation coefficients as result

of the mixing of comparisons between CALIPSO data and EARLINET data representing different time scales. A total of 20 MB is collected as external files for the relational database for the Version 3 and 8 MB for the Version 2.

As for the V2 study, comparisons within 100 km (Case A measurements) and different time shifts are used to study the temporal variability of the aerosol field, while almost simultaneous measurements (within 10 minutes of the CALIPSO overpass) at different horizontal distances are selected in order to study the spatial variability. Fig. 8.3 reports the count distributions of all CALIPSO and EARLINET aerosol backscatter measurements. Mean values of the two distributions are 0.0019 $km^{-1}sr^{-1}$ and 0.0020 $km^{-1}sr^{-1}$ for CALIPSO and EARLINET, respectively. A reasonable correlation coefficient between the two distributions of 0.80 is found. In spite of this good agreement on average, there are some differences in the shape of the distribution. For lower values, there is a high population of values around 0.001 $km^{-1}sr^{-1}$ and a missing of counts around 0.0015 $km^{-1}sr^{-1}$ in CALIPSO observations.

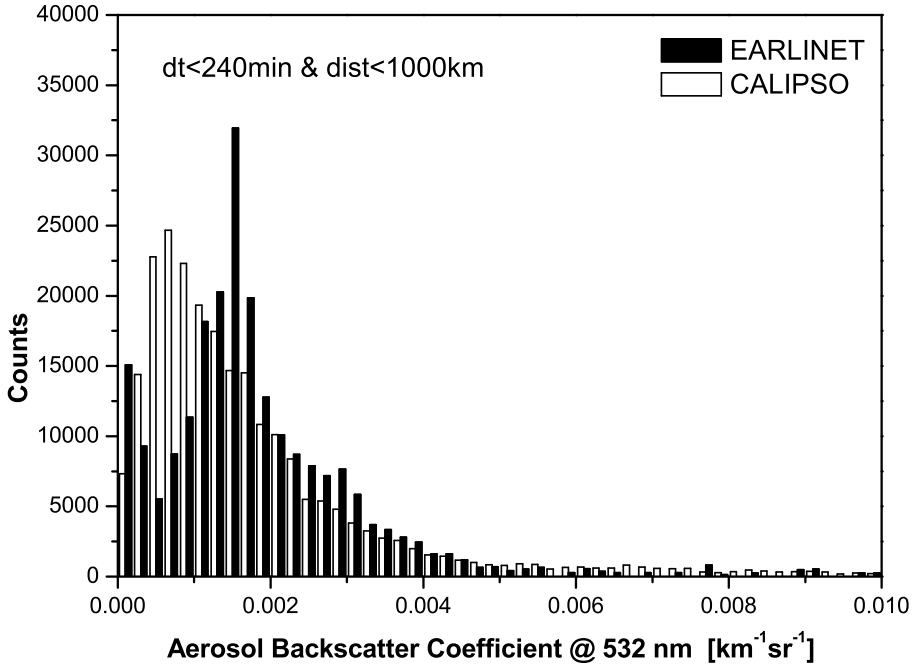

Figure 8.3: Count distributions of EARLINET and CALIPSO measured values of aerosol backscatter coefficient at 532 nm for distances lower than 1000 km and 240 minutes.

Count distributions of the aerosol backscatter values measured by CALIPSO and EARLINET are investigated for different altitudes and reported in Fig. 8.4 for altitude ranges 0–1 km (a), 1–2 km (b), 2–3 km (c) and 3–4 km (d). The main difference, related to the high population of low aerosol backscatter values observed in Fig. 8.3, is mainly due to the altitude ranges 0–1 km and 3–4 km. These altitude ranges correspond to regions where

the CALIPSO aerosol backscatter is noisier. The lowest range (0–1 km) is highly noisy because of the natural variability within the PBL region and the higher attenuation of the signal toward the ground. The 3–4 km range is noisy instead because the tail of the Saharan dust layer for this May 2008 case is typically at these altitudes. The agreement between EARLINET and CALIPSO distributions is pretty good for the 1–2 and 2–3 km altitude ranges.

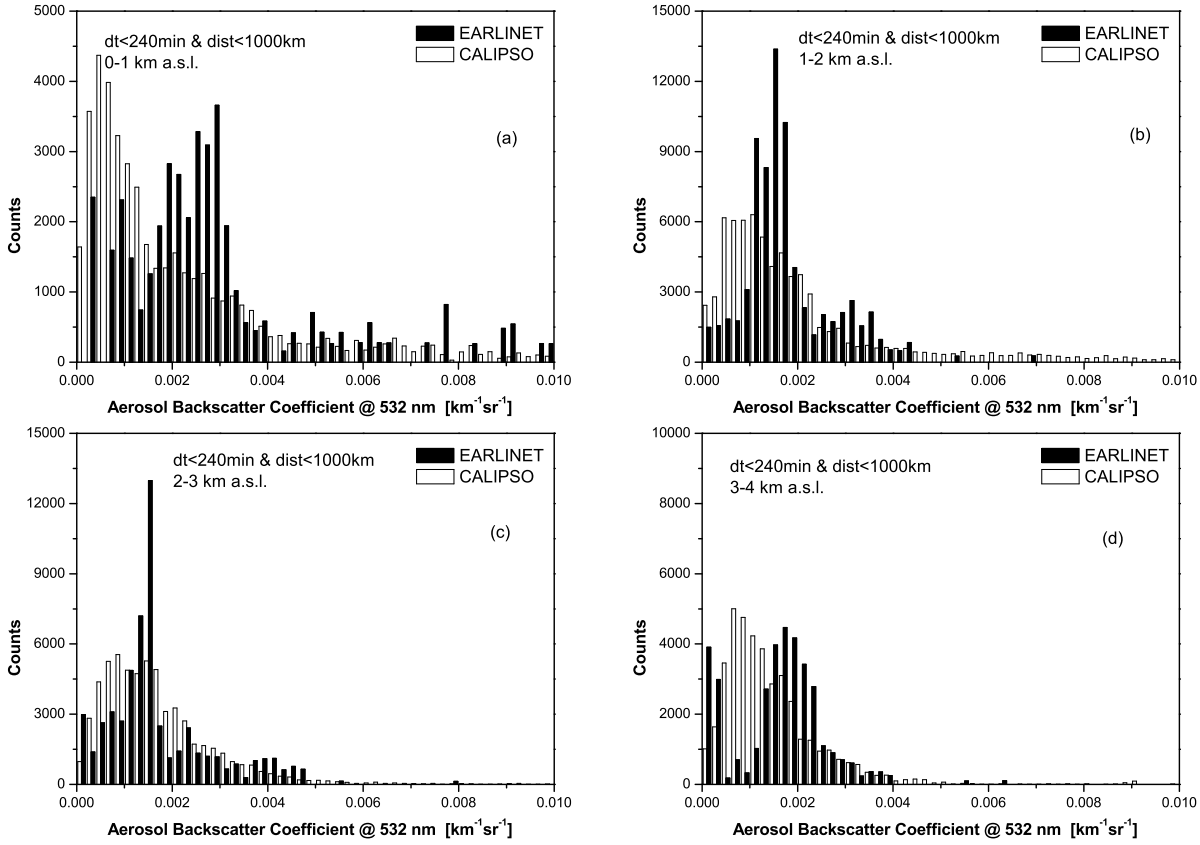

Figure 8.4: Count distributions of aerosol backscatter coefficient at 532 nm measured with EARLINET and CALIPSO within 1000 km and 240 minutes for four different altitude ranges: a) 0–1 km, b) 1–2 km, c) 2–3 km and d) 3–4 km.

Starting from the distance in time and space reported in Part D of the database, all difference profiles related to spaceborne vs ground-based lidar horizontal distance below 100 km (Case A measurements) are selected and classified in classes on the base of the time shift between the two observations. Fig. 8.5 reports the mean of observed backscatter-coefficient differences for each one of these classes, i.e. for time shifts lower than 10, 30, 60, and 120 minutes.

An improvement is observed with respect to the Version 2 comparison (see Fig. 7.4). In particular, CALIPSO backscatter in the low altitudes (0–2 km) is significantly improved

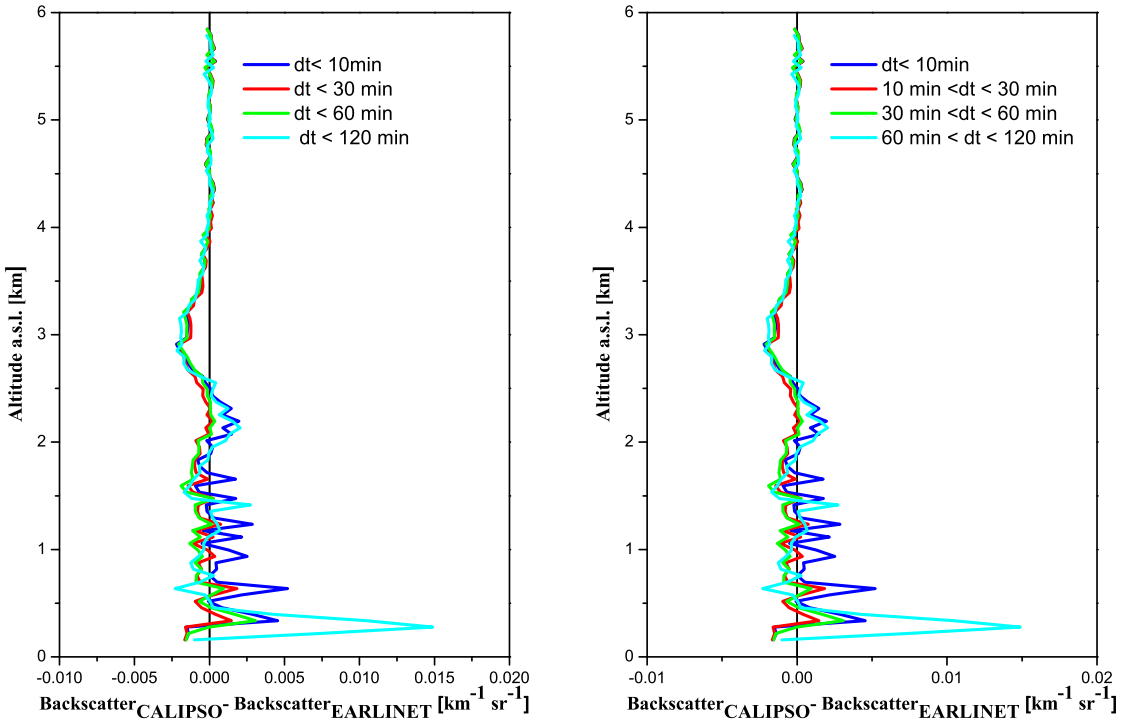

Figure 8.5: Backscatter-coefficient difference profiles as obtained averaging over 25–31 May 2008 cases with a spaceborne vs ground-based lidar horizontal distance below 100 km and divided in four time shift classes: time shifts (dt) lower than 10, 30, 60, and 120 minutes.

and results in a mean difference from EARLINET observations close to zero. On the contrary, in the 2–4 km range deviations from corresponding EARLINET profiles are observed also at short horizontal distance. An almost perfect agreement is found above 4 km height. Finally, difference profiles are not smoothed as for the Version 2 study. This could be related to more noise affecting the 5-km CALIPSO V3 profiles in comparison to the 40-km V2 ones.

Figure 8.6 reports the aerosol backscatter coefficient as observed by the two platforms for the four time shift classes. Large differences within the Saharan dust layer are evident also for the smallest distance (100 km, 10 min). This could be related to the assumed lidar-ratio value for the CALIPSO retrieval that strongly affects the resulting backscatter especially in the most intense part of the layer (around 3 km in this particular case). This lidar-ratio effect is also more evident in the comparison for the profiles acquired with a temporal distance between 10 and 30 minutes. The same vertical shape is observed by CALIPSO and EARLINET stations, but an altitude-dependent disagreement is observed. This kind of an increasing disagreement toward the ground is the typical result of a wrong assumption on the lidar ratio in the simple elastic-backscatter retrieval. If the chosen lidar ratio is too small, as it seems to be the case here, the signal attenuation is underestimated and not completely corrected for, so that the resulting backscatter coefficient is too small.

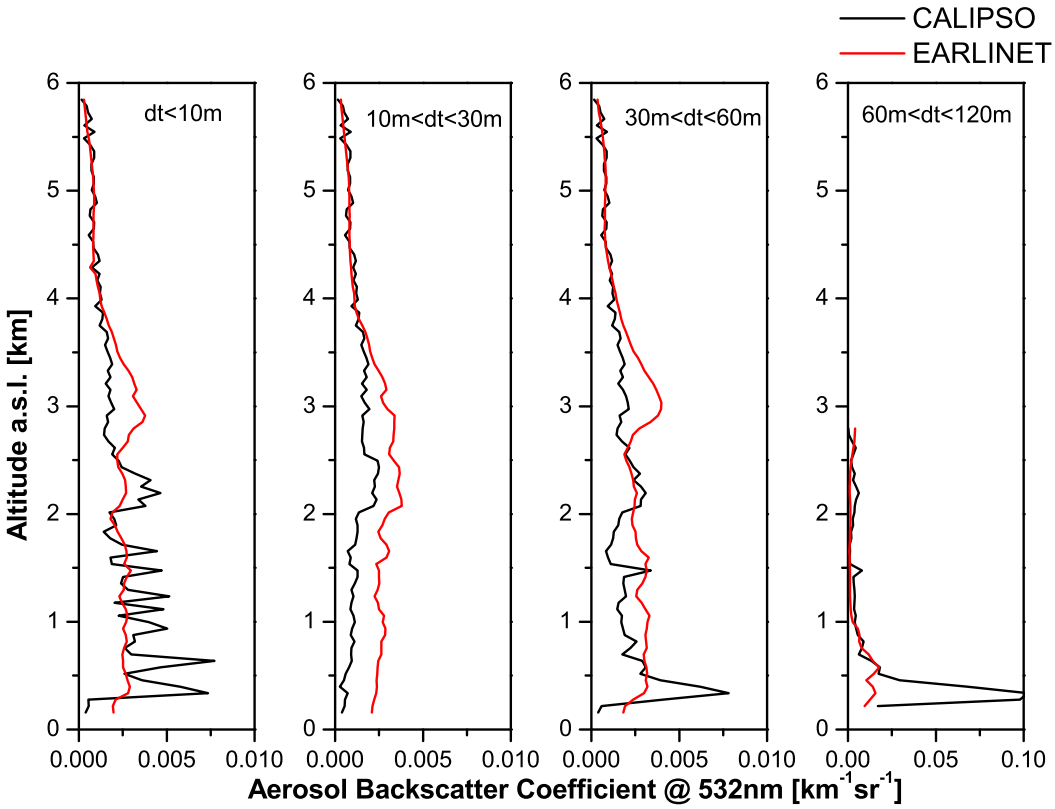

Figure 8.6: Mean backscatter-coefficient profiles measured by CALIPSO and EARLINET as obtained averaging over 25–31 May 2008 cases with a spaceborne vs ground-based lidar horizontal distance below 100 km and divided in four time shift classes: time shifts (dt) lower than 10, 30, 60, and 120 minutes.

Regarding this point, it is also interesting to note that this Saharan dust case influenced also low altitudes and often aged dust also mixed with continental polluted aerosol was observed, as resulting from the EARLINET feature classification.

Figure 8.7 reports the mean of observed backscatter-coefficient differences for different horizontal distances (below 100 km, 200 km, 300 km, 400 km, 500 km, and 1000 km) for a fixed maximum time shift of 10 minutes. As for Fig. 8.5, a good agreement is found on average. The differences observed around 3 and 2 km for distances below 100 km are progressively smoothed out when larger distances are considered too, as effect of an average on a larger data set. From the right panel, instead, one can observe that the difference for the larger horizontal distance ranges (400–500 km and 500–1000 km) correspond to large differences on the whole investigated altitude ranges.

The performed study on CALIPSO Version 2 data (see Chapter 7 showed that the representativeness of the aerosol backscatter profiles can be investigated by means of the relation between the count distribution correlation coefficient as a function of temporal

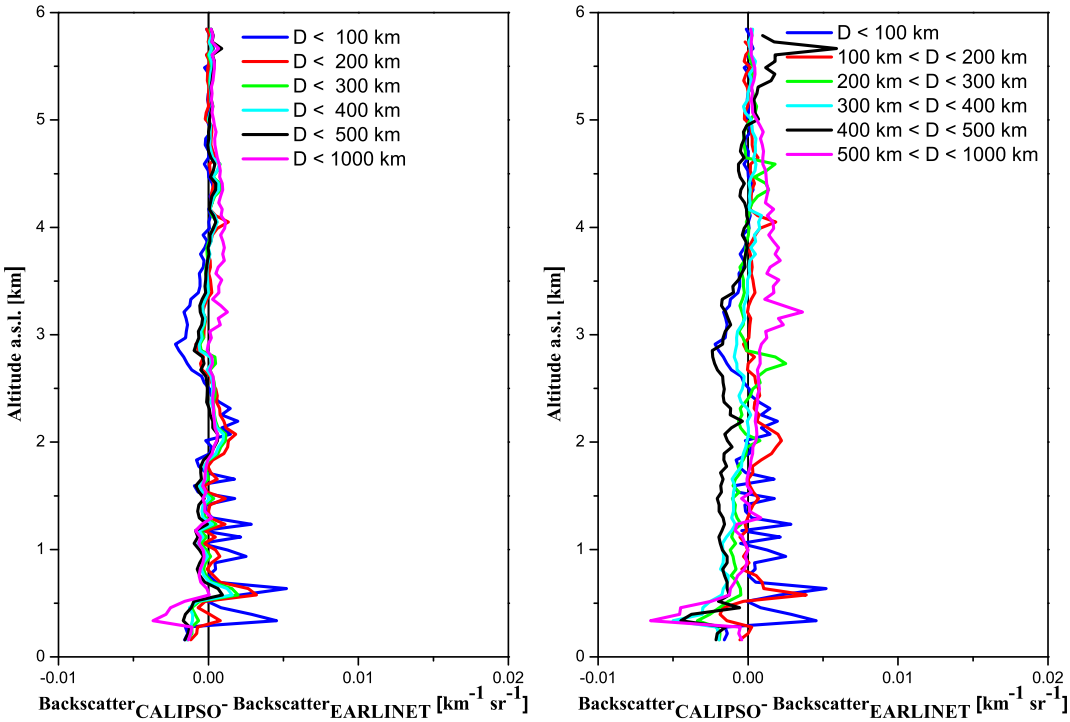

Figure 8.7: Backscatter coefficient differences profiles as obtained averaging over 25–31 May 2008 cases with a space-borne vs ground-based lidar time shift below 10 minutes and divided in 6 horizontal distance (D) classes from 100 km to 1000 km.

and horizontal distance. In the following, the same approach is applied to the Version 3 data. Fig. 8.8 reports the correlation coefficient between the CALIPSO and EARLINET aerosol backscatter count distributions as a function of the horizontal (left panel) and temporal distance (right panel). Low values of the correlation coefficients are found for all distances considered and no reasonable behavior with respect to the distance is obtained. This would lead to the wrong conclusion that there is no link between the observation distance (both in time and space) and their correlation. Results obtained from Version 2 are strongly in disagreement with these plots, indicating instead that the main cause of this unphysical result lies in the new release of the CALIPSO data.

To better understand this point, an example of count distribution for one of the horizontal distance ranges, namely 200 km and 10 minutes as maximum distances, is presented in Fig. 8.9. These distributions show a high occurrence of low backscatter values (around 0.0005 $km^{-1}sr^{-1}$) in the CALIPSO observations, not present in the EARLINET profiles. In addition, CALIPSO observed more values higher than 0.005 $km^{-1}sr^{-1}$. It is likely that the noise affecting CALIPSO 5-km profiles (see Sec. 8.2) is the cause of the high occurrence of both too small and too high aerosol backscatter values.

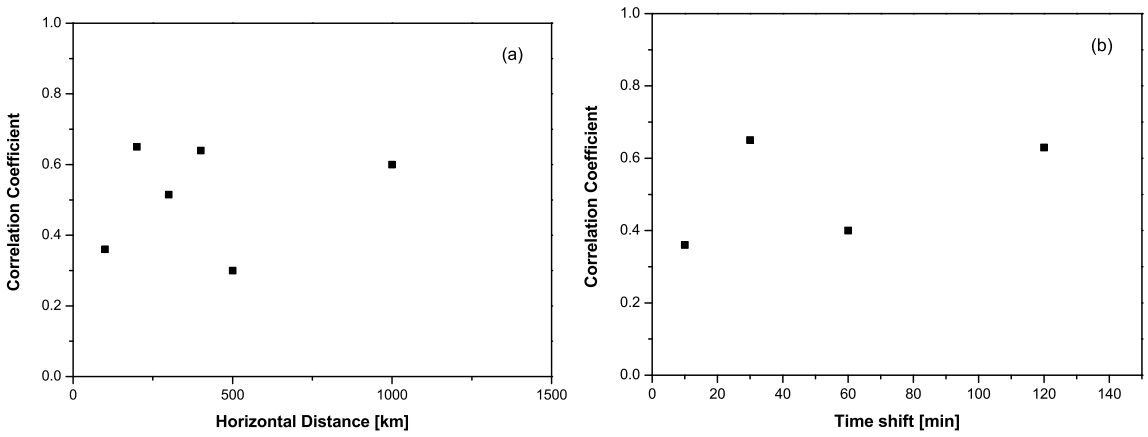

Figure 8.8: Correlation coefficient between CALIPSO and EARLINET backscatter count distributions for a) time shifts lower than 10 minutes reported as a function of the maximum horizontal distance between the two observations and b) for horizontal distances lower than 100 km as a function of the maximum considered time shift between the observations.

A devoted approach should be suited for the Version 3, because the lower SNR inhibits this kind of study based on the count distribution. Reasonable results could be obtained, if an average is considered. This could be performed for example considering the count distribution of backscatter values within the mean profiles calculated for each class of horizontal and temporal distances. The better agreement obtained in this way is evident comparing Fig. 8.9 and the analogous Fig. 8.10. Considering mean profiles for each distance class instead of all acquired profiles, the correlation coefficient (see Fig. 8.11) decreases with the distance following the behavior observed for Version 2 data. The only exception is the shorter distance class (100 km, 10 minutes) which has a low value of the correlation, probably because the noise in the CALIPSO data is not removed as shown in Fig. 8.5 and 8.7. In particular, a sharp decrease in the correlation coefficient is found at 300 km horizontal distance, and observations are not correlated for temporal distances larger than 60 minutes.

In spite of the promising capability of exploring short-distance representativeness thanks to the 5-km profiles, the results obtained applying the methodology used for Version 2 data on Version 3 profiles suggest that these latter profiles are not the most suitable to be handled for this kind of investigation. A more detailed study about SNR versus averaged horizontal resolution for CALIPSO V3 data is needed for a more complete and exhaustive representativeness study.

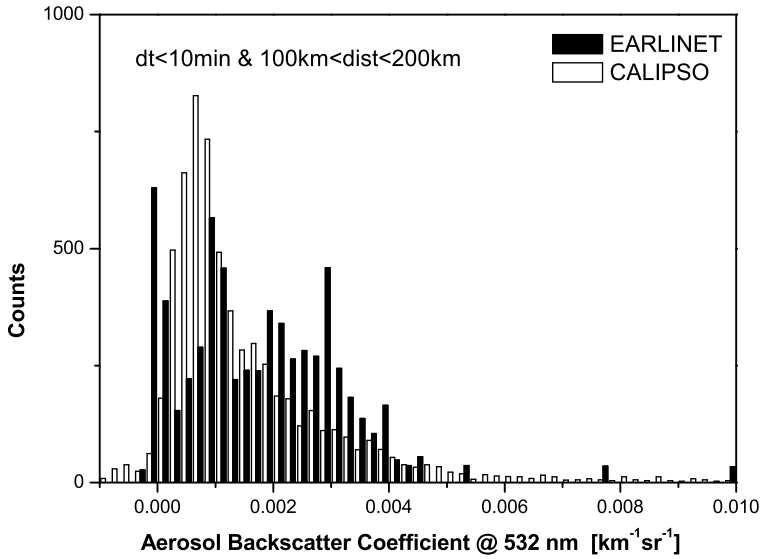

Figure 8.9: Count distributions of EARLINET and CALIPSO measured values of aerosol backscatter coefficient at 532 nm for a time shift lower than 10 minutes and distances between 100 and 200 km.

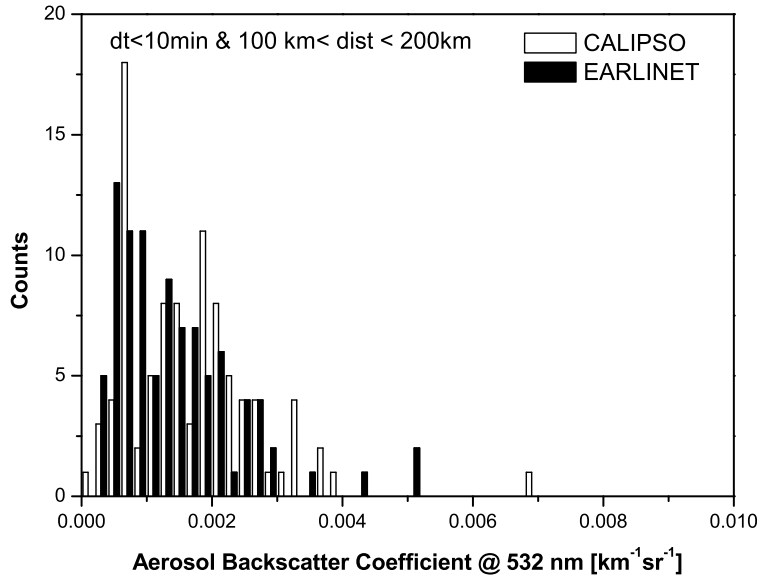

Figure 8.10: Same as Fig. 8.9, but calculated on the mean profiles observed within 10 minutes as time shift and for distances between 100 and 200 km.

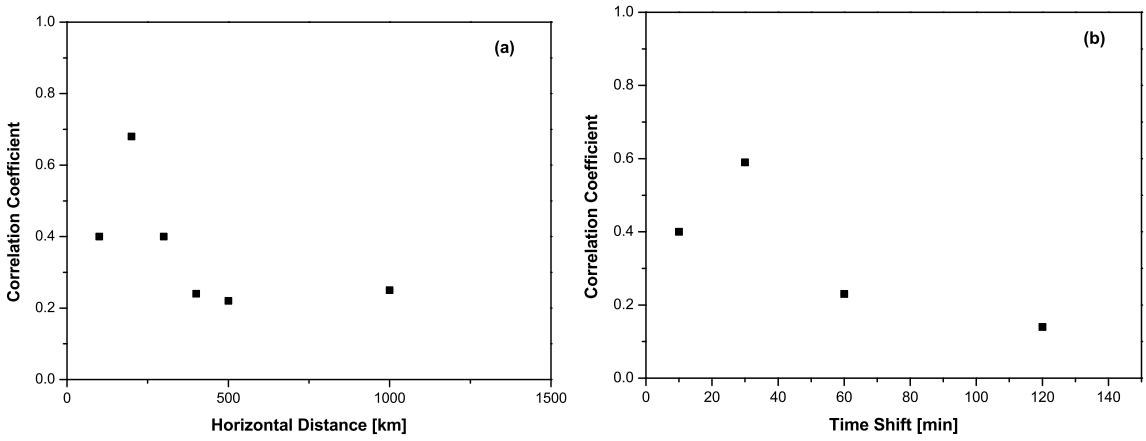

Figure 8.11: Same as Fig. 8.8, but calculated on the mean profiles observed within a) the 6 horizontal distance classes and b) the different time shift ranges.

Chapter 9

Conclusions and recommendations

In this report, we have presented first steps to establish a long-term aerosol and cloud database from ground-based and spaceborne lidar observations in order to harmonize global observations from space with different sensors over the next decade. For this purpose, a correlative set of data taken with the ground-based network EARLINET and with CALIOP onboard CALIPSO over a period of 18 months has been collected and exploited. Sixteen EARLINET stations participated in the study. They provided measurements at multiple wavelengths which have been used to derive wavelength conversion factors to relate spaceborne observations from CALIPSO with its lidar operating at 532 and 1064 nm to future observations with 355-nm high-spectral-resolution lidars. Furthermore, the spatial distribution of stations allowed us to study the representativeness of cross sections along an orbit against network observations.

Based on a comprehensive sample of more than 1300 observations performed by EARLINET stations during overpasses of CALIPSO from May 2008 to October 2009, a relational database has been set up which contains information on EARLINET and CALIPSO Level 2 profile data, EARLINET-CALIPSO difference profiles, geometrical and optical data of a large number of selected aerosol and cloud layers from EARLINET measurements and respective comparisons of EARLINET and CALIPSO layer products. An aerosol and cloud classification scheme has been developed and applied to the database. The aerosol classification has been evaluated in detail, based on a critical assessment of the CALIPSO typing schemes and built on the expert knowledge within EARLINET and the experience of the partners gained in field experiments around the world.

Without repeating the results reported in the previous chapters, in the following we summarize our conclusions and recommendations with specific view on ongoing and future algorithm development studies related to the EarthCARE and ADM missions. Finally, we discuss the gaps in the database and the possibilities to fill them with additional

experimental data.

Recommendations for EarthCARE algorithm developments

In the course of the study, we gained experience with CALIPSO data which can be useful for ongoing algorithm developments for upcoming ESA missions, in particular EarthCARE with its high-spectral-resolution lidar ATLID.

Cloud-aerosol discrimination
From the EARLINET–CALIPSO comparison studies we found that cloud-aerosol discrimination is a very critical issue. Problems occur in particular for thick dust layers and thin ice clouds (with optical thicknesses of the order of 1–2), because these targets exhibit very similar optical properties. Thus a reliable aerosol-cloud discrimination should consider not only optical data but a multitude of parameters, i.e. lidar-derived products, auxiliary data, and geographical constraints.

Conversion factors
Conversion factors can only be applied based on a common and reliable aerosol typing for different spaceborne missions, i.e., a common typing scheme for CALIPSO and EarthCARE is required. We have shown that, in principle, it is possible to distinguish major aerosol types with ATLID in the same way as with CALIOP, even if a different set of parameters is used in the classification. Thus we recommend to develop an ATLID aerosol classification scheme which uses the same pure aerosol types as the CALIPSO algorithm. However, we have also demonstrated that aerosol mixtures play an important role. Therefore, we recommend to consider aerosol mixtures in a more sophisticated way than in the CALIPSO algorithm, e.g., by using probability density functions in a multi-parameter space (or at least for the two-dimensional lidar-ratio–depolarization-ratio relation).

Multiple scattering
We have found that multiple scattering is an issue, not only for clouds but also for aerosol, in particular mineral dust. The consequences for extinction and optical depth retrievals have to be studied carefully with view on the ATLID algorithm developments. Aerosol typing becomes a new relevance in context. The identification of dust and the quantification of the dust content in mixed aerosol is an important task. Dust identification mainly relies on the measurement of the particle depolarization ratio, which thus has to be derived with care. The knowledge on microphysical particle properties—multiple-scattering effects are controlled by the particle size—has to be improved. Studies with multiwavelength lidars and the inversion of particle microphysical parameters are very valuable in this context.

Uncertainties and underestimation of aerosol load
The CALIPSO layer approach obviously leads to uncertainties and an underestimation

of aerosol load. Aerosol layers which are clearly seen in Level 1 data often do not appear in Level 2 products. The aerosol layer detection often suffers from apparent layer lower boundaries caused by strong attenuation. Even if the situation has remarkably improved with the release of the CALIPSO Level 2 Version 3 data—the algorithm is forced now to derive parameters from the lowest identified layer down to the ground—, we believe that this issue would need further investigation. In contrast to CALIPSO, for ATLID a profile approach is foreseen, i.e. Level 2 products will be delivered as closed profiles from the top of the atmosphere to the ground. Layer products will be retrieved in addition. It has to be studied, which consequences the different approaches have with view on the conversion and comparability of products from the different missions.

Appropriate horizontal averaging

Appropriate horizontal averaging is a critical aspect regarding aerosol detection. CALIPSO aerosol profile data in Level 2 Version 2 products are provided with 40 km resolution. Level 2 Version 3 products have 5 km resolution, but up to 80 km horizontal averaging is used for the layer detection. ATLID data are planned to be provided with 10-km horizontal resolution, probably with a downscaling to 1 km, but horizontal averaging of the order of 100 km will be required to detect thin aerosol layers as well. Also here, the consequences for reliable conversion schemes and the comparability of the products have to be studied.

Conclusions for ALADIN

The importance of depolarization-ratio measurements for aerosol typing and ice-water cloud discrimination has clearly been shown in this study. Conversion factors are only useful when a trustworthy aerosol classification is possible. For ALADIN, the concept developed in this study cannot be directly applied. Because ALADIN is primarily designed for wind measurements, the instrument has several drawbacks for aerosol and cloud detection.

ALADIN transmits circular-polarized light. Only the co-polar component of the backscattered light is detected. This will cause a systematic underestimation of the backscatter coefficient for depolarizing targets, i.e. ice clouds and dust/soil/ash-containing aerosols. There is not much experience in the measurement of circular depolarization ratios with ground-based instruments. From scattering theory, a relationship between linear (δ^l) and circular depolarization (δ^c) follows, which holds for symmetric particle shapes and random orientation:

$$\delta^c = \frac{2\delta^l}{1-\delta^l}\,. \tag{9.1}$$

If we consider typical linear depolarization ratios of 0.4–0.6 for cirrus clouds and 0.35 for large dust and ash particles, we find circular depolarization ratios of 1.3–3 for ice clouds and 0–1 for aerosols, i.e. the cross-polar component can be up to three times higher than

the co-polar component in ice clouds. Therefore, ALADIN will underestimate the backscatter coefficient by 50% to 75% in ice clouds and by up to 50% in dust/ash-containing aerosols. Extinction measurements are not influenced by depolarization effects. Thus the extinction-to-backscatter ratio (lidar ratio) will be overestimated by the same factor by which the backscatter coefficient is underestimated, i.e. neither the depolarization ratio nor a trustworthy value of the lidar ratio is measured. Therefore, aerosol typing and ice/water discrimination after the methods discussed and applied in this study will practically not be possible with ALADIN. Vice versa, because such information is missing, empirical corrections of the polarization losses will be very difficult. This problem could only be overcome when supplementary information, e.g., aerosol typing from independent observations with other sensors, would be used.

Gaps and recommendations for future developments

The long-term aerosol and cloud database is fed with data from a continental European network so far. Therefore, it lacks information content on aerosol properties in other regions of the globe. In particular, data of clean marine aerosol, continental pollution in Eastern and Southeastern Asia, Asian dust, and tropical and sub-tropical biomass-burning aerosol are required to cover major aerosol sources not considered in the database so far. Observations with multiwavelength lidars to derive conversion factors are available from a number of field experiments and targeted observations performed by partners of this study over the past 15 years:

- During the Aerosol Characterization Experiment ACE–2 in Portugal in 1997, the multiwavelength lidar of the Leibniz Institute for Tropospheric Research (IfT) took measurements in Sagres at the most southwesterly point of Europe in a marine environment. Observations pollution plumes and clean marine aerosol are available from this campaign (*Ansmann et al.*, 2001, 2002).

- Four campaigns distributed over one year and thus covering different seasons were performed by IfT in the frame of INDOEX (Indian Ocean Experiment) in the Maledives from 1999–2000. Observations of marine aerosol as well as pollution plumes from Southern and Southeastern Asia have been investigated and classified in detail (*Franke et al.*, 2001, 2003).

- The optical properties of clean Saharan dust were analyzed during the Saharan Mineral Dust Experiment SAMUM–1 in Morocco in May–June 2006. In this campaign, a specific focus was on the depolarization measurements at multiple wavelengths. Three ground-based lidars of MIM (Meteorological Institute of the University of Munich) and IfT and the airborne HSRL onboard the Falcon aircraft of DLR (Deutsches Zentrum für Luft- und Raumfahrt) were involved (*Freudenthaler et al.*, 2009; *Tesche et al.*, 2009b).

- The same instrumentation was applied during SAMUM–2 at Cape Verde in January–February 2008. Aged dust, marine aerosol, African biomass-burning smoke, and mixtures of dust and smoke were observed (*Tesche*, 2011; *Tesche et al.*, 2011; *Groß et al.*, 2011).

- A series of autonomously operated, multiwavelength Raman lidars named Polly^{XT} has been developed at IfT. They are used for targeted observations all over the world (see http://polly.tropos.de/lidar/index.php). One year of observations in the Amazonian Rain Forest in 2008/09 give insight into biomass-burning aerosol properties in South America. Cross sections along the Atlantic onboard the research vessel Polarstern (cruises in 2009, 2010, 2011), four months of measurements at Punta Arenas (Southern Chile) in 2009/10 and four months at Stellenbosch (South Africa) in 2010/11 deliver data for the southern hemisphere. Through cooperation within the Polly Network, also observations in the most populated areas of the world are available. The Finnish Meteorological Institute performed measurements near New Delhi, India, for one year in 2009/10. Another Polly system is operated by Baengnyeon Island Amospheric Research Center in South Korea since 2010.

The majority of data from these campaigns has been carefully evaluated and the results are published in the literature. The quality of the data is proven and their implementation in the long-term database would be possible without any risk. Correlative CALIPSO observations are available for all campaigns performed after July 2006.

In April–May 2010, EARLINET has monitored the dispersion of the Eyjafjallajökull ash plume over Europe. The respective data set has been evaluated with high priority and would be available for implementation in the long-term database as well. Volcanic ash is listed as one of the pure aerosol types, but no data are stored in the database yet.

Deficiencies also exist regarding quantitative observations of the particle linear depolarization ratio and its wavelength dependence. Simultaneous and well-calibrated measurements at the ATLID and CALIPSO wavelengths of 355 and 532 nm, respectively, are available from the SAMUM campaigns. Dedicated activities to improve depolarization-ratio observations and to establish a more comprehensive data set for different aerosol types are highly recommended. With respect to ALADIN, an in-depth investigation of the relationship of circular and linear depolarization ratios is of interest as well.

Only a limited number of cloud observations is included in the database so far. Clouds are highly variable in space and time. For most EARLINET stations the distance to the closest CALIPSO ground track is of the order of 20–40 km. Thus correlative cloud observations are hard to realize and often not representative. Furthermore, the different observation geometries from space and ground prevent quantitative comparisons of cloud properties in many cases. Optically thick clouds are not penetrated by the laser beam.

Thus the cloud properties can be investigated either near the cloud base with the ground-based lidar or near the cloud top with the spaceborne system. Multiple scattering effects influence ground-based and spaceborne cloud measurements in different ways. Also depolarization observations are ambiguous, because most EARLINET lidars are vertically pointing whereas CALIOP is pointing off-nadir. Targeted measurements in the vicinity of the satellite track together with a dedicated observation and data evaluation strategy, probably in combination with other instruments such as cloud radars, are required for an in-depth cloud comparison study in the future.

External use of the long-term aerosol and cloud database

Even if the long-term aerosol and cloud database requires further efforts and input in the future, it already represents a valuable tool for a variety of investigations. The database has been used in VRAME (Vertically Resolved Aerosol Model for Europe from a Synergy of EARLINET and AERONET data) to derive characteristic aerosol optical properties that shall be implemented in an aerosol model used for atmospheric corrections in ocean-color retrievals. The database as well as other results from the present study will also be made available for LIVAS (Lidar Climatology of Vertical Aerosol Structure for Space-Based Lidar Simulation Studies). This upcoming project could also help improving the database by contributing new data sets.

Bibliography

Ackermann, J. (1998), The extinction-to-backscatter ratio of tropospheric aerosol: A numerical study, *J. Atmos. Ocean. Tech.*, *15*, 1043–1050.

Amiridis, V., D. Balis, E. Giannakaki, A. Stohl, S. Kazadzis, and M. Koukouli (2008), Optical characteristics of smoke aerosols over SE Europe determined from Raman lidar and sunphotometric measurements, presented at EARLINET Workshop, Thessaloniki, Greece.

Anderson, T. L., S. J. Masonis, D. S. Covert, N. C. Ahlquist, S. G. Howell, A. D. Clarke, and C. S. McNaughton (2003), Variability of aerosol optical properties derived from in situ aircraft measurements during ACE-Asia, *J. Geophys. Res.*, *108*, 8647, doi: 10.1029/2002JD003247.

Anselmo, T., et al. (2006), Cloud–Aerosol LIDAR Pathfinder Satellite Observations, Data Management System, Data Products Catalog, *Tech. rep.*, available at http://www-calipso.larc.nasa.gov/resources/project_documentation.php.

Ansmann, A., M. Riebesell, and C. Weitkamp (1990), Measurements of atmospheric aerosol extinction profiles with a Raman lidar, *Optics Letts.*, *15*, 746–748.

Ansmann, A., U. Wandinger, M. Riebesell, C. Weitkamp, and W. Michaelis (1992a), Independent measurement of extinction and backscatter profiles in cirrus clouds by using a combined Raman elastic-backscatter lidar, *Appl. Opt.*, *31*, 7113–7131.

Ansmann, A., U. Wandinger, M. Riebesell, C. Weitkamp, E. Voss, W. Lahmann, and W. Michaelis (1992b), Combined Raman elastic-backscatter lidar for vertical profiling of moisture, aerosol extinction, backscatter and lidar ratio, *Appl. Phys. B*, *55*, 18–28.

Ansmann, A., I. Mattis, U. Wandinger, F. Wagner, J. Reichardt, and T. Deshler (1997), Evolution of the Pinatubo aerosol: Raman lidar observations of particle optical depth, effective radius, mass, and surface area over central Europe at 53.4° N, *J. Atmos. Sciences*, *54*, 2630–2641.

Ansmann, A., F. Wagner, D. Althausen, D. Müller, A. Herber, and U. Wandinger (2001), European pollution outbreaks during ACE 2: Lofted aerosol plumes observed with Raman lidar at the Portuguese coast, *J. Geophys. Res.*, *106*, 20,725–20,733.

Ansmann, A., F. Wagner, D. Müller, D. Althausen, A. Herber, W. v. Hoyningen-Huene, and U. Wandinger (2002), European pollution outbreaks during ACE 2: Optical particle properties inferred from multiwavelength lidar and star/Sun photometry, *J. Geophys. Res.*, *107*, 4259, doi:10.1029/2001JD001109.

Ansmann, A., R. Engelmann, D. Althausen, U. Wandinger, M. Hu, Y. Zhang, and Q. He (2005), High aerosol load over the Pearl River Delta, China, observed with Raman lidar and Sun photometer, *Geophys. Res. Letts.*, *32*, L13815, doi:10.1029/2005GL023094.

Ansmann, A., U. Wandinger, O. L. Rille, D. Lajas, and A. G. Straume (2006), Particle backscatter and extinction profiling with the spaceborne high-spectral–resolution Doppler lidar ALADIN: methodology and simulations, *Appl. Opt.*, *46*, 6606–6622.

Ansmann, A., et al. (2003), Long-range transport of Saharan dust to northern Europe: The 11–16 October 2001 outbreak observed with EARLINET, *J. Geophys. Res.*, *108*, 4783, doi:10.1029/2003JD003757.

Ansmann, A., et al. (2010), The 16 April 2010 major volcanic ash plume over central Europe: EARLINET lidar and AERONET photometer observations at Leipzig and Munich, Germany, *Geophys. Res. Letts.*, *37*, L13810, doi:10.1029/2010GL043809.

Baars, H., A. Ansmann, R. Engelmann, and D. Althausen (2008), Continuous monitoring of the boundary-layer top with lidar, *Atmos. Chem. Phys. Discuss.*, *8*, 10,749–10,790.

Bissonnette, L. R. (1986), Sensitivity analysis of lidar inversion algorithm, *Appl. Opt.*, *25*, 2112–2125.

Böckmann, C., et al. (2004), Aerosol lidar intercomparison in the framework of the EARLINET project. 2. Aerosol backscatter algorithms, *Appl. Opt.*, *43*, 977–989.

Brooks, I. M. (2003), Finding boundary layer top: Application of a wavelet covariance transform to lidar backscatter profiles, *J. Atmos. Ocean. Tech.*, *20*, 1092–1105.

Cattrall, C., J. Reagan, K. Thome, and O. Dubovik (2005), Variability of aerosol and spectral lidar and backscatter and extinction ratios of key aerosol types derived from selected Aerosol Robotic Network locations, *J. Geophys. Res.*, *110*, D10S11, doi:10.1029/2004JD005124.

De Tomasi, F., A. M. Tafuro, and M. R. Perrone (2006), Height and seasonal dependence of aerosol optical properties over southeast Italy, *J. Geophys. Res.*, *111*, D10203, doi:10.1029/2005JD006779.

Diner, D. J., et al. (2004), PARAGON: An integrated approach for characterizing aerosol climatic and environmental interactions, *Bull. American Meteorol. Soc.*, *85*, 1491–1501.

Draxler, R. R. (2003), Evaluation of an ensemble dispersion calculation, *J. Appl. Meteor.*, *42*, 308–317.

Draxler, R. R., and G. D. Hess (1997), Description of the HYSPLIT_4 modeling system, *Tech. rep.*, http://www.arl.noaa.gov/ready/hysplit4.html.

Draxler, R. R., and G. D. Hess (1998), An overview of the HYSPLIT_4 modelling system for trajectories, dispersion, and deposition, *Aust. Meteor. Mag.*, *47*, 295–308.

Emanuel, K. A., and M. Živković-Rothman (1999), Development and evaluation of a convection scheme for use in climate models, *J. Atmos. Sciences*, *56*, 1766–1782.

European Space Agency (ESA) (2004), Earth Clouds, Aerosols, and Radiation Explorer, ESA SP–1279(1), *Tech. rep.*, ESTEC, Noordwijk, The Netherlands.

Fernald, F. G. (1984), Analysis of atmospheric lidar observations: Some comments, *Appl. Opt.*, *23*, 652–653.

Fernald, F. G., B. M. Herman, and J. A. Reagan (1972), Determination of aerosol height distributions by lidar, *J. Appl. Meteor.*, *11*, 482–489.

Flamant, C., J. Pelon, P. H. Flamant, and P. Durant (1997), Lidar determination of the entrainment zone thickness at the top of the unstable marine atmospheric boundary layer, *Boundary-Layer Meteorol.*, *83*, 247–284.

Forster, P., et al. (2007), in *Climate Change 2007: The Physical Science Basis, Contribution of Working Group I to the Fourth Assessment Report of the Intergovernmental Panel on Climate Change*, edited by S. Solomon, D. Qin, M. Manning, Z. Chen, M. Marquis, K. B. Averyt, M. Tignor, and H. L. Miller, Cambridge Univ. Press (http://www.ipcc.ch), New York.

Franke, K., A. Ansmann, D. Müller, D. Althausen, F. Wagner, and R. Scheele (2001), One-year observations of particle lidar ratio over the tropical Indian Ocean with Raman lidar, *Geophys. Res. Letts.*, *28*, 4559–4562.

Franke, K., A. Ansmann, D. Müller, D. Althausen, C. Venkataraman, M. S. Reddy, F. Wagner, and R. Scheele (2003), Optical properties of the Indo-Asian haze layer over the tropical Indian Ocean, *J. Geophys. Res.*, *108*, 4059, doi:10.1029/2002JD002473.

Freudenthaler, V., et al. (2009), Depolarization ratio profiling at several wavelengths in pure Saharan dust during SAMUM 2006, *Tellus, Ser. B*, *61*, 165–179.

Gonzales, R. (1988), Recursive technique for inverting the lidar equation, *Appl. Opt.*, *27*, 2741–2745.

Groß, S., M. Tesche, V. Freudenthaler, C. Toledano, M. Wiegner, A. Ansmann, D. Althausen, and M. Seefeldner (2011), Characterization of Saharan dust, marine aerosols and a mixture of biomass burning aerosols and dust by means of multiwavelength depolarization and Raman measurements during SAMUM-2, *Tellus, Ser. B*, *63, in press.*

Heintzenberg, J., et al. (2003), Arctic haze over Central Europe, *Tellus, Ser. B*, *55*, 796–807.

Hogan, R. J., M. D. Behera, E. J. O'Connor, and A. J. Illingworth (2004), Estimate of the global distribution of stratiform supercooled liquid water clouds using the LITE lidar, *Geophys. Res. Letts.*, *31*, L05106, doi:10.1029/2003GL018977.

Hostetler, C. A., Z. Liu, J. Reagan, M. Vaughan, D. Winker, M. Osborne, W. H. Hunt, K. A. Powell, and C. Trepte (2006), CALIOP Algorithm Theoretical Basis Document, Calibration and Level 1 Data Products, *Tech. rep.*, available at http://www-calipso.larc.nasa.gov/resources/project_documentation.php.

Hu, Y. (2007), Depolarization ratio–effective lidar ratio relation: Theoretical basis for space lidar cloud phase discrimination, *Geophys. Res. Letts.*, *34*, L11812, doi: 10.1029/2007GL029584.

Hu, Y., Z. Liu, D. Winker, M. Vaughan, V. Noel, L. Bissonnette, G. Roy, and M. McGill (2006), Simple relation between lidar multiple scattering and depolarization ratio for water clouds, *Optics Letts.*, *31*, 1809–1811.

Hu, Y., et al. (2007), The depolarization–attenuated backscatter relation: CALIPSO lidar measurements vs. theory, *Opt. Express*, *15*, 5327–5332.

Hu, Y., et al. (2009), CALIPSO/CALIOP Cloud Phase Discrimination Algorithm, *J. Atmos. Ocean. Tech.*, *26*, 2293–2309.

Jäger, H., and T. Deshler (2002), Lidar backscatter to extinction, mass and area conversions for stratospheric aerosols based on midlatitude balloonborne size distribution measurements, *Geophys. Res. Letts.*, *29*, 1929, doi:10.1029/2002GL015609.

Kaufman, Y. F., B. N. Holben, D. Tanré, I. Slutsker, A. Smirnov, and T. F. Eck (2000), Will aerosol measurements from Terra and Aqua polar orbiting satellites represent the daily aerosol abundance and properties?, *Geophys. Res. Letts.*, *27*, 3861–3864.

Klett, F. G. (1981), Stable analytical solution for processing lidar returns, *Appl. Opt.*, *20*, 211–220.

Klett, F. G. (1985), Lidar inversion with variable backscatter/extinction ratios, *Appl. Opt.*, *24*, 1638–1643.

Kovalev, V. A. (1995), Sensitivity of the lidar solution to errors of the aerosol backscatter–to–extinction ratio: Influence of a monotonic change in the aerosol extinction coefficient, *Appl. Opt.*, *34*, 3457–3462.

Kovalev, V. A., and W. E. Eichinger (Eds.) (2004), *Elastic Lidar. Theory, Practice, and Analysis Methods*, 400 pp., Wiley-VCH, Weinheim, Germany.

Kunz, G. J. (1996), Transmission as an input boundary value for an analytical solution of a single-scatter lidar equation, *Appl. Opt.*, *35*, 3255–3260.

Liu, Z., M. A. Vaughan, D. M. Winker, C. Hostetler, L. R. Poole, D. Hlavka, W. Hart, and M. McGill (2004), Use of probability distribution functions for discriminating between cloud and aerosol in lidar backscatter data, *J. Geophys. Res.*, *109*, D15202, doi: 10.1029/2004JD004732.

Liu, Z., A. H. Omar, Y. Hu, M. A. Vaughan, and D. M. Winker (2005), CALIOP Algorithm Theoretical Basis Document, Part 3: Scene Classification Algorithms, *Tech. rep.*, available at http://www-calipso.larc.nasa.gov/resources/project_documentation.php.

Liu, Z., R. Kuehn, M. Vaughan, D. Winker, A. Omar, K. Powell, C. Trepte, Y. Hu, and C. Hosttler (2010), The CALIPSO cloud and aerosol discrimination: version 3 algorithm and test results, in *Proceedings of the 25th International Laser Radar Conference*, pp. 1245–1248, St. Petersburg, Russia, 5–9 July 2010.

Liu, Z., et al. (2008), CALIPSO lidar observations of the optical properties of Saharan dust: A case study of long-range transport, *J. Geophys. Res.*, *113*, D07207, doi: 10.1029/2007JD008878.

Liu, Z., et al. (2009), The CALIPSO lidar cloud and aerosol discrimination: Version 2 algorithm and initial assessment of performance, *J. Atmos. Ocean. Tech.*, *26*, 1198–1213.

Matthias, V., et al. (2004), Vertical aerosol distribution over Europe: Statistical analysis of Raman lidar data from 10 European Aerosol Research Lidar Network (EARLINET) stations, *J. Geophys. Res.*, *109*, D18201, doi:10.1029/2004JD004638.

Mattis, I., A. Ansmann, D. Müller, U. Wandinger, and D. Althausen (2002), Dual-wavelength Raman lidar observations of the extinction-to-backscatter ratio of Saharan dust, *Geophys. Res. Letts.*, *29*, 1306, doi:10.1029/2002GL014721.

Mattis, I., A. Ansmann, U. Wandinger, and D. Müller (2003), Unexpectedly high aerosol load in the free troposphere over central Europe in spring/summer 2003, *Geophys. Res. Letts.*, *30*, 2178, doi:10.1029/2003GL018442.

Mattis, I., A. Ansmann, D. Müller, U. Wandinger, and D. Althausen (2004), Multiyear aerosol observations with dual-wavelength Raman lidar in the framework of EARLINET, *J. Geophys. Res.*, *109*, D13203, doi:10.1029/2004JD004600.

Mattis, I., et al. (2010), Volcanic aerosol layers observed with multiwavelength Raman lidar over central Europe in 2008–2009, *J. Geophys. Res.*, *115*, D00L04, doi:10.1029/2009JD013472.

Menut, L., C. Flamant, J. Pelon, and P. H. Flamant (1999), Urban boundary-layer height determination from lidar measurements over the Paris area, *Appl. Opt.*, *38*, 945–954.

Mona, L., A. Amodeo, M. Pandolfi, and G. Pappalardo (2006), Saharan dust intrusions in the Mediterranean area: Three years of Raman lidar measurements, *J. Geophys. Res.*, *111*, D16203, doi:10.1029/2005JD006569.

Mona, L., G. Pappalardo, A. Amodeo, G. D'Amico, F. Madonna, A. Boselli, A. Giunta, F. Russo, and V. Cuomo (2009), One year of CNR–IMAA multi-wavelength Raman lidar measurements in correspondence of CALIPSO overpass: Level 1 products comparison, *Atmos. Chem. Phys.*, *9*, 7213–7228.

Müller, D., I. Mattis, U. Wandinger, D. Althausen, A. Ansmann, O. Dubovik, S. Eckhardt, and A. Stohl (2003), Saharan dust over a Central European EARLINET–AERONET site: Combined observations with Raman lidar and Sun photometer, *J. Geophys. Res.*, *108*, 4345, doi:10.1029/2002JD002918.

Müller, D., I. Mattis, B. Wehner, D. Althausen, U. Wandinger, A. Ansmann, and O. Dubovik (2004), Comprehensive characterization of Arctic haze from combined observations with Raman lidar and Sun photometer, *J. Geophys. Res.*, *109*, D13206, doi:10.1029/2003JD004200.

Müller, D., I. Mattis, U. Wandinger, A. Ansmann, D. Althausen, and A. Stohl (2005), Raman lidar observations of aged Siberian and Canadian forest-fire smoke in the free troposphere over Germany in 2003: Microphysical particle characterization, *J. Geophys. Res.*, *110*, D17201, doi:10.1029/2004JD005756.

Müller, D., M. Tesche, H. Eichler, R. Engelmann, D. Althausen, A. Ansmann, Y. F. Cheng, Y. H. Zhang, and M. Hu (2006), Strong particle light-absorption over the Pearl River Delta (South China) and Beijing (North China) determined from combined Raman lidar and Sun photometer observations, *Geophys. Res. Letts.*, *33*, L20811, doi:10.1029/2006GL027196.

Müller, D., I. Mattis, A. Ansmann, U. Wandinger, C. Ritter, and D. Kaiser (2007), Multiwavelength Raman lidar observations of particle growth during long-range transport of forest-fire smoke in the free troposphere, *Geophys. Res. Letts.*, *34*, L05803, doi: 10.1029/2006GL027936.

Nickovic, S., A. Papadopoulos, O. Kakaliagou, and G. Kallos (2001), Model for prediciton of desert dust cycle in the atmosphere, *J. Geophys. Res.*, *106*, 18,113–18,129.

O'Connor, E. J., A. J. Illingworth, and R. Hogan (2004), A technique for autocalibration of cloud lidar, *J. Atmos. Ocean. Tech.*, *21*, 777–786.

Omar, A. H., J.-G. Won, D. M. Winker, S.-C. Yoon, O. Dubovik, and M. P. McCormick (2005), Development of global aerosol models using cluster analysis of Aerosol Robotic Network (AERONET) measurements, *J. Geophys. Res.*, *110*, D10S14, doi: 10.1029/2004JD004874.

Omar, A. H., et al. (2009), The CALIPSO automated aerosol classification and lidar ratio selection algorithm, *J. Atmos. Ocean. Tech.*, *126*, 1994–2014.

Papayannis, A., et al. (2008), Systematic lidar observations of aerosol optical properties during Saharan dust intrusions over Europe, in the frame of EARLINET (2000-2002): Statistical analysis and results, *J. Geophys. Res.*, *113*, D10204, doi: 10.10129/2007JD9028.

Pappalardo, G., A. Amodeo, L. Mona, M. Pandolfi, N. Pergola, and V. Cuomo (2004a), Raman lidar observations of aerosol emitted during the 2002 Etna eruption, *Geophys. Res. Letts.*, *31*, L05120, doi:10.1029/2003GL019073.

Pappalardo, G., et al. (2004b), Aerosol lidar intercomparison in the framework of the EARLINET project. 3. Raman lidar algorithm for aerosol extinction, backscatter and lidar ratio, *Appl. Opt.*, *43*, 5370–5385.

Pappalardo, G., et al. (2010), EARLINET correlative measurements for CALIPSO: first intercomparison results, *J. Geophys. Res.*, *115*, D00H19, doi:10.1029/2009JD012147.

Pérez, C., S. Nickovic, J. M. Baldasano, M. Sicard, F. Rocadenbosch, and V. E. Cachorro (2006a), A long Saharan dust event over the western Mediterranean: Lidar, Sun photometer observations, and regional dust modeling, *J. Geophys. Res.*, *111*, D15214, doi:10.1029/2005JD006579.

Pérez, C., S. Nickovic, G. Pejanovic, J. M. Baldasano, and E. Özsoy (2006b), Interactive dust-radiation modeling: A step to improve weather forecasts, *J. Geophys. Res.*, *111*, D16206, doi:10.1029/2005JD006717.

Powell, K. A., M. Vaughan, R. Rogers, R. Kuehn, W. H. Hunt, K.-P. Lee, and T. D. Murray (2010), The CALIOP 532 nm channel daytime calibration: version 3 algorithm, in *Proceedings of the 25th International Laser Radar Conference*, pp. 1367–1370, St. Petersburg, Russia, 5–9 July 2010.

Prospero, J. M., P. Ginoux, O. Torres, S. Nicholson, and T. Gill (2002), Environmental characterization of global sources of atmospheric soil dust identified with Nimbus 7 Total Ozone Mapping Spectrometer (TOMS) absorbing aerosol product, *Rev. Geophys.*, *40*, 1002, doi:10.1029/2000RG000095.

Sakai, T., T. Nagai, Y. Zaizen, and Y. Mano (2010), Backscattering linear depolarization ratio measurements of mineral, sea-salt, and ammonium sulfate particles simulated in a laboratory chamber, *Appl. Opt.*, *49*, 4441–4449.

Sasano, Y., E. V. Browell, and S. Ismail (1985), Error caused by using a constant extinction/backscatter ratio in the lidar solution, *Appl. Opt.*, *24*, 3929–3932.

Schepanski, K., I. Tegen, B. Laurent, B. Heinold, and A. Macke (2007), A new Saharan dust source activation frequency map derived from MSG-SEVIRI IR-channels, *Geophys. Res. Letts.*, *34*, L18803, doi:10.1029/2007GL030168.

Stoffelen, A., G.-J. Marseille, E. Andersson, and D. G. H. Tan (2005), The Atmospheric Dynamics Mission for global wind field measurement, *Bull. American Meteorol. Soc.*, *86*, 73–87.

Stohl, A., and D. J. Thomson (1999), A density correction for Lagrangian particle dispersion models, *Boundary-Layer Meteorol.*, *90*, 155–167.

Stohl, A., M. Hittenberger, and G. Wotawa (1998), Validation of the Lagrangian particle dispersion model FLEXPART against large scale tracer experiment data, *Atmos. Env.*, *32*, 4245–4264.

Tao, Z., M. P. McCormick, D. Wu, Z. Liu, and M. A. Vaughan (2008), Measurements of cirrus cloud backscatter color ratio with a two-wavelength lidar, *Appl. Opt.*, *47*, 1478–1485.

Tesche, M. (2011), Vertical profiling of aerosol optical properties with multiwavelength aerosol lidar during the Saharan Mineral Dust Experiments. PhD Dissertation, University of Leipzig, 163 pp.

Tesche, M., A. Ansmann, D. Müller, D. Althausen, R. Engelmann, M. Hu, and Y. Zhang (2007), Particle backscatter, extinction, and lidar ratio profiling with Raman lidar in south and north China, *Appl. Opt.*, *46*, 6302–6308.

Tesche, M., A. Ansmann, D. Müller, D. Althausen, R. Engelmann, V. Freudenthaler, and S. Groß (2009a), Vertically resolved separation of dust and smoke over Cape Verde using multiwavelength Raman and polarization lidars during Saharan Mineral Dust Experiment 2008, *J. Geophys. Res.*, *114*, D13202, doi:10.1029/2009JD011862.

Tesche, M., et al. (2009b), Vertical profiling of Saharan dust with Raman lidars and airborne HSRL in southern Morocco during SAMUM, *Tellus, Ser. B*, *60*, 144–164.

Tesche, M., et al. (2011), Lidar profiling of ash and sulfate particle mass over central Europe after the eruption of the Eyjafjallajökull volcano, *J. Geophys. Res.*, *115, in press*, doi:10.1029/2010JD015567.

Vaughan, M., S. Young, D. Winker, K. Powell, A. Omar, Z. Liu, Y. Hu, and C. Hostetler (2004), Fully automated analysis of space-based lidar data: an overview of the CALIPSO retrieval algorithms and data products, in *Laser Radar Techniques for Atmospheric Sensing, Proc. of SPIE, Vol. 5575*, edited by U. N. Singh, pp. 16–30, SPIE, Bellingham, Wa., doi:10.1117/12.572024.

Vaughan, M., et al. (2010), Strategies for improved CALIPSO aerosol optical depth estimates, in *Proceedings of the 25th International Laser Radar Conference*, pp. 1340–1343, St. Petersburg, Russia, 5–9 July 2010.

Vaughan, M. A., D. M. Winker, and K. A. Powell (2005), CALIOP Algorithm Theoretical Basis Document, Part 2: Feature Detection and Layer Properties Algorithm, *Tech. rep.*, available at http://www-calipso.larc.nasa.gov/resources/project_documentation.php.

Vaughan, M. A., et al. (2009), Fully automated detection of cloud and aerosol layers in the CALIPSO lidar measurements, *J. Atmos. Ocean. Tech.*, *26*, 2034–2050.

Villani, M. G., L. Mona, A. Maurizi, G. Pappalardo, A. Tiesi, M. Pandolfi, M. D'Isidoro, V. Cuomo, and F. Tampieri (2006), Transport of volcanic aerosol in the troposphere: the case study of the 2002 Etna plume, *J. Geophys. Res.*, *111*, D21102, doi: 10.1029/2006JD007126.

Wandinger, U. (1998), Multiple-scattering influence on extinction- and backscatter-coefficient measurements with Raman and high-spectral-resolution lidars, *Appl. Opt.*, *37*, 417–427.

Wandinger, U., and A. Ansmann (2002), Experimental determination of the lidar overlap profile with Raman lidar, *Appl. Opt.*, *41*, 511–514.

Wandinger, U., A. Ansmann, J. Reichardt, and T. Deshler (1995), Determination of stratospheric aerosol microphysical properties from independent extinction and backscattering measurements with a Raman lidar, *Appl. Opt.*, *34*, 8315–8329.

Wandinger, U., M. Tesche, P. Seifert, A. Ansmann, D. Müller, and D. Althausen (2010), Size matters: Influence of multiple scattering on calipso light-extinction profiling in desert dust, *Geophys. Res. Letts.*, *37*, L10801, doi:10.1029/2010GL042815.

Wandinger, U., et al. (2002), Optical and microphysical characterization of biomass-burning and industrial-pollution aerosols from multiwavelength lidar and aircraft measurements, *J. Geophys. Res.*, *107*, 8125, doi:10.1029/2000JD000202.

Wandinger, U., et al. (2004), Air mass modification over Europe: EARLINET aerosol observations from Wales to Belarus, *J. Geophys. Res.*, *109*, D24205, doi: 10.1029/2004JD005142.

Wang, X., et al. (2008), Volcanic dust characterization by EARLINET during Etna's eruptions in 2001-2002, *Atmos. Env.*, *42*, 893–9056.

Weinzierl, B., A. Petzold, M. Esselborn, M. Wirth, K. Rasp, K. Kandler, L. Schütz, P. Köpke, and M. Fiebig (2009), Airborne measurements of dust layer properties, particle size distribution and mixing state of Saharan dust during SAMUM 2006, *Tellus, Ser. B*, *61*, 96–117.

Weisz, E., J. Li, W. P. Menzel, A. K. Heidinger, B. H. Kahn, and C.-Y. Liu (2007), Comparison of AIRS, MODIS, CloudSat and CALIPSO cloud top height retrievals, *Geophys. Res. Letts.*, *34*, L17811, doi:10.1029/2007GL030676.

Winker, D. M., J. R. Pelon, and M. P. McCormick (2003), The CALIPSO mission: Spaceborne lidar for observation of aerosols and clouds, in *Lidar Remote Sensing for Industry and Environment monitoring III, Proceedings of the Meeting, SPIE Volume: 4893*, edited by U. N. Singh, T. Itabe, and Z. Liu, pp. 1–11, SPIE EurOpto Series, Bellingham, Wa.

Winker, D. M., M. A. Vaughan, A. Omar, Y. Hu, K. A. Powell, Z. Liu, W. H. Hunt, and S. A. Young (2009), Overview of the CALIPSO mission and CALIOP data processing algorithms, *J. Atmos. Ocean. Tech.*, *26*, 2310–2323.

Young, S. A., D. M. Winker, M. A. Vaughan, Y. Hu, and R. E. Kuehn (2008), CALIOP Algorithm Theoretical Basis Document, Part 4: Extinction Retrieval Algorithms, *Tech. rep.*, available at http://www-calipso.larc.nasa.gov/resources/project_documentation.php.

Zerefos, C., et al. (2006), A complex study of Etna's plume from ground-based, in situ and space borne onservations, *Int. J. Remote Sensing*, *27*, 1855–1864.

Appendix A

Database access

The relational database established in this study is maintained by the Leibniz Institute for Tropospheric Research, Leipzig, Germany. It is based on open-source software (PostgreSQL) and allows platform-independent access. A graphical user interface (pgAdmin III) is provided. External files are stored in NetCDF and HDF formats. The access to the database server is granted via secure channels (openVPN). Each channel is dedicated to a single user/computer which is identified by a crypto certificate (key).

The database is open for scientific use. Potential users should contact:

Dr. Ulla Wandinger
Leibniz Institute for Tropospheric Research
Permoserstr. 15
04318 Leipzig
Germany
ulla@tropos.de